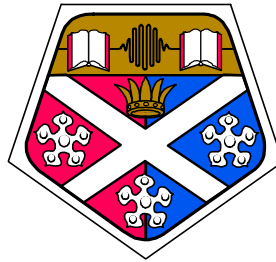# Highly Polarised Ytterbium Doped Photonic Crystal Fibre Lasers

A thesis presented in fulfilment
of the requirements for the degree of
Doctor of Philosophy

By

Fiona Cameron Wright

Department of Physics, University of Strathclyde

2010

This thesis is dedicated to my Gran, Evelyn Frame. A wonderful woman who we all miss dearly.

Abstract

The work presented in this thesis concerns the demonstration and characterisation of the first double cladding highly polarised, through form birefringence alone, Yb^{3+} doped Photonic Crystal Fibre (PCF) laser. A numerical model developed as part of this work investigates the power characteristics of PCF lasers as well as their polarisation properties. Numerical mode modelling is carried out for the novel PCF laser structure and optimum geometry is proposed.

The polarisation maintaining PCF laser had fibre attenuation of $0.48dBm^{-1}$, operating wavelength between 1020nm and 1080nm depending on fibre length, internal quantum efficiency of 77%, polarisation ratio of 200:1 and a core to cladding loss of $0.05Wm^{-1}$, which was confirmed by numerical modelling developed as part of this work. 2.9W of highly polarised single mode output was carried by the core and a difference in output power from both ends of the laser was again shown to be in agreement with numerical modelling results. The laser had an elliptical fundamental mode profile with $1/e^2$ radii 3μm by 6μm with M^2 values 1.72 and 2.8. Numerical mode modelling was carried out to determine the optimum PCF structure that would minimise the loss of light from the core to the cladding. The theoretical modelling, carried out as part of this research, predicts that the highly polarised PCF laser could be optimised by increasing the small air hole radii to 2.5μm, reducing the larger air hole diameters to 3.6μm and by reducing the pitch of the air holes to less than 7μm.

Based on the same PCF structure as the highly polarised PCF laser, a 75% Bragg grating was incorporated into the PCF laser which allowed the first demonstration and characterisation of a double cladding highly polarised Yb^{3+} doped PCF laser with a 75% incorporated Bragg grating. The self pulsing nature of this laser is discussed and a double pumping scheme, using a 980nm and a 940nm diode laser, is employed to

successfully suppress these pulsations. The maximum output laser power was 6.5W at 1061.6nm.

Both of these highly polarised PCF lasers are used to demonstrate second harmonic generation, in a lithium triborate crystal. An integer number of passes, n, through the crystal are shown to increase the intensity of the second harmonic light by a factor of n^2. Second harmonic generation using a periodically poled lithium niobate crystal and the highly polarised PCF laser with the incorporated Bragg grating is also demonstrated.

Fibre end facet angle polishing methods are explored and the successful suppression of stimulated emission from the PCF laser is achieved leading to the first demonstration of Q-switched operation of the novel highly polarised PCF laser.

Acknowledgements

First and foremost I would like to thank my supervisor Professor Erling Riis for his help and advice throughout my PhD. His encouragement and continued support has been invaluable and he has taught me a great deal during my time at Strathclyde. I also want to thank my second supervisor Dr Nigel Langford who gave advice and a second opinion when needed. Thanks must also go to NKT A/S for their financial support throughout the research.

I would like to thank the technicians from the Photonics workshop, Bob Wylie, Ewan MacLagan, Paul Hynd and Lisa Reid for all of their efforts. In particular, I would like to thank Ewan for all of his effort and patience during the early trial and error stages of the fibre cleaving and polishing. This leads me on to thanking Bob Dawson whose fibre polishing expertise was invaluable to my PhD.

My time spent at Strathclyde would never have been the same without the friendship and support of all the members of the Photonics Group, past and present: Gail McConnell, Richard Abram, Craig Garvie, Wei Zhang, Ian Norris, Kyle Gardner and Stephen McGinily. Kyle's practical jokes and enthusiasm has kept a smile on all of our faces in the group throughout the years. I can't imagine enjoying my time spent at Strathclyde as much as I have, without these friends, so thanks to you all. A special note of thanks must go to Stephen McGinily, a true friend, who has supported and encouraged me throughout my PhD. The countless nights of chi tea lattes have kept me going and without his support I would not be where I am today.

Throughout the years my family have been very supportive through everything I have done and the choices I have made so thank you. Finally I would like to thank my best friend, colleague and husband Stephen Wright for all of his love, support and encouragement.

Table of Contents

Chapter 1

Introduction

This introductory chapter provides the background and the motivation for the research presented in this thesis. A historical overview of optical fibre lasers and their constant development are detailed. A synopsis of each chapter and the principal results are also included.

1.1 Technological Background

Since the first laser demonstration of the ruby laser in 1960 by Maiman [1,2] the development of the first optical fibre laser was soon to follow and was achieved in 1961 by Snitzer [3]. It consisted of a glass fibre with a 300μm core diameter doped with neodymium (Nd) and side pumped by a pulsed flash-lamp. Despite this pumping scheme being inefficient at absorbing the pump power the early fibre lasers demonstrated the ability to provide very high gain amplification. Further work was continued in the 1960's by Koester *et al* [4] and Holst *et al* [5] leading to a Nd doped fibre laser with a gain of 47dB. The low threshold characteristic of fibre lasers was not exploited until 1973 by the development of fibre end pumping schemes [6, 7]. A significant advance in the fibre laser technology came in 1985 by Poole *et al* [8], who demonstrated lasing and amplification in mono-mode silica fibres pumped with low power semiconductor lasers. Coming soon after Poole's development, the first Continuous Wave (CW) single-mode Nd doped fibre laser system was constructed by Mears *et al* [9] which led to their demonstration of the first erbium (Er) doped CW and Q-switched fibre laser in 1986 [10]. This discovery proved invaluable for the telecommunications industry as the emission wavelength of 1.55μm, from Er, falls within the low loss third telecommunications window. Therefore, extensive research has been carried out over the years on Er doped fibre lasers and amplifiers [11]. Aside from applications in telecommunications, fibre lasers are suitable for

applications in sensing, medical devices, data storage, high resolution spectroscopy and material processing due to the extensive range of operating wavelengths from the ultraviolet to the mid-infrared accessible through various rare-earth dopants. Such dopants include Nd, Er, ytterbium (Yb), thulium (Tm), holmium (Hm) and praseodymium (Pr). The first Yb doped silica fibre laser was reported by Hanna *et al* in 1988 [12] which produced 4mW of output power tunable over the range 1.015 – 1.14µm when pumped by 40mW of 840nm light. Since then extensive research has been carried out using Yb as a dopant in fibre lasers [13-18]. Tm [19-23] and Hm [24-26] doped fibre lasers are of particular interest because they can oscillate at the eye safe wavelength of 2.0 µm making them suitable for applications in atmospheric pollution monitoring and coherent radar applications. Pr is another rare earth which has been explored as a dopant in fibre lasers due to its diverse lasing wavelength [27-29].

The most recent addition to the fibre laser family is the introduction of photonic crystal and photonic bandgap fibre lasers. Back in 1987 Sejeev John from the University of Toronto and Eli Yablonovitch from Bell Communications Research predicted the guidance of light by means of the photonic bandgap effect [30,31]. This is analogous to the theory of band structures in semiconductors, with forbidden bands, resulting from interactions between electrons and the periodic variations in potential created by the crystal lattice. It was proposed that photonic crystals, with optical bandgaps, could be created by replacing Schrödinger's equation with the classical wave equation for magnetic field interaction as well as replacing periodic variations in electric potential with periodic variations in refractive index. This would create a photonic structure which would inhibit the propagation of wavelengths corresponding to the photonic bandgaps but at the same time would allow the transmission of all other wavelengths. Although the principle of operation of these photonic structures was simple it was the manufacturing of them which proved to be difficult. In fact the first photonic bandgap material was not created by Yablonovitch until 1991 [32]. At the time this research was a hot topic of interest within the optics community. The basic concept was of interest to a group of researchers at the University of Southampton who believed they could apply the

photonic bandgap concept to optical fibres. Construction of the fibre structure proved difficult as they initially tried to drill air holes into a block of silica glass then draw the fibre down to the desired diameter. They were able to drill the central hollow core but were unable to drill the surrounding air hole structure. Therefore they changed their fabrication approach and opted to stack an arrangement of capillary tubes and solid glass rods in the desired structure to create their preform before drawing it down to the desired fibre diameter. By 1995 Russell and his research team had successfully created the first Photonic Crystal Fibre (PCF) [33]. The fibre they created had a solid glass core rather than the hollow core that they had initially intended. The cladding consisted of a triangular arrangement of micro structured air holes running the full length of the fibre. The guiding mechanism was by means of modified Total Internal Reflection (TIR) rather than by photonic bandgap guiding. They did not achieve photonic bandgap guiding because the air holes within the fibre were too small to achieve a sufficiently large air-filling fraction required for the photonic bandgap effect. This first demonstration of a new fibre technology set the foundations of an extensive and rapidly developing research field of optics.

In 1996, Russell moved his research group to the University of Bath where they continued to improve their fabrication methods. In 1999 they created the first true photonic bandgap guiding optical fibre [34]. Since then, world-wide research groups have carried out work exploring the characteristics of the PCF and photonic bandgap fibre. As the manufacturers are free to control the design of the complex micro structures they have great freedom and control over important fibre parameters such as their dispersion [35], non-linearity [36,37], numerical aperture, birefringence [38-41] and single or multi mode transmission characteristics [42]. The first photonic crystal fibre laser was demonstrated in 2000 by Wadsworth *et al* [43] and was doped with Yb^{3+}. Since then many photonic crystal fibre lasers have been reported scaling to high powers [44,45] of up to 1.36kW [46] using cladding pumped techniques. To date the main leaders in exploring the fabrication and application technology of these PCF and photonic bandgap fibres has been Russell and his colleagues from the University of Bath along with Richardson and his colleagues from the University of

Southampton. The main leader in high power PCF lasers and amplifiers to date has been carried out by Tunnermann and his colleagues at the Friedrich Schiller University in Jena, Germany. A spin-off company, Blaze Photonics, from the University of Bath was the first manufacturer of PCF and photonic bandgap fibre and they held all of the original patents for producing these structures. However, in 2000 a Danish company called Crystal Fibre A/S [47] was established as a spin out company from the Technical University of Denmark and in 2004 they acquired the assets of Blaze Photonics. Crystal Fibre is now the leading commercial company supplying a wide variety of PCF and photonic bandgap fibre world-wide. In fact the PCF lasers characterised in this research were manufactured and supplied by Crystal Fibre A/S. To date extensive research has been carried out exploring the endless technological possibilities of this relatively new technology and it continues to expand as the boundaries and limitations of this technology are continuously being stretched.

1.2 Solid State Lasers

Fibre lasers, the subject of this thesis, form a small group of the laser family of solid state lasers. These are lasers based on solid state gain media such as glass or crystals and are doped with rare earth or transition metal ions. Examples of solid state lasers include bulk lasers, fibre lasers or other types of waveguide lasers such as thin disc lasers. The long upper state lifetimes makes solid state lasers very suitable for Q-switching and mode locking applications. Many solid state lasers have traditionally been optically pumped by flash lamps which are relatively inexpensive and can provide high power. However, this type of pumping leads to moderate lifetime, fairly low power efficiency and unwanted thermal lensing effects in the gain medium. Diode lasers provide modern alternative pump sources, to the flash lamp pumps, for solid state lasers due to their long lifetime, compactness and higher beam quality.

A bulk laser is a solid state laser which has a bulk piece of doped crystal or glass as the gain medium. There is no waveguide structure therefore the beam propagates in free space between optical components and the beam radius is determined by the

design of the laser resonator rather than the gain medium. Bulk lasers are preferable for devices operating with high peak power, whereas low threshold and high gain operation is more easily achieved with waveguide lasers. A Nd^{3+}:YAG (ytterbium aluminium garnet) laser is an example of a popular bulk solid state laser which most commonly emits at 1064nm. In terms of their potential for wavelength tuning, most rare earth doped laser crystal such as Nd^{3+}:YAG, have a small gain bandwidth of the order of 10nm or less such that tuning is possible only in a limited range.

A thin disk laser is another type of diode pumped solid state laser which was introduced in the 1990s. The geometry of the gain medium, the laser crystal, is a thin disk where the thickness is considerably smaller than the laser beam diameter. Typical disk thickness is 100-200µm for a Yb:YAG thin disk laser. The heat which is generated is extracted longitudinally rather than transversely which results in weak thermal lensing. Thus, operation with very high beam quality and high output power up to 1kW can be achieved in comparison to only a few watts of output power produced by bulk solid state lasers.

Optical fibre lasers are lightweight, compact and have high potential for high average output power, high beam quality, high power efficiency and broad wavelength tunability. Due to the high gain efficiency fibre lasers have the potential to operate with very low pump powers. The fibre geometry allows heat distribution over a long length and good thermal management negates the need for extra heat dissipation units. Fibre gain media have a large gain bandwidth due to strongly broadened laser transitions in glasses which permit wide wavelength tuning ranges. Fibre lasers also have broad spectral regions with good pump absorption which makes the exact pump wavelength non-critical. Therefore, temperature stabilization of the pump diode is usually not necessary. Diffraction limited beam quality is easily obtained when using single mode fibres. Double cladding fibre structures, which consist of a single mode core with refractive index n_1, surrounded by an inner-cladding region of refractive index $n_2 < n_1$, which in turn is surrounded by an outer-cladding region of refractive index $n_3 < n_2$, allows high pump conversion efficiency. The inner-cladding region forms a second waveguide which can support multiple modes. Thus, single

mode output can be achieved when pumping with inexpensive multimode diode lasers. Polarisation maintaining lasers are used for sensing, laser cutting and nonlinear applications such as second harmonic generation. PCF lasers push the boundaries of existing fibre lasers, generating more desirable laser sources.

1.3 Thesis Outline

In **Chapter 2**, the basic theory of laser action will be given. Three and four level laser systems will be discussed and the spectroscopic properties of Yb^{3+} will be detailed.

Chapter 3 will give an overview of wave propagation in free space, step-index optical fibre and PCF. An overview of silica optical fibres and their geometry is given highlighting the differences between single mode and multimode fibres. A discussion of various fibre structures is presented emphasising double-cladding fibres as well as an introduction to different types of PCF. Various modelling techniques, which are employed to analyse properties of PCF's, will be discussed. A description of Gaussian beam properties will be given and the methodology utilised in this research to analyse the quality of real laser beams will be presented.

Chapter 4 will present a numerical model, developed as part of this research, which analyses the power characteristics of PCF lasers. The model gives an accurate representation of a real PCF laser as it includes loss of power from the core to the cladding as well as polarisation properties. The theoretical results obtained will be compared to the experimental results obtained as part of this research.

Chapter 5 begins with a discussion on fibre birefringence and the characterisation of test geometry PCF lasers leading to the presentation of the first highly polarised Yb^{3+} doped PCF laser through form birefringence alone. Experimental details and results for characterising this novel PCF laser in terms of power, fibre length dependence, beam quality and polarisation analysis are given. Numerical modelling carried out as part of this research leading to the prediction of an optimised highly polarised PCF laser structure is presented.

Chapter 6 reviews nonlinear optics and the basic theory of important nonlinear effects. A brief discussion of nonlinear materials and their properties will be given. For second harmonic generation a polarised light source is required, therefore second harmonic generation using the novel highly polarised Yb^{3+} doped PCF laser will be demonstrated for the first time. An integer number of passes, n, through the crystal are shown to increase the intensity of the second harmonic light by a factor of n^2.

A review of the theory of Q-switched lasers and the methods employed to create such lasers will be given in **Chapter 7**. Fibre end facet angle polishing methods carried will be explored and the successful suppression of stimulated emission from the PCF laser is achieved leading to the first demonstration of Q-switched operation of the novel highly polarised PCF laser.

The focus of **Chapter 8** will be the characterisation of a highly polarised Yb^{3+} doped PCF laser which has a 75% fibre Bragg grating written into the novel fibre structure. The self pulsing nature of this laser will be discussed along with pulse suppression techniques that were carried out as part of this research.

Chapter 9 presents the principal results, overall conclusions of the work presented in this thesis and possible future work. The work presented in this thesis was published in Optics Express [48], reviewed by Hecht [49], featured in Photonics Spectra [50], formed the basis of an oral presentation at the QEOD Europhoton Conference [51], featured as a poster presentation at the 17th International Laser Spectroscopy Conference [52] and won a poster prize at the NKT summer academy conference [53].

1.4 References

[1]   T. H. Maiman, "Stimulated optical radiation in ruby", Nature, Vol. 187, 1960 (pp493-494)

[2]   T. H. Maiman, "Optical and microwave-optical experiments in ruby", Physical Review Letters, Vol. 4, No. 11, 1960 (pp564-566)

[3]   E. Snitzer, "Optical maser action of Nd^{3+} in a barium crown glass", Physical Review Letters, Vol. 7, No. 12, 1961 (pp444-446)

[4]   C. J. Koester, E. Snitzer, "Amplification in a fiber laser", Appl. Opt. Vol. 3, 1964 (pp1182-1186)

[5]   G. C. Holst, E. Snitzer, R. Wallace, "High-coherence high-power laser system at 1.0621μ ", IEEE J. Quant. Electron. Vol. 5, 1969 (p342)

[6]   J. Stone, C. A. Burrus, "Neodymium-doped silica lasers in end-pumped fiber geometry", Appl. Phys. Lett. Vol. 23, 1973 (pp388-389)

[7]   J. Stone, C. A. Burrus, "Neodymium-doped fiber lasers: room temperature cw operation with an injection laser pump", Appl. Opt. Vol. 13, 1974 (pp1256-1258)

[8]   S. B. Poole, D. N. Payne, M. E. Fermann, "Fabrication of low loss optical fibres containing rare earth ions", Elect. Lett. Vol. 21, 1985 (pp737-738)

[9]   R. J. Mears, L. Reekie, S. B. Poole, D. N. Payne, "Neodymium-doped silica single-mode fibre lasers", Elec. Lett. Vol. 21, 1985 (pp738-740)

[10]   R. J. Mears, L. Reekie, S. B. Poole, D. N. Payne, "Low-threshold tuneable CW and Q-switched fibre laser operating at 1.55 μm", Elec. Lett. Vol. 22, 1986 (pp159-160)

[11]   E. Desurvire, "Erbium-doped fiber amplifiers", Wiley Interscience, New York, 1994

[12]   D. C. Hanna, R. M. Percival, I. R. Perry, R. G. Smart, P. J. Suni, J. E. Townsend, A. C. Tropper, "Continuous-wave oscillation of a monomode ytterbium-doped fibre laser", Elect. Lett. Vol. 24, No. 17, 1988 (p1111-1113)

[13]   J. R. Armitage, R. Wyatt, B. J. Ainslie, S. P. Craig-Ryan, "Highly efficient 980 nm operation of an Yb^{3+} - doped silica fibre laser", Elect. Lett. Vol. 25, 1989 (p299)

[14]   C. J. Mackenchnie, W. L. Barnes, D. C. Hanna, J. E. Townsend, "High power ytterbium (Yb^{3+}) – doped fibre laser operating at 1.12 μm region", Elect. Lett. Vol. 29, 1993 (p52)

[15]   J. Y. Allain, J. F. Bayon, M. Monerie, P. Bernage, P. Niay, "Ytterbium doped silica fibre laser with intracore Bragg gratings operating at 1.02 μm", Elect. Lett. Vol. 29, 1993 (p309)

[16]   J. M. Dawes, H. M. Pask, J. L. Archambault, J. E. Townsend, D. C. Hanna, L. Reekie, A. C. Tropper, "Single frequency lasers and efficient cladding-pumped lasers using Yb^{3+} doped silica fibre", Proceedings of the Euoropean Conference on Lasers and Electro-Optics CHJ1 1994

[17]   J. Y. Allain, M. Monerie, H. Poignant, "Ytterbium-doped fluoride fibre laser operating at 1.02 μm", Elect. Lett. Vol. 28, 1992 (p988)

[18]   J. Y. Allain, M. Monerie, H. Poignant, "High-efficient ytterbium-doped fluoride fibre laser", Journal of Non-Crystalline Solids, Vol. 161, 1993 (p270)

[19]   D. C. Hanna, I. M. Jauncey, R. M. Percival, I. R. Perry, R. G. Smart, P. J. Suni, J. E. Townsend, A. C. Tropper, "Continuous-wave oscillation of a monomode thulium-doped fibre laser", Elect. Lett. Vol. 24, 1988 (p1222-1223)

[20]   D. C. Hanna, J. M. McCarthy, I. R. Perry, P. J. Suni, "Efficient high power continuous wave operation of a monomode Tm-doped fibre laser at 2 μm pumped by Nd:YAG laser at 1.064 μm", Elect. Lett. Vol. 25, 1989 (p1365)

[21]   D. C. Hanna, R. M. Percival, R. G. Smart, A. Tropper, "Efficient and tunable operation of a Tm-doped fibre laser", Opt. Com. Vol. 75, 1990 (p283)

[22]   D. C. Hanna, I. R. Perry, J. R. Lincoln, J. E. Townsend, "A 1-watt thulium doped CW fibre laser operating at 2 μm", Opt. Com. Vol. 80, 1990 (p52-56)

[23]   S. Boj, E. Delevaque, J. Y. Allain, J. F. Bayon, P. Niay, P.Bernage, "High-efficiency diode pumped thulium doped silica fibre lasers with intracore Bragg gratings in the 1.9 – 2.1 μm band", Elect. Lett. Vol. 30, 1994 (p1019)

[24]   M. C. Brierley, P. W. Franc, C. A. Miller, "Lasing at 2.08 μm and 1.38 μm in a holmium doped fluorozirconate fibre laser", Elect. Lett. Vol. 24, 1988 (p539)

[25]   L. Wetenkamp, "Efficient CW operation of a 2.9 μm Ho^{3+} - doped fluorozirconate fibre laser pumped at 640 nm", Elec. Lett. 1990 (p883)

[26]   J. Y. Allain, M. Monerie, H. Poignant, "Room temperature CW tunable green upconversion holmium fibre laser", Elect. Lett. Vol. 26, 1991 (p261)

[27]   J. Y. Allain, M. Monerie, H. Paignant, "Tunable CW lasing around 610, 635, 695, 715, 885 and 910 nm in praseodymium-doped fluorozirconate fibre", Elect. Lett. Vol. 27, 1990 (p189)

[28]   R. G. Smart, D. C. Hanna, A. Tropper, S. T. Davey, S. F Carter, D. Szebesta, "CW room temperature upconversion lasing at blue, green and red wavelengths in infrared-pumped Pr^{3+} doped fluoride fibre", Elect. Lett. Vol. 27 1991 (p1307)

[29]   H. Doring, J. Peupelmann, F. Wenzel, "Pr^{3+} doped 1.3 μm fibre laser using direct coated dichroic mirrors", Elect. Lett. Vol. 31, 1995 (p1068)

[30]   S. John, "Strong localization of photons in certain disordered dielectric superlattices", Phys. Rev. Lett., Vol. 58, 1987, (pp2486-2489)

[31]   E. Yablonovitch, "Inhibited spontaneous emission in solid state Physics and electronics", Phys. Rev. Lett., Vol. 58, 1987, (pp2059-2062)

[32]   E. Yablonovitch, "Photonic band structure: The face-centered-cubic-case employing non-spherical atoms", Phys. Rev. Lett., Vol. 67, 1991, (pp2295-2298)

[33]   J. C. Knight, T. A. Birks, P. St. J.Russel, D. M. Atkin, "All-silica single-mode optical fiber with photonic crystal cladding", Opt. Lett. Vol. 21, No. 19, October 1996 (pp1547-1549)

[34]   R. F. Cregan, B. J. Mangan, J. C. Knight, T. A. Birks, P. St. J.Russel, P. J. Roberts, D. C. Allan, "Single-mode photonic bandgap guidance of light in air", Science 1999 (pp1537-1539)

[35]   J. C. Knight, J. Arriaga, T. A. Birks, A. Ortigosa-Blanch, W. J. Wadsworth, P. St. J. Russell, "Anomalous dispersion in photonic crystal fiber", IEEE Photonics Technology Lett. Vol. 12, No. 7, 2000 (pp807-809)

[36]   N. G. Broderick, T. M. Monro , P. J. Bennett, D. J. Richardson, "Nonlinearity in holey optical fibres: measurements and future opportunities", IEE Elect. Lett. Vol. 24, No. 20, 2000 (pp1395-1397)

[37]   K. J. Ranka, S. R. Windeler, A. J. Stentz, "Visible continuum generation "in air-silica microstructure optical fibers with anomalous dispersison at 800 nm", Optics Lett. Vol. 25, 2000 (pp25-27)

[38]   A. Oritigosa-Blancg, J. C. Knight, W. J. Wadsworth, J. Arriaga, B. J. Mangan, T. A. Birks, P. St. J.Russel, "Highly birefringerent photonic crystal fibres", Optics Lett. Vol. 25, No. 18, 2000 (pp1325-1327)

[39]   T. P. Hansen, J. Broeng, S. E. B. Libori, E. Knudsen, A. Bjarklev, J. R. Jenson, H. Simonsen, "Highly birefringent index-guiding photonic crystal fibres", IEEE Photonics Tech. Lett. Vol. 13, No. 6, 2001 (pp588-590)

[40]   K. Suzki, H. Kubota, S. Kawanishi, M. Tanaka, M. Fujita, "Optical properties of a low-loss polarization-maintaining photonic crystal fiber", Optics Express, Vol. 9, No.13, 2001 (pp676-680)

[41]   T. Ritari, H. Ludvigsen, M. Wegmuller, M. Legre, N. Gisin, J. R. Folkenberg, M D. Nielsen, "Experimental study of polarization properties of highly birefringent photonic crystal fibers", Optics Express, Vol. 12, No. 24, 2004 (pp5931-5939)

[42]   T. A. Birks, J. C. Knight, St. J. Russell, "Endlessly single-mode photonic crystal fiber", Optics Lett. Vol. 22, 1997 (pp961-963)

[43]   W. J. Wadsworth, J. C. Knight, W. H. Reeves, P. S. J. Russell, J Arriaga, "Yb^{3+}-doped photonic crystal fibre laser", Electronics Lett. Vol. 36, 2000 (pp1452 – 1454)

[44]   W. J. Wadsworth, R. M. Percival, G. Bouwmans, J. C. Knight, P. S. J. Russell, "High power air-clad photonic crystal fibre laser", Optics Express, Vol. 11. No. 1, 2003 (pp48-53)

[45]   J. Limpert, T. Schriber, S. Nolte, H. Zellmer, A. Tunnermann, R. Lliew, F. Lederer, J. Broeng, G. Vienne, A. Petersson, C. Jakobsen, "High-power air-clad large-mode-area photonic crystal fiber laser", Optics Express, Vol. 11, No. 7, 2003 (pp818-823)

[46]   Y. Jeong, J. K. Sahu, D. N. Payne, J. Nilsson, "Ytterbium-doped large –core fiber laser with 1.36kW continuous-wave output power", Optics Express, Vol. 12, No. 25, 2004 (pp6088-6092)

[47]   http://www.crystal-fibre.com, visited March 2006

[48]   F. C. McNeillie, E. Riis, J. Broeng, J. R. Folkenberg, A. Petersson, H. Simonsen, C. Jacobsen, "Highly polarised photonic crystal fiber laser", Optics Express, Vol. 12, No. 17, 2004, (pp3981-3987)

[49]   J. Hecht, "Fiber lasers take off in diverse directions", Laser Focus World, http://www.laserfocusworld.com/display_article/218558/12/ARCHI/none/Feat/Fib

[50]   F. C. McNeillie, E. Riis, B. Hitz, "Photonic crystal fiber laser is highly polarized", Photonics Spectra, 2004, (pp92-94)

[51]   F. C. McNeillie, "Highly polarised photonic crystal fibre laser", QEOD Europhoton Conference, Switzerland, 2004

[52]   F. C. McNeillie, "Highly polarised photonic crystal fibre laser", The 17th International Laser Spectroscopy Conference, Aviemore, Scotland, 2005

[53]   F. C. McNeillie, "Highly polarised photonic crystal fibre laser", NKT
        Summer Academy Conference, 2006

[54]   M. Y. Chen, Y. K. Zhang, "Improved design of polarisation-maintaining
        photonic crystal fibers", Optics Letters, Vol. 33, No. 21, 2008, (pp2542-2544)

Chapter 2

Theory of Laser Action

This chapter describes basic laser theory including the concepts of population inversion, gain, gain saturation and threshold. Three and four level laser systems will be discussed and the spectroscopic properties of Yb^{3+} will be detailed.

2.1 Energy Level Interactions

In general a laser cavity contains an active material made up of atoms or ions which contain several electronic energy levels. When an electron in the atom or ion undergoes a transition between two energy levels it either emits or absorbs a photon of frequency, υ, where $\upsilon = \Delta E/h$, ΔE being the energy difference between the two levels concerned and h being Planck's constant. In the case of a fibre laser the active material contains rare earth ions whose energy levels are split into several Stark levels [1]. These Stark levels are sufficiently close to each other to be strongly thermally coupled and are therefore in thermal equilibrium with each other. Thus, the population distribution of these Stark levels follows a Boltzmann distribution which allows the energy level to be treated as a single entity with the population determined by the laser rate equations. This research focuses on Yb^{3+} doped fibre lasers, thus the electronic structure of this ion will be described in section **2.3** but first, the mechanisms required for laser action to occur will be described.

2.1.1 Absorption

Consider the electron transitions which may occur between the two energy levels of the hypothetical atomic system shown in *Figure 2.1*.
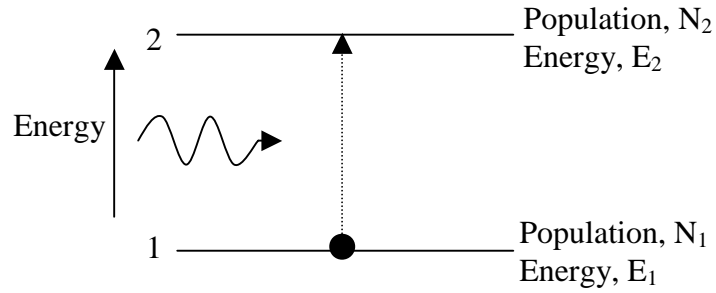
Figure 2.1: Energy level diagram showing stimulated absorption.

Let N_1 and N_2 represent the number of electrons per unit volume in levels 1 and 2 respectively. An electron in the lower level, E_1, may be excited to the upper level, E_2, by absorbing a photon of energy $(E_2 - E_1) = h\upsilon$. This process is termed stimulated absorption. Assuming a monochromatic beam of intensity I_υ and frequency υ propagating through the medium the number of photons crossing a unit area per unit time is [2]

$$\phi_\upsilon = \frac{I_\upsilon}{h\upsilon} \qquad (2.1)$$

The rate of change of N_1 due to (stimulated) absorption is

$$\left(\frac{dN_1}{dt}\right)_{abs} = -\sigma_a(\upsilon)\frac{I_\upsilon}{h\upsilon}N_1 \qquad (2.2)$$

where $\sigma_a(\upsilon)$ is the absorption cross section. The rate of absorption is dependent on the amount of pumping or the density of radiation at the particular energy separating the two levels involved. Once an electron in the higher lying energy level transfers back to the lower lying energy level it emits a photon.

2.1.2 Spontaneous Emission

The emission process can occur in two distinct ways, spontaneous or stimulated. The former of these is depicted in *Figure 2.2*, whereby the electron drops to the lower level in an entirely random way, emitting a photon in the process.
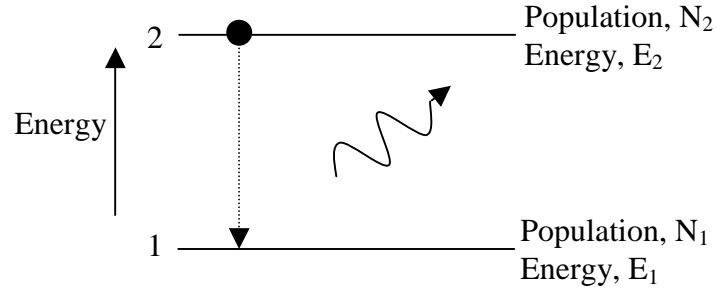
Figure 2.2: *Energy level diagram showing spontaneous emission.*

The spontaneous rate of decay, $\left(dN_2/dt\right)_{sp}$, from level 2 to 1 of the electrons is proportional to the number of electrons, N_2, occupying level 2, thus [2]

$$\left(\frac{dN_2}{dt}\right)_{sp} = -A_{21}N_2 = -\frac{N_2}{\tau_{sp}} \qquad (2.3)$$

where A_{21} is the Einstein A coefficient which represents the spontaneous transition rate associated with a transition from level 2 to 1. It is related to the spontaneous emission lifetime, $\tau_{sp} = 1/A_{21}$, ie. time for electron to transfer from level 2 to 1. As the spontaneous radiation from any atom or ion is emitted at random the radiation emitted by a large number of ions will clearly be incoherent. Note that a nonradiative transition can also take place whereby the energy emitted is not in the form of an electromagnetic wave but instead the energy is given to surrounding electrons in the form of translational, vibrational, rotational or electronic energy.

2.1.3 Stimulated Emission

Stimulated emission is the process whereby an electron is triggered to undergo the transition from the upper level to the lower level by the presence of a photon of energy (E_2 - E_1). See *Figure 2.3*.
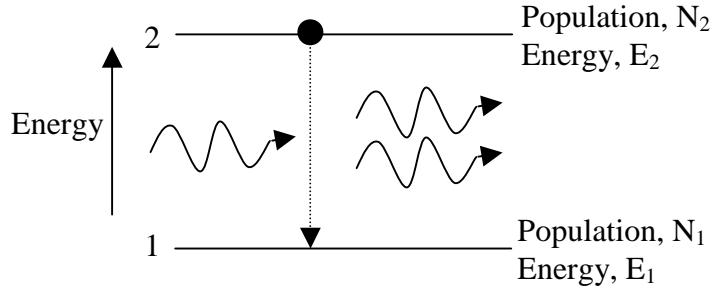
Figure 2.3: *Energy level diagram showing stimulated emission.*

In contrast to spontaneous emission the stimulated process results in coherent radiation since the waves associated with the stimulating and stimulated photons have identical frequencies, are in phase, have the same state of polarisation and propagate in the same direction. Note that this process is the inverse of stimulated absorption. In the presence of a population inversion, $N_2 > N_1$, the amplitude of an incident wave can grow as it passes through the system.

The rate at which transitions occur from level 2 to 1 as a result of stimulated emission is [2]

$$\left(\frac{dN_2}{dt}\right)_{st} = -\sigma_e(\upsilon)\frac{I_\upsilon}{h\upsilon}N_2 \qquad (2.4)$$

where $\sigma_e(\upsilon)$ is the emission cross section. The population inversion condition required for laser action is a non-equilibrium distribution of atoms or ions whereby $N_2 > N_1$, as stated previously. This relies on a finite upper level lifetime and an excitation process, ie. pumping. Yb^{3+} has a relatively long upper level lifetime of 1-2ms, which is ideal for laser action and applications such as Q-switching which will be demonstrated in **Chapter 7**. Once an electron undergoes a spontaneous transition

and emits a photon it starts the stimulated emission process. However with the two level system, as the transition probability for absorption is equal to that of emission, once electrons are excited into the upper level the probabilities of further stimulated absorption or emission are equal so that even with very intense pumping the best that can be achieved is equality of the populations of the two levels. Therefore, we must consider laser materials with either three of four energy levels. The Yb^{3+} PCF lasers, within this thesis, can be described using these systems.

2.2   Three-level and Four-level Laser Systems

Figure 2.4 depicts the energy level diagram for a three-level laser system.
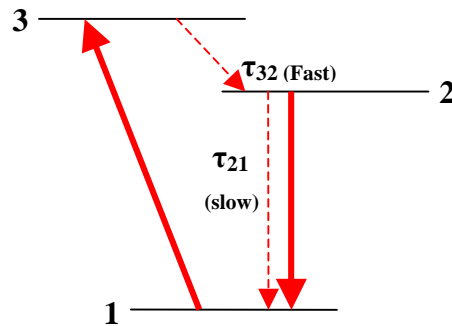
Figure 2.4: *Energy level diagram for a three-level laser system. (Red solid lines indicate absorption and stimulated emission and red dashed lines indicate relaxation processes).*

For any laser system gain is achieved when the population in the upper laser level is greater than that of the lower laser level. In a three level system the lower laser level is the ground state and the gain condition is not readily achievable as there will always be population in the ground state. This means that to achieve population inversion in a three-level system more than half of the population initially in the ground state must be pumped to the upper pumping level, level 3, where it non-radiatively decays to level 2, before any inversion at all is obtained on the lasing transition. A common problem which affects a three-level system is ground state reabsorption whereby a significant fraction of the intracavity intensity is reabsorbed. This reabsorption raises the threshold for achieving population inversion. Therefore, for a three-level fibre laser there is an optimum fibre length; if the fibre is too short

there is insufficient pump absorption but if it is too long the intracavity laser power is reabsorbed. This reabsorption process will be illustrated in the numerical modelling featured in the forthcoming **Chapter 4**.

Figure 2.5 depicts an energy level diagram for a four-level laser system.

Figure 2.5: *Energy level diagram for a four-level laser system. (Red solid lines indicate absorption and stimulated emission and red dashed lines indicate relaxation processes).*

In a four-level laser system the terminating level is well separated in energy space from the ground state. The lifetime of level 4 is short in comparison to the lifetime of level 3. Therefore, the population in level 3 will be much greater than that in level 4. Similarly, the lifetime of level 2 is short in comparison to level 3 such that the population in level 3 is much greater than in level 2 and level 2 is quickly depopulated non-radiatively ensuring no reabsorption (provided that there is no absorption on other transitions). Thus, there is no absorption of the gain medium in the unpumped state and the gain usually rises linearly with the absorbed pump power. These lifetime parameters ensure that a population inversion is readily achieved for the level 3 to 2 laser transition. With a four-level fibre laser the threshold power decreases inversely with fibre length.

A quasi-three-level system falls mid-way between a three and a four-level laser system and is depicted in *Figure 2.6*.
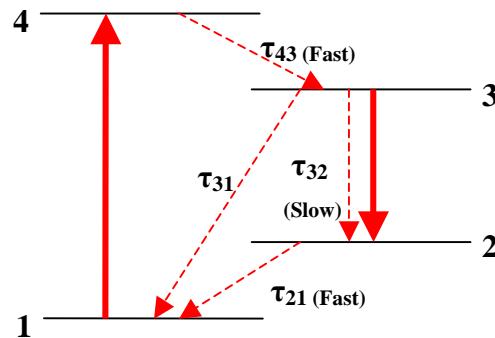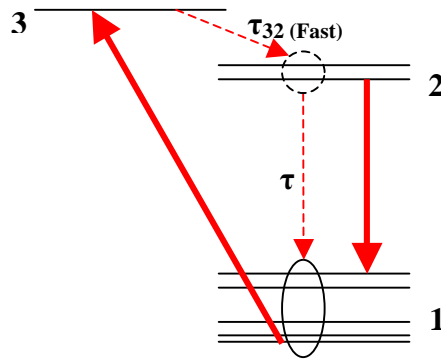
Figure 2.6*: Energy level diagram for a quasi-three-level laser system. (Red solid lines indicate absorption and stimulated emission and red dashed lines indicate relaxation processes).*

In the quasi-three-level system example illustrated in *Figure 2.6* levels 1 and 2 are broadened to form manifolds and transitions to and from any of these levels within the manifolds are permitted. This structure resembles a four level system in that the population inversion requirements are decreased. The lower laser level is so close to the ground state that an appreciable population in that level can occur at some thermal equilibrium with the ground state, at the operating temperature. As a consequence of this the unpumped gain medium causes some loss at the laser wavelength due to reabsorption and transparency is reached only for some finite pump intensity. For higher pump intensities there is gain which is required for laser operation. An important fact is that the spectral shape of the optical gain in a quasi-three level system depends on this excitation rate which affects the balance between emission and reabsorption. Therefore, the laser wavelength obtained may depend on the resonator losses, i.e. high resonator losses require high gain and thus a higher excitation rate which leads to shorter wavelength of maximum gain.

2.3   Ytterbium as a Dopant

The rare earths are divided into two groups; the lanthanides and the actinides. The lanthanides are characterised by the filling of the 4f shell whereas the actinides are characterised by the filling of the 5f shell. Only the lanthanides will be considered here as the rare earth ion Yb^{3+} considered in this research falls under the lanthanide category. When Yb is doped into a glass host it is triply ionised with only one

electron short of a full 4f shell. Hence there are only two electronic energy levels; the ground state, $^2F_{7/2}$, and the excited state, $^2F_{5/2}$, separated by approximately 11,000cm^{-1}, which are Stark split as shown in *Figure 2.7*. The 4f electrons are shielded from the effects of the environment. Thus the consequences for the static interactions are energy levels that are relatively insensitive to host, have small host induced splittings and are only weakly mixed with energy states. The dynamic consequences are little or no vibronic structure and weak nonradiative relaxation of excited states which occurs through phonon emission. The net results are optical transitions between 4f states that manifest themselves as narrow, weak bands or sharp lines and emission that can be highly efficient. These properties are different from the transition metals that have much stronger interaction with the host and are characterised by broad, strong emission and absorption bands that are due to vibronically assisted transitions [1].
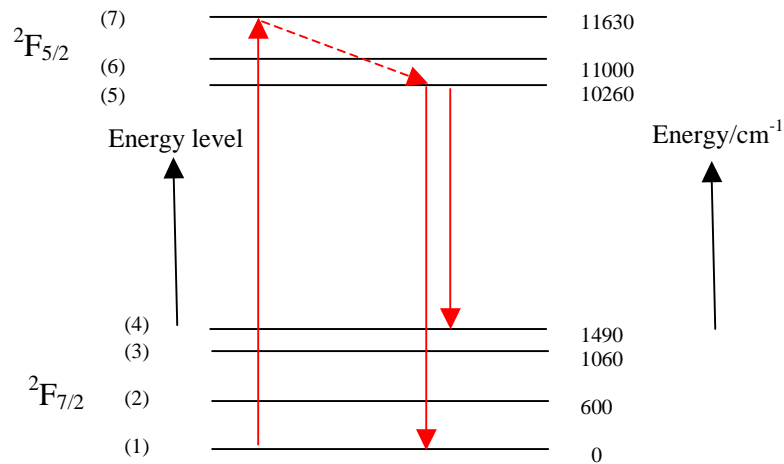
Figure 2.7: *Energy level diagram for Yb^{3+}.*

A Yb^{3+} doped fibre laser is typically pumped in order to populate the higher sublevels of the $^2F_{5/2}$ manifold. It is well known to behave as a true three level system but in some circumstances its operation is better described by a quasi-three level system e.g. at emission wavelengths below 900nm it can be described using a true three-level system, whereas at longer wavelengths it behaves as a quasi-three level system.

Looking at the absorption and emission spectra illustrated in *Figure 2.8* we can see that it has a broad absorption band that stretches from below 850nm to above 1070nm which allows inexpensive and readily available diode lasers to be used as pump sources. It also has a broad emission band stretching from 970nm to 1200nm which is broader than that of its counterpart neodymium (Nd). Thus Yb^{3+} offers an attractive wide tuning wavelength range.
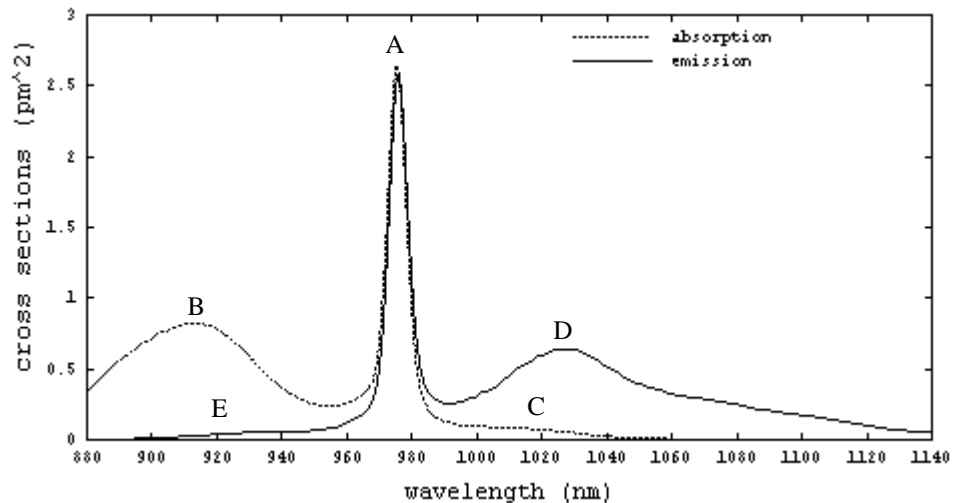
Figure 2.8: Ground state absorption and emission spectrum of Yb^{3+} in silica [3] (Labels A-E are explained in the following text).

Labels (A) to (E) have been placed on the most obvious features of the absorption and emission spectra. The narrow line at 975nm, represented by label (A), in both the absorption and the emission spectra corresponds to transitions between the lowest stark levels in each manifold. Laser action on this narrow peak where emission is into the lowest stark level is characterised as a true three-level system. The absorption peak, labelled (B), at shorter wavelengths corresponds to transitions from levels (1) to (6) and (1) to (7). The long wavelength absorption, labelled (C), corresponds to transitions from level 2 to (6) and (2) to (7). This weak shoulder is due to reabsorption which has a significant effect on the threshold for lasing at wavelengths within the dip in the emission spectrum. The second peak in the emission spectrum, labelled (D), corresponds to transitions from level (5) to levels (2), (3) and (4). Laser action on these transitions at longer wavelengths is better described using a quasi-three level system as the emission is into levels (3) and (4)

which are essentially empty levels. Transitions from level (6), corresponding to label (E), are also evident but the small thermal population of level (6) means that these transitions are weak.

To illustrate the pump rate dependent gain described in section **2.2**, *Figure 2.9* depicts this optical gain dependence on excitation rate for a Yb^{3+} doped fibre laser pumped at 840nm.
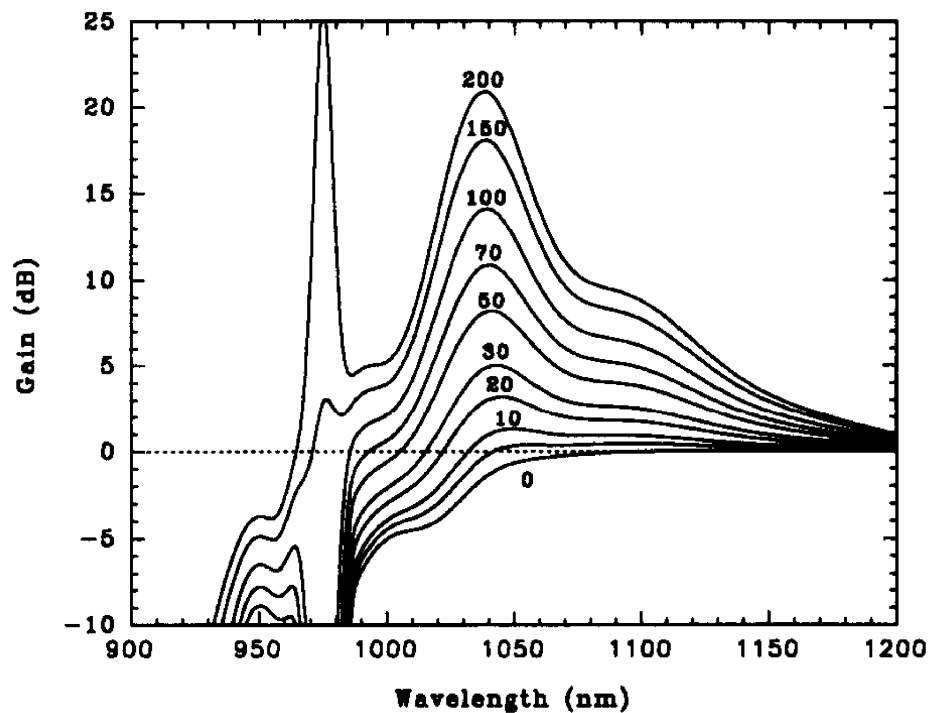
Figure 2.9: *Gain spectrum for 1m length Yb^{3+} doped fibre laser pumped at 840nm, fibre diameter 3.75μm, NA = 0.17, dopant concentration 550ppm, launched pump power varied from 5mW to 200mW. (Curves are labelled with launched pump power in milil watts) [3].*

There can actually be a smooth transition from three-level to four-level gain characteristics with increasing laser wavelength. Yb^{3+} doped silica exhibits pronounced three-level behaviour for wavelengths below approximately 1040nm. At longer wavelengths, there is hardly any reabsorption thus a very low excitation density will be sufficient to obtain the required gain.

Pask *et al* [3] demonstrated that the lasing wavelength of Yb^{3+} doped fibre lasers can be changed by controlling the Q of the resonator or by changing the length of the fibre. The lasing wavelength will correspond to the wavelength which has peak gain at the threshold for laser oscillation. Changing the Q changes the gain required to reach threshold and therefore changes the wavelength of peak gain. Increasing the length of the fibre shifts the gain maxima to longer wavelengths as a result of reabsorption. On comparing *Figure 2.9* with *Figure 2.10*, this effect is clearly illustrated.
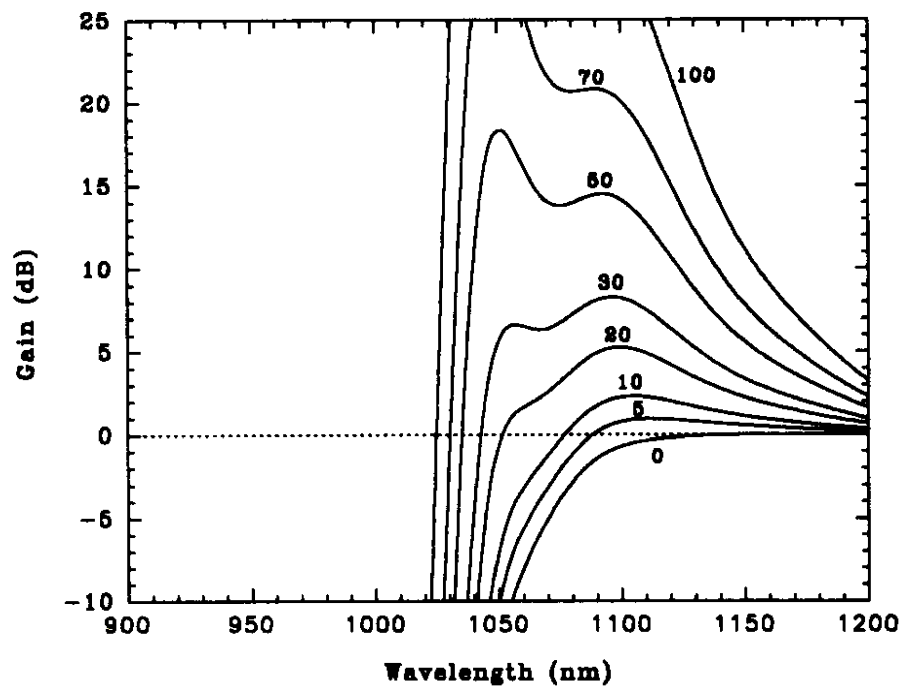
Figure 2.10*: Gain spectrum for 20m length Yb^{3+} doped fibre laser pumped at 840nm, fibre diameter 3.75μm, NA = 0.17, dopant concentration 550ppm, launched pump power varied from 5mW to 100mW. (Curves are labelled with launched pump power in milliwatts) [3].*

Note that reabsorption does not constitute a real loss of energy as the process excites electrons into the upper level enabling stimulated emission to occur again at a later time. Pronounced three-level behaviour is favoured for gain media with a very small quantum defect as this enforces a small energy spacing between the lower laser level and the ground state. Thus, the thermal population of the lower laser level is significant.

2.4 Laser Rate Equations

A three-level laser system can be analysed by writing the rate equations for each level, using the diagram shown in *Figure 2.4*, and then solving them for their steady state solutions. Assuming that there is a laser pumping process that produces a stimulated transition probability $W_{13} = W_{31} = W_p$, the rate equations for the upper levels 3 and 2 respectively, are [4]

$$\frac{dN_3}{dt} = W_p(N_1 - N_3) - \frac{N_3}{\tau_3} \qquad (2.5)$$

and

$$\frac{dN_2}{dt} = \frac{N_3}{\tau_{32}} - \frac{N_2}{\tau_{21}} \qquad (2.6)$$

For steady state $\frac{dN_2}{dt} = 0$ and $\frac{dN_3}{dt} = 0$, thus equation *(2.6)* becomes

$$\frac{N_3}{\tau_{32}} = \frac{N_2}{\tau_{21}} \qquad (2.7)$$

The conservation equation $N_1 + N_2 + N_3 = N$ is valid and on rearranging equation *(2.7)* we obtain the relaxation time ratio, Θ, corresponding to levels 2 and 3.

$$\Theta = \frac{N_3}{N_2} = \frac{\tau_{32}}{\tau_{21}} \qquad (2.8)$$

Another dimensionless parameter, the fluorescent quantum efficiency parameter, η, is normally defined as the number of fluorescent photons spontaneously emitted on the laser transition divided by the number of pump photons absorbed on the pump transition when the laser material is below threshold. It can be expressed as follows [4].

$$\eta = \frac{\tau_3 \tau_{21}}{\tau_{32} \tau_{rad}} \qquad (2.9)$$

where τ_{rad} is the radiative decay rate on the laser transition itself. Thus the steady state population difference for the level 2 to 1 transition can be found to be [4]

$$\frac{N_2 - N_1}{N} = \frac{(1-\Theta)\eta W_p \tau_{rad} - 1}{(1+2\Theta)\eta W_p \tau_{rad} + 1} \qquad (2.10)$$

Thus population inversion in the three-level system can only be obtained if $\Theta < 1$ and if the pumping rate exceeds a threshold value given by

$$W_p \tau_{rad} \geq \frac{1}{\eta(1-\Theta)} \qquad (2.11)$$

These conditions can only be met when the relaxation from the upper pumping level 3 to the upper laser level 2 is very fast such that $\Theta \to 0$ and when the relaxation from the upper laser level 2 down to the ground state is purely radiative such that $\eta \to 1$. Therefore the steady state population inversion for a three-level system is found to be [4]

$$\frac{N_2 - N_1}{N} \approx \frac{W_p \tau_{rad} - 1}{W_p \tau_{rad} + 1} \qquad \text{if } \eta \to 1 \text{ and } \Theta \to 0 \qquad (2.12)$$

For the four-level laser system, shown in *Figure 2.5,* again let us assume that there is a laser pumping process that produces a stimulated transition probability $W_{14} = W_{41} = W_p$, the rate equation for level 4 is [4]

$$\frac{dN_4}{dt} = W_p (N_1 - N_4) - \frac{N_4}{\tau_4} \qquad (2.13)$$

where τ_4 is the total lifetime for decay to all other lower lying levels. The steady state population of level 4, when $dN_4/dt = 0$, is given by [4]

$$N_4 \approx W_p \tau_4 N_1 \qquad \text{if } W_p \tau_4 \ll 1 \qquad (2.14)$$

The normalised pumping rate, $W_p \tau_4$, does in fact have a value much less than unity in many practical laser systems. The rate equations for levels 3 and 2, respectively, are

$$\frac{dN_3}{dt} = \frac{N_4}{\tau_{43}} - \frac{N_3}{\tau_3} \qquad (2.15)$$

and

$$\frac{dN_2}{dt} = \frac{N_4}{\tau_{42}} + \frac{N_3}{\tau_{32}} - \frac{N_2}{\tau_{21}} \qquad (2.16)$$

For the four-level laser system the parameter Θ becomes

$$\Theta = \frac{N_2}{N_3} \approx \frac{\tau_{21}}{\tau_{32}} \qquad (2.17)$$

which is typically much less than unity. The fluorescent quantum efficiency, η, for the four-level system is

$$\eta = \frac{\tau_4 \tau_3}{\tau_{43} \tau_{rad}} \qquad (2.18)$$

Again the conservation equation $N_1 + N_2 + N_3 + N_4 = N$ is valid and we can solve for the population inversion for the four-level system [4].

$$\frac{N_3 - N_2}{N} \approx \frac{W_p \tau_{rad}}{1 + W_p \tau_{rad}} \qquad \text{if } \beta \to 0 \qquad (2.19)$$

Comparing equations *(2.12)* and *(2.19)* we see that population inversion is much more easily obtained in a four-level system compared to a three-level system. Thus, a four-level laser system typically has a much lower pumping threshold than a three-level system. The population inversion for both systems depends on the radiative lifetime and the pumping rate. This dependence is actually not linear which leads to saturation of the population inversion for large pump rates.

2.5   *Laser Oscillation*

Let us consider the simple case of an optical resonator consisting of a gain medium of length, L, placed between two mirrors, M_1 and M_2 which have reflectivity R_1 and R_2, respectively. Assume that the gain medium fills the space between the two mirrors. We have already described that a population inversion must be established to achieve gain and laser oscillation. A minimum small signal gain coefficient, k, must be large enough to overcome the losses in the cavity in order to sustain laser oscillations. The total loss in the system can be attributed to many sources. For simplicity let us combine all of these losses, except those due to transmission at the mirrors, into a single loss coefficient, γ. This loss coefficient will reduce the effective small signal gain coefficient to (k-γ). As previously mentioned, in section **2.1.2**, the initial stimulus in the cavity is provided by any spontaneous transitions taking place between energy levels which leads to spontaneous emission whereby the emitted photon propagates along the axis of the system. The signal is amplified as it propagates through the medium and is retro-reflected by the cavity mirrors. Threshold is reached when the gain provided by the medium is equal to the loss incurred during one round trip of the cavity. The threshold small signal gain coefficient, k_{th}, can be determined by considering the change in irradiance of the beam of light as it undergoes one complete roundtrip of the cavity. On travelling from the first mirror to the second mirror the beam irradiance increases from I_0 to I in accordance with

$$I = I_0 e^{(k-\gamma)L} \qquad\qquad (2.20)$$

where k is the small signal gain coefficient, γ is cavity loss coefficient and L is the cavity length. When the beam is reflected by the second mirror the beam irradiance will be equal to equation *(2.20)* multiplied by R_2. After one complete round trip of the cavity the final beam irradiance will be such that the round trip gain, G, is [5]

$$G = \frac{I}{I_0} = R_1 R_2 e^{2(k-\gamma)L} \hspace{2cm} (2.21)$$

If the round trip gain is greater than unity then the laser oscillations will grow. However if the roundtrip gain is less than unity then the oscillations will die out. Therefore a threshold condition exists such that equation *(2.21)* must be equal to unity and the small signal gain coefficient, k, in equation *(2.21)* must be replaced by the small signal gain coefficient at threshold, k_{th} which is given by

$$k_{th} = \gamma + \frac{1}{2L}\ln\left(\frac{1}{R_1 R_2}\right) \hspace{2cm} (2.19)$$

This threshold small signal gain coefficient determines the minimum population inversion required. In continuous wave lasers this threshold gain is equal to the steady state gain coefficient, k_{ss}. The pump establishes a population inversion, which in the absence of any optical field has the value ΔN_o. The presence of an optical field induces stimulated absorption and stimulated emission transitions, previously described in sections **2.1.1** and **2.1.3,** from levels 1 to 2 and 2 to 1, respectively. Since, $N_2 > N_1$ and the stimulated absorption and stimulated emission rates are equal, it follows that more electrons undergo transitions from level 2 to 1 than from level 1 to 2. Therefore, the new equilibrium population inversion will be smaller than ΔN_o. This reduction in the population inversion and hence the reduction in the gain constant, due to the presence of the optical field, is called gain saturation.

The saturation pump power, P_{sat}, which is the power required to decrease the absorption coefficient to one half of its small signal value, is particularly important for fibre lasers. This is because as a rule of thumb, the length of fibre required to

absorb a given input power is equal to the extinction length multiplied by the ratio of the pump power to the saturation power, where the extinction length is the length of fibre that causes a small signal power decrease of a factor e^{-1}. It is given by [1]

$$P_{sat} = \frac{h\upsilon_p A_x}{(\sigma_e + \sigma_a)\tau}$$

(2.21)

where h is Planck's constant, $h\upsilon_p$ is the energy of the photon, A_x is the cross sectional area of gain medium, τ is the upper state lifetime, σ_e and σ_a is the emission cross section and the absorption cross section of the gain at the emission wavelength.

The laser theory presented in this chapter will form the basis for a numerical model, of PCF lasers, developed in **Chapter 4**.

2.6 References

[1]   M. J. F. Digonnet, "Rare-earth-doped fiber lasers and amplifiers", Second Edition, Marcel Dekker, Inc., 2001

[2]   A. Ghatak, K. Thyagarajan, "Introduction to fiber optics", Cambridge University Press, 1998

[3]   H. M. Pask, R. J. Carmen, D. C. Hanna, A. C. Tropper, C. J. MacKechnie, P. R. Barber, J. M. Dawes, "Ytterbium-doped silica fiber lasers: Versatile sources for the 1-1.2µm region", IEEE Journal of Selected Topics in Quantum Electronics, Vol. 1, No. 1, 1995, (pp453-465)

[4]   A. E. Siegman, "Lasers", 1st Edition, Oxford University Press, 1986

[5]   J. Wilson, J. F. B. Hawkes, "Optoelectronics:An Introduction", Prentice Hall International Inc., 1983

[6]   A. Yariv, "Optical Electronics, Fourth Edition", Saunders College Publishing, 1971

Chapter 3

Theory of Wave Propagation

Laser beams, including those in higher order modes, propagate according to the laws of Gaussian Optics. Starting from Maxwell's Equations, wave propagation in free space will be discussed leading to a description of wave propagation in standard step-index optical fibre and PCF. Various numerical modelling techniques, which are employed to analyse properties of PCF's, are considered. Gaussian beam properties will then be discussed leading to a description of the methodology utilised in this research to analyse M^2 properties of real laser beams.

3.1   Wave Propagation

3.1.1 Wave Propagation in Free Space

In vacuum, electromagnetic fields propagate at the velocity of light, c_0, where the refractive index $n_{vac} = 1$ and there exists neither current nor charge. Therefore, Maxwell's equations can be simplified [1]

$$\nabla \cdot \overline{E} = 0 \qquad\qquad (3.1)$$

$$\nabla \times \overline{E} = -\mu_0 \frac{\partial \overline{H}}{\partial t} \qquad (3.2)$$

$$\nabla \cdot \overline{H} = 0 \qquad\qquad (3.3)$$

$$\nabla \times \overline{H} = \varepsilon_0 \frac{\partial \overline{E}}{\partial t} \qquad (3.4)$$

where $\overline{E}$ is the electric field vector, $\overline{H}$ is the magnetic field vector, μ_0 is the permeability of free space and $\varepsilon_0 = \dfrac{1}{c_0{}^2 \mu_0}$ is the permittivity of free space. Using the vector identity, $\nabla \times (\nabla \times \overline{E}) = \nabla(\nabla \cdot \overline{E}) - \nabla^2 \overline{E}$, the wave equation in free space is

$$\left(\nabla^2 - \frac{1}{c_0{}^2} \frac{\partial^2}{\partial t^2} \right) \overline{E}(r,t) = 0 \qquad (3.5)$$

In homogeneous material the phase velocity $c \to \dfrac{c}{n}$, thus the wave equation becomes

$$\left(\nabla^2 - \left(\frac{n}{c} \right)^2 \frac{\partial^2}{\partial t^2} \right) \overline{E}(r,t) = 0 \qquad (3.6)$$

The wave equation can be simplified if monochromatic waves with harmonic development are permitted. The use of complex numbers allows many waveforms to be clearly discussed. Only the real part of the complex amplitude is considered as a physically real quantity.

$$\overline{E}(r,t) = \Re e\left\{ \overline{E}(r) e^{-i\omega t} \right\} \qquad (3.7)$$

where $\omega^2 = \dfrac{c^2}{n^2} k^2$ and r denotes the position of the field. Equation (3.7) can be substituted into equation (3.6) to yield the Helmholtz equation;

$$(\nabla^2 + k^2) \overline{E}(r) = 0 \qquad (3.8)$$

3.1.2 Wave Propagation in Step-Index Optical Fibre

A step-index optical fibre is characterised by its refractive index distribution

$$n(r) = n_1 \qquad 0 < r < a \qquad \text{core} \qquad (3.9)$$

$$n(r) = n_2 \qquad r > a \qquad \text{cladding} \qquad (3.10)$$

In real fibres $n_1 \approx n_2$ which allows the use of the scalar wave approximation [2]. The modes are assumed to be nearly transverse and can have an arbitrary state of polarisation. Thus, the two independent sets of modes can be assumed to be x-polarised and y-polarised. These Linearly Polarised (LP) modes both have the same propagation constant, $\beta = n\omega/c$, and the transverse component of the electric field satisfies the previously stated wave equation *(3.6)* [2].

$$\left(\nabla^2 - \left(\frac{n}{c} \right)^2 \frac{\partial^2}{\partial t^2} \right) \psi(r,t) = 0 \qquad (3.11)$$

With n^2 depending only on the transverse coordinates r and ϕ, the modes of the system can be represented by

$$\psi(r,\phi,z,t) = \psi(r,\phi)e^{i(\omega t - \beta z)} \qquad (3.12)$$

Substituting equation *(3.12)* into equation *(3.11)* we obtain

$$\left(\nabla^2 - \frac{\partial^2}{\partial z^2} \right) \psi + \left[\frac{\omega^2}{c^2} n^2(r,\phi) - \beta^2 \right] \psi = 0 \qquad (3.13)$$

For most practical fibres n^2 depends only on the cylindrical coordinate r. Therefore it is convenient to express equation *(3.13)* using the cylindrical coordinates system [2]

$$\frac{\partial^2 \psi}{\partial r^2} + \frac{1}{r}\frac{\partial \psi}{\partial r} + \frac{1}{r^2}\frac{\partial^2 \psi}{\partial \phi^2} + \left[k^2 n^2(r) - \beta^2\right]\psi = 0 \qquad (3.14)$$

As an optical fibre has cylindrical symmetry we can solve equation *(3.14)* by means of separation of variables

$$\psi(r,\phi) = R(r)\Phi(\phi) \qquad (3.15)$$

Substituting equation *(3.15)* into equation *(3.14)* and division of equation *(3.14)* by $\psi(r,\phi)/r^2$ we obtain

$$\frac{r^2}{R}\left(\frac{d^2 R}{dr^2} + \frac{1}{r}\frac{dR}{dr}\right) + r^2\left[n^2(r)k^2 - \beta^2\right] = -\frac{1}{\Phi}\frac{d^2\Phi}{d\phi^2} = +l^2 \qquad (3.16)$$

where *l* is a constant. The ϕ dependence will be of the form cos $(l\phi)$ or sin $(l\phi)$ and for the function to be single valued we must have $l = 0,1,2,3...,$etc. The radial part of equation *(3.16)* gives

$$r^2\frac{d^2 R}{dr^2} + r\frac{dR}{dr} + \left\{\left[n^2(r)k^2 - \beta^2\right]r^2 - l^2\right\}R = 0 \qquad (3.17)$$

and the complete transverse field is given by

$$\psi(r,\phi,z,t) = R(r)e^{i(\omega t - \beta z)}\begin{Bmatrix}\cos(l\phi)\\ \sin(l\phi)\end{Bmatrix} \qquad (3.18)$$

By substituting n^2(r) in equation *(3.17)* with the refractive index distributions given by equations *(3.9)* and *(3.10)* respectively, we obtain

$$r^2\frac{d^2 R}{dr^2} + r\frac{dR}{dr} + \left(U^2\frac{r^2}{a^2} - l^2\right)R = 0; \qquad 0 < r < a \qquad (3.19)$$

36

where $U = a(k_0{}^2 n_1{}^2 - \beta^2)^{1/2}$ and

$$r^2 \frac{d^2 R}{dr^2} + r \frac{dR}{dr} - \left(W^2 \frac{r^2}{a^2} + l^2 \right) R = 0 \; ; \qquad r > a \qquad (3.20)$$

where $W = a(\beta^2 - k^2 n_2{}^2)^{1/2}$. The normalised waveguide parameter V is

$$V = (U^2 + W^2)^{1/2} = ka(n_1{}^2 - n_2{}^2)^{1/2} \qquad (3.21)$$

where, as usual, k $= 2\pi/\lambda$, a is the core radius, n_1 and n_2 are assumed to be wavelength independent and are the refractive indices in the core and cladding respectively. Equations *(3.19)* and *(3.20)* are of standard form of Bessel's equation. The solutions of equation *(3.19)* are Bessel functions, $J_l(x)$ and $Y_l(x)$ where $x = \dfrac{Ur}{a}$. The solution $Y_l(x)$ is disregarded as it diverges as $x \to 0$. The solutions of equation *(3.20)* are modified Bessel functions, $K_l(x')$ and $I_l(x')$ where $x' = \dfrac{Wr}{a}$. The solution $I_l(x')$ is disregarded as it diverges as $x' \to \infty$. Therefore, the transverse dependence of the modal field is given by

$$\psi(r, \phi) = \begin{cases} \dfrac{A}{J_l(U)} J_l\left(\dfrac{Ur}{a} \right) \begin{bmatrix} \cos l\phi \\ \sin l\phi \end{bmatrix} ; & r < a \\[4mm] \dfrac{A}{K_l(W)} K_l\left(\dfrac{Wr}{a} \right) \begin{bmatrix} \cos l\phi \\ \sin l\phi \end{bmatrix} ; & r > a \end{cases} \qquad (3.22)$$

Guided modes correspond to $n_2{}^2 k^2 < \beta^2 < n_1{}^2 k^2$, thus for guided modes both U and W are real. For β^2 lying in the range $n_2{}^2 k^2 < \beta^2 < n_1{}^2 k^2$, the fields R(r) are oscillatory in the core and decay in the cladding. When $\beta^2 < k^2 n_2{}^2$ the fields are oscillatory even in the cladding. *Figure 3.1* compares the modal intensity pattern of

a Bessel function with a Gaussian function. Realistically, the Bessel function mode patterns observed in fibre lasers are approximated by Gaussian beam modes.
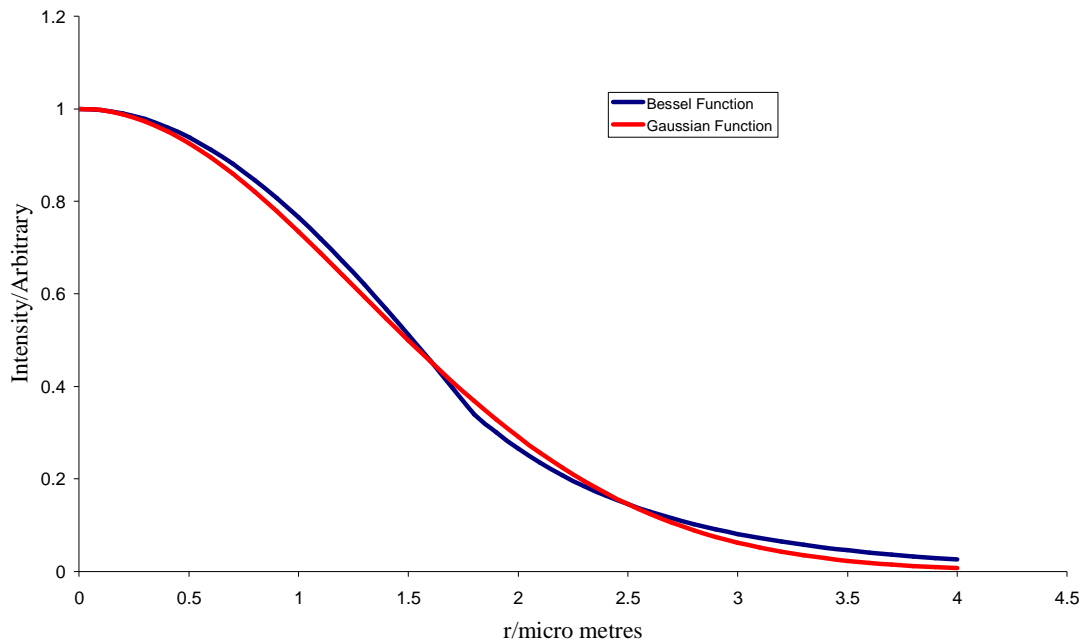
Figure 3.1: *Modal intensity pattern for Bessel function (dashed line) and Gaussian function (solid line).*

3.1.3   *Wave Propagation in Photonic Crystal Fibre*

The complex nature of micro-structured optical fibres means that the standard modelling methods from traditional fibre theory, as outlined above, do not lend themselves for direct use with micro-structured fibres. For example, photonic bandgap fibres require the full vectorial nature of the electromagnetic waves to be taken into account [3]. Often they are modelled using a method closely related to the plane-wave method used for calculating electronic bandgaps in semiconductors [4]. As the micro-structured fibres employed in this work were all index-guiding PCF the wave propagation modelling descriptions given will be restricted to these types of fibre only.

3.1.3.1 Effective Index Approach

A simple scalar model, developed by Birks *et al* [5] and based on an effective refractive index of the cladding can be applied to establish qualitative mode propagation properties for index guiding PCF. As the refractive index in the core is greater than the average index of the cladding, the PCF can guide by the same mechanism as a standard step-index fibre; i.e. total internal reflection. Thus, there are propagation constants, β, available to the light in the core but not to light propagating in the cladding. The Fundamental Space-filling Mode (FSM) is the fundamental mode of the infinite photonic crystal cladding if the core is absent. Therefore, β_{FSM} is the maximum propagation constant allowed in the cladding and is used to define the effective index of the cladding as

$$n_{eff} = \frac{\beta_{FSM}}{k} \qquad (3.23)$$

where as usual $k = \dfrac{2\pi}{\lambda}$, is the free-space propagation constant of light with wavelength λ. As the FSM is a fundamental mode with the same symmetries as the photonic crystal itself, it is found by solving the scalar wave equation within a unit cell centred on one of the holes of diameter, d, as shown in *Figure 3.2*.

(a)   (b)
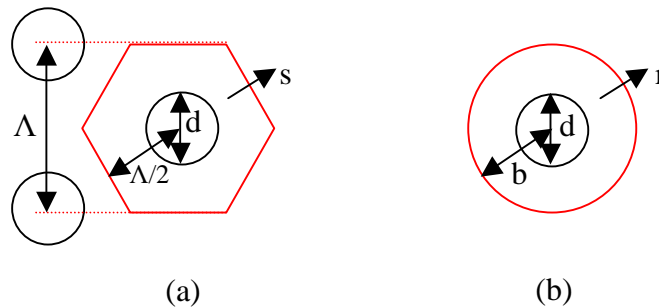
Figure 3.2: (a) Hexagonally shaped cladding cell (b) Circular approximation of cladding cell [5].

The diameter of these hexagonal cells is equal to the pitch, Λ (the centre to centre spacing between the air holes). Their hexagonal shape is approximated by circular

areas such that a general circular symmetric mode solution is possible. By reflection symmetry, the boundary condition at the cell edge is $\dfrac{d\psi}{ds} = 0$, where s is the coordinate normal to the cell edge. We can approximate this with a circular outer boundary at radius r = b, where $\dfrac{d\psi}{dr} = 0$. This is a reasonable approximation if the air holes are not too large (hole diameter $\approx 1\mu m$) because the field variation on a circle intersecting the hexagonal boundary will be small. Equating the model's filling fraction to the actual value gives *b*. The field in both regions is expressed in terms of Bessel functions of order 0, and the application of boundary conditions yields β_{FSM}.

An effective V parameter, such as that given by equation *(3.21)* for the step-index fibre, can be derived for the index guiding PCF which takes into account the wavelength dependence of the refractive indices caused by the air-glass matrix of the PCF [3].

$$V = ka(n_{co}^{\,2} - n_{eff}^{\,2})^{\frac{1}{2}} \qquad\qquad (3.24)$$

where n_{co} is the core refractive index.

This effective-index method does provide some insight into PCF operation but it cannot accurately predict the fibre modal properties such as dispersion or birefringence, both of which are dependent on the size and positioning of the air holes in the PCF. Thus, several numerical models have been developed to address such problems, with each model encompassing its own advantages and disadvantages.

3.2 Single Mode Optical Fibre

As already discussed in section 3.1.2, the number of modes allowed to propagate within a fibre waveguide depends on the normalised waveguide parameter, V. This V parameter can be related to the Numerical Aperture (NA) of the fibre by

$$V = ka(NA) \qquad\qquad (3.25)$$

When $0 < V < 2.405$ only one mode, namely the $LP_{0,1}$ mode, will be guided [2]. Thus a single mode fibre is one which supports the lowest order bound mode that can propagate at the wavelength of interest. Typically, single mode fibres have small core dimensions with core radius between 5μm and 8μm and have a cladding radius in the order of 120μm. The NA of a single mode fibre is generally in the order of 0.1. As the value of V becomes increasingly smaller the mode field intensity distributions extend further into the cladding region of the fibre. This extension of the field further into the cladding means the fibre is more sensitive to bending losses.

The wavelength at which a mode is no longer guided is known as the cut-off wavelength, λ_c.

$$\lambda_c = \frac{2\pi a(NA)}{2.405} \qquad\qquad (3.26)$$

If the wavelength of the light to be guided is greater than the cut-off wavelength then the fibre is no-longer single mode, instead it operates as a multi-mode fibre.

3.3 Multi-Mode Fibres

Multi-mode fibres are fibres which can support multiple transverse modes for a given wavelength. Generally they are defined as having a V parameter greater than 2.405. When $V \gg 1$ then the total number of modes in the waveguide is approximately equal to $V^2/2$. Multi-mode fibres have larger core diameters compared to those of single mode fibres, typically of the order of tens of micro metres which make them

more suitable for carrying high power beams often required in laser cutting and welding applications. This larger core diameter facilitates easier pump coupling when compared to single-mode fibres but the output intensity pattern is dependent on the pump launch conditions.

3.4 Double-Cladding Fibre

High quality, high power, diffraction-limited output beams are often desirable from optical fibre laser devices. However, to obtain these output beams from single-mode fibre lasers, diffraction-limited pump sources with high beam quality are required but these generally operate at low power levels. Thus, to achieve high beam quality, the output power must generally be sacrificed. To overcome this problem, optical fibre with a double-cladding structure was introduced in 1988 by Snitzer [6]. The structure of a double-cladding fibre consists of a single mode core with refractive index, n_1, which is surrounded by an inner-cladding region of refractive index, $n_2 < n_1$. This inner-cladding is then surrounded by a second cladding, the outer-cladding region, with refractive index, $n_3 < n_2$. Therefore, the inner-cladding region forms a second waveguide with a high NA which can support multiple modes. As the area of the inner-cladding is typically 10-100 times larger than the core area and has a large NA it is possible to efficiently pump the fibre laser using a large area laser diode array which, unlike a single mode laser diode, can emit high output power in excess of 100W. At some point, the light in the inner-cladding will pass through the single mode core and will contribute to lasing. Thus the double-cladding structure allows for efficient conversion of low-brightness, multi-mode pump light from a high power laser diode to high-brightness, single-mode laser radiation. Coupling into the large area inner-cladding increases alignment tolerance compared to coupling into the small core area of a single-mode fibre. As the spatial overlap between the pump and the doped core is reduced in a double-cladding fibre structure, the pump power absorbed per unit length is also reduced. Therefore, to achieve the equivalent absorption associated with core pumped fibre lasers, the length of the double-cladding fibre lasers must be increased [7]. This fibre length increase depends on the area ratio of the core and inner cladding; typical area ratios of the order 100-1000 are common.

If the core is centred in the circularly symmetric inner-cladding then many of the modes guided in the inner-cladding region do not intercept with the doped core due to their helical ray motion. Therefore, to further increase the coupling efficiency of the pump power, the core shape and positioning is often refined. By setting the core off-centre in the inner-cladding the number of modes interacting with the doped core is greatly increased [8-11]. By replacing the circular symmetric inner-cladding shape with a D-shaped, rectangular or scalloped structure the symmetry in the fibre is broken which allows more modes to interact with the doped core [2]. An example of such fibre structures are shown in *Figure 3.3*.
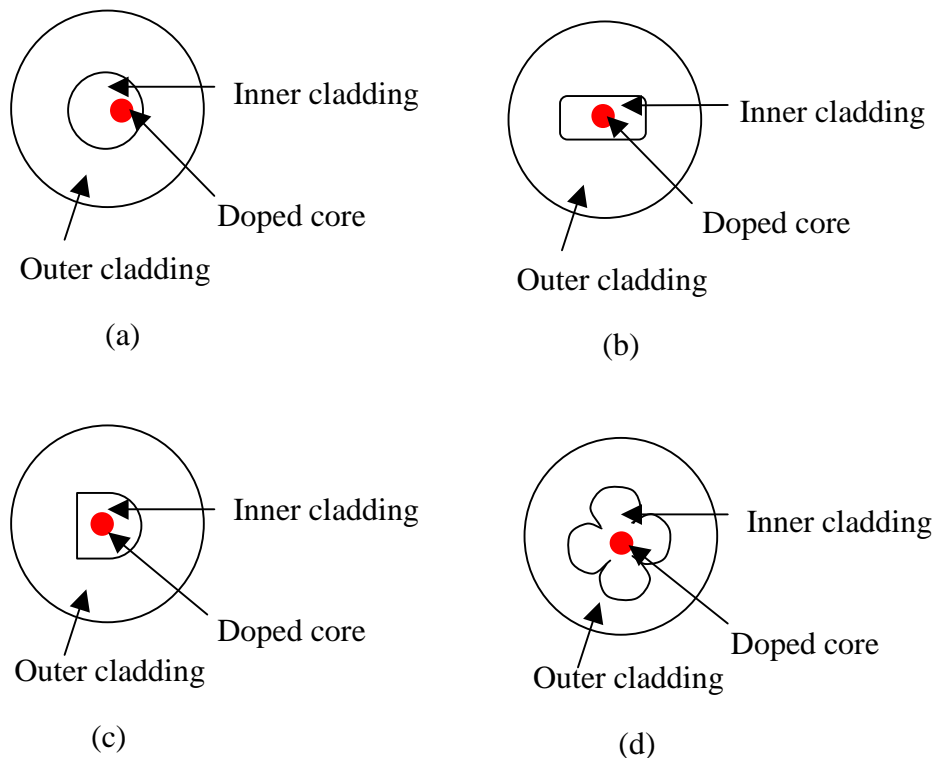
Figure 3.3: Double cladding fibre with various structures: (a) off-centre core, (b) rectangular cladding, (c) D-shaped cladding, (d) scalloped cladding.

Rectangular inner-cladding structures have a geometry which matches the output pattern from a multiple-stripe diode laser which minimises the area of the inner-cladding. This reduction in the inner-cladding area increases the core/cladding area ratio which in turn reduces the overall length of the fibre laser required for efficient pump absorption. With a D-shaped inner-cladding the helical rays are coupled to the

meridional rays which allow all pump rays to interact with the doped core. These modified cladding structures increase the pump absorption by more than one order of magnitude in comparison to the circular symmetric inner-cladding structures with centred cores.

The low refractive index polymer used to form the outer cladding has drawbacks as it restricts the inner cladding numerical aperture and the polymer cladding itself can be damaged through degradation or even burning due to high optical pump power. Using PCF technology, air-clad fibres can overcome these problems by replacing the polymer by an arrangement of air holes which permits higher output powers. Such double cladding PCF structures will be described in more detail in section **3.5.1.**

3.5 *Photonic Crystal Fibre*

There are many different types of PCF depending on the diameter, geometry and placement of the air holes within the air silica fibre waveguide. There are two main classes of PCF: high-index guiding and low-index guiding. High-index guiding fibre guides light in a solid core by means of modified total internal reflection which is a result of the lower effective refractive index in the air hole micro-structured cladding. Low-index guiding fibre guides light in a low-index core, which can be hollow, by the photonic bandgap effect, whereby the optical mode is confined to the core by periodic variations of the refractive index within the cladding. The cladding acts like a mirror, with reflections at the multiple air and silica interfaces which add together to produce strong reflection overall, thus confining propagation of light to the core.

All of the PCF's considered in this research were high-index guiding fibres that guide light by the modified total internal reflection mechanism. The manufacturer's freedom of design over the geometry, size and orientation of the micro-structured air holes gives them control over a wide range of properties such as dispersion, birefringence, non-linearity, numerical aperture and single or multi-mode guidance. The research in this theis characterises the optical properties of a double-cladding Yb^{3+} doped PCF laser and presents the first demonstration and characterisation of a

polarisation maintaining Yb^{3+} doped PCF fibre laser created by form birefringence alone [12-14].

3.5.1   Types of Microstructured Fibre

Large mode area PCF enable high power levels without nonlinear effects or material damage. Unlike standard large mode area fibres, the PCF type allow single mode guidance at practically all wavelengths [15]. Such fibres can be produced by designing fibres with a large pitch, typically around 10λ, and with air hole sizes, d/Λ, around 0.45 or smaller [3] where d is the diameter of the air hole and Λ is the pitch. A typical example of large mode area PCF's is shown in *Figure 3.4*.
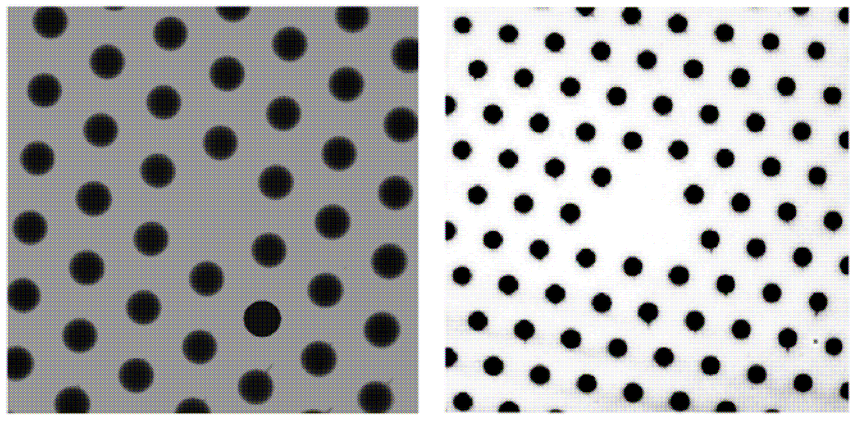

Figure 3.4: Images of large mode area PCF [16].

Like the standard double-cladding fibre structures discussed previously, in section **3.4**, double-cladding PCF's have an inner and outer cladding region but the polymer outer cladding in the standard fibre is replaced by an arrangement of air holes which overcomes damage limitations permitting higher pump powers to be facilitated. Also the use of very thin silica bridges between the air holes allows a large air filling factor to be achieved in the cladding which leads to a higher NA value than is possible in standard double-cladding fibres. Thus, with an increased NA the coupling efficiency of the multimode pump source into the PCF fibre is improved and the fibre length can consequently be shortened. An example of a double-cladding PCF structure is shown in *Figure 3.5*.
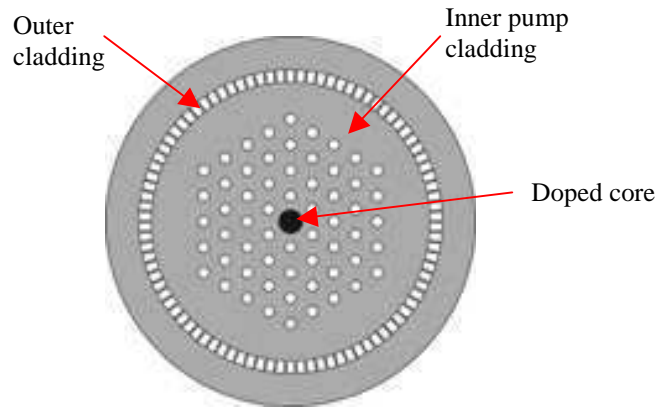
Figure 3.5: Double-cladding PCF structure [17].

Another group of PCF's, known as highly non-linear PCF's, have the potential to exhibit anomalous dispersion below about 1.3μm which is the lower limit for standard optical fibres [18]. As they can have nonlinear coefficients three orders of magnitude less than or several order of magnitude greater than standard optical fibre these non-linear PCF's make themselves attractive for many non-linear applications such as supercontinuum generation [19], which is the formation of broad continuous spectra by propagation of high power pulses through nonlinear media. Typically these non-linear PCF's characteristically have small core sizes, diameters down to 1μm, combined with a very large core/cladding index contrast up to 0.4 which enables fibres with extremely small effective areas and high nonlinear coefficients. An example of a highly non-linear PCF structure is shown in *Figure 3.6*.

(a)   (b)   (c)
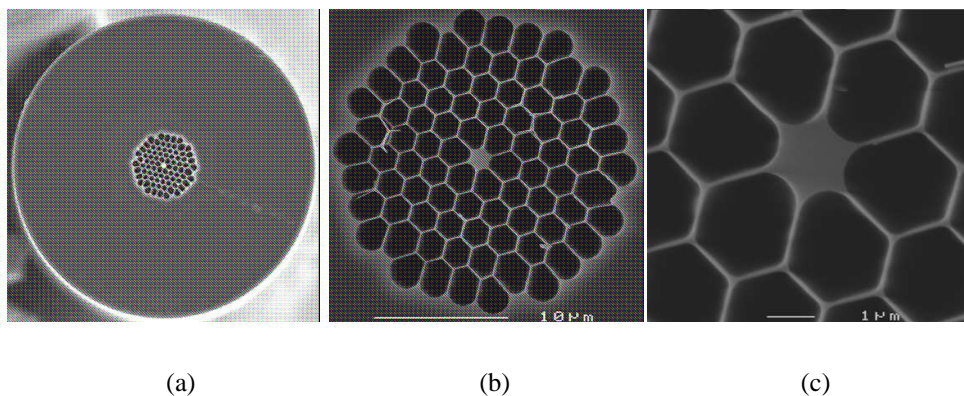
Figure 3.6: Scanning electron microscope image of highly nonlinear PCF with core diameter 1.5μm (a) Full scale, (b) close up of inner hole structure, (c) close up of core region [20].

As previously mentioned, in section **3.5**, PBG fibre can guide light even when the refractive index of the core is lower than that of the cladding e.g. when the core is an air hole. PBG fibres are bend-insensitive as a less than 1cm diameter bend can be imposed on the fibre without any change in optical transmission. Their properties make them suitable choices for sensing, high power pulse transmission and gas laser applications. *Figure 3.7* illustrates an example of a PBG fibre with a hollow core.
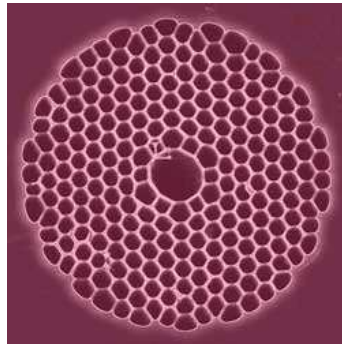
Figure 3.7: Hollow core PBG fibre [21].

As only a small variety of microstructured fibres have been discussed here, the reader is directed to Bjarklev *et al* [3] for a fuller description of the wide range of microstructured fibre available. Polarisation maintaining PCF forms a major part of this research and so a complete discussion of this specific type of PCF will be given later in **Chapter 5**.

3.6   PCF Modelling Techniques

In order to improve the effective index model a number of numerical techniques have been introduced. The localised basis functions method developed in 1998 by Mogilevtsev *et al* [22] which is based on the direct solutions of Maxwell's equations using a representation of the refractive index and the field distributions as sums of localised basis functions has been applied for calculating the properties of many different structures of index-guiding PCF's. However, this method is inefficient at analysing photonic bandgap fibres. The full-vectorial plane-wave expansion method [23,24] is well-suited for analysing photonic bandgap fibers but requires large supercells to model complex structures.

The biorthonormal-basis method first developed in 1998 by Silvestre *et al* [25] and further developed by Ferrando *et al* [26] takes into account the full vector character of light propagation in PCF's. Unlike any of the previous models described, this model allows accurate analysis and calculations of the dispersion properties of PCF's. A crucial drawback of the vectorial methods listed is that they use periodic boundary conditions, therefore they cannot be used to calculate the confinement losses of the PCF structures.

The multipole method developed by White *et al* [27,28] allows for these confinement losses to be calculated. The method is based on treating every hole as a scattering element around which the surrounding electromagnetic field can be expressed. By applying rules from Maxwell's equations to combine the individual field distributions, a system of equations is formed which leads to the overall solution which is applicable for predicting leakage losses in PCF's. However, this method cannot be applied to arbitrary cladding structures and is restricted to circular air holes only.

Poladian *et al* [29] provide an alternative method, the fourier decomposition method, to calculate the confinement losses in structures which are not restricted to circular air holes. This method is based on a function expansion technique which determines the field outside the computational domain satisfying the outward radiating boundary condition.

In 2001 Qiu *et al* [30] proposed the finite-difference time-domain method which was a full-wave analysis of guided modes in PCF. Zhu *et al* [31] provided an alternative finite-difference frequency domain method which determined the solution of Maxwell's equations via a frequency approach.

The Beam Propagation Method (BPM) which is well established in the field of electromagnetics, was applied to PCF's in 2001 by Fogli *et al* [32]. The BPM can be used to simulate the propagation of the initial field along a PCF, and more recently the imaginary distance BPM [33] has been used to extract a limited number of

individual modes. This method is computationally intensive as it needs to consider a fully three-dimensional structure.

A more flexible and powerful method known as the finite-element method was applied to PCF's in 2000 by Brechet *et al* [34]. In order to obtain a description of the field distribution over a fibre cross section the classical Maxwell differential equations must be solved for a large set of properly chosen elementary subspaces which results in a mesh of triangles. These finite triangular elements can be different shapes and sizes which allow any complex waveguide to be represented. The flexibility of the finite-element method to represent a cross-section of a PCF with arbitrary hole sizes, orientation and shape makes this method of numerical modelling superior to simpler, semi-analytical methods previously described. Thus, the finite-element method is the preferred modelling choice for analysing birefringence in polarisation maintaining PCF's [35,36].

Manufacturing costs of PCF's are extremely high thus it is advantages to carry out numerical modelling to determine optimum geometry of the air hole structures prior to manufacturing. The PCF's in this research cost around $200,000 per fibre to produce. Therefore, in **Chapter 5** numerical modelling of various PCF structures will be carried out to determine the optimum fibre geometry for a polarisation maintaining PCF laser. This modelling will be carried out using Lumercials' mode solutions modelling software [37], which is a fully-vectorial mode solver that determines the modes of any waveguide structure of arbitrary geometry created by the user. It hosts a frequency-domain solver that discretizes the structure and a mesh system is employed to aid in analysis. A simple example of the capabilities of the software is shown below for a large mode area PCF fibre with fibre radius 150μm, air hole radius 5.6μm and pitch 23.2μm. The material properties, electric field intensity, electric field components in the x and y directions for one of the fundamental degenerate polarisation modes and the electric field intensity for higher order modes for this fibre structure are illustrated in *Figure 3.8*.
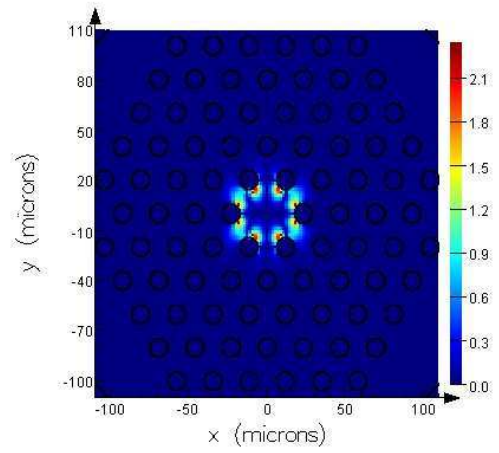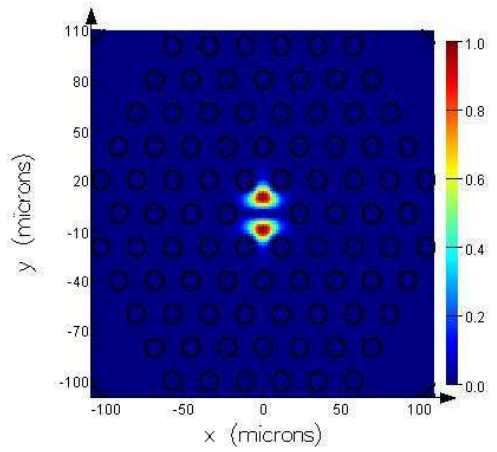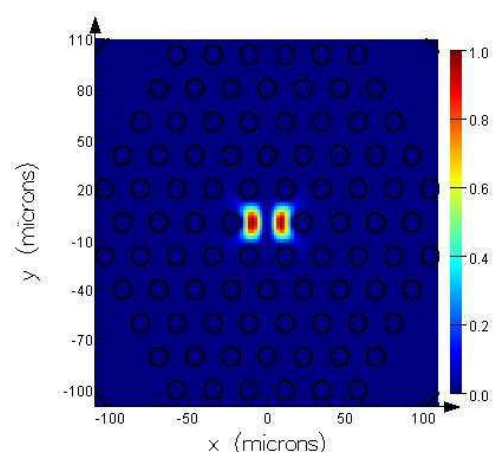
(a)

(b)

(c)

(d)

(e)

(f)

(g)   *(h)*
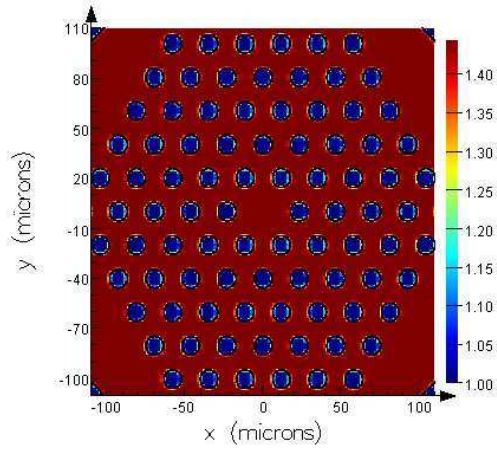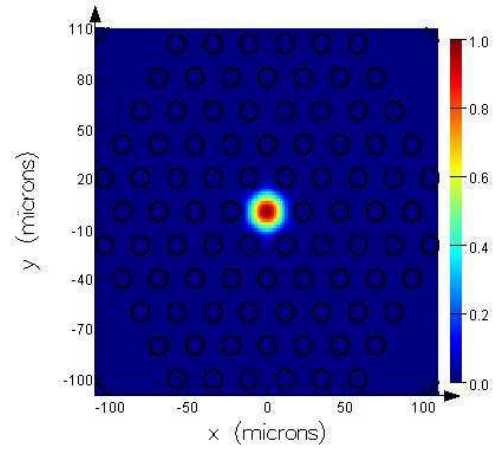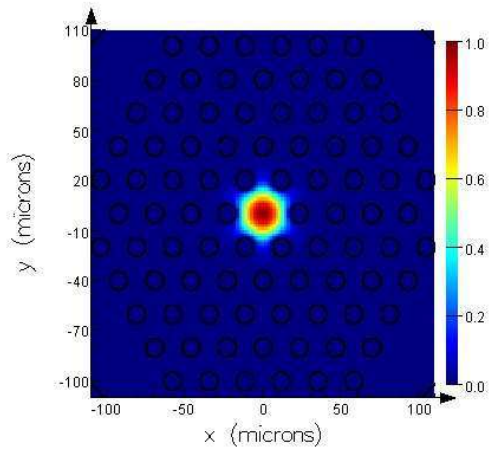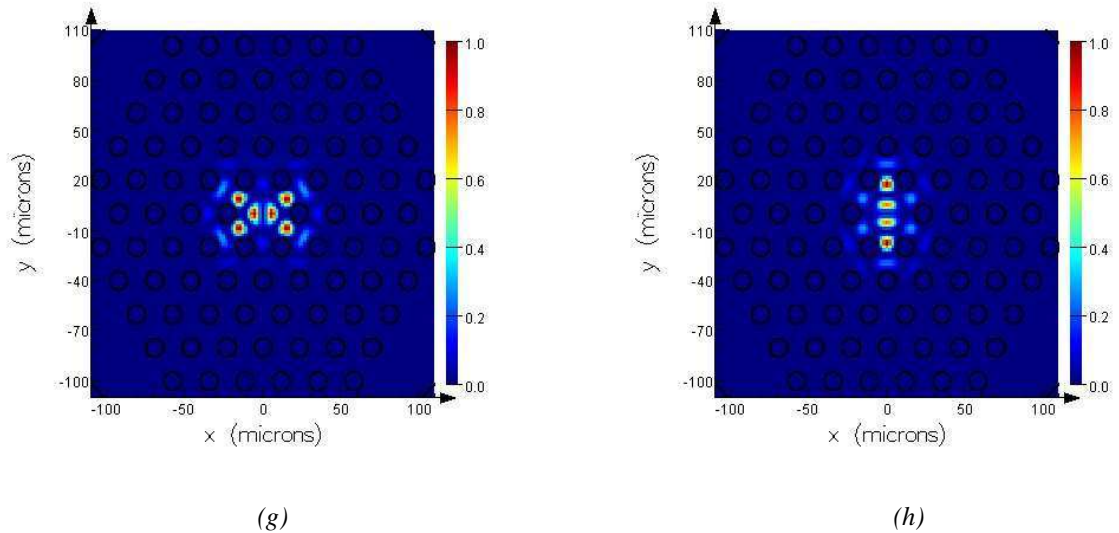
Figure 3.8: *Large mode area PCF with fibre radius 150 μm, air hole radius 5.6 μm and pitch 23.2 μm; (a) material properties, (b) intensity of fundamental mode, (c) electric field in x direction for fundamental mode, (d) electric field in y direction for fundamental mode, (e) intensity for 2nd higher order mode, (f) intensity for 3nd higher order mode, (g) intensity for 4th higher order mode, (h) intensity for 5th higher order mode.*

Note that the intensity of the PCF fundamental mode shown in *Figure 3.8 (b)* is similar to the fundamental mode of a step index optical fibre. This similarity is quantified by using the software to perform an overlap analysis between the PCF fundamental mode and a Gaussian beam mode to determine mode profile area and power coupling capabilities. *Figure 3.9* represents a Gaussian beam with 7μm beam radius that was used in an overlap analysis with the fundamental mode shown in *Figure 3.8 (b).*
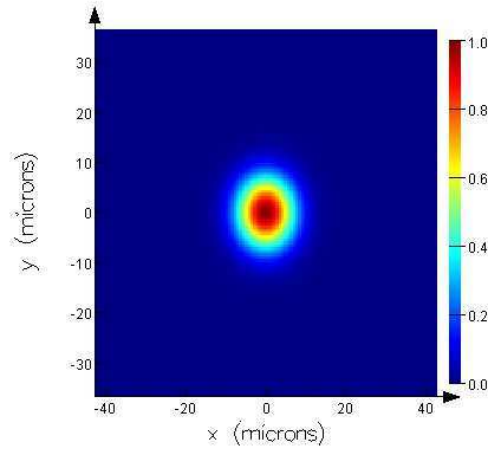
Figure 3.9: *Gaussian beam profile with 10μm beam radius.*

For this example the overlap and power coupling possibility between the Gaussian beam profile and the fundamental mode profile of the PCF structure in *Figure 3.8 (b)* was 92% and 89%, respectively. This method of overlap analysis will be used later in **Chapter 5** to determine the optimum PCF structure in terms of core light confinement.

3.7   Gaussian Beam Properties

As previously discussed in section *3.1.2* wave propagation in an optical fibre can be approximated by a Gaussian function. Thus, let us now consider Gaussian beam properties. The fundamental, Gaussian, paraxial solution to Maxwell's wave equation is denoted as the TEM_{00} mode. This is the simplest mode in which a beam can propagate and is referred to as a Gaussian beam. The geometry and behaviour of Gaussian beams are governed by a set of related beam parameters which are the beam radius w(z), radius of curvature R(z), Raleigh range z_R, confocal parameter b and the beam divergence θ. During paraxial propagation a Gaussian beam stays Gaussian, with only its parameters evolving.

The beam radius, w(z), of a Gaussian beam is the distance from the centre of the beam to the point where the electric field has dropped to 1/e of its value at the beam centre. Measurements concerning real laser beams are based on their intensity rather than their electric field values. Therefore, in terms of a real Gaussian laser beam, the

52

beam radius corresponds to the distance from the centre of the laser beam to the point where the intensity has dropped to $1/e^2$ of the maximum value. The minimum beam radius, known as the beam waist, w_0, occurs at the origin of the z axis, $z = 0$, when the phase front profile is flat. The beam diverges from the beam waist position as shown in *Figure 3.10*.
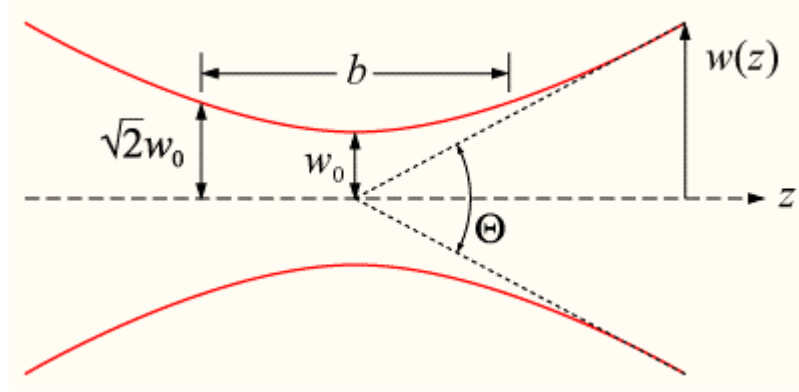
***Figure 3.10**: Propagation of TEM$_{00}$ Gaussian beam mode parallel to the z axis.*

The beam radius, w(z), varies along the propagation direction according to [38]

$$w(z) = w_0 \sqrt{1 + \left(\frac{z}{z_R}\right)^2} \qquad (3.27)$$

where w_0 is again the minimum beam radius, z is the distance propagated from the plane where the wave front is flat and z_R is the Rayleigh range. The Rayleigh range is equivalent to the distance from the beam waist to a position where the beam radius has expanded by a factor of $\sqrt{2}$.

$$z_R = \frac{\pi w_0^2}{\lambda} \qquad (3.28)$$

where λ is the wavelength of the light in the medium of propagation. The distance between these two points is known as the confocal parameter, b.

$$b = 2z_R = \frac{2\pi\omega_0{}^2}{\lambda} \qquad (3.29)$$

The radius of curvature of the beam wave fronts, R(z), as a function of position, z, is

$$R(z) = z\left(1 + \left(\frac{z_R}{z}\right)^2\right) \qquad (3.30)$$

As illustrated in *Figure 3.10*, the beam radius parameter, w(z), tends to a straight line at position $z \gg z_R$. The angle between this straight line and the central axis of the beam is equivalent to the divergence of the beam.

$$\theta \approx \frac{\lambda}{\pi\omega_0} \qquad (3.31)$$

The total angular spread of the beam, measured from a position far from the beam waist is

$$\Theta = 2\theta \qquad (3.32)$$

3.7.1 *Root Mean Square Beam Radius and M² Factor*

The $1/e^2$ radius of the intensity distribution is only a useful quantity for the fundamental Transverse Electric and Magnetic mode (TEM$_{00}$). A more generalised measurement for the beam radius is required for higher order modes. This is found through the variance of the spatial intensity distribution. The second moment of the transverse intensity distribution, I(x,y), at a position of interest along the beam is expressed as [39]

$$\sigma_x^{\;2} = \frac{\int\limits_{\infty}^{\infty}(x-x_0)^2\,I(x,y)dxdy}{\int\limits_{\infty}^{\infty}I(x,y)dxdy} \qquad (3.33)$$

where x_0 is the centre of gravity of the beam. There is an equivalent expression for the second moment in y. This second moment obeys a quadratic free space propagation rule of the form

$$\sigma_x^{\;2}(z) = \sigma_{x_0}^{\;2} + \sigma_\theta^{\;2}(z-z_0)^2 \qquad (3.34)$$

where σ_{x_0} is the variance at the beam waist, σ_θ is the variance of the angular spread of the beam departing from the beam waist and z_0 is the location of the beam waist along the z axis. This quadratic propagation dependence is valid for any arbitrary real laser beam, whether it be Gaussian or non-Gaussian, single mode or multiple transverse mode, fully coherent or partially incoherent in character.

For a Gaussian beam profile of the form $I(x) = \exp[-2x^2/w_x^{\;2}]$, the beam radius is equal to twice the variance. The Root-Mean-Square (RMS) beam radius, W_x, is equal to the $1/e^2$ intensity radius. The RMS radius can be calculated for other higher order modes and propagates along the z axis in an equivalent manner to w(z) for the TEM$_{00}$ mode. For higher order Hermite-Gaussian (HG) modes the RMS radius can be different in each of the x and y symmetry directions. In general for a HG mode the RMS radii are related to w(z) by [40]

$$W_{nm_x}^{\;2} = (2n+1)w(z)^2 = M_x^{\;2}w(z)^2 \qquad (3.35)$$

$$W_{nm_y}^{\;2} = (2m+1)w(z)^2 = M_y^{\;2}w(z)^2 \qquad (3.36)$$

where the parameters $M_x^{\;2}$ and $M_y^{\;2}$ have been introduced to describe the extra beam size in both the x and y directions. The beam will propagate according to

$$W_x(z)^2 = W_{x_0}^2 \left\{ 1 + M_x^4 \left(\frac{\lambda z}{n\pi W_{x_0}^2} \right)^2 \right\} = W_{x_0}^2 \left\{ 1 + \left(\frac{z}{z_R} \right)^2 \right\} \qquad (3.37)$$

where $z_R = \dfrac{n\pi W_{x_0}^2}{M_x^2 \lambda}$. Equation *(3.37)* is equivalent to that for a TEM$_{00}$ mode except that the far-field beam radius has increased by a factor of M_x^2 and the Rayleigh range has decreased by a factor of M_x^2.

3.7.2 *Real Laser Beams and the M^2 Parameter*

Real laser beams do not generally propagate as a simple TEM$_{nm}$ mode. More complex modes can be described as a combination of many TEM$_{nm}$ modes. The M^2 parameter is useful as an indication of beam quality. For example, a beam whose transverse intensity profile at some value of z resembles a Gaussian may propagate in a very different manner to a TEM$_{00}$ mode. Performing an M^2 measurement reveals the beam's inherent quality. The closer the M^2 parameter is to unity the nearer the beam is to a TEM$_{00}$ mode.

3.7.3 *Fitting to the M^2 Function*

The second moment based beam widths, $W_x(z)$ and $W_y(z)$, propagate with distance in free space exactly like the Gaussian beam width w(z) of an ideal Gaussian beam, except for the insertion of an $M_{(x,y)}^2$ factor in the far-field spreading of the beam. Thus, the second moment beam width definitions for any arbitrary beam are

$$W_x^2(z) = W_{0_x}^2 + M_x^4 \left(\frac{\lambda}{\pi W_{0_x}} \right)^2 \left(z - z_{0_x} \right)^2 \qquad (3.38)$$

$$W_y^2(z) = W_{0_y}^2 + M_y^4 \left(\frac{\lambda}{\pi W_{0_y}} \right)^2 \left(z - z_{0_y} \right)^2 \qquad (3.39)$$

where W_{0x} and W_{0y} are the beam waists at positions z_{ox} and z_{oy} and M_x^2 and M_y^2 are the M^2 parameters. Using these definitions the near-field far-field product of any arbitrary beam can be written in the form

$$W_{0_x} W_x(z) \approx M_x^2 \frac{z\lambda}{\pi} \quad \text{as } z \to \infty \qquad (3.40)$$

$$W_{0_y} W_y(z) \approx M_y^2 \frac{z\lambda}{\pi} \quad \text{as } z \to \infty \qquad (3.41)$$

Thus, the M^2 parameters, M_x^2 and M_y^2, give a measure of the quality of the beam. The M^2 values evidently give a measure of how many times diffraction limited the real beam is in each transverse direction.

Hajek [41] used geometrical arguments to fit a set of data points to equation *(3.40)*. His method was simple and reliable but was only applicable where $M^2 = 1$. An algorithm developed by Snadden [42] gives the best fit parameters without resorting to an iterative fitting technique. This method forms the basis of the M^2 analysis that will be carried out in this research. The method involves finding an appropriately weighted sum and then minimising it in a manner analogous to that for linear, muti-parameter least square fits. $W^2(z)$ is first expressed as a polynomial in z without the x and y subscripts as the same method must be applied for both sets of points.

$$W^2(z) = W_0^2 + \left(\frac{\lambda}{\pi}\right)^2 M^4 \frac{(z - z_0)^2}{W_0^2} \qquad (3.42)$$

$$= az^2 + bz + c$$
$$= f(a,b,c)$$

where
$$\begin{cases} a = \left(\dfrac{\lambda}{\pi}\right)^2 \dfrac{M^4}{W_0^2} \\[2mm] b = -2z_0 a \\[2mm] c = W_0^2 + z_0^2 a \end{cases}$$

To find the best fit the following sum is minimised

$$S = \sum_i \frac{\left\{W_i^2 - f_i(a,b,c)\right\}^2}{4W_i^2} \qquad (3.43)$$

where the W_i^2 factor in the denominator gives the correct weighting to the terms, as in a linear fit

$$S = \sum_i \left(W_i - \sqrt{f_i}\right)^2 \frac{\left(W_i + \sqrt{f_i}\right)^2}{4W_i^2} \approx \sum_i \left(W_i - \sqrt{f_i}\right)^2 \qquad (3.44)$$

The derivatives of S with respect to a, b and c are then set to zero. In matrix form this becomes

$$\begin{pmatrix} \sum_i \frac{z_i^4}{W_i^2} & \sum_i \frac{z_i^3}{W_i^2} & \sum_i \frac{z_i^2}{W_i^2} \\ \sum_i \frac{z_i^3}{W_i^2} & \sum_i \frac{z_i^2}{W_i^2} & \sum_i \frac{z_i}{W_i^2} \\ \sum_i \frac{z_i^2}{W_i^2} & \sum_i \frac{z_i}{W_i^2} & \sum_i \frac{1}{W_i^2} \end{pmatrix} \begin{pmatrix} a \\ b \\ c \end{pmatrix} = \begin{pmatrix} \sum_i z_i^2 \\ \sum_i z_i \\ i \end{pmatrix} \qquad (3.45)$$

To obtain the fitting parameters the sums in equation *(3.45)* are calculated using the experimental data and the equation is then solved for a, b and c using Gauss-Jordon elimination [43] to obtain

$$z_0 = -\frac{b}{2a} \qquad (3.46)$$

$$W_0^2 = c - \frac{b^2}{4a} \qquad (3.46)$$

$$M^2 = \frac{\pi}{\lambda}\sqrt{ac - \frac{b^2}{4}} \qquad (3.48)$$

The W_i's are exponential values that can be obtained either as variances (equation *(3.33)*) from images of the beam or when the power values are too high for this method, as in the case in this research, they can be obtained from knife edge measurements fitted with an error function (see equation *(5.6)*, **Chapter 5**.)

3.8 References

[1]   D. Meschede, "Optics, Light and Lasers", Wiley, 2004

[2]   A. Ghatak, K. Thyagagajan, "Introduction to Fiber Optics", Cambridge University Press, 1998

[3]   A. Bjarklev, J. Broeng, A. S. Bjarklev, "Photonic Crystal Fibres", Kluwer Academic Publishers, 2003

[4]   A. Yariv, "Optical Electronics, Fourth Edition", Saunders College Publishing, 1971

[5]   T. Birks, J. Knight, P. St. J. Russell, "Endlessly single-mode photonic crystal fiber", Optics Letters, Vol. 22, 1997, (pp961-963)

[6]   E. Snitzer, H. Po. F. Hakimi, R. Tumminelli, B. C. McCollum, "Double-clad offset core Nd fiber laser", Proc. Conf. Optical Fiber Sensors, Postdeadline Paper PD5, 1988

[7]   M. J. F. Digonnet, "Rare-earth doped fiber lasers and amplifiers", Marcel Dekker Inc. Second Edition, 2001

[8]   L. Zenteno, "High-power double-clad fiber lasers", J. Lightwave Technol. Vol. 11, 1993 (pp1435-1446)

[9]   T. Webber, W. Luthy, H. P. Weber, V. Neumann, H. Berthou, G. Kotrotsios, J. P. Dan, H. E. Hintermann, "Cladding-pumped fiber laser", IEEE J. Quant. Electron. Vol. 31, 1995 (pp326-329)

[10]   A. Liu, K. Ueda, "The absorption characteristics of circular, offset, and rectangular double-clad fibers", Opt. Commun. Vol. 132, 1996 (pp511-518)

[11]   D. J. DiGiovanni, M. H. Muendel, "High-power fiber lasers", Opt. Photon. News Vol. 20, 1999 (pp26-30)

[12]   F. C. McNeillie, E. Riis, J. Broeng, J. R. Folkenberg, A. Petersson, H. Simonsen, C. Jacobsen, "Highly polarised photonic crystal fiber laser", Optics Express, Vol. 12, No. 17, 2004, (pp3981-3987)

[13]   J. Hecht, "Fiber lasers take off in diverse directions", Laser Focus World, http://www.laserfocusworld.com/display_article/218558/12/ARCHI/none/Feat/Fib

[14]   F. C. McNeillie, E. Riis, B. Hitz, "Photonic crystal fiber laser is highly polarized", Photonics Spectra, 2004, (pp92-94)

[15]   J. C. Knight, T. A. Birks, R. F. Cregan, P. St. J. Russell, J. P. De Sandro, "Large mode area photonic crystal fibre", IEE Electronics Letters, Vol. 34, 1998, (pp1347-1348)

[16]   N. A. Mortensen, M. D. Nielsen, J. R. Folkenberg, A. Petersson, H. R. Simonsen, "Improved large-mode-area endlessly single-mode photonic crystal fibers", Optics Letters, Vol. 28, No. 6, 2003, (pp393-395)

[17]   Crystal Fibre A/C website: www.crystalfibre.com/support/dictionary.shtm, visited August 2009

[18]   K. P. Hansen, J. R. Folkenberg, C. Peucheret, A. Bjarklev, "Fully dispersion controlled triangular-core nonlinear photonic crystal fiber", OFC 03, March 27th, Atlanta, USA,, Post Deadline Paper PD3, 2003

[19]   S. Coen, A. H. L. Chau, R. Leonhsrdt, J. D. Hsrvey, "Supercontinuum generation via stimulated Raman scattering and parametric four-wave mixing

in photonic crystal fibers", The Journal of the Optical Society of America B, Vol. 26, 2002, (p753)

[20]   Crystal Fibre A/C, Blaze Photonics data sheet: NL-15-670, web site: www.crystalfibre.com/products/nonlinear.shtm, visited August 2009

[21]   F. Benabid, G. Bouwmans, J. C. Knight, P. St. J. Russell, F. Couny, "Ultrahigh efficiency laser wavelength conversion in a gas-filled hollow core photonic crystal fiber by pure stimulated rotational raman scattering in molecular Hydrogen", Phys. Rev. Lett., Vol. 93, Issue 12, 2004

[22]   D. Mogilevtsev, T. A. Birks, P. St. J. Russell, "Group velocity dispersion in photonic crystal fibers", Optics Letters, Vol. 23, 1998, (pp1662-1664)

[23]   K. M. Ho, C. T. Chan, C.M. Soukoulis,"Existence of a photonic gap in periodic dielectric structures", Phys. Rev. Lett., Vol. 65, 1990, (pp352-3155)

[24]   R. D. Meade, A. M. Rappe, K. D. Brommer, J. D. Joannopoulos, O. L Alerhand, "Accurate theoretical analysis of photonic bandgap materials", Physical Review B, Vol. 48, 1993, (pp8434-8437)

[25]   E. Silvestre, M. V. Andres, P. Andres, "Biorthonormal-basis method for the vector description of optical-fiber modes", IEEE Journal Lightwave Technology, Vol. 16, 1998, (pp923-928)

[26]   A. Ferrando, E. Silvestre, J. J. Miret, P. Andres, M. V. Andres, "Full-vector analysis of a realistic photonic crystal fiber", Optics Letters, Vol. 24, No. 5, 1999, (pp276-278)

[27]   T. P. White, R. C. McPhedran, L. C. Botten, G. H. Smith, C. M. de Sterke, "Calculations of air-guided mods in photonic crystal fibers using the multipole method", Optics Express, Vol. 11, 2001, (pp721-732)

[28]   T. P. White, R. C. McPhedran, C. M. de Sterke , L. C. Botten, M. L. Steel, "Confinement losses in microstructured optical fibres", Optics Letters, Vol. 26, 2001, (pp1660-1662)

[29]   L. Poladian, N. A. Issa, T. M. Monro, "Fourier decomposition algorithm for leaky modes of fibres with arbitrary geometry", Optics Express, Vol. 10, No. 10, 2002, (pp449-454)

[30]   M. Qiu, "Analysis of guided modes in photonic crystal fibers using the finite-difference time-domain method", Microwave and Optical Technology Letters, Vol. 30, No. 5, 2001, (pp327-330)

[31]   Z. Zhu, T. G. Brown, "Full-vectorial finite-difference analysis of microstructured optical fibres", Optics Express, Vol. 10, No. 17, 2002, (pp853-864)

[32]   F. Fogli, L. Saccomandi, P. Bassi, G. Bellanca, S. Trillo, "Full vectorial BPM modeling of index-guiding photonic crystal fibers and couplers", Optics Express, Vol. 10, No. 1, 2001, (pp54-59)

[33]   K. Saitoh, M. Koshiba, "Full-vectorial imaginary-distance beam propagation method based on a finite element scheme: Application to photonic crystal fibers", IEEE Journal Quantum Electron, Vol. 38, Issue 7, 2002, (pp927-933)

[34]   F. Brechet, J. Marcou, D. Pagnoux, P. Roy, "Complete analysis of the characteristics of propagation into photonic crystal fibers, by the finite element method", Optical Fiber Technology, Vol. 6, 2000, (pp181-191)

[35]   Yang Yue, Guiyun Kai, Zhi Wang, Tingting Sun, Long Jin, Yunfei Lu, Chunshu Zhang, Jianguo Liu, Yan Li, Yange Liu, Shuzhong Yuan, Xiaoyi Dong, "Highly birefringent elliptical-hole photonic crystal fiber with squeezed hexagonal lattice", Optics Letters, Vol. 32, No. 5, 2007, (469-471)

[36]   B. M. A Rahman, A. K. M. S. Kabir, M. Rajarajan, K. T. V. Grattan, V. Rakocevic, "Birefringence study of photonic crystal fibers by using the full-vectorial finite element method", Appl. Phys. B, Vol. 84, 2006, (pp75-82)

[37]   Lumercial Solutions Inc, http://www.lumerical.com/mode.php., visited 04/07/08

[38]   A. E. Siegman, "Lasers", University Science Books, 1986

[39]   A. E. Siegman, "How to (maybe) measure laser beam quality", Tutorial Presented at the Optical Society of America Annual Meeting, 1997, (pp1-18)

[40]   A. E. Siegman, "Defining and measuring laser beam quality", In Solid State Lasers: New developments and applications, M. Ingusico and R. Waleenstein, Plenum Press, New York, 1993, (pp13-28)

[41]   M. Hajek, "Waist parameter determination from measured spot sizes", Applied Optics, Vol. 29, 1989, (pp5285-5287)

[42]   M. J. Snadden, "High-resolution spectroscopy of laser-cooled rubidium atoms", PhD Thesis, Strathclyde University, 1996

[43]   W. H. Press, B. P. Flannery, S. A. Teukolsy, W. T. Vetterling, "Numerical recipes in C", Cambridge Press, 1988

Chapter 4

PCF Laser Model

For a laser operating with the same mirror reflectivity in both ends, under equilibrium, one would expect equal output power from both ends. A striking observation with the PCF lasers used in this work was a significantly higher output power from the opposite end from the pump. A theoretical model developed as part of this work will consider the difference in the output laser power from both ends of a PCF laser. This difference in power will be explained by modelling the leakage of core light to the cladding and will be expressed as a function of fibre length. A numerical model depicting the polarisation loss in a polarisation maintaining PCF laser will also be presented. Both theoretical models will be used to explain the experimental observations in **Chapter 5** and **8**.

4.1   Laser Gain Model

If the air hole structure in a PCF laser is not optimised, as was the case of the PCF lasers in this research, then there can be a loss of light from the core to the cladding. Experimentally this leakage of light can manifest itself in a difference in the output power from both ends of the PCF laser as will be shown later in **Chapter 5**. The difference in output power from the front end and the back end of a double cladding Yb^{3+} doped PCF laser can be explained using a numerical model where five coupled differential equations describe the relations between pump power, forward laser power in the core and in the cladding (propagating from the front pump end to the back end of the fibre laser), the backward laser power in the core and in the cladding (propagating from the back end to the front end of the fibre laser).

4.1.1 Pump and Signal Variation

First, in a preliminary model, let us assume that there is no leakage of core light to the cladding. Thus, only three coupled differential equations will be involved in this simplified model.

Assuming the doped core has an ion density of $N_t(r)$ up to a radius b which in general could differ from the core radius a, then the radial distribution of $N_t(r)$ is assumed to be

$$N_t(r) = N_{t0}; \qquad 0 \leq r \leq b$$
$$= 0; \qquad r \geq b \qquad\qquad (4.1)$$

let $N_1(r,z)$ and $N_2(r,z)$ be the population density of Yb^{3+} ion in the ground state, $E_1(^2F_{7/2})$, and the lasing level, $E_2(^2F_{5/2})$, respectively where r represents the cylindrical radial coordinate and z is along the axis of the fibre. As this is a three level laser model, like the system described in section **2.2**, Chapter **2**, pumping at 980nm takes the Yb^{3+} ions from the ground state, E_1 to the upper pump level E_3 whereby the ions rapidly relax to the lasing level E_2. As the relaxation rate of level E_3 is very rapid we can assume that level E_3 is unpopulated, thus [1]

$$N_1(r,z) + N_2(r,z) \approx N_t(r) \qquad (4.2)$$

Let $I_p(r,z)$ and $I_s(r,z)$ represent the intensity distributions of the pump and signal (laser) beams, respectively. Let σ_{pa} represent the absorption cross section at pump, σ_{sa} represent the absorption cross section at the signal and σ_{se} represent the emission cross section at the signal. As already discussed in **Chapter 2,** three energy level transitions can occur – (stimulated) absorption, stimulated emission and spontaneous emission. Using the relevant equations *(2.2), (2.3), (2.4)* for each of these transitions the rate of change of population of the ground level E_1 is [1]

$$\frac{dN_1}{dt} = -\frac{\sigma_{pa} I_p}{h \upsilon_p} N_1 - \frac{\sigma_{sa} I_s}{h \upsilon_s} N_1 + \frac{\sigma_{se} I_s}{h \upsilon_s} N_2 + \frac{N_2}{t_{sp}} \qquad (4.3)$$

where h is Planck's constant, υ_p is the frequency of the pump, υ_s is the frequency of the signal and t_{sp} is the spontaneous emission time. The first group of terms in equation (4.3), $\frac{\sigma_{pa} I_p}{h \upsilon_p} N_1$, represents the number of absorptions per unit time per unit volume from level E_1 to the upper pump level E_3 due to the pump at υ_p, as previously stated by equation (2.2). The second group of terms, $\frac{\sigma_{sa} I_s}{h \upsilon_s} N$, represents the number of absorptions per unit time per unit volume from level E_1 to the upper amplifier level E_2 due to the signal at υ_s, as previously stated by equation (2.2). The third group of terms, $\frac{\sigma_{se} I_s}{h \upsilon_s} N_2$, represents the number of stimulated emissions per unit time per unit volume from level E_2 to level E_1 due to the signal at υ_s, as previously stated by equation (2.4). The final group of terms, $\frac{N_2}{t_{sp}}$, as previously stated by equation (2.3), represents the number of spontaneous emissions per unit time per unit volume from level E_2 to level E_1. The ratio of the emission cross section at the signal and the absorption cross section at the signal is denoted as $\eta_s = \frac{\sigma_{se}}{\sigma_{sa}}$. Therefore, equation (4.3) can be re-written as

$$\frac{dN_1}{dt} = -\frac{\sigma_{pa} I_p}{h \upsilon_p} N_1 + \frac{\sigma_{sa} I_s}{h \upsilon_s} (\eta_s N_2 - N_1) + \frac{N_2}{t_{sp}} \qquad (4.4)$$

At steady state, $\frac{dN_1}{dt} = 0$ therefore equation (4.4) can be re-written as [8]

$$\frac{N_2(r,z)}{N_1(r,z)} = \frac{\overline{I_p} + \dfrac{\overline{I_s}}{(1+\eta_s)}}{1 + \dfrac{\eta_s}{(1+\eta_s)}\overline{I_s}} \qquad (4.5)$$

where;

$$\overline{I_s}(r,z) = \frac{I_s(r,z)}{I_{s0}}$$

$$I_{s0} = \frac{h\upsilon_s}{\sigma_{sa}t_{sp}(1+\eta_s)} = \frac{h\upsilon_s}{(\sigma_{sa}+\sigma_{se})t_{sp}}$$

$$\overline{I_p}(r,z) = \frac{I_p(r,z)}{I_{p0}}$$

$$I_{p0} = \frac{h\upsilon_p}{\sigma_{pa}t_{sp}}$$

Using equation *(4.5)* and since $N_1(r,z) + N_2(r,z) \approx N_t(r)$ we can obtain expressions for N_2 and N_1 as follows

$$N_2(r,z) = \frac{\overline{I_p} + \dfrac{\overline{I_s}}{(1+\eta_s)}}{1 + \overline{I_p} + \overline{I_s}} N_t \qquad (4.6)$$

and

$$N_1(r,z) = \frac{1 + \dfrac{\eta_s}{(1+\eta_s)}\overline{I_s}}{1 + \overline{I_p} + \overline{I_s}} N_t \qquad (4.7)$$

which represent the steady state populations of the energy levels E_2 and E_1, respectively

The rate of change of pump intensity, as a function of distance, z, propagated i.e. fibre laser length, can be expressed as [1]

$$\frac{dI_p}{dz} = -\sigma_{pa} N_1(r,z) I_p(r,z) \qquad (4.8)$$

By substitution of equation *(4.7)* into equation *(4.8)* and taking into account the forward and backwards propagating laser signal in the core, $I_{s,f}^{co}$, $I_{s,b}^{co}$, respectively, where $I_s = I_{s,f}^{co} + I_{s,b}^{co}$, we obtain the first of our three model differential equations;

$$\frac{dI_p}{dz} = -\sigma_{pa} N_t(r) \frac{1 + \dfrac{\eta_s}{(1+\eta_s)} \dfrac{I_{s,f}^{co} + I_{s,b}^{co}}{I_{s0}}}{1 + \dfrac{I_p}{I_{p0}} + \dfrac{I_{s,f}^{co} + I_{s,b}^{co}}{I_{s0}}} I_p(r,z) \qquad (4.9)$$

Similarly the rate of change of signal intensity when propagating forward (from the front to back of the fibre laser) can be expressed as

$$\frac{dI_{s,f}^{co}}{dz} = \sigma_{sa}(\eta_s N_2 - N_1) I_s(r,z) \qquad (4.10)$$

and by substitution of equations *(4.6)* and *(4.7)* into equation *(4.10)* we obtain the second of our three model differential equations;

$$\frac{dI_{s,f}^{co}}{dz} = \sigma_{sa} N_t(r) \frac{\left(\eta_s \dfrac{I_p}{I_{p0}} - 1\right) I_{s,f}^{co}(r,z)}{1 + \dfrac{I_p}{I_{p0}} + \dfrac{I_{s,f}^{co} + I_{s,b}^{co}}{I_{s0}}} I_p(r,z) \qquad (4.11)$$

Similarly after undergoing a 4% Fresnel reflection from the fibre laser end facet the rate of change of signal intensity propagating backwards (from the back end to the front end of the fibre laser) is our final model differential equation

$$\frac{dI_{s,b}^{co}}{dz} = -\sigma_{sa} N_t(r) \frac{\left(\eta_s \frac{I_p}{I_{p0}} - 1\right) I_{s,b}^{co}(r,z)}{1 + \frac{I_p}{I_{p0}} + \frac{I_{s,f}^{co} + I_{s,b}^{co}}{I_{s0}}} I_p(r,z) \qquad (4.12)$$

The three differential equations can be rewritten in terms of power if the following relationship between intensity and power is assumed and w is taken to be the 1/e radius.

$$I_p(r,z) = \frac{1}{A_{clad}} P_p(z) \qquad (4.13)$$

$$I_{s,f}^{co}(r,z) = \frac{1}{A_{core}} \cdot e^{-\left(r^2/w(z)^2\right)} P_{s,f}^{co}(z) \qquad (4.14)$$

$$I_{s,b}^{co}(r,z) = \frac{1}{A_{core}} \cdot e^{-\left(r^2/w(z)^2\right)} P_{s,b}^{co}(z) \qquad (4.15)$$

where $A_{core} = \pi a^2$ is the area of the core with radius a, and $A_{clad} = (\sqrt{3}/2)(d_{clad}^2)$ is the area of the hexagonal inner cladding where d_{clad} is the inner cladding pump diameter. $P_p(z)$ is the power of the pump, $P_{s,f}^{co}(z)$ and $P_{s,b}^{co}(z)$ is the power of the signal in the core in the forward and backwards direction respectively. Therefore, the three model differential equations are as follows [1];

$$\frac{dP_p}{dz} = 2\pi \int_0^\infty \frac{dI_p}{dz} r \, dr$$

$$= -\sigma_{pa} N_{t0} \frac{A_{core}}{A_{clad}} P_p(z) \left[\frac{U}{W} \ln\left\{ \frac{X + W}{X + We^{-b^2/w(z)^2}} \right\} + \frac{1}{X} \ln\left\{ \frac{W + Xe^{b^2/w(z)^2}}{W + X} \right\} \right] (4.16)$$

$$\frac{dP_{s,f}^{co}}{dz} = \sigma_{sa} N_0 P_{s,f}^{co} \left[\frac{V}{W} \ln\left\{ \frac{X + W}{X + We^{-b^2/w(z)^2}} \right\} \right] \qquad (4.17)$$

$$\frac{dP_{s,b}^{co}}{dz} = -\sigma_{sa} N_0 P_{s,b}^{co} \left[\frac{V}{W} \ln \left\{ \frac{X+W}{X+We^{-b^2/w(z)^2}} \right\} \right] \qquad (4.18)$$

where;

$$U = \frac{\eta_s}{\eta_s + 1} \frac{P_{s,f}^{core}(z) + P_{s,b}^{core}(z)}{P_{s0}(z)} \qquad (4.19)$$

$$V = \eta_s \frac{P_p(z)}{P_{p0}(z)} - 1 \qquad (4.20)$$

$$W = \frac{P_{s,f}^{core}(z) + P_{s,b}^{core}(z)}{P_{s0}(z)} \qquad (4.21)$$

$$X = 1 + \frac{P_p(z)}{P_{p0}(z)} \qquad (4.22)$$

$$P_{p0} = I_{p0} A_{clad} \qquad (4.23)$$

$$P_{s0} = I_{s0} A_{core} \qquad (4.24)$$

The boundary conditions for the three differential equations are

$$P_p(0) = T_{in} P_{p,in} \qquad (4.25)$$

$$P_{s,f}^{co}(0) = R_1 P_{s,b}^{co}(0) \qquad (4.26)$$

$$P_{s,b}^{co}(L) = R_2 P_{s,f}^{co}(L) \qquad (4.27)$$

where R_1 and R_2 is the reflectivity at both ends (in this case $R_1 = R_2 = 0.04$) and T_{in} is the percentage of the pump power coupled into the fibre. The differential equations were solved using Mathematica [2] and to match the boundary conditions in both ends of the fibre a shooting to a fitting point method was used [3]. The numerical values used in the following simulations were: $l = 10m$, $P_p(z) = 4W$, $\lambda_p = 978nm$, $\lambda_s =$

1040nm, a = 3μm, d_{clad} = 140μm, t_{sp} = 0.95ms, σ_{pa} = 2.6x10^{-24} m^2, σ_{sa} = 0.07x10^{-24} m^2, σ_{se} = 0.8x10^{-24} m^2 [4].

The coupled pump power and the forward and backwards laser power was modelled in *Figure 4.1* for a 10m length PCF laser operating without any loss.
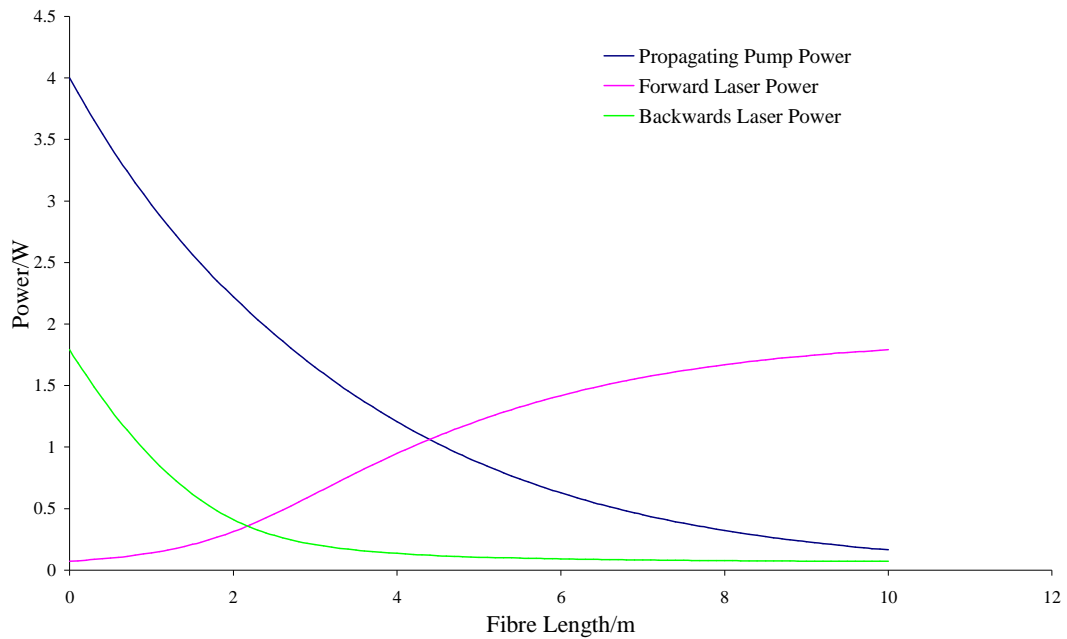
Figure 4.1*: Propagating pump power, forwards and backwards laser power for 10m PCF laser pumped by 4W 976nm. (At length 4m, from top to bottom, the plots follow the order of the series labels).*

This model was repeated for a longer fibre length, up to 25m as shown in *Figure 4.2*.
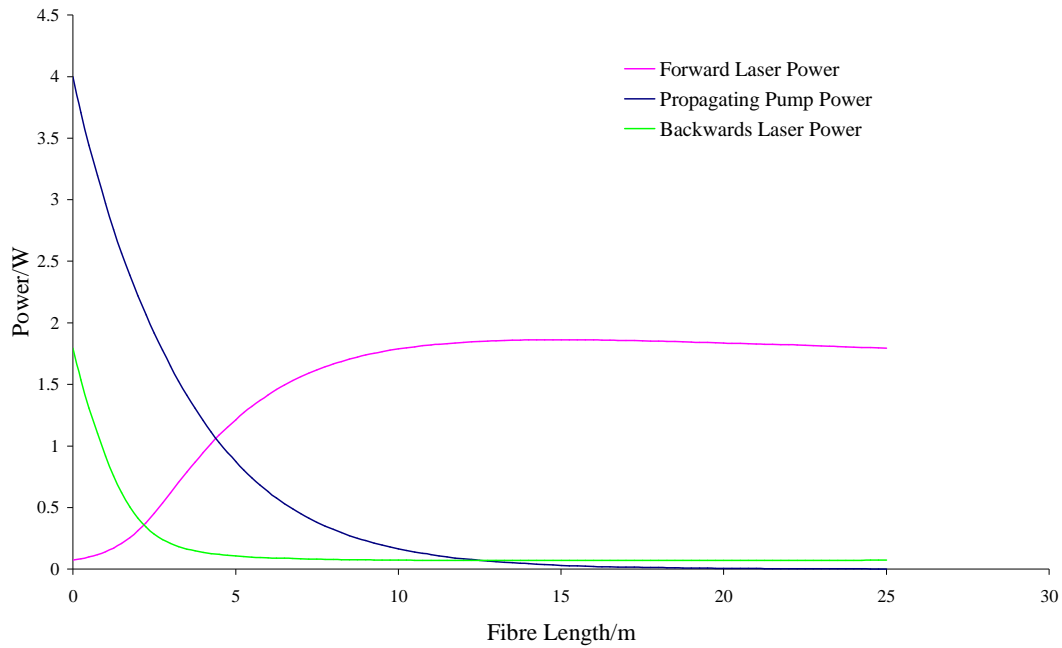
Figure 4.2*: Coupled pump power, forwards and backwards laser power for 25m PCF pumped by 4W 976nm. (At length 10m, from top to bottom, the plots follow the order of the series labels).*

These results show that, as there is no loss in the PCF laser, the laser power output from both ends of the fibre laser is the same, 1.79W. As a result of pump depletion, both the forward and the backward mode in the core have the highest gain in the front end of the fibre laser. On examining equation *(4.16)* the rate of change of the pump power with respect to distance propagated along the fibre axis will always be negative but this is not the case for the rate of change of the signal power which is mostly positive. As the pump power is continuously being depleted by the absorbing ions in the doped core of the fibre laser the rate of change of pump power must always be negative. Thus, the population inversion will keep reducing with increasing distance, z, along the fibre axis. This in turn reduces the gain and at some z value the pump power will drop below the critical value at which point the fibre will become attenuating rather than amplifying. Indeed, in this example the forward laser power begins to drop after 15m (See *Figure 4.2*). Thus, the rate of change of the signal power with respect to distance propagated along the fibre axis can be positive or negative depending on whether the fibre laser is amplifying or attenuating the signal. Beyond the z position corresponding to the critical pump power value the fibre will reabsorb the amplified signal which will reduce the gain in the fibre laser.

The forward laser power and the total laser power (forwards + backwards laser power) was plotted as a function of coupled pump power as shown in *Figure 4.3*.
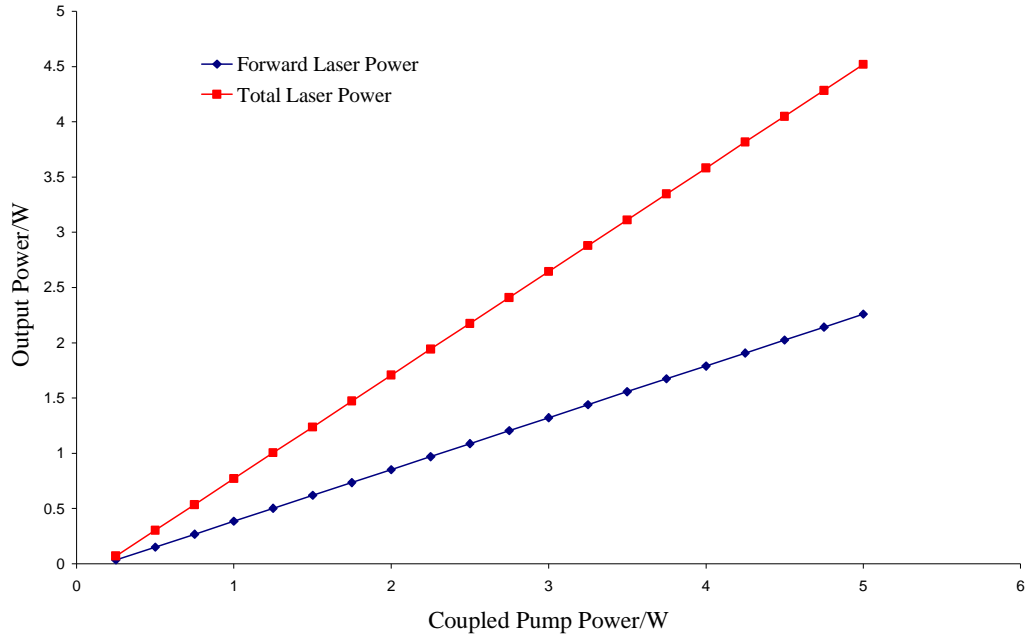

Figure 4.3: *Forward and total laser power (forward + backwards laser power) for 10m PCF laser pumped by 4W.*

Since there is no loss in the PCF laser the forward and backwards laser power is the same thus the total output laser power, (4.5W) is equal to twice the forward laser power. The forward propagating laser power was plotted as a function of coupled pump power for various fibre lengths. For each fibre length the efficiency and threshold of the laser was recorded and plotted in *Figures 4.4* and *4.5*.
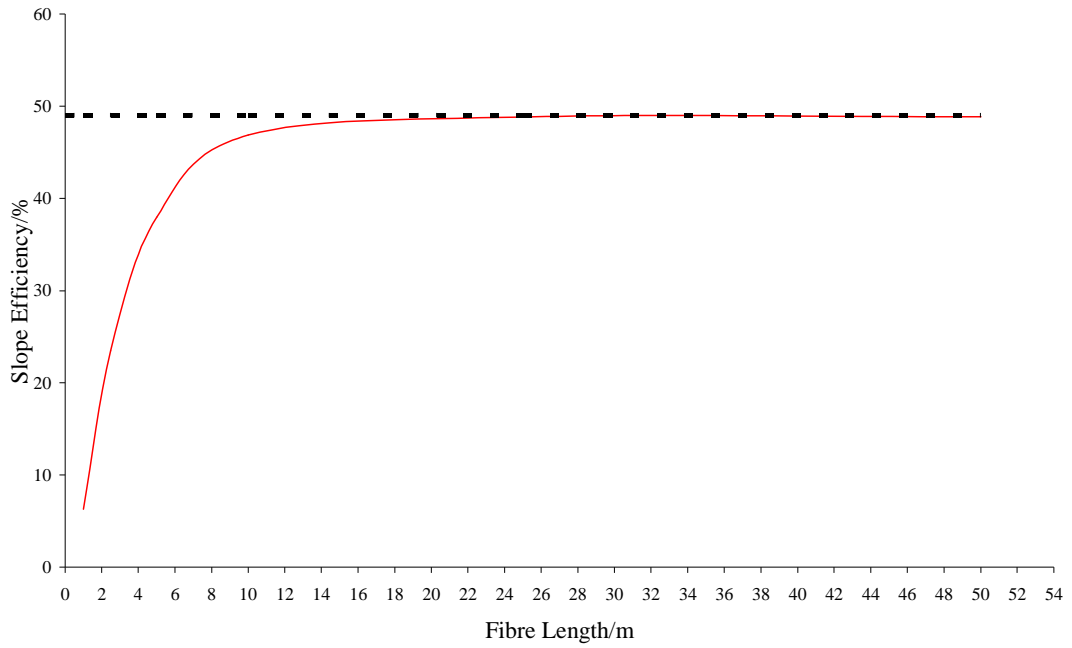
Figure 4.4*: Slope efficiency of PCF laser based on forward propagating laser power and coupled pump power as a function of fibre length (Dashed line represents theoretical maximum slope efficiency).*
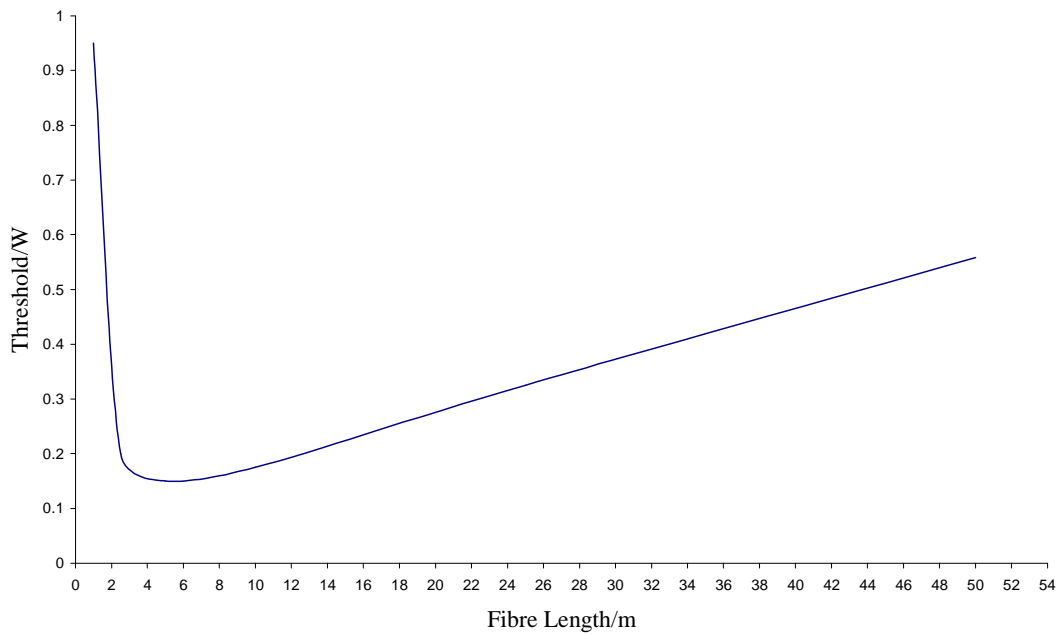
Figure 4.5*: Threshold of PCF laser based on forward propagating laser power and coupled pump power as a function of fibre length.*

Figure 4.4 shows that after 10m fibre length the efficiency of the PCF laser begins to level off and no further increase in laser efficiency is observed. This result is expected as on examining *Figure 4.2* we see that there is no further increase in the forward laser power after 15m, thus there can be no further increase in laser efficiency. *Figure 4.5* shows that for short fibre length, less than 1m, the threshold of the PCF laser is high which is expected as *Figure 4.1* shows that there has only been 25% pump absorption at 1m. Beyond 1m, the threshold reduces rapidly as the pump absorption increases. After 2.5m the pump absorption has almost doubled to 48% with a corresponding decrease in threshold by 21% in comparison to a 1m fibre length. The minimum threshold of 0.15W corresponds to a PCF laser length of 6m whereby 84% of the pump has been absorbed.

4.1.2 Core to Cladding Loss

Now let us extend the model to include a loss of laser light from the core to the inner cladding as this situation was experimentally observed during this research and is detailed in **Chapter 5**. The two model differential equations *(4.17)* and *(4.18)*, previously presented, must be modified to include this leakage of light from the core to the inner cladding such that

$$\frac{dP_{s,f}^{co}}{dz} = \sigma_{sa} N_0 P_{s,f}^{co} \left[\frac{V}{W} \ln\left\{ \frac{X+W}{X+We^{-b^2/w(z)^2}} \right\} \right] - \alpha_0 P_{s,f}^{co} \qquad (4.28)$$

$$\frac{dP_{s,b}^{co}}{dz} = -\sigma_{sa} N_0 P_{s,b}^{co} \left[\frac{V}{W} \ln\left\{ \frac{X+W}{X+We^{-b^2/w(z)^2}} \right\} \right] + \alpha_0 P_{s,b}^{co} \qquad (4.29)$$

where α_0 represents the loss of laser power from the core to the inner cladding. Hence, the differential equations that describe the rate of change of laser power in the cladding, propagating forwards and backwards, are

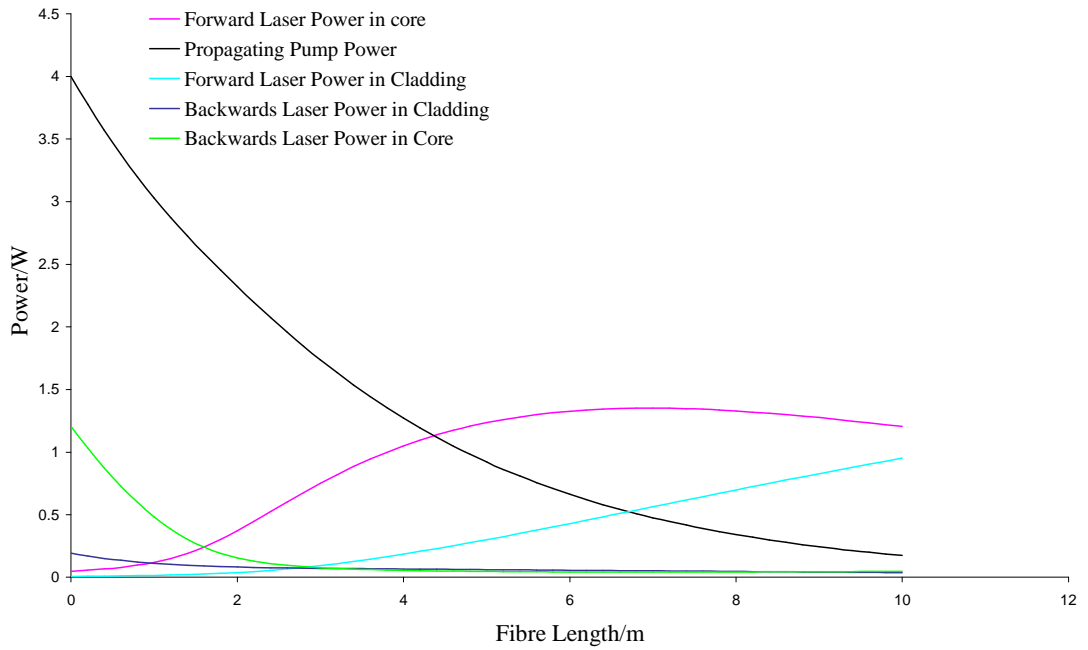$$\frac{dP_{s,f}^{cl}}{dz} = \alpha_0 P_{s,f}^{co}(r,z) \qquad\qquad (4.30)$$

$$\frac{dP_{s,b}^{cl}}{dz} = -\alpha_0 P_{s,b}^{co}(r,z) \qquad\qquad (4.31)$$

with boundary conditions

$$P_{s,f}^{cl}(0) = R_1 P_{s,b}^{cl}(0) \qquad\qquad (4.32)$$

$$P_{s,b}^{cl}(L) = R_2 P_{s,f}^{cl}(L) \qquad\qquad (4.33)$$

Using equations *(4.28-4.33)*, the following theoretical results were obtained when a loss of 0.05m^{-1} was included in the model.


Figure 4.6*: Power characteristics of 10m length PCF laser, pumped by 4W, when 0.05m^{-1} loss of core light to cladding is included. (At length 6m, from top to bottom, the plots follow the order of the series labels).*
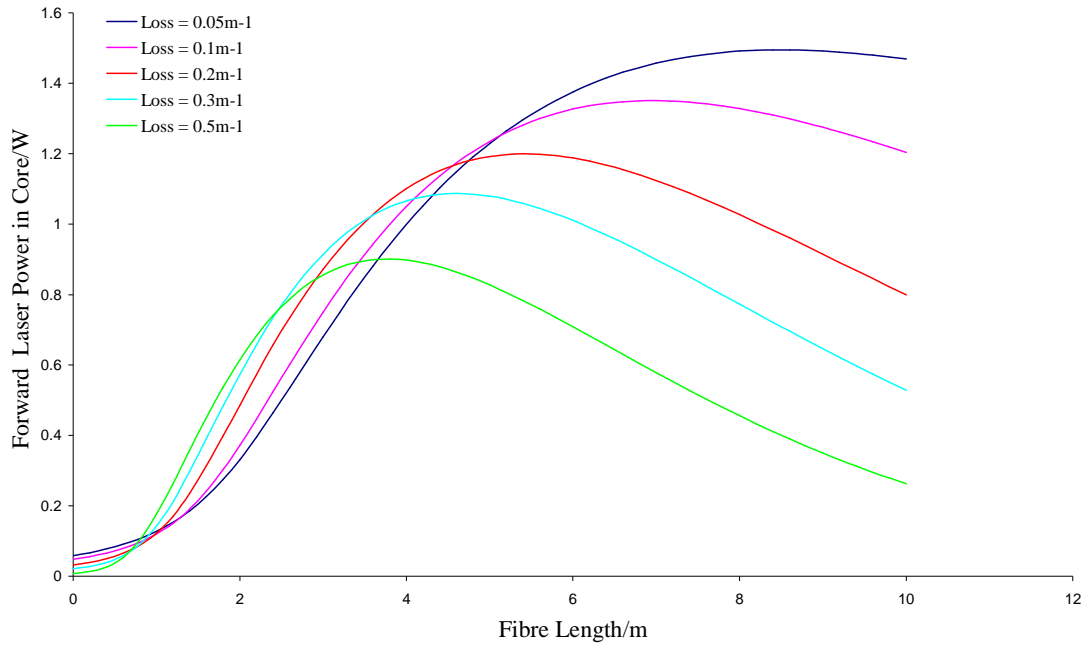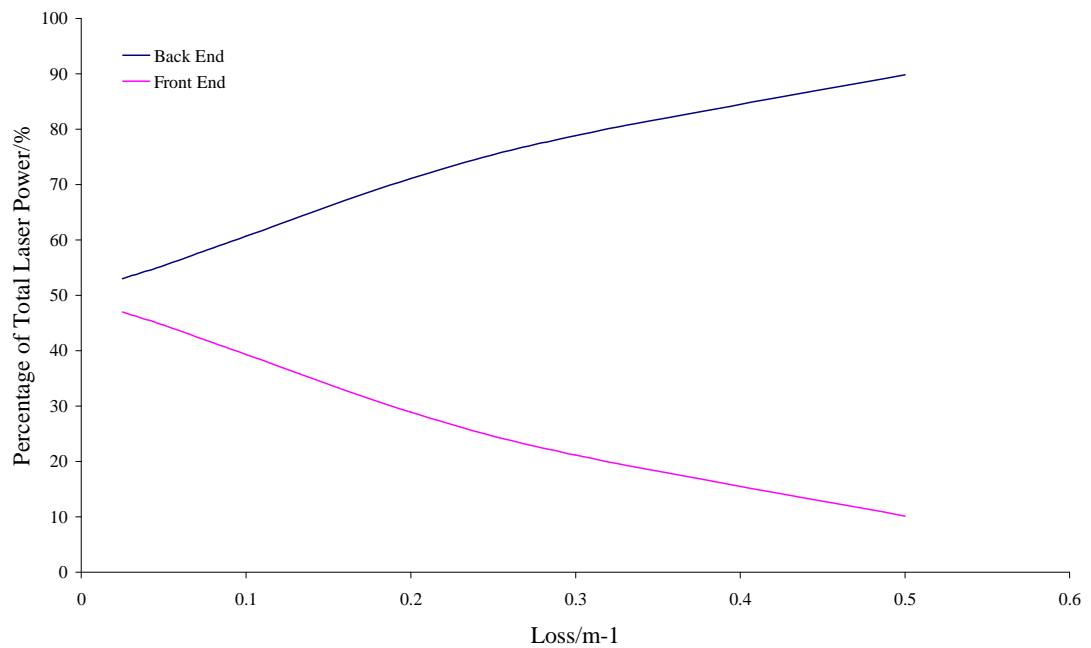
Figure 4.7: *Forward laser power in core as a function of fibre length for PCF laser with 4W coupled pump power (At length 6m, from top to bottom, the plots follow the order of the series labels).*

Figure 4.7 shows that increasing the loss from the core to the cladding reduces the output laser power in the core. Also, with increasing loss values we see that the output laser power roll over point, whereby the laser becomes attenuating instead of amplifying, occurs at shorter fibre lengths. The percentage of laser power in the core was modelled for both ends of the PCF laser.
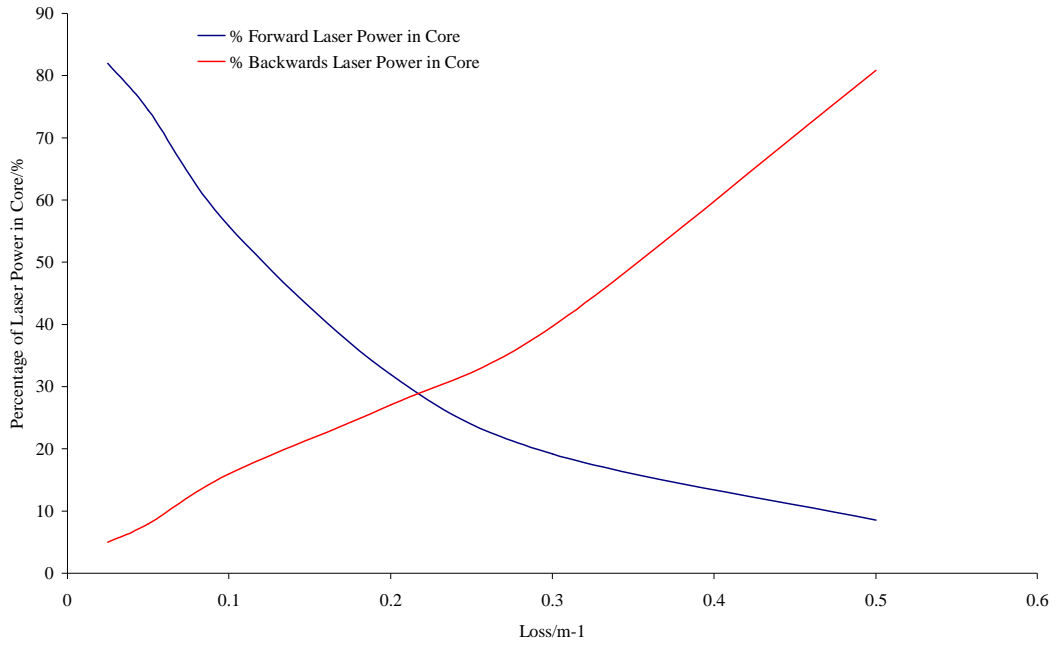
Figure 4.8: *Percentage of laser power in the core as a function of core to cladding loss for a 20m length fibre with 4W coupled pump power.*

Figure 4.9: *Percentage of total laser power (forward propagating power in core and cladding plus backwards propagating laser power in core and cladding) measured at the front and back end of the PCF laser as a function of core to cladding loss for a 20m length fibre with 4W coupled pump power.*
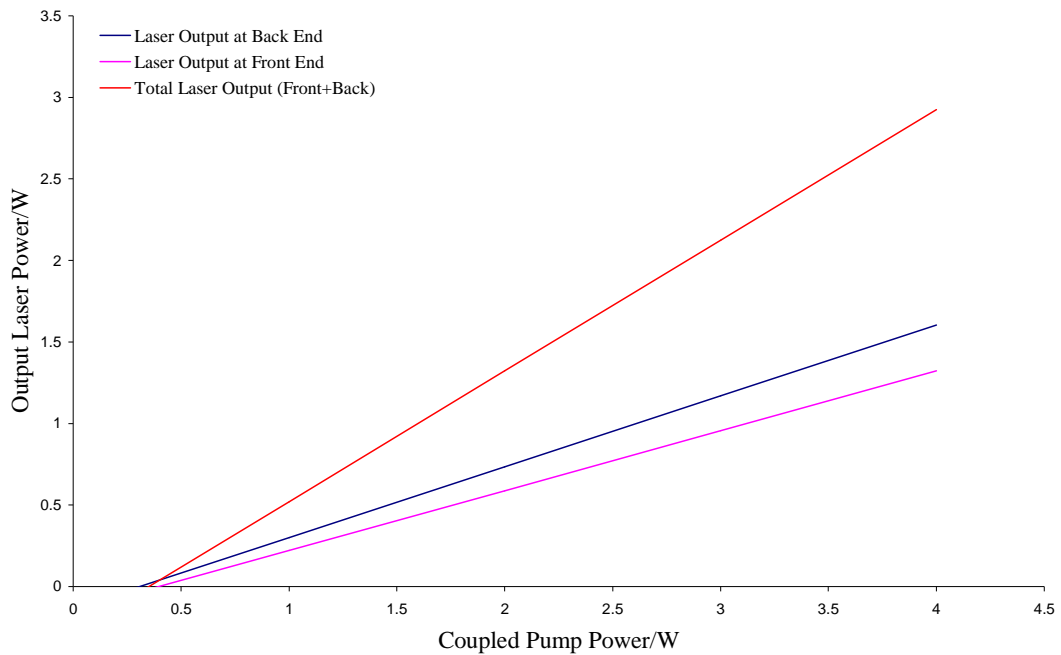
Figure 4.10: *Output laser power for 20m PCF laser with a core to cladding loss of 0.05m^{-1} as a function of coupled pump power.*

Figure 4.10 is based on a 20m length fibre, core to cladding loss of 0.05m^{-1} with pump absorption 0.48dBm^{-1}. For this fibre length there is 11% of unabsorbed pump power therefore the output power values in *Figure 4.10* have been corrected for this unabsorbed pump power. The total output laser power slope efficiency is 77% compared to the theoretical maximum, 91%, given by the ratio of the PCF laser and pump photon energies.

These modelling results show that when a loss of 0.05m^{-1} out of the core and into the inner cladding is included in the laser model, the laser power output coming out of the back end is larger than the power output from the front end of the PCF laser. *Figure 4.8* shows that for a 20m PCF laser with a 0.05m^{-1} loss, 75% of the forward propagating light is in the core. *Figure 4.9* shows that for a 20m PCF laser with a 0.05m^{-1} loss that 55% of the total laser power (forward propagating power in core and cladding plus backwards propagating power in core and cladding) is at the back end of the PCF laser. This difference in output power occurs because the backward propagating mode in the core experiences most of its gain in the front end of the fibre, only little of its power is lost out into the inner cladding. On the other hand,

the forward propagating mode in the core experiences most of its gain at the beginning i.e. in the back end of the fibre laser. Thus, a much larger fraction of the laser power can be coupled out of the core as the light propagates along the length of fibre. There is therefore a change in the ratio of the output power in either end of the fibre laser compared to when there is no loss from the core to the inner cladding. Numerical mode modelling, developed as part of this research, will be presented at the end of **Chapter 5** which will theoretically optimise the experimental PCF laser structure so as to reduce this core to cladding loss.

4.1.3   Polarisation Maintaining PCF Laser

To describe the polarisation properties of the fibre laser we have to introduce equations like *(4.28)* and *(4.29)* for both horizontal and vertical polarisations. For each directions, they will in general have different values of loss, α_0, as well as a coupling, β, between them. As the main focus of this research is a polarisation maintaining PCF laser the polarisation ratio is modelled as a function of horizontal loss for a variety of polarisation coupling values. The differential equations *(4.28)* and *(4.29)* must be modified to include the polarisation coupling loss, β. Therefore, the rate of change of laser power propagating in the forward and backwards direction must also be separated into horizontal and vertical components such that

$$\left(\frac{dP_{s,f,H}^{co}}{dz}\right) = \sigma_{sa}N_0 P_{s,f,H}^{co}\left[\frac{V}{W}\ln\left\{\frac{X+W}{X+We^{-b^2/w(z)^2}}\right\}\right] - \alpha_{0H}P_{s,f,H}^{co} - \beta(P_{s,f,H}^{co} - P_{s,f,V}^{co})$$

(4.34)

$$\left(\frac{dP_{s,f,V}^{co}}{dz}\right) = \sigma_{sa}N_0 P_{s,f,V}^{co}\left[\frac{V}{W}\ln\left\{\frac{X+W}{X+We^{-b^2/w(z)^2}}\right\}\right] - \alpha_{0V}P_{s,f,V}^{co} - \beta(P_{s,f,V}^{co} - P_{s,f,H}^{co})$$

(4.35)

$$\left(\frac{dP_{s,b,H}^{co}}{dz}\right) = -\sigma_{sa}N_0 P_{s,b,H}^{co}\left[\frac{V}{W}\ln\left\{\frac{X+W}{X+We^{-b^2/w(z)^2}}\right\}\right] + \alpha_{0H}P_{s,b,H}^{co} - \beta(P_{s,b,H}^{co} - P_{s,b,V}^{co})$$

(4.36)

$$\left(\frac{dP^{co}_{s,b,V}}{dz}\right) = -\sigma_{sa}N_0 P^{co}_{s,b,V}\left[\frac{V}{W}\ln\left\{\frac{X+W}{X+We^{-b^2/w(z)^2}}\right\}\right] + \alpha_{0V}P^{co}_{s,b,V} - \beta(P^{co}_{s,b,V} - P^{co}_{s,b,H})$$

<div align="right">(4.37)</div>

where the sub-scripts H and V represent horizontal and vertical components, respectively. Both the horizontal and vertical components of the polarisation leak into the cladding which then becomes unpolarised. The rate of change of laser power propagating in the forward and backwards direction in the cladding is
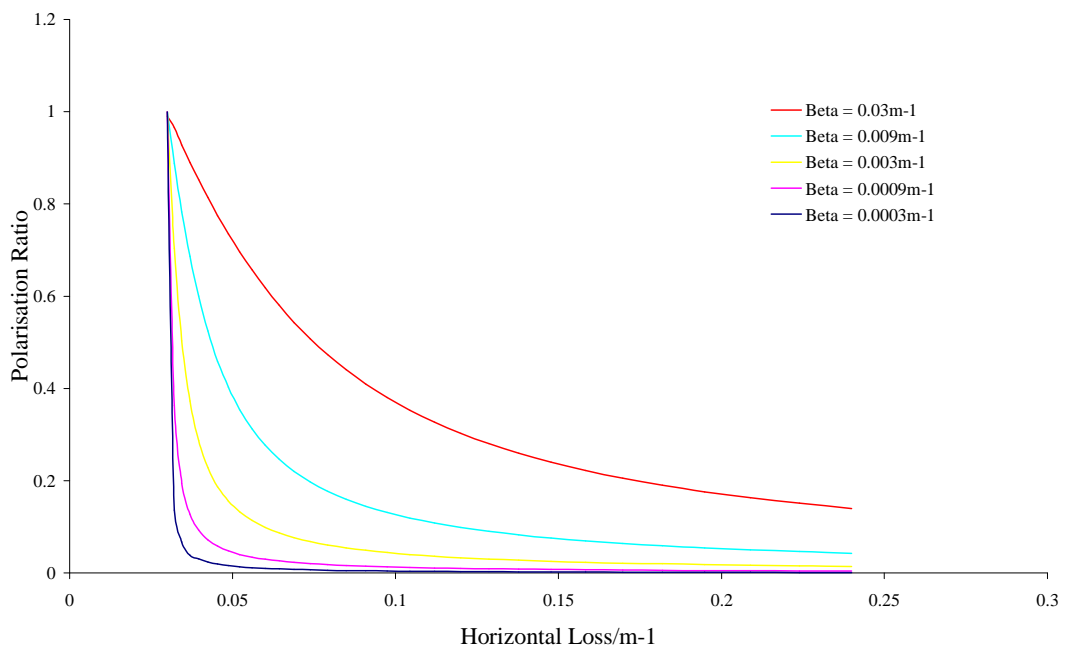
$$\frac{dP^{cl}_{s,f}}{dz} = \left(\alpha_{0H}P^{co}_{s,f,H} + \alpha_{0V}P^{co}_{s,f,V}\right) + \left(P^{co}_{s,f,V} - P^{co}_{s,f,H}\right) + \left(P^{co}_{s,f,V} - P^{co}_{s,f,H}\right) \qquad (4.38)$$

$$\frac{dP^{cl}_{s,b}}{dz} = -\left(\alpha_{0V}P^{co}_{s,b,H} + \alpha_{0V}P^{co}_{s,b,V}\right) - \left(P^{co}_{s,b,V} - P^{co}_{s,b,H}\right) - \left(P^{co}_{s,b,V} - P^{co}_{s,b,H}\right) \qquad (4.39)$$

The polarisation ratio, which is equal to the vertical loss divided by the horizontal loss as a function of polarisation coupling loss was modelled as shown in *Figure 4.11*.
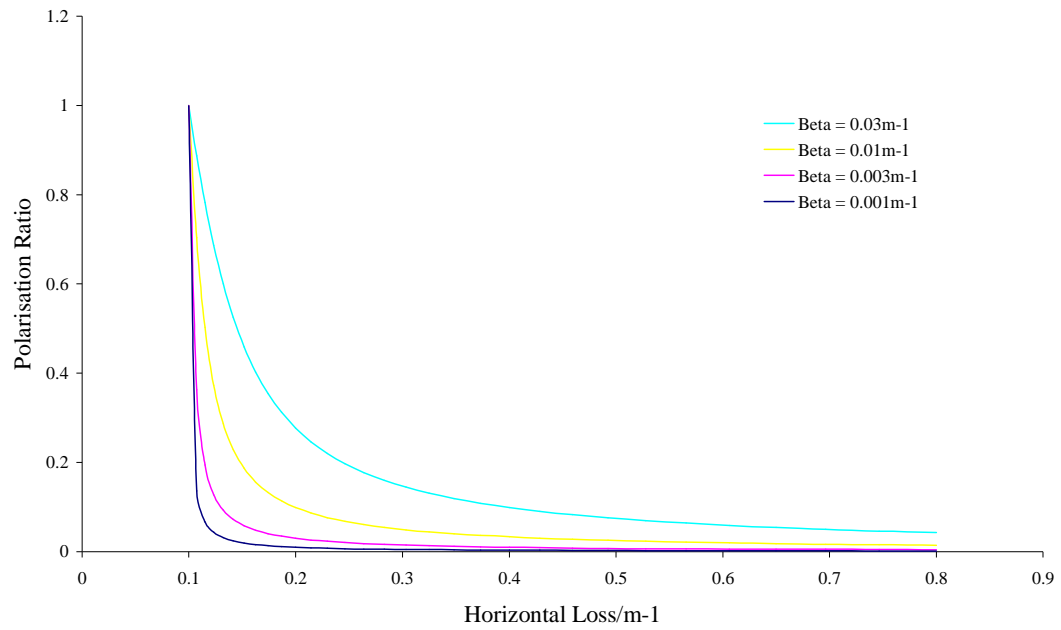
(a)

*(b)*

Figure 4.11: *Polarisation ratio as a function of horizontal loss for various polarisation coupling values, beta, when (a) vertical loss = 0. 1m⁻¹ (At horizontal loss 0.2m⁻¹, from top to bottom, the plots follow the order of the series labels), (b) vertical loss = 0. 03m⁻¹ (At horizontal loss 0.05m⁻¹, from top to bottom, the plots follow the order of the series labels).*

When the horizontal and the vertical losses are equal, corresponding to a polarisation ratio of 1, the guided laser light will be un-polarised. The polarisation ratio is dependent on the differential loss between the horizontal and vertical polarisation states. *Figure 4.11* shows that for small values of coupling loss, beta, only a small difference in the horizontal and vertical loss component is required to obtain a good polarisation.

The output laser power characteristics for the 20m PCF laser including a horizontal loss 0.02m^{-1} and vertical loss $= 0.01\text{m}^{-1}$ is shown in *Figure 4.12*.
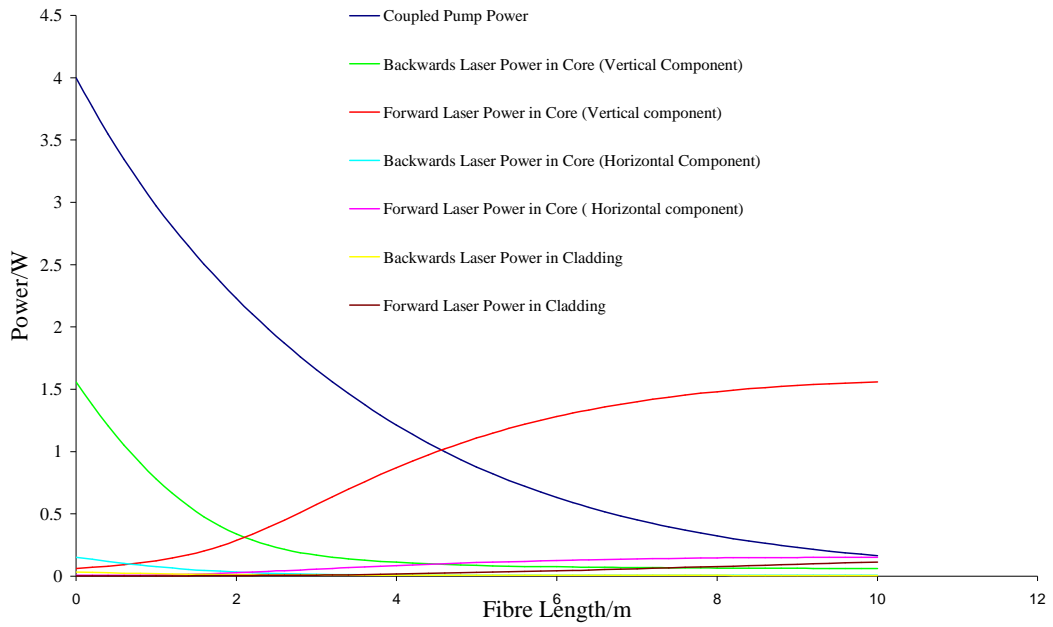
(a)
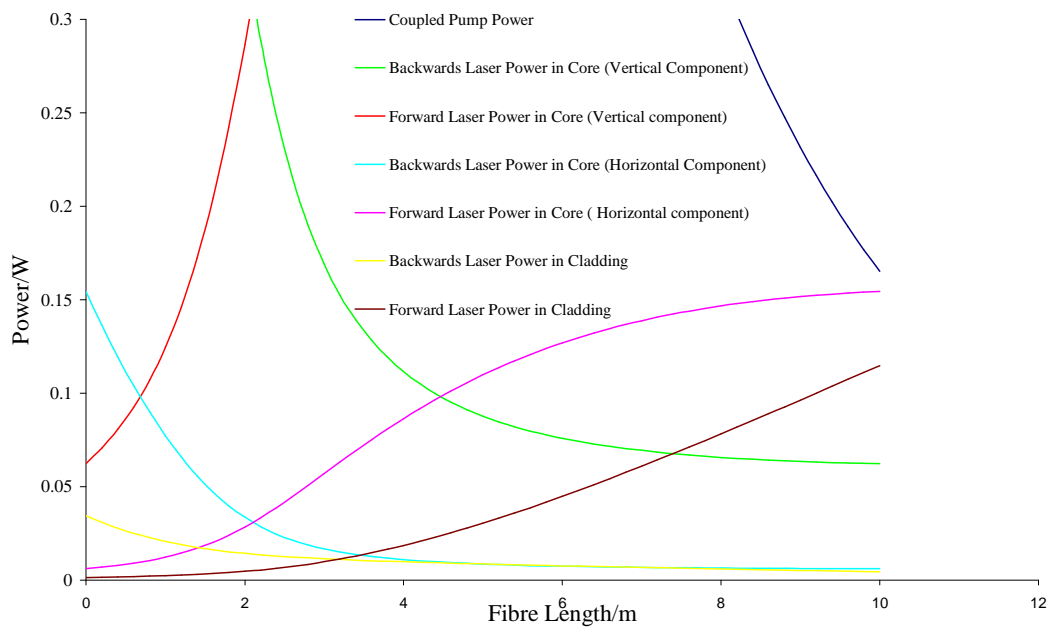
*(b)*

Figure 4.12: *Output power characteristics for 10m length PCF laser, pumped by 4W, when horizontal loss = 0.02m⁻¹, vertical loss = 0.01m⁻¹ and polarisation coupling = 0.001m⁻¹; (a) Full scale, (b) zoomed in scale. (At fibre length 2m, from top to bottom, the plots follow the order of the series labels).*

4.1.4   75% Bragg Grating PCF Laser

To mimic the highly polarised PCF laser with incorporated 75% Bragg grating described in the forthcoming **Chapter 8** of this thesis, $R_1 = 0.04$ in the previous model was replaced by $R_1 = 0.75$. Thus, the simulations carried out in the previous section, which include the loss from the core to the cladding and the polarisation coupling loss will be repeated for this new laser cavity.
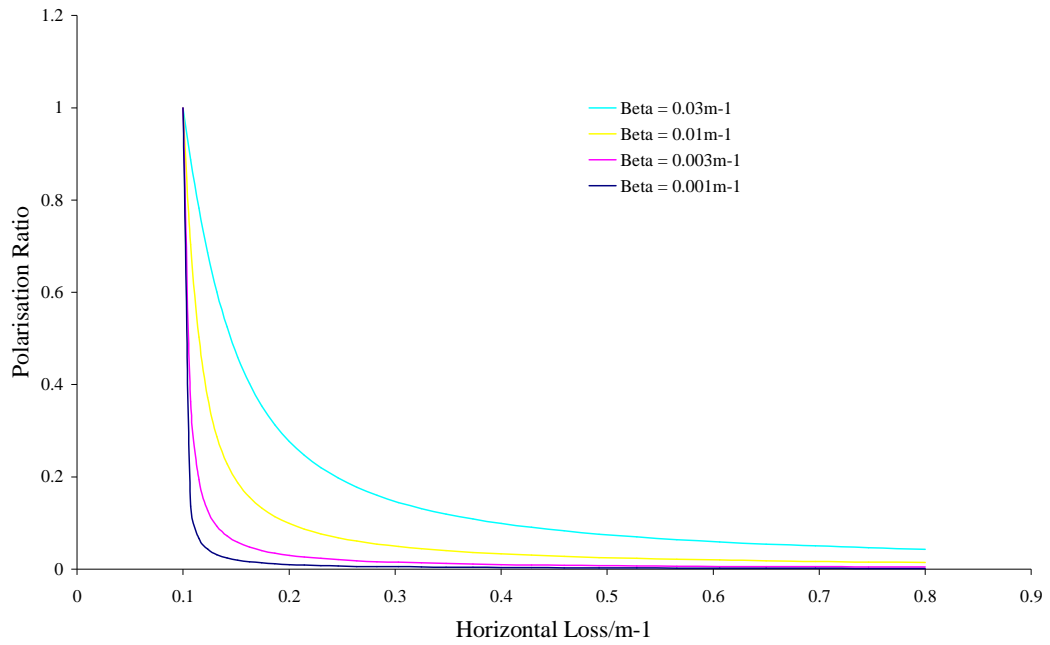
(a)
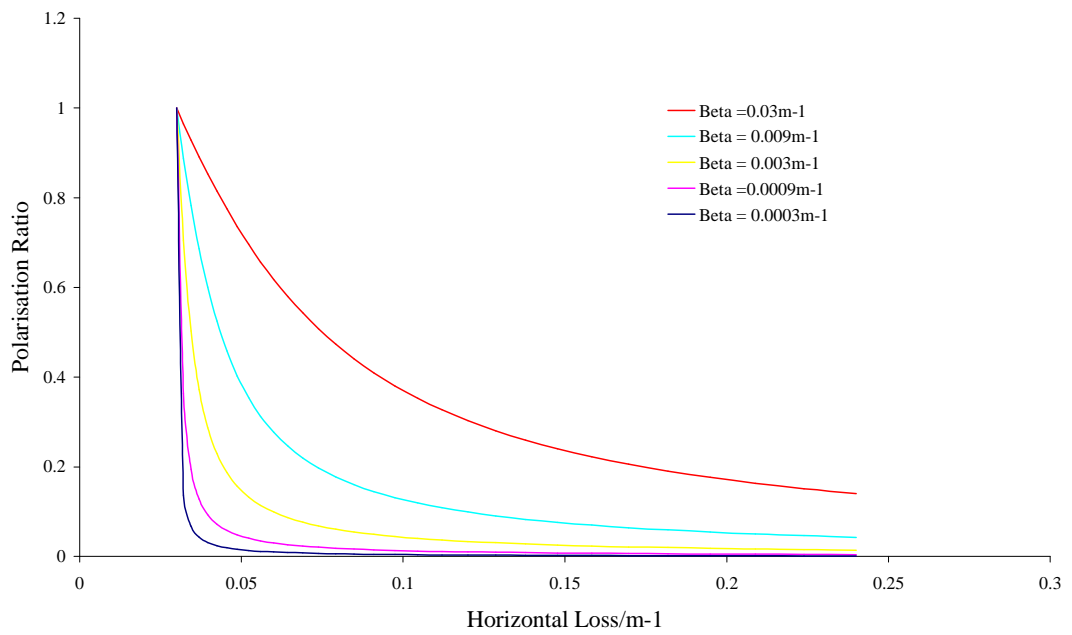
(b)

Figure 4.13:*Polarisation ratio as a function of horizontal loss for various polarisation coupling values, beta, for 75% Bragg grating PCF laser when (a) vertical loss = 0.1m⁻¹ (At horizontal loss 0.5m⁻¹, from top to bottom, the plots follow the order of the series labels), (b) vertical loss = 0. 03m⁻¹ (At horizontal loss 0.05m⁻¹, from top to bottom, the plots follow the order of the series labels).*

As expected, the polarisation ratio results shown in *Figure 4.13* are unchanged form those shown in *Figure 4.11* because changing the reflectivity of the cavity mirrors only effects power, threshold and efficiency characteristics not the polarisation coupling strength. The following figures will illustrate how changing the mirror reflectivity changes the power, threshold and efficiency characteristics.
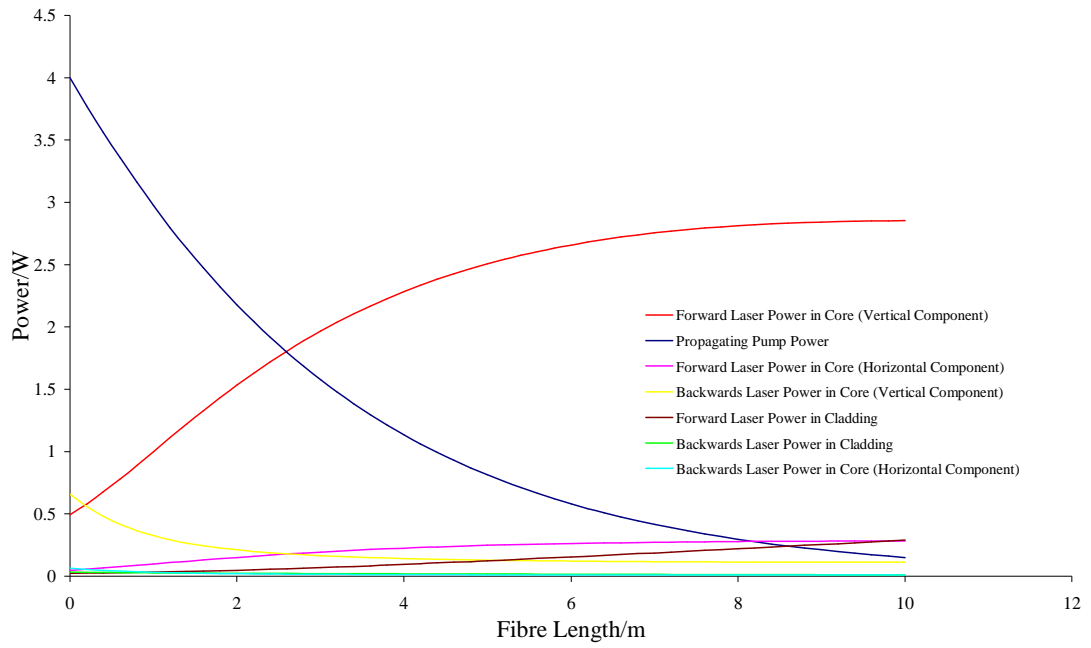
(a)
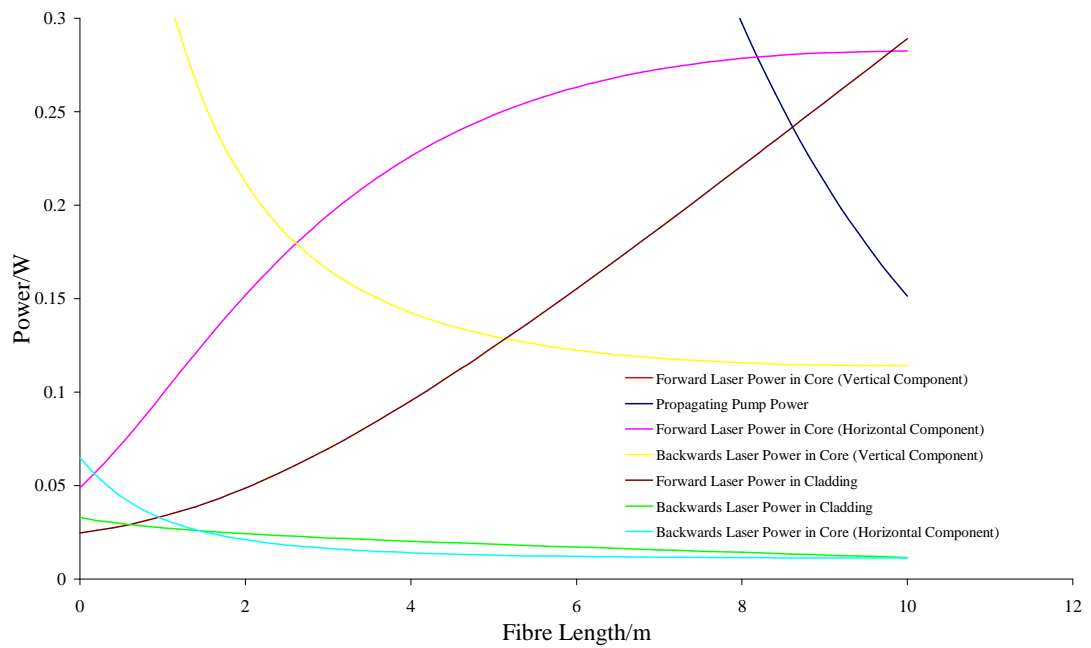
(b)

Figure 4.14: *Output power characteristics for 10m length PCF laser with 75% Bragg grating, pumped by 4W, when horizontal loss = 0.02m^{-1}, vertical loss = 0.01m^{-1} and polarisation coupling = 0.001m^{-1} (At length 4m, from top to bottom, the plots follow the order of the series labels).*
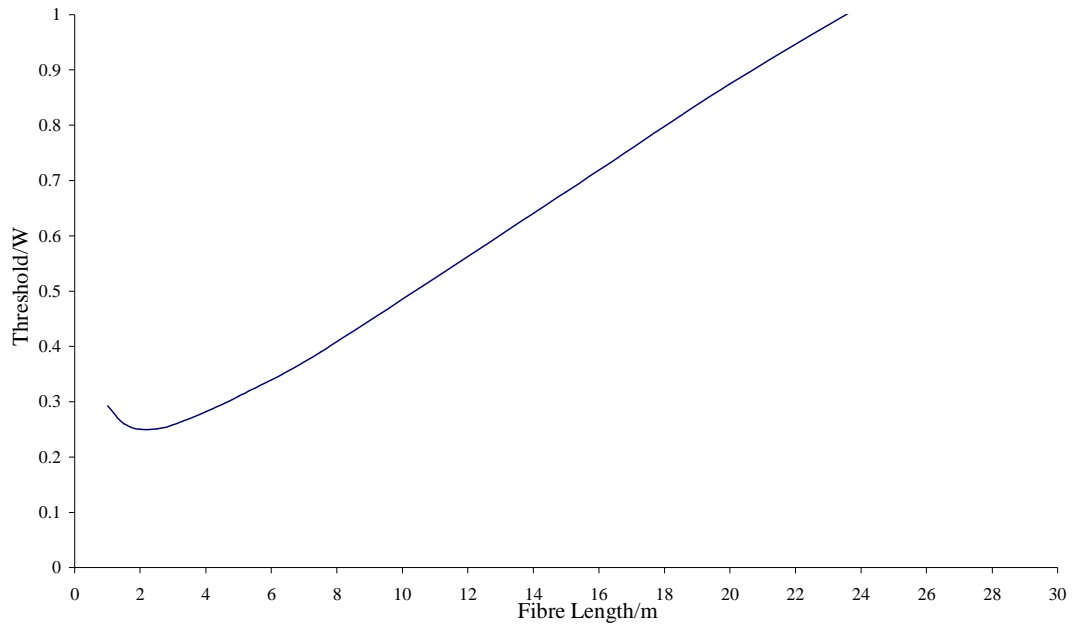
Figure 4.15*: Threshold of PCF laser with 75% Bragg grating, wavelength 1061nm, based on forward propagating laser power and coupled pump power as a function of fibre length.*
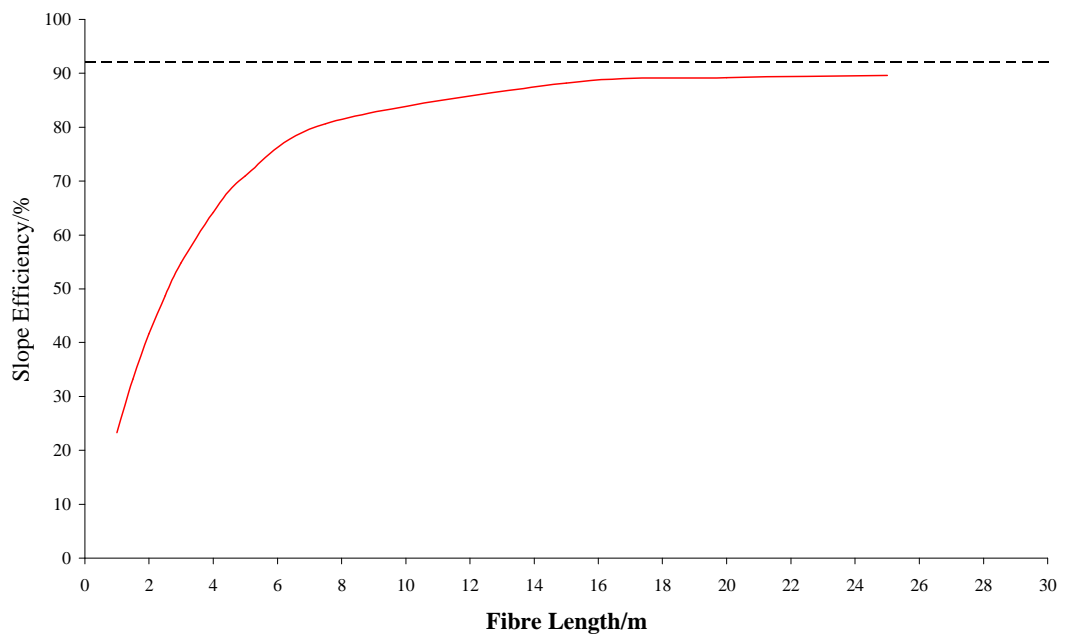
Figure 4.16*: Slope efficiency of PCF laser with 75% Bragg grating, wavelength 1061nm, based on forward propagating laser power and coupled pump power as a function of fibre length (Dashed line represents theoretical maximum slope efficiency)*

Figure 4.15 shows that for the 75% Bragg grating PCF the minimum threshold of 0.25W occurs for fibre length 2m. Beyond 2m the threshold increases linearly.

The threshold and the slope efficiency was modelled as a function of cavity mirror reflectivity for a 15m length fibre as shown in *Figure 4.17*.
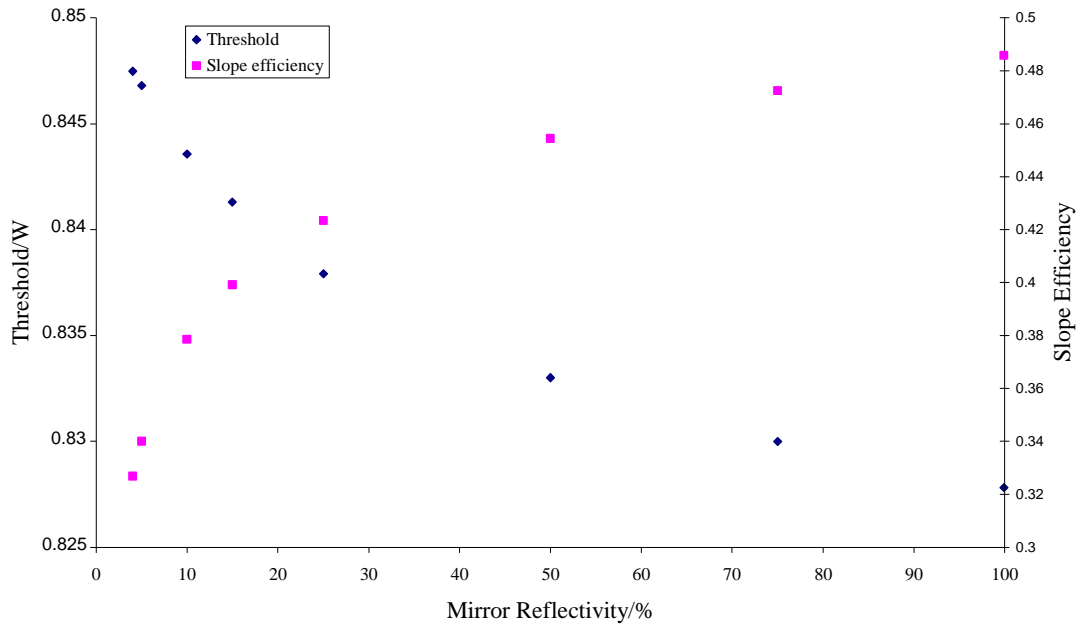
Figure 4.17*: Threshold and Slope efficiency of PCF laser with 75% Bragg grating, wavelength 1061nm, based on forward propagating laser power and coupled pump power as a function of mirror reflectivity for a 15m length fibre.*

Figure 4.17 shows, as expected, that the threshold of the PCF laser decreases and the slope efficiency increases as the cavity mirror reflectivity is increased because the losses in the laser cavity have effectively been reduced.

4.2 Conclusions

A numerical model has been developed to illustrate the power characteristics of PCF lasers. In order to give an accurate representation of real PCF lasers, the model included a power loss from the core to the cladding. The theoretical results will be used to analyse the experimental results in the forthcoming **Chapter 5.** The polarisation coupling and power characteristics in a polarisation maintaining PCF laser with and without a 75% Bragg grating were also modelled.

4.3 References

[1]   A. Ghatak, K. Thyagarajan, "Introduction to Fiber Optics", Cambridge University Press, 1998

[2]   Mathematica numerical modelling software, http://wolfram.com/, visited July 2009

[3]   W. H. Press, B. P. Flannery, S. A. Teukolsy, W. T. Vetterling, "Numerical recipes in C++", Cambridge Press, 1988

[4]   M. J. F. Digonnet, "Rare-earth-doped fiber lasers and amplifiers", Second Edition, Marcel Dekker, Inc., 2001

Chapter 5

Polarisation Maintaining

PCF Laser

Polarisation maintaining step-index fibres were first demonstrated in the 1980's [1-3] and are used for sensing, laser cutting and nonlinear applications such as second harmonic generation. With the development of PCF technology in the 1990's the first example of a polarisation maintaining PCF was demonstrated in 2000 [4]. As already discussed in **Chapter 3** microstructured fibres have a number of free design parameters including structure morphology, structure dimensions and core profile which makes them particularly well suited for tailoring their polarisation properties. This research will present the first double cladding polarisation maintaining Yb^{3+} doped PCF laser through form birefringence. .

5.1 *Birefringence*

Real fibres are generally drawn without perfect symmetry which leads to an effective birefringence with a beat length over which the polarisation will evolve and return to its initial state. The inherent birefringence causes the fibre to have fast and slow axes. Thus, at any given point inside the fibre the light has some elliptical polarisation state with varying ellipticity and orientation. The polarisation of light propagating in the fibre gradually changes in an uncontrolled, wavelength-dependent, way. It is important to note the distinction between single polarisation fibre and polarisation maintaining fibre. Single polarisation fibre can transmit light with a certain linear polarisation direction, whereas light with the orthogonal polarisation direction experiences strong optical losses or is simply not guided. Polarisation maintaining fibre guides light with any polarisation state but it can preserve a linear polarisation state when the polarisation direction is aligned with one of the

birefringent axis of the fibre. *Figure 5.1* illustrates the evolution of the polarisation state within a fibre when the propagating electric field has a component along each axis.
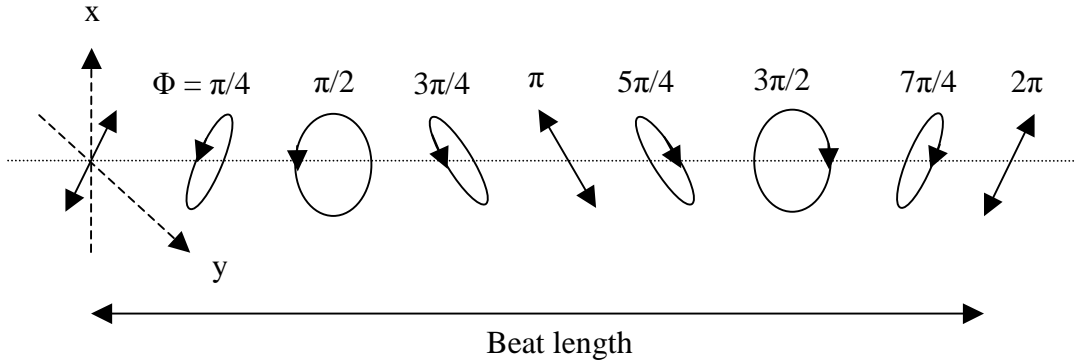
Figure 5.1: Change in polarisation state of the light as it propagates along birefringent fibre, with fast and slow axes represented by x and y respectively.

As the two orthogonal modes propagate along the fibre their phase relationship will change due to the birefringence. The two modes travel with slightly different velocities, c/n_x and c/n_y, where n_x and n_y are the effective refractive indexes for each polarisation mode. Therefore after a distance L, the difference in the phase between the propagating modes will be [5]

$$\Delta\varphi = (n_x - n_y)\frac{2\pi L}{\lambda} \qquad (5.1)$$

After a certain distance known as the beat length, L_b, the phase difference reaches 2π and the original input polarisation state returns. This beat length is related to the wavelength of the propagating light in vacuum, λ, and the effective refractive index difference. Typically this beat length is of the order of about one metre for conventional step-index optical fibre.

$$L_b = \frac{\lambda}{(n_x - n_y)} \qquad (5.2)$$

95

For polarisation maintaining fibres the modal birefringence, B, is generally quantified in terms of the normalised difference of the orthogonal propagation constants, β_x and β_y, of the two modes.

$$B = \frac{\lambda}{2\pi}\left[(\beta_x - \beta_y)\right] \qquad\qquad (5.3)$$

and it is related to the polarisation beat length, $L_b = \lambda/B$. Typical modal birefringence for a polarisation maintaining fibre is of the order 5×10^{-4} [6].

When orthogonal polarisation modes are propagating with similar propagation constants the fibre will experience mode coupling. Thus, a power transfer between the modes will take place resulting in an output wave with a random state of polarisation. Therefore if the propagation constants of the orthogonal modes are sufficiently different no such energy transfer will take place and the fibre will maintain the polarisation state. Thus the purpose of creating highly birefringent fibre is to reduce the coupling between the orthogonal states of the fundamental mode. This concept has already been shown in **Chapter 4,** *Figure 4.12,* whereby introducing a small polarisation coupling loss, β, resulted in a desired polarised output. There are two commonly used ways to create a polarisation maintaining fibre; using stress induced birefringence or form birefringence as illustrated in *Figure 5.2.*

(a) Panda   (b) Bow tie   (c) Elliptical core
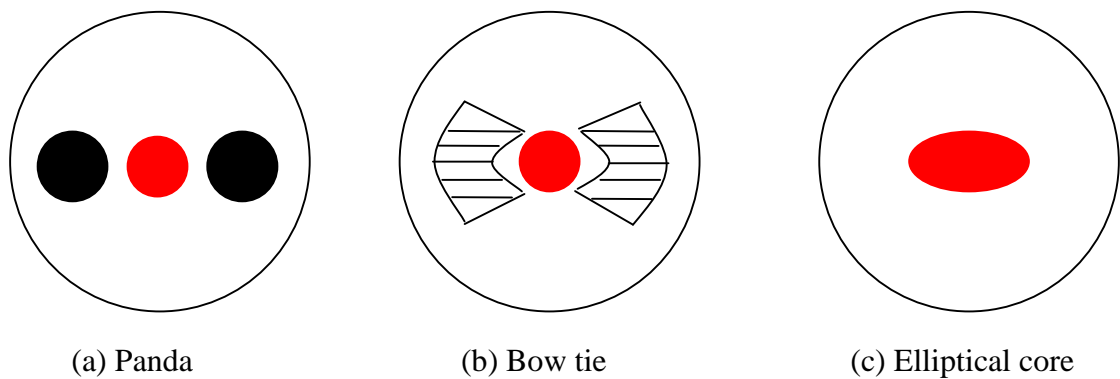
Figure 5.2: *Various types of polarisation maintaining fibre: (a) and (b) have stress forming regions within the cladding inducing stress birefringence, (c) has an elliptical core which induces form birefringence.*

Stress induced birefringence involves including stress regions within the fibre cladding in the form of doped silica that have large thermal expansion coefficients. These regions introduce directional stress when cooled after the fibre drawing process which results in a tensile force in one cross-sectional direction and a compressive force in the orthogonal direction which induces a change in the refractive indices by the photo-elastic effect. Hence a strong birefringence is created within the glass.

Form birefringence involves changing the geometry of the circular symmetric waveguide. An elliptical core can be employed which sets up an asymmetry in the fibre structure thus causing form birefringence.

5.1.1 PCF Birefringence

Polarisation maintaining PCF is based on the same concepts as the standard step index polarisation maintaining counterpart. In the PCF type the stress induced birefringence is established by introducing stress elements into the fibre cladding before the fibre drawing process. PCF form birefringence is achieved by reducing the axial symmetry of the fibre to two-fold symmetry or no axial symmetry. The

nature of PCF technology gives the manufacturer freedom to control the air hole dimensions near the core [7], the air hole shape and pitch [8] and the core shape [9] in order to achieve the form birefringence. Such form birefringent polarisation maintaining PCF's exhibit a modal birefringence of up to one order of magnitude larger than conventional step-index polarisation maintaining fibre [9].

The first example of a polarisation maintaining large mode area, single mode PCF with stress applying parts was demonstrated in 2004 by Folkenberg *et al* [10]. This was the first polarisation maintaining PCF to be single mode at any wavelength as well as maintaining a constant high birefringence of 1.5×10^{-4}. The cross-sectional structure of this fibre is illustrated in *Figure 5.3* and consists of an undoped silica core surrounded by a triangular lattice of air holes forming the cladding. Two stress-applying parts made from boron-doped silica have been placed opposite each other, outside the cladding.

Boron-doped silica stress areas

Air hole cladding structure

50 µm
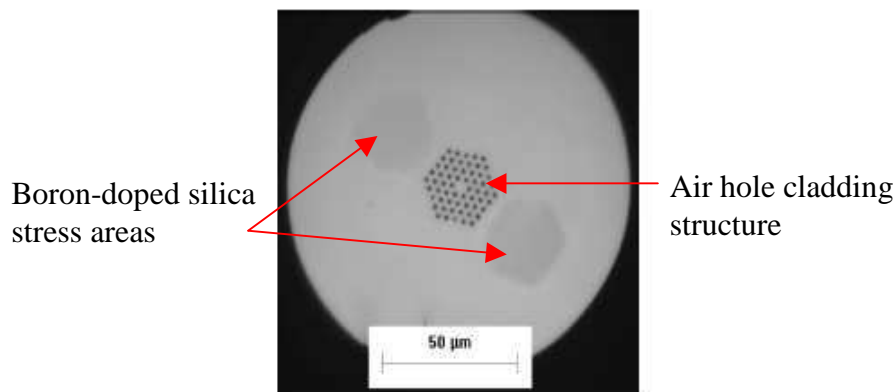
Figure 5.3: *Microscope image of large mode area, single mode PCF with stress applying parts [10].*

A more economical alternative to the stress-applying parts technique is form birefringence. An example of a highly birefringent PCF based on form birefringence, as demonstrated by Ortigosa-Blanch *et al* [4] is illustrated in *Figure 5.4*.
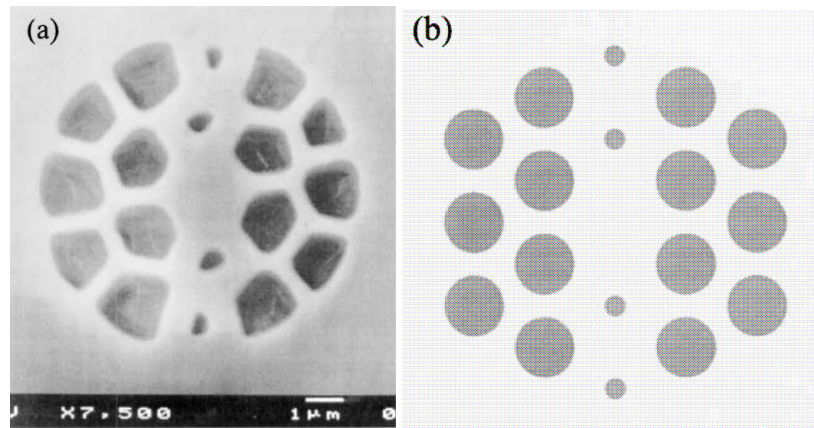
Figure 5.4*: (a) Microscope image of cross-section of polarisation maintaining PCF, (b) Idealised structure [4].*

The form birefringence is created by varying the size of the air holes. The larger holes are diameter 1.16μm and the smaller holes are diameter 0.4μm. The pitch was 1.96μm and the fibre diameter was 63μm. The manufacturer's freedom of design over these microstructures enables the birefringence in PCF's to be created in a variety of structures based on the number of air holes, hole size, hole shape, hole position and pitch.

The highly birefringent polarisation maintaining PCF structure created in this research combines a form birefringence design as well as a differential loss of the two polarisation states but unlike any other polarisation maintaining PCF demonstrated to date, this design is double cladding and the core is doped with Yb^{3+} which allows efficient laser operation.

5.2 *Experimental Details*

A variety of polarisation maintaining PCF laser structures were tested to determine the optimal fibre geometry with the most promising lasing and polarisation maintaining characteristics which would ultimately be pursued for the duration of the research. The most promising structure will be fully characterised in terms of power analysis, spectral output, polarisation maintaining capabilities and beam quality.

5.2.1 Initial Fibre Designs

The initial PCF structures were double cladding with a rectangular shaped inner cladding consisting of air holes surrounding an elliptical core which was doped with Yb^{3+}. All of the initial test fibre structures were drawn from the same pre-form so they all had the same air hole pattern as that shown in *Figure 5.5*.
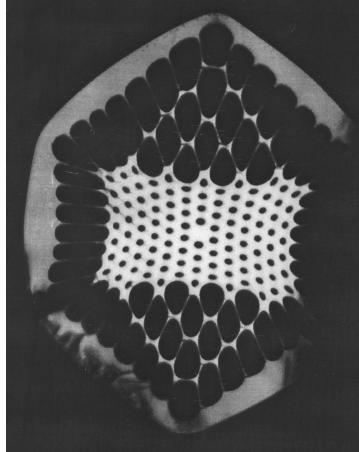
Figure 5.5: *Polarisation maintaining PCF test structure corresponding to Fibre 3 in Table 5.1.*

Table 5.1 represents the dimensions of each of the photonic structures tested.

Name	Outer dimension/ μm	Inner cladding dimension/ μm	Core dimension/ μm
Fibre 1	190 x 165	85 x 55	11 x 7
Fibre 2	215 x 195	105 x 60	13 x 9
Fibre 3	235 x 195	105 x 60	11 x 7
Fibre 4	170 x 140	85 x 50	9 x 7
Fibre 5	140 x 125	70 x 45	8 x 5

Table 5.1: *Table representing dimensions of various PCF laser structures tested.*

Each of the fibre lasers, up to 30m in length, were pumped by up to 10W from a LIMO Laser Systems 980nm diode laser (see **Appendix A**) which was coupled into a 200µm diameter fibre with NA=0.2 as illustrated in *Figure 5.6*.
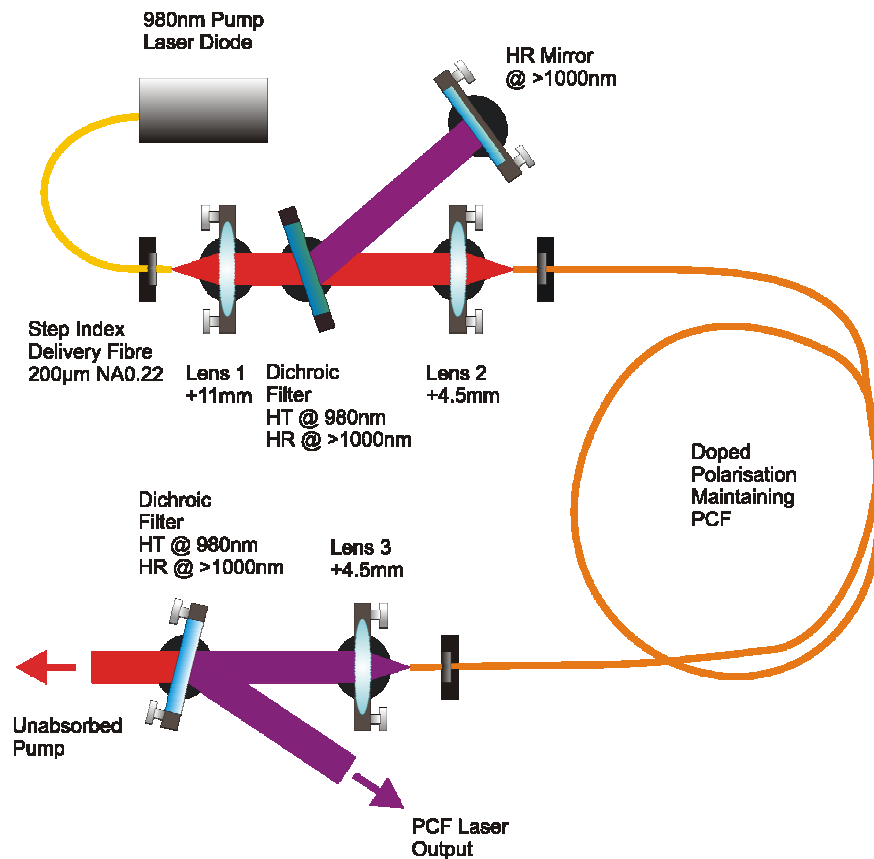
Figure 5.6: *General experimental set-up for power analysis of PCF laser.*

The pump output was collimated using an 11mm focal length lens and was coupled into each test fibre laser using a 4.5mm focal length lens with NA=0.55. Assuming this system does not introduce significant aberrations this would lead to a pump spot diameter in the region of 82μm. A dichroic beam splitter set at its maximum transmission angle (7°) for the pump light was placed in the collimated beam section between the two lenses. At this angle the dichroic beam splitter is highly reflective for wavelengths in the range 1000-1100nm. The PCF laser can operate from the 4% Fresnel reflections from the fibre end facets without the use of external feedback components. However, for most measurements presented in this research the laser output at the pump end is retro-reflected to provide a strong laser feedback. In obtaining all of the results in this research it was essential to rotate the input end of the fibre such that the PCF laser polarisation was either pure s or pure p-polarisation relative to the tilted dichroic beam splitter at the pump end of the cavity. Otherwise, a mixed state of polarisation on the dielectric coating would lead to a rotation of the

polarisation of the reflected feedback laser light which would lead to a mixing of the polarisation states of the fibre laser. When stripping the coating from the PCF the commonly used method of using nitro morse was not feasible as the air holes in the fibre caused a capillary effect with the nitro morse which led to the fibre end going on fire when operated as a laser. Instead, the fibre coating was stripped using the tip of a flame from a gas lighter and the fibre was cleaved using a Photon Kinetics FK11 diamond fibre cleaver. The PCF's in this research were all very fragile so care was taken when handling them to avoid breakage. Both ends of the PCF laser were held in brass fibre chucks and the fibre ends were always cleaved after the fibre was held in these chucks to avoid dirt or damage to the fibre ends. The fibre chucks were mounted in x, y, z translation stages which allowed fine control over pump coupling into the PCF laser. An Ophir thermopile power meter was positioned at the back end of the PCF laser to detect the laser output which allowed the optimum alignment of the PCF laser.

Before analysis of the PCF lasers could take place, the 980nm pump diode laser was first characterised by measuring the output power as a function of the input current as shown in *Figure 5.7*.
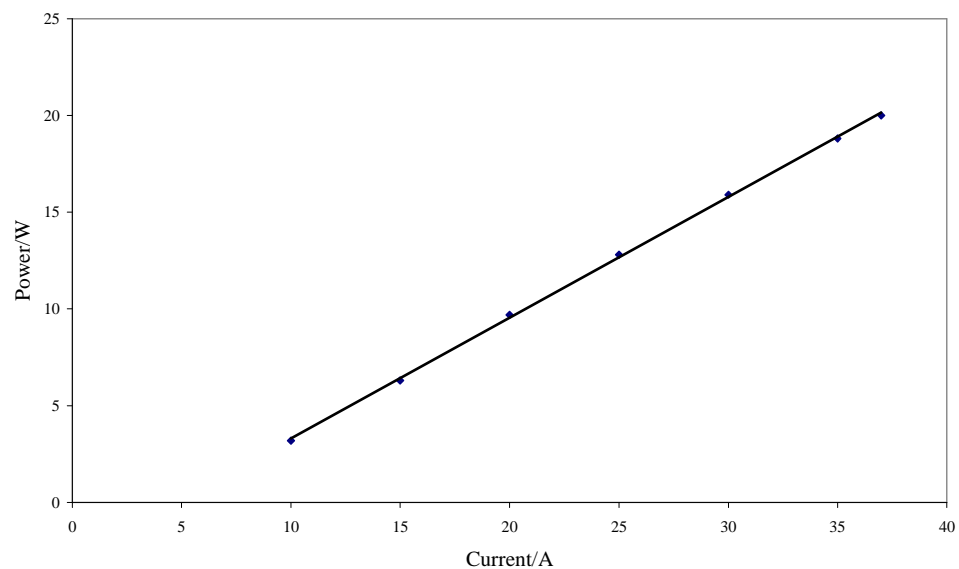
Figure 5.7: *Pump power as a function of current. Efficiency is 0.62W/A with a threshold of 5A.*

The efficiency of the pump was found to be 0.62W/A. Throughout this research the pump diode laser was limited to 10W output power due to observed damage to the PCF laser end facets after prolonged use of the pump at higher power levels. The pump power as a function of temperature was investigated as shown in *Figure 5.8*.
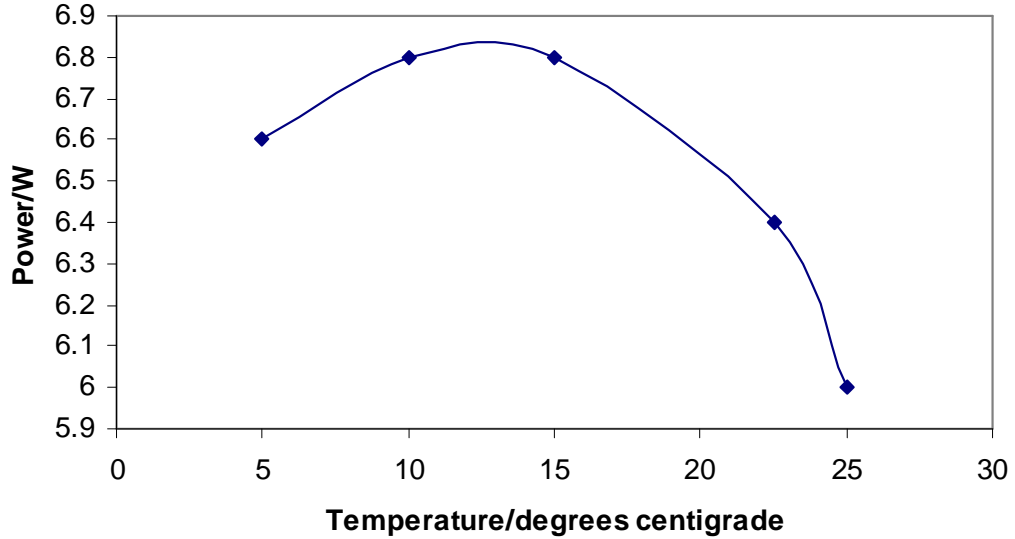
Figure 5.8: Pump power as a function of temperature with input current fixed at I=15A.

Changing the temperature of the diode laser alters the operating wavelength which in turn changes the output power from the diode laser. *Figure 5.8* illustrates that the maximum power output occurs when the temperature of the diode laser was between 10°C and 15°C. Therefore, throughout this research the pump diode laser was set at 15°C which corresponded to a pump wavelength of 978nm.

The output from the PCF laser was then analysed using the spectrometer set-up shown in *Figure 5.9*.
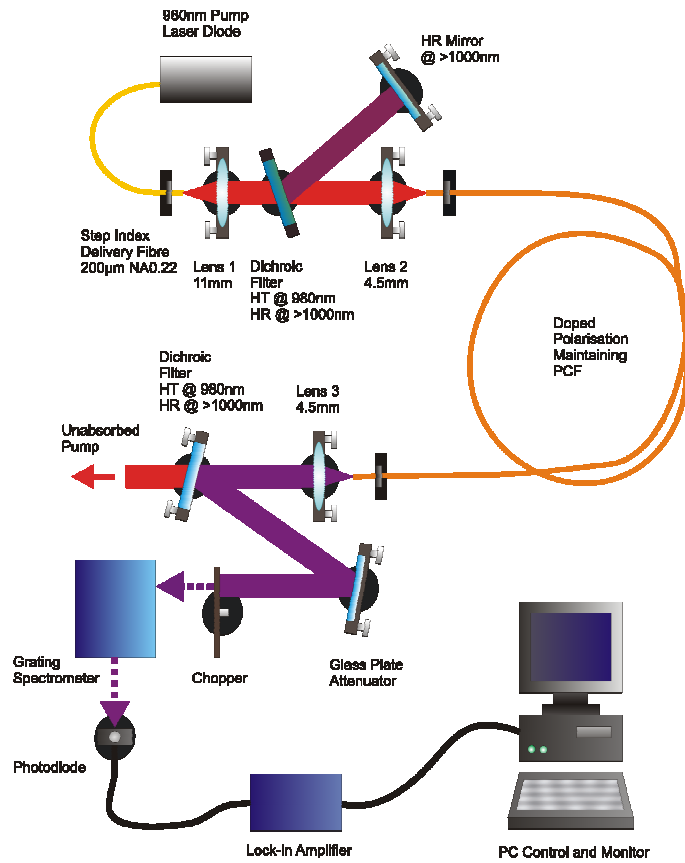
Figure 5.9*: Experimental set-up for analysing spectral output from PCF laser.*

Using a glass plate, 6% of the PCF laser light was reflected through a chopper to a grating spectrometer, 1200 lines per mm and 0.5m path length, which allowed spectral analysis of the PCF laser light to be performed. *Figure 5.10* shows that for a 13m piece of test *Fibre 1* the operating wavelength of the laser was 1040nm.
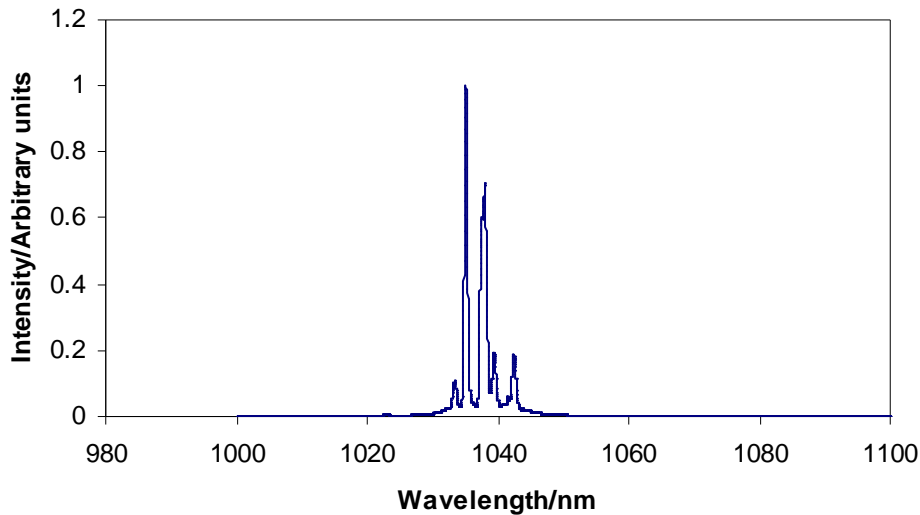
Figure 5.10: *Spectrum for 13m test Fibre 1, pump power 10W.*

The laser output was expected to be close to linearly polarised, thus it was analysed using a half-wave plate followed by a polarising beam splitting cube. The half-wave plate was rotated and the corresponding laser power transmitted through the cube was measured. Power, spectral and polarisation analysis were carried out on every test PCF laser listed in *Table 5.1*. However, none of these PCF lasers showed any signs of their laser output being polarised. Therefore, to improve the polarisation maintaining properties of the PCF laser, the microstructure of the fibre was changed. A full description of the new successful polarisation maintaining PCF laser design will follow.

5.2.2 Successful Fibre Geometry

The first step in the development of our efficient polarisation maintaining PCF laser was to fabricate a series of passive and active test fibres without the outer air-cladding. These were made to determine the optimum, structural parameters for the final fibre laser. The air-cladding was eliminated to allow simpler characterisation of the core properties (stripping of disturbing cladding light is more troublesome in double-clad fibres). All of the PCF employed in this research was manufactured by Crystal Fibre A/S [11]. An optical microscope image of the active new polarisation maintaining PCF laser with the air cladding, provided by the manufacturers, is

illustrated in *Figure 5.11* along with the near field mode distribution recorded at wavelength 950nm for one of the non-air-clad passive test fibres.
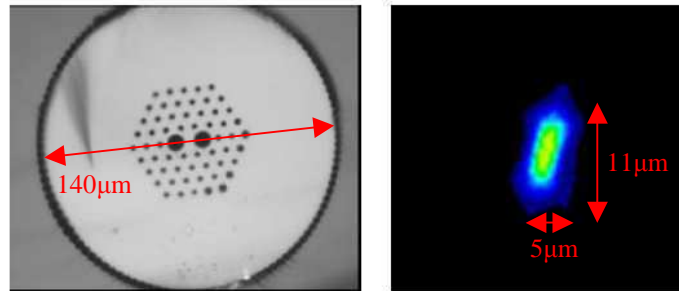
Figure 5.11: (a) Optical microscope image of polarisation maintaining PCF design, (b) Near-field mode distribution recorded at wavelength 950nm for non-air-clad passive test fibre.

The new microstructure was still double-cladding but the rectangular inner-cladding was replaced with a hexagonal inner cladding structure comprising of two sizes of air holes. Three active fibres with the same microstructure shown in *Figure 5.11* but with varying hole dimensions were experimentally tested to determine which geometry possessed the most promising laser efficiency and polarisation maintaining properties which resulted in the final PCF design consisting of small holes with pitch 7μm and diameter 2.7μm placed in layers around the core which provide the microstructure defining the laser mode and provide light confinement hereto.   Two larger air holes, diameter 8.2μm, were placed on either side of the core to introduce strong form birefringence. The larger air holes enforce a substantially elliptical core shape with approximate dimensions of 5μm by 11μm. The inner cladding pump guide was 140μm in diameter with a typical loss level of less than 30dB/km. The NA of the fibre is around 0.67 at wavelength 950nm with a slightly higher value expected at 980nm. The core of the active fibre was doped with Yb, Germanium (Ge), Aluminium (Al) and Fluorine (F). The doped region of the core has an extent of approximately 3μm by 7μm. Ge co-doping was chosen to allow Bragg gratings to be written into the fibre at a later date. The Yb, Ge and Al concentrations were kept relatively low in order to allow F co-doping to partly compensate their increasing effect on the core refractive index profile. The core absorption of the fibre was around 400dB/m at 975nm.   The manufacturers found the active fibre showed a birefringence of around 1.4×10^{-4} at 1100nm and a differential loss on the order of

100dB/km for the two polarisation states which is equal to $\Delta\alpha_0 = 0.023\text{m}^{-1}$. The numerical modelling results in *Figure 4.11 (b)*, **Chapter 4** shows that for a differential loss of the order $\Delta\alpha_0 = 0.023\text{m}^{-1}$ the corresponding polarisation coupling value that will result in a good polarisation is 0.0003m^{-1}.

5.2.3   Power Analysis

The coupling efficiency and the pump absorption of the PCF laser were determined by measuring the PCF laser output power and unabsorbed pump power transmitted for a range of fibre lengths from 0.5 m to 30 m using the same experimental setup previously described in section **5.2.1.** These results are shown in *Figure 5.12*.
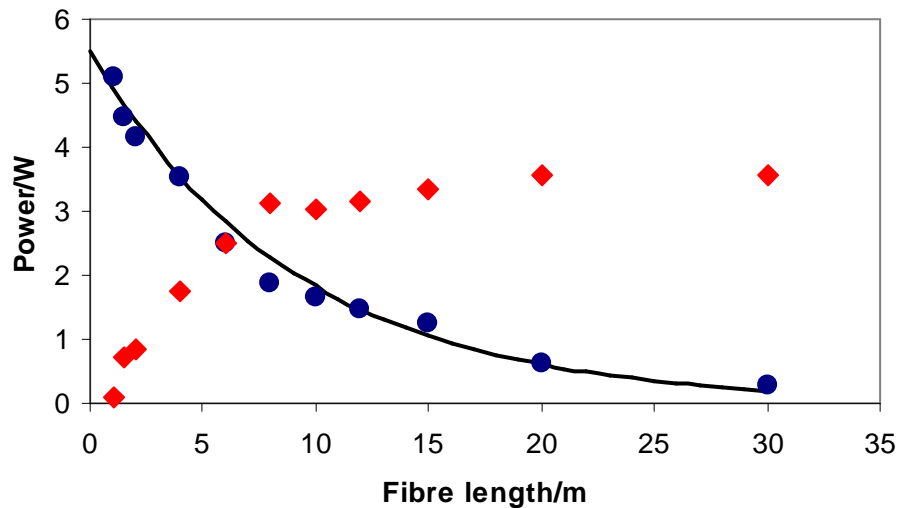
Figure 5.12: *Transmitted pump power (blue dots) and laser output power (red diamonds) as a function of fibre length when the laser is operated with feedback from a high-reflecting mirror. The smooth curve represents an exponential fit corresponding to a pump coupling efficiency of 55% and fibre attenuation of 0.48 dB/m*

The Beer-Lambert law [12] permits an exponential fit to be fitted to the experimental data points which yield a fibre attenuation of 0.48 dB/m and pump power coupling efficiency of 55%. The absorption was found to be in good agreement with the manufacturers' data. The relatively low coupling efficiency of 55% was observed despite the fact that the pump spot on the fibre and its NA were both calculated to be lower than the respective values of the fibre cladding. This result indicates a

relatively low efficiency for pumping into a region of relatively large air holes. It should be noted that any light impinging on an air hole will refract into the inner cladding and travel across it at a sufficiently steep angle that it will refract out through the air cladding. However, for this fibre and pump geometries the air holes constitute less than 30% of the pump spot and the low pump coupling efficiency may therefore partly be attributed to non-optimum coupling optics. The output laser power from the PCF laser as a function of coupled pump power is shown in *Figure 5.13* for a 20m length of fibre.
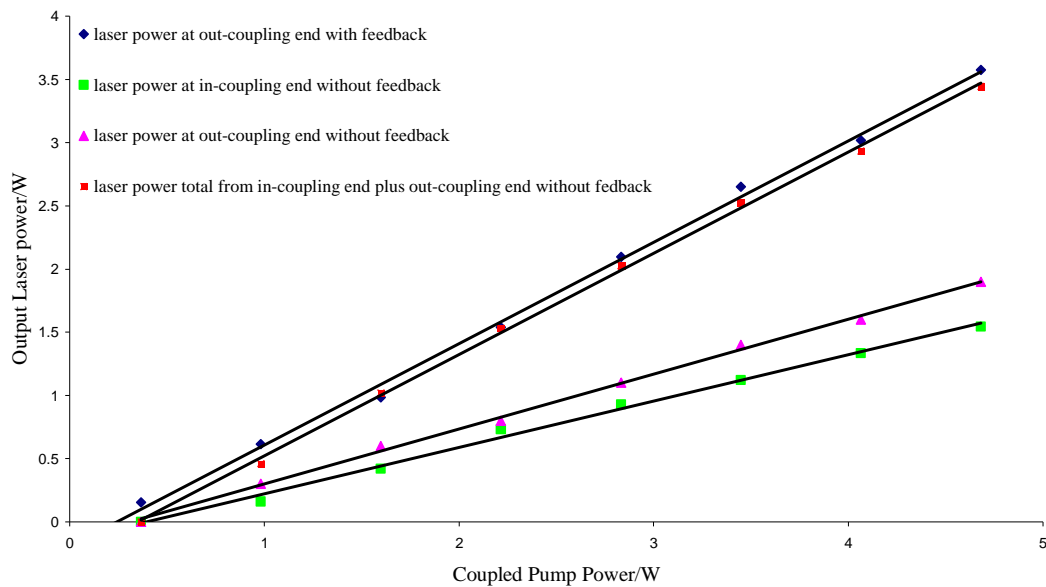
Figure 5.13: *Laser output power vs. coupled pump power for a 20 m length of fibre.*

When describing the laser cavity, we will refer to the PCF laser operating "without feedback" when the PCF laser operates using only the Fresnel reflections from the fibre end facets. When the PCF laser is described as operating "with feedback" the laser cavity has additional feedback from an external high-reflector. *Figure 5.12* represents output power measurements recorded from each end of the PCF fibre laser when the laser was operated with or without external feedback. The red data points in *Figure 5.12* represent the sum of the two output powers from each end of the PCF laser. The blue data points were measured at the output end of the fibre when the PCF laser was operating with feedback. In this configuration the observed slope efficiency was 68%. However, it is important to note that for a 20 m length of this

fibre, 11% of the coupled pump power is transmitted through the fibre as shown in *Figure 5.12*. Therefore, taking this unabsorbed pump power into consideration the internal quantum efficiency of the fibre laser is 77% compared with the 91% theoretical maximum given by the ratio of the PCF laser and pump photon energies. These power characteristics were previously predicted by the numerical modelling presented in Chapter 4 based on a PCF laser with core to cladding coupling loss $0.05m^{-1}$. The power output measured at each end of the fibre when the laser was operated without feedback was found to be different. The laser power at the back end of the PCF laser was found to be 55% of the total laser power from both ends of the laser. The sum of the two outputs from each end of the fibre when operating without feedback, indicated by the red data, has the same slope efficiency but slightly higher threshold than blue data recorded when the power was measured at the back end of the fibre when feedback was applied to the laser. On comparing these results with the modelling results in **Chapter 4**, *Figures 4.8-4.10*, we can conclude that this experimental PCF laser had a core to cladding loss equal to $0.05m^{-1}$

It is important to discuss the spatial mode of the output from this particular PCF laser. Due to a limited number of holes surrounding the core, a fraction of the light leaks out into the cladding throughout the fibre which results in a component of the laser output in the cladding mode. Numerical mode modelling will be carried out at the end of this chapter to determine the optimum PCF structure that will minimise this loss.

5.2.4   Polarisation Analysis

In examining the inherent polarising properties of the polarisation maintaining PCF laser it was essential to distinguish between the laser output in the single mode core and the laser output that has leaked into the multimode cladding. The latter would be expected to be un-polarised. In order to analyze only the light from the core, the laser output was imaged onto a CCD detector and measurements were made only over the core region. Examples of the observed CCD images of the laser output when the PCF laser was operating below and above lasing threshold are shown in *Figure 5.14*
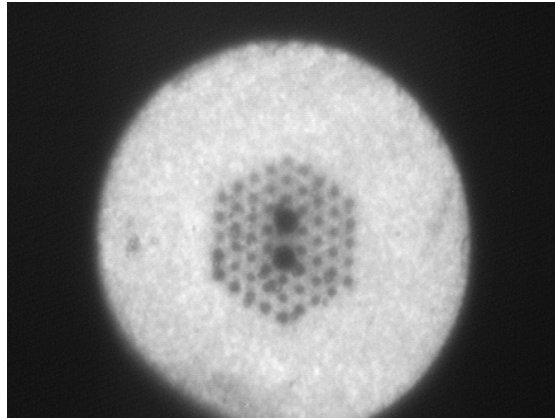
(a)
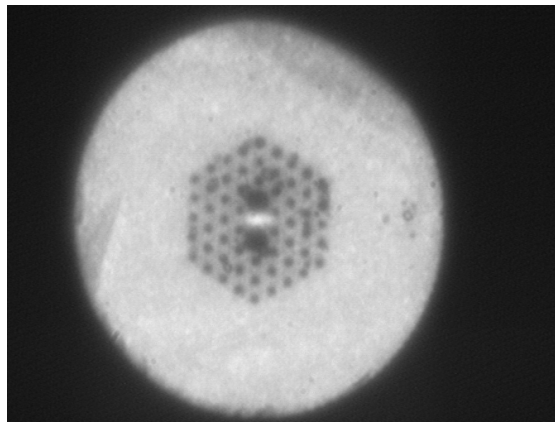
(b)

Figure 5.14: *(a) CCD image of laser ouput when fibre laser is below lasing threshold, (b) CCD image of laser output when fibre laser is above lasing threshold.*

The elliptical single mode laser output confined to the core region can clearly be seen in *Figure 5.14* when the fibre laser is operating above its lasing threshold. It is this elliptical region which the polarisation analysis measurements were carried out on. When analysing the images, care was taken to introduce sufficient attenuation of the laser light to ensure that the CCD detector operated within its region of linear response to intensity. The experimental setup for the measuring the CCD detector response to intensity is illustrated in *Figure 5.15*.
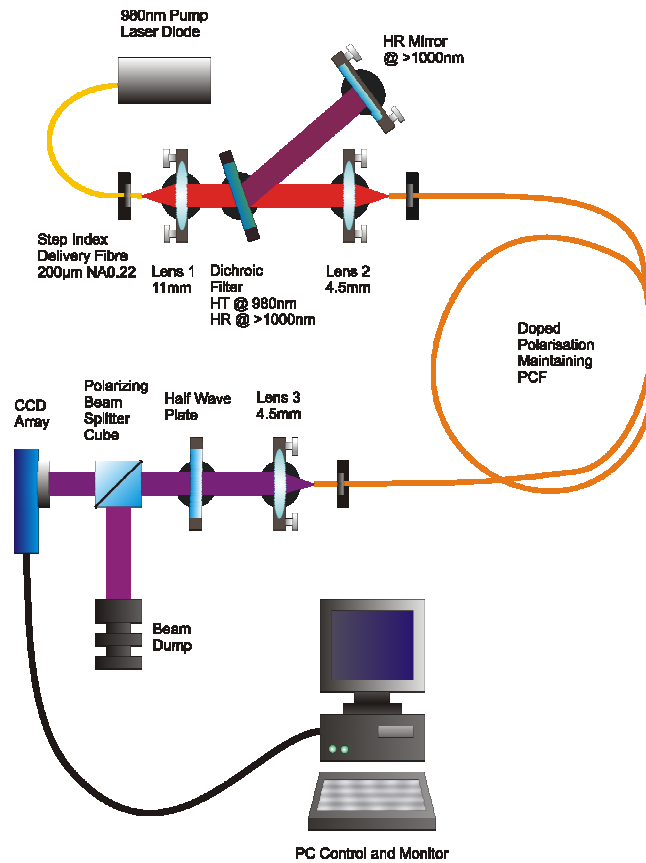
Figure 5.15: *Experimental setup for measuring CCD detector response to intensity.*

The half-wave plate was set to allow maximum intensity transmission through the polarising beam splitter. The single mode laser light visible in the elliptical core region was detected by the CCD array and displayed on the computer screen. Using the computer software the light intensity in the rectangular area selected, containing the core light, was analysed in both dimensions i.e. along the x and y-axis respectively.
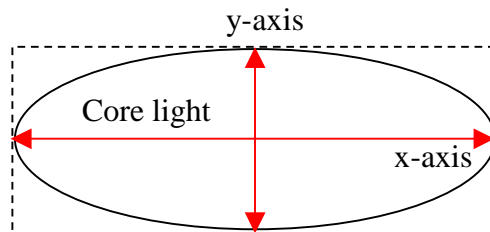
Figure 5.16: *Core light selected to measure intensity response of the CCD detector.*

111

The light intensity was analysed for various input currents to the LIMO 980 nm pump diode laser. The results of which can be seen in *Figure 5.17*.
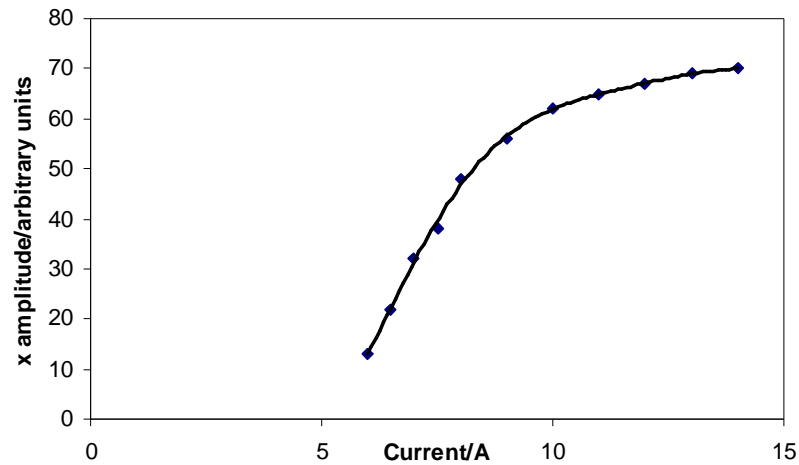
(a)
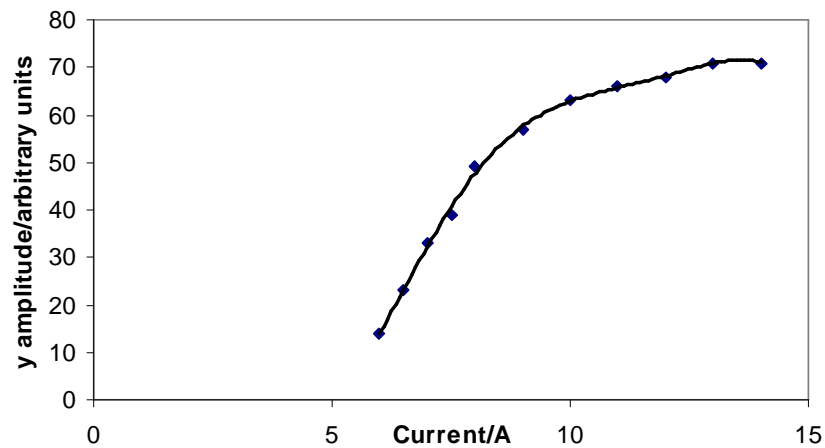
(b)

Figure 5.17: CCD intensity response measured over the elliptical core region of the fibre laser output with varied input currents to the 980 nm pump diode laser for (a) The x-dimension of the analysis rectangle, (b) y-dimension of the analysis rectangle.

The calibration curves for the intensity response of the CCD detector show that in order to operate the camera within its linear response to intensity, the maximum light amplitude detected must be maintained below 50 in the camera's amplitude scale. In the polarisation analysis results to follow this was achieved by the addition of a variety of neutral density filters positioned after the polarising beam splitting cube and before the CCD array in the experimental set up illustrated in *Figure 5.15*.

112

The peak intensity in the core transmitted through the polarising beam splitter cube was then determined as a function of the rotation angle of the half-wave plate. Data for a 20m fibre operating with total output power of 3.7 W is shown in *Figure 5.18*.
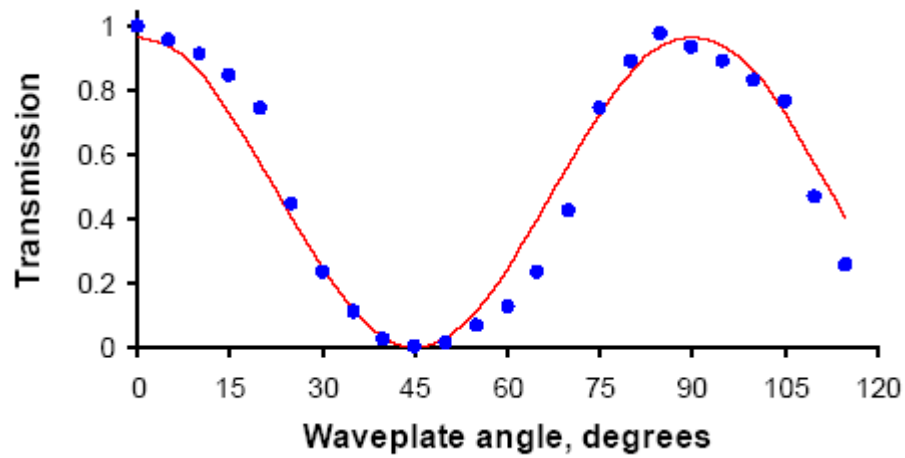
Figure 5.18: *Polarisation analysis of the laser light in the fibre core. The relative transmission of PCF laser light in the core through the polarizer is shown as a function of the rotation angle of the half-wave plate. The solid curve represents the expected sinusoidal dependence.*

The polarisation ratio, the ratio between the maximum and minimum power transmitted through the polarizer, was found to be in excess of 200:1. No significant variation of this polarisation ratio was observed when varying the fibre laser operating power as shown in *Figure 5.19*.
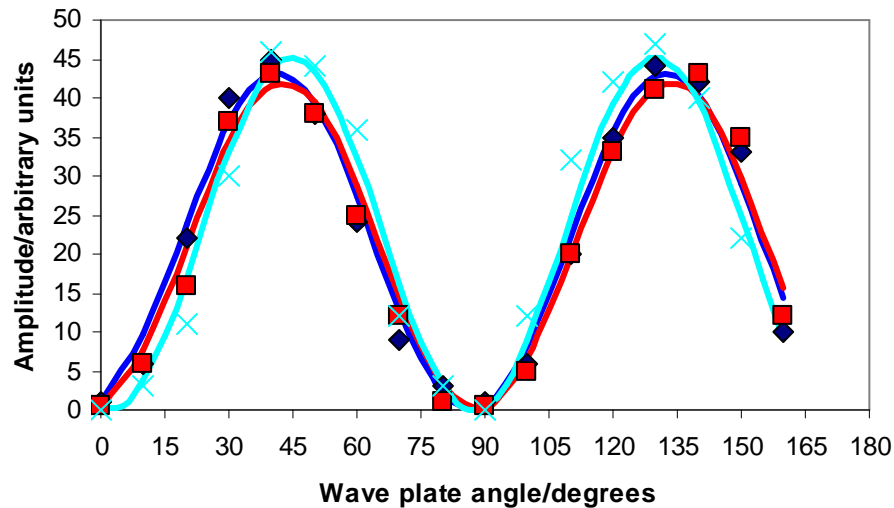
Figure 5.19*: Polarisation analysis of the laser light in the fibre core for a variety of pump powers. The relative transmission of PCF laser light in the core through the polarizer is shown as a function of the rotation angle of the half-wave plate. The solid curves represent the expected sinusoidal dependence. (Dark blue diamonds represent experimental results when pump power P=1.9W, red squares represent experimental results when pump power P=3.2W and light blue crosses represent experimental results when pump power P=8.9W)*

The fibre laser length was reduced and the corresponding maximum and minimum transmission values through the polarizer, on rotation of the half-wave plate, were noted to determine the dependence of the polarisation ratio on fibre length. The results of which are shown in *Table 5.2*.

Fibre length/m	Core polarisation ratio
20	200:1
8	50:1
2	3.4:1

Table 5.2*: Core polarisation ratios as a function of fibre length.*

A polarisation ratio of better then 50:1 was observed for fibre length of down to 8 m. *Figure 5.12* shows that the output power from the fibre laser drops significantly for fibre lengths shorter than 8 m. The polarisation measurements show a corresponding drop in core polarisation ratio to 3.4:1 for a fibre length of 2 m.

With the highly polarised core we can estimate the fraction of light that has leaked into the cladding mode. Assuming this leaked light in the cladding mode is unpolarised, half of it will be transmitted through a polarizer set to block the light from the core. When the polarizer is set in the opposite position we detect the other half of the light in the cladding and all of the light in the core. By simply using an Ophir thermopile power meter to measure the power transmitted through the polarizer set in these two different configurations, we typically measured a ratio of 9.5:1 for a 20 m length of fibre. From the following calculation we can calculate the percentage of light that was carried by the core.

$$\frac{\frac{1}{2}I_{cl}}{I_{co}+\frac{1}{2}I_{cl}}=\frac{1}{9.5} \qquad (5.4)$$

where I_{cl} represents the power in the cladding and I_{co} represents the power in the core. Dividing the left hand side of equation (5.4) by $\frac{1}{2}I_{cl}$ simplifies to

$$\frac{1}{\frac{2I_{core}}{I_{cl}}+1}=\frac{1}{9.5}$$

and by rearrangement we have

$$\frac{2I_{core}}{I_{cl}}+1=9.5$$

$$\frac{I_{core}}{I_{cl}}=4.25$$

Thus

$$I_{core}=4.25I_{cl} \qquad (5.5)$$

On substitution of equation (5.5) into equation (5.4) the percentage of light carried by the core is calculated to be 81%. The polarised laser light emitted in the cladding indicates an up to 30% asymmetry in favour of the core polarisation. This decreases

the core fraction of the light to 79% corresponding to 2.9W of highly polarised single-mode output. We have already shown that the experimental power results match the modelling results in **Chapter 4** if a core to cladding loss of 0.05m^{-1} is included. Thus, if we compare the experimentally measured value of 79% carried by the core to the predicted 75% shown in *Figure 4.8*, again corresponding to a loss value of 0.05m^{-1}, we can see that the experiment value is close to the theoretical value. The light propagating in the highly multi-mode inner cladding was found to have the memory of the core polarisation. This memory of the polarised light is due to the length of fibre not being long enough for all of the light that leaks into the cladding mode to become fully scrambled. In obtaining all of the results in this research it was essential to rotate the input end of the fibre such that the PCF laser polarisation was either pure s or pure p-polarisation relative to the tilted dichroic beam splitter at the pump end of the cavity. Otherwise, a mixed state of polarisation on the dielectric coating would lead to a rotation of the polarisation of the reflected feedback laser light which would lead to a mixing of the polarisation states of the fibre laser.

5.2.5   *Polarisation Analysis Without External Feedback*

As previously stated, the PCF laser can also be operated without the use of the external feedback mirror. Thus, the two 4% Fresnel reflections from the fibre end facets provide the only feedback to the laser. The main difference in characteristics between the two laser configurations is that the PCF laser tended to self-pulse when operated without feedback and for fibre lengths longer than approximately 6m. This self-pulsing feature will be discussed in more detail in **Chapter 7**. The tendency of the PCF laser to self-pulse prevented the CCD detector from being used to monitor the core polarisation ratio. However, the more robust detection of the ratio of the two polarisations of the total laser output, previously discussed, yields the same ratio of 9.5:1 from the back end of a 20m fibre. This indicates that the polarisation in the core has not deteriorated significantly despite the significant reduction in circulating power. Assuming that the leakage from core to the cladding is unchanged in this

configuration an easily detectable change in the ratio to 8.5:1 would correspond to a core polarisation ratio of approximately 50:1. With the feedback blocked we now have access to the output from the front end of the PCF laser. As the laser gain is higher in this end, coupling into the cladding mode can be expected to be less significant. Indeed, the polarisation ratio for the total output from this end was measured resulting in a ratio increase from 9.5:1 to 15:1. This higher ratio corresponds to more than 86% of the light propagating in the core in the laser end, where the gain is highest. This asymmetry in polarisation ratio between the fibre ends is mirrored in the asymmetry in output power measured from each end of the PCF laser, as previously discussed.

5.2.6   Beam Properties

The numerical aperture of the PCF laser, the beam quality and the fundamental mode profile will now be analysed.

5.2.6.1   Numerical Aperture

As already discussed in **Chapter 3**, the NA of an optical fibre is a measure of its light gathering capability. To measure the NA of the PCF laser the experimental set-up shown in *Figure 5.20* was implemented.
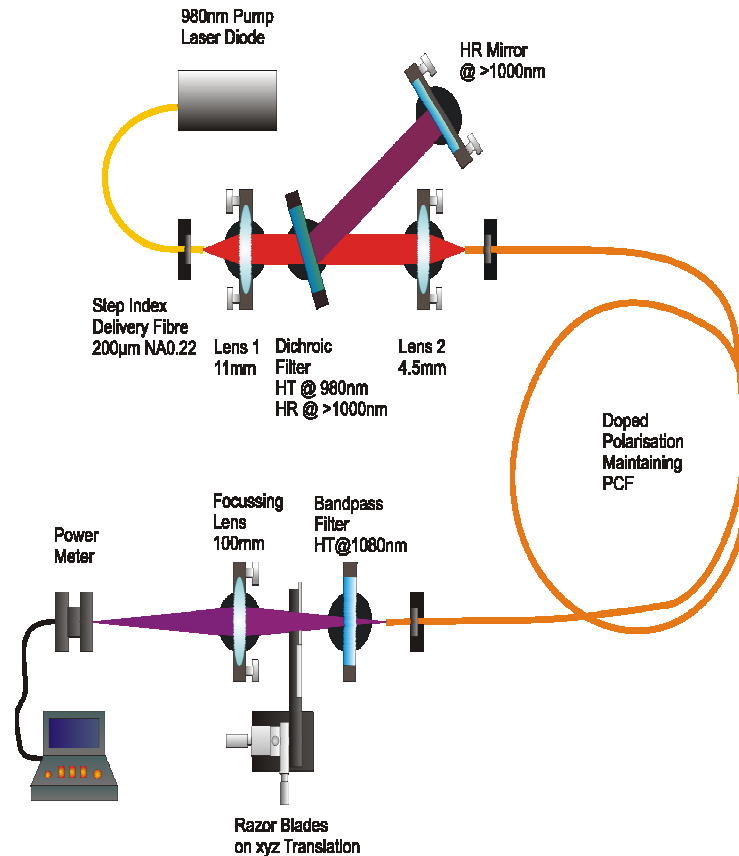
Figure 5.20*: Experimental set-up implemented to measure the NA of the highly polarised PCF laser.*

With no collimating lens in place at the back end of the PCF laser, the output from the PCF laser was free to expand and propagate through a 1080nm band pass filter (T = 50%). This filter eliminated the unabsorbed 980nm pump light from the PCF laser output. A razor blade on a translation stage, positioned at the outer edge of the expanded single mode core light, was scanned across the larger dimension of the ellipse. A 100mm focal length lens was used to focus the light onto an Ophir thermopile power meter to permit power measurements to be recorded. The back end of the PCF laser was then rotated through 90 degrees to allow the same analysis to be carried out for the opposite dimension of the ellipse. The results were graphed, as shown in *Figure 5.21*, and the $1/e^2$ radius of the PCF laser beam, in both dimensions x and y, were determined based on a least squares difference method between the experimentally measured power, relative to the razor blade position in the beam, and the theoretical power based on the integral of the intensity distribution

of the beam. This intensity distribution is equal to an error function (ERF) in excel whereby

$$\int\limits_{-\infty}^{x_0} dx \int\limits_{-\infty}^{\infty} e^{-(x^2+y^2)/2w^2}\, dy = \pi w^2 \left[1 + ERF\left(\frac{x_0}{\sqrt{2} \cdot w} \right) \right] \qquad (5.6)$$

The results are shown in *Figure 5.21*.
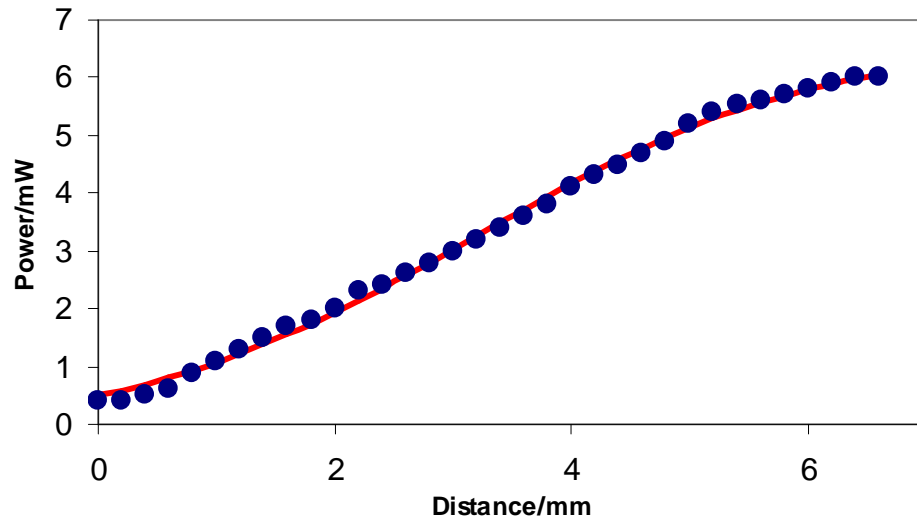
(a)
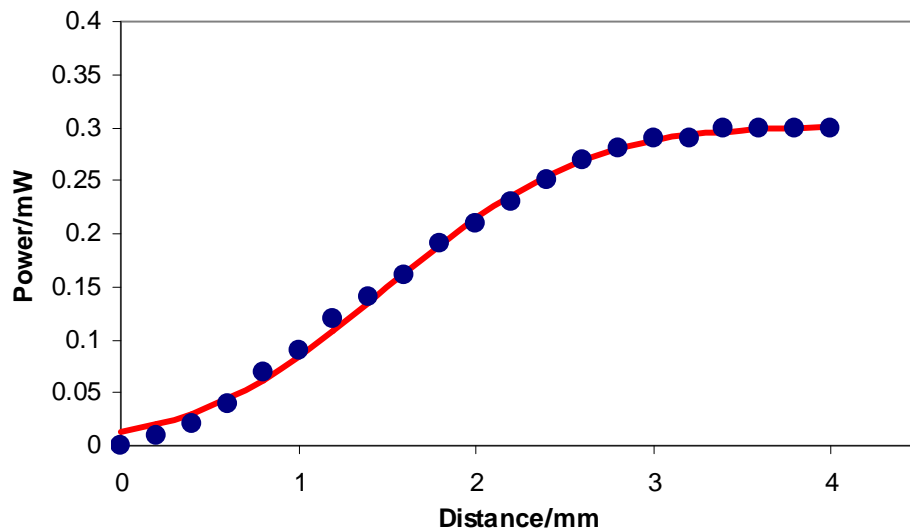
(b)

Figure 5.21: *Power measurements when scanning across elliptical laser beam with a razor blade; (a) smaller dimension of ellipse, (b) larger dimension of ellipse.*

For the smaller dimension of the elliptical beam the $1/e^2$ radius, measured 85mm from the fibre end, was found to be 4.45 mm. The NA is related to the divergence half angle, θ, by $NA = \sin(\theta)$. By measuring the $1/e^2$ radius at a particular distance from the end of the fibre we can determine the divergence half angle which in turn can be used to calculate the resulting NA. Therefore, the results related to the small dimension of the ellipse correspond to an NA value of 0.05. The data recorded in *Figure 5.21 (b),* associated with the larger dimension of the ellipse, yield a $1/e^2$ radius of 1.74mm measured 16mm from the fibre end. Again, using the relationship of NA with the divergence half angle the corresponding NA value of 0.11 was calculated. Using the small angle approximation, $\sin(\theta) = \tan(\theta)$ we can calculate the $1/e^2$ radii waists of the elliptical mode in the fibre to be approximately 3μm by 6μm.

5.2.6.2 M^2 *Measurement*

As already discussed in **Chapter 3**, the laser beam parameter M^2 is a measure of the beam quality of the laser output. The M^2 values associated with each dimension of the elliptical beam from the PCF laser were determined using a similar experimental method to that previously described for the NA measurements. In this case a 6.24mm focal length lens was used to converge the output from the PCF laser to a focus point. The razor blade method was employed for each dimension of the elliptical beam to determine the $1/e^2$ diameter of the beam at a particular position. To allow the focal profile of the PCF laser beam to be mapped the blade was translated in 2 mm increments either side of the focus and the corresponding $1/e^2$ diameter at each position was recorded. Far field measurements were carried out at distances of 50 mm, 100 mm and 150 mm.
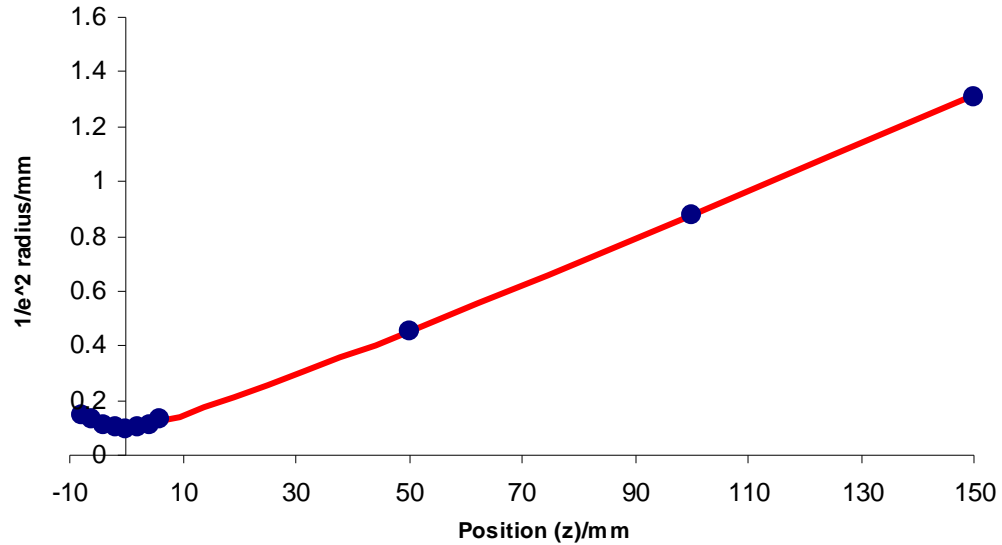
(a)
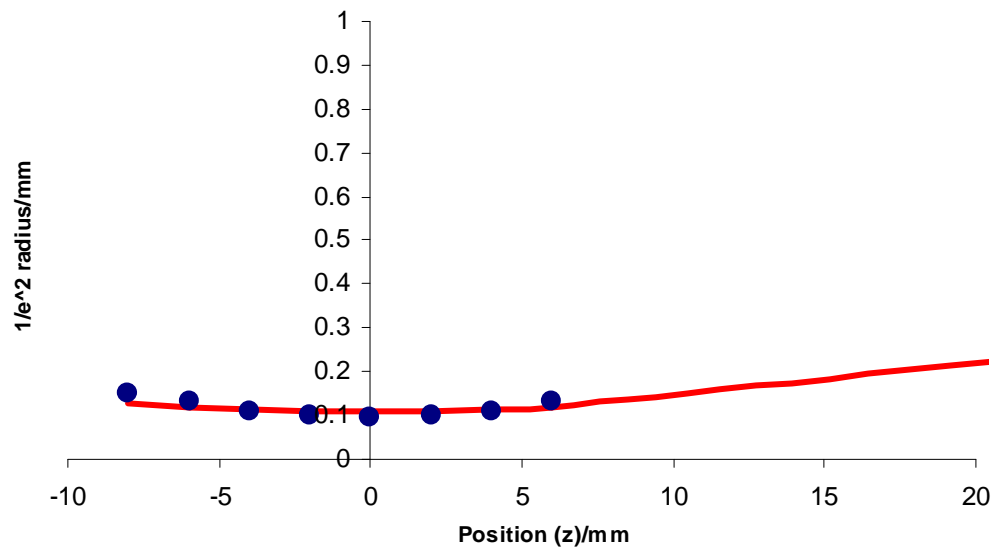
(b)

Figure 5.22: *1/e² diameter as a function of distance away from focus, (a) full scale,(b) zoomed in scale.*

Figure 5.22 illustrates the expected Gaussian beam propagation focal profile shape, according to equation *(3.37)* and *Figure 3.10* in **Chapter 3**. Rotation of the fibre end by 90 degrees allowed the same measurements to be carried out for the opposite dimension of the ellipse as shown in *Figure 5.23*

121

.
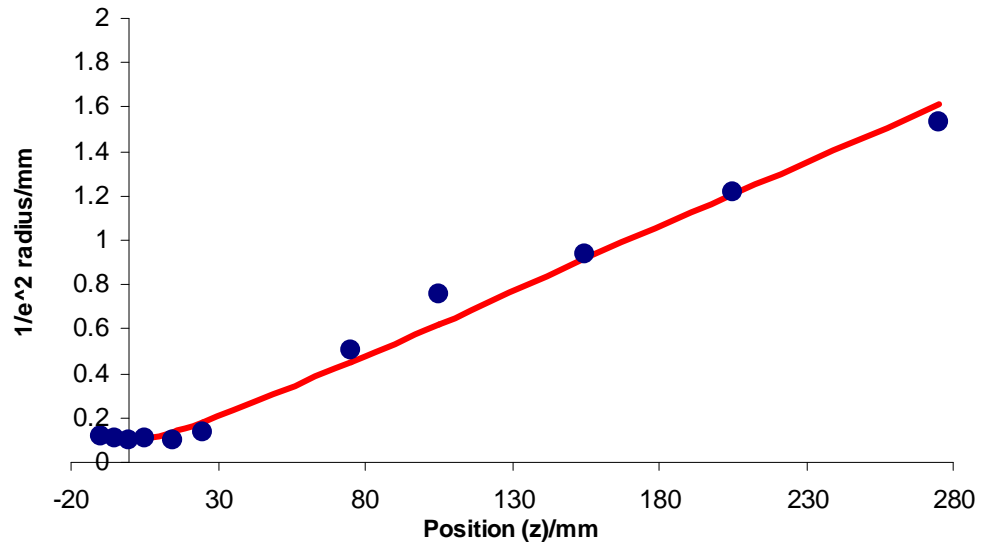
(a)
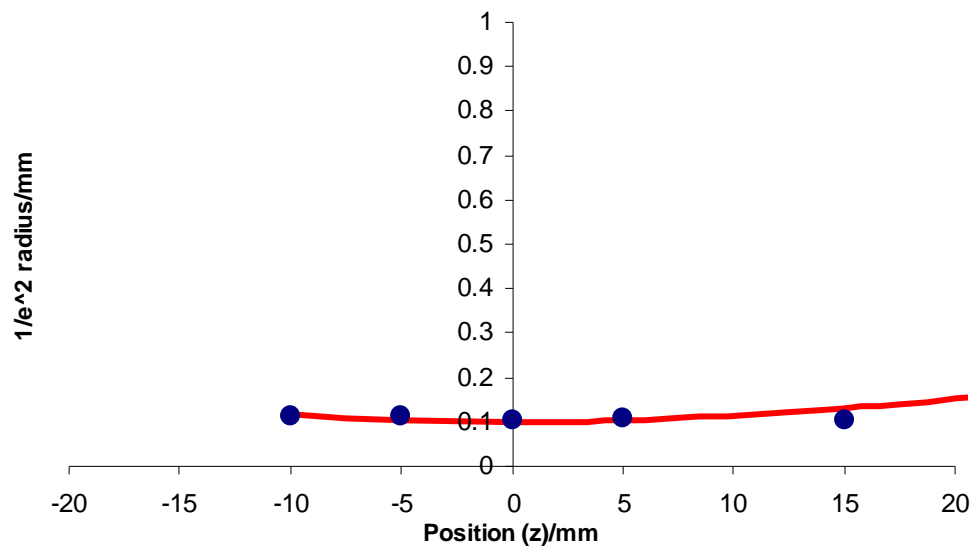
(b)

Figure 5.23: *1/e² diameter as a function of distance away from focus, (a) full scale, (b) zoomed in scale.*

Using the numerical fitting model in section **3.7.3,** in **Chapter 3**, the data obtained in *Figures 3.22* and *3.23* yield M² values of 2.8 and 1.72 corresponding to the larger and smaller dimension of the ellipse, respectively.

5.2.6.3   Beam Profile

The beam profile of the PCF laser output was analysed using the set-up shown in *Figure 5.24*. The 1064nm anti-reflective coated prism was necessary to reduce the intensity of the laser beam to below the Coherent beam profiler's damage threshold.
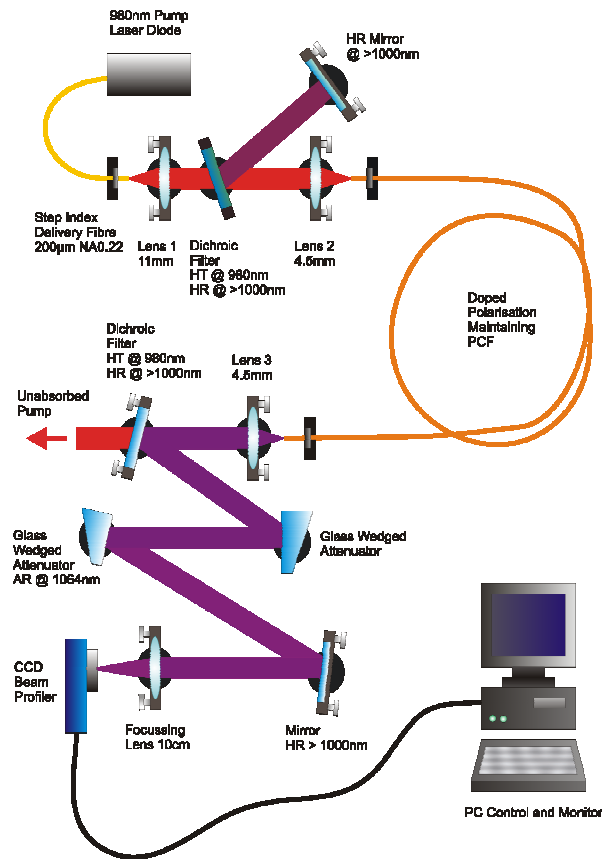
Figure 5.24: Experimental set-up to record beam profile of PCF laser.

The beam profile observed for 20m of the PCF laser is shown in *Figure 5.25*.
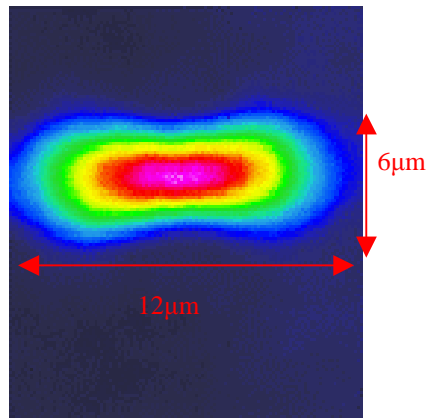
(a)
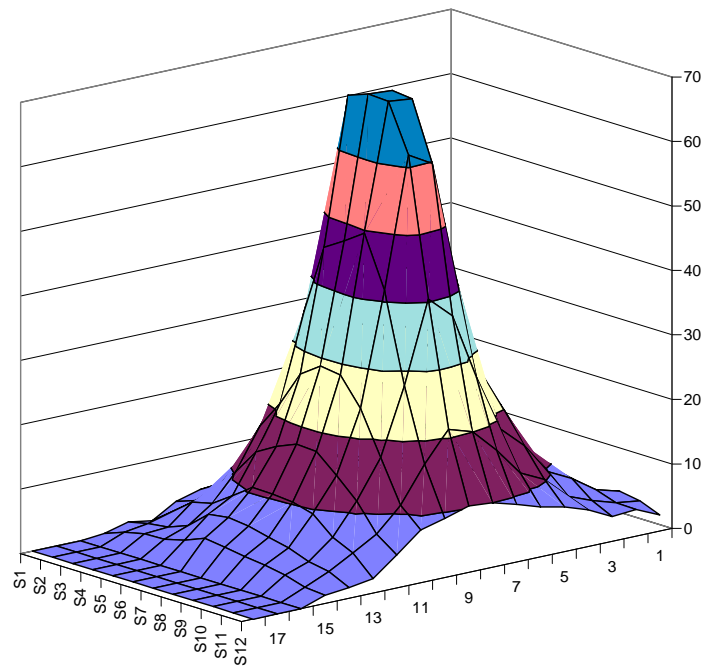
(b)

Figure 5.25: *Beam profile image from output of 20 m of PCF laser (a) 1-D image, (b) 3-D image.*

Beam profile images were recorded for various lengths of fibre from 2m up to 20m, over which no significant change in profile was observed. Siegman [13] has shown that even if an accurate Gaussian beam profile is observed, such as that shown in *Figure 5.25*, then the beam could appear as a non-TEM$_{00}$ Gaussian beam which is synthesized from an incoherent superposition of higher order Laguerre-Gaussian modes. This type of beam will propagate almost perfectly Gaussian but since it has an M^2 value much greater than 1, the beam will diverge M^2 times as rapidly with

124

distance as a true TEM_{00} beam. Thus, based on the observed beam profile and M^2 measurements it is thought that the output from the PCF laser in this research is synthesised from an incoherent superposition of higher order Hermite-Gaussian modes.

5.2.7 *Optical Spectrum Analysis*

The operating wavelength range of the PCF laser was investigated using the set-up shown in *Figure 5.9* for a range of fibre lengths between 1m and 20m. *Figure 5.26* depicts the optical spectra obtained for a 1m and a 20m length of fibre.
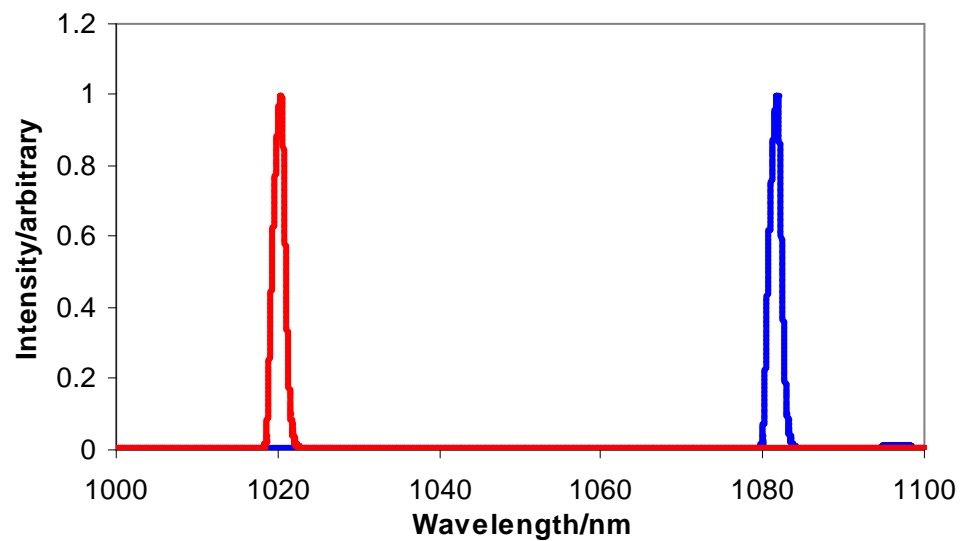
Figure 5.26: *Optical spectral output from PCF laser, red line represents data from 1m fibre; blue line represents data from 20m fibre.*

As shown above, the PCF laser operates at a wavelength of 1021nm for short fibre length (1m) and the operating wavelength increases with increasing fibre length up to 1082nm for a 20m length of fibre. These results are in keeping with the energy level theory described in **Chapter 2** whereby the lasing wavelength corresponds to the wavelength which has peak gain at the threshold for laser oscillation. Switching the Q of the cavity from low to high and vice versa changes the gain required to reach threshold and therefore changes the wavelength of peak gain. Increasing the length of the fibre shifts the gain maxima to longer wavelengths as a result of reabsorption.

Thus, for short fibre lengths the PCF laser behaves like a 3 level laser whereas, for longer fibre lengths, the PCF laser tends to 4 level laser behaviour.

To determine a more accurate measurement of the bandwidth of the PCF laser, the 1200 lines per mm, 0.5m path length grating spectrometer was replaced by an Agilent Technologies HP86140A optical spectrum analyser. *Figure 5.27* represents the optical spectra recorded when 26m length PCF laser, operating with and without the external mirror feedback, was pumped by 9.7W of 980nm pump light.
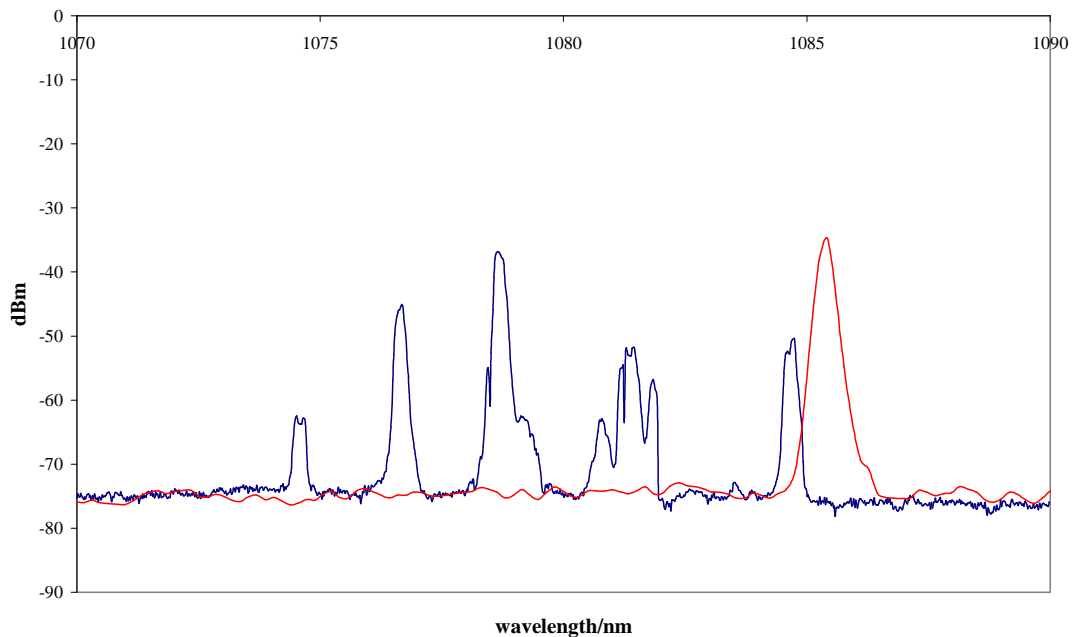
Figure 5.27: *Optical spectra recorded for 26m PCF laser pumped by 9.7W 980nm. Blue data recorded without external feedback mirror, red data recorded with external feedback mirror.*

When the PCF laser was operated with feedback from the external mirror the output lasing wavelength was stable at 1085.5nm, with FWHM 0.7nm. Whereas, when the PCF laser was operated without feedback the output wavelength varies over a 10nm range. This instability in wavelength coincides with the instability observed in CW output as the PCF laser tends to self-pulse when no external feedback is applied. When including a butt coupled HR mirror at the back end of the fibre, the cavity losses are decreased such that a CW output with stable wavelength was observed from the front end of the fibre. Decreasing the cavity losses by increasing the

reflectivity increased the PCF laser wavelength. Again, these results coincide with the theory presented in **Chapter 2** whereby switching the Q of the cavity from low to high and vice versa, changes the gain required to reach threshold and therefore changes the wavelength of peak gain.

5.3 Numerical Mode Modelling

As already discussed in section **5.2.3** and modelled in **Chapter 4** the highly polarised PCF lasers in this research experienced a loss of light from the core to the cladding. Since manufacturing costs are extremely high ($200,000 per fibre) optimised hole geometry is desirable prior to manufacturing. Therefore in order to determine the optimum hole structure, for this highly polarised PCF laser, that would allow full mode confinement and thus greater laser power to be carried by the core, numerical mode modelling was carried out as part of this work using Lumercials' mode solutions modelling software [14]. This software is a fully-vectorial mode solver that determines the electromagnetic fields of any waveguide structure of arbitrary geometry created by the user. It hosts a frequency-domain solver that discretizes the structure and a mesh system is employed to aid in analysis. Throughout all of the simulations carried out in this research the background index of the simulation area was set at 1.5 and the air holes were set to have refractive index of 1. Only the inner cladding and core regions of the PCF structures were modelled for simplicity and the structures were assumed to be passive where the wavelength of interest was selected to be 1080nm, which matched the experimental wavelength for a 20m fibre length, to represent the guided PCF laser output.

5.3.1 Rectangular Hole Structure

The first structure to be considered was the initial test, rectangular inner cladding, hole structure previously discussed in section **5.2.1**. The air hole radius was 2μm and pitch 8μm. The material properties, electric field intensity and the electric field in the x and y direction for one of the degenerate polarisation modes is shown in *Figure 5.30*.

(a)

(b)

(c)

(d)
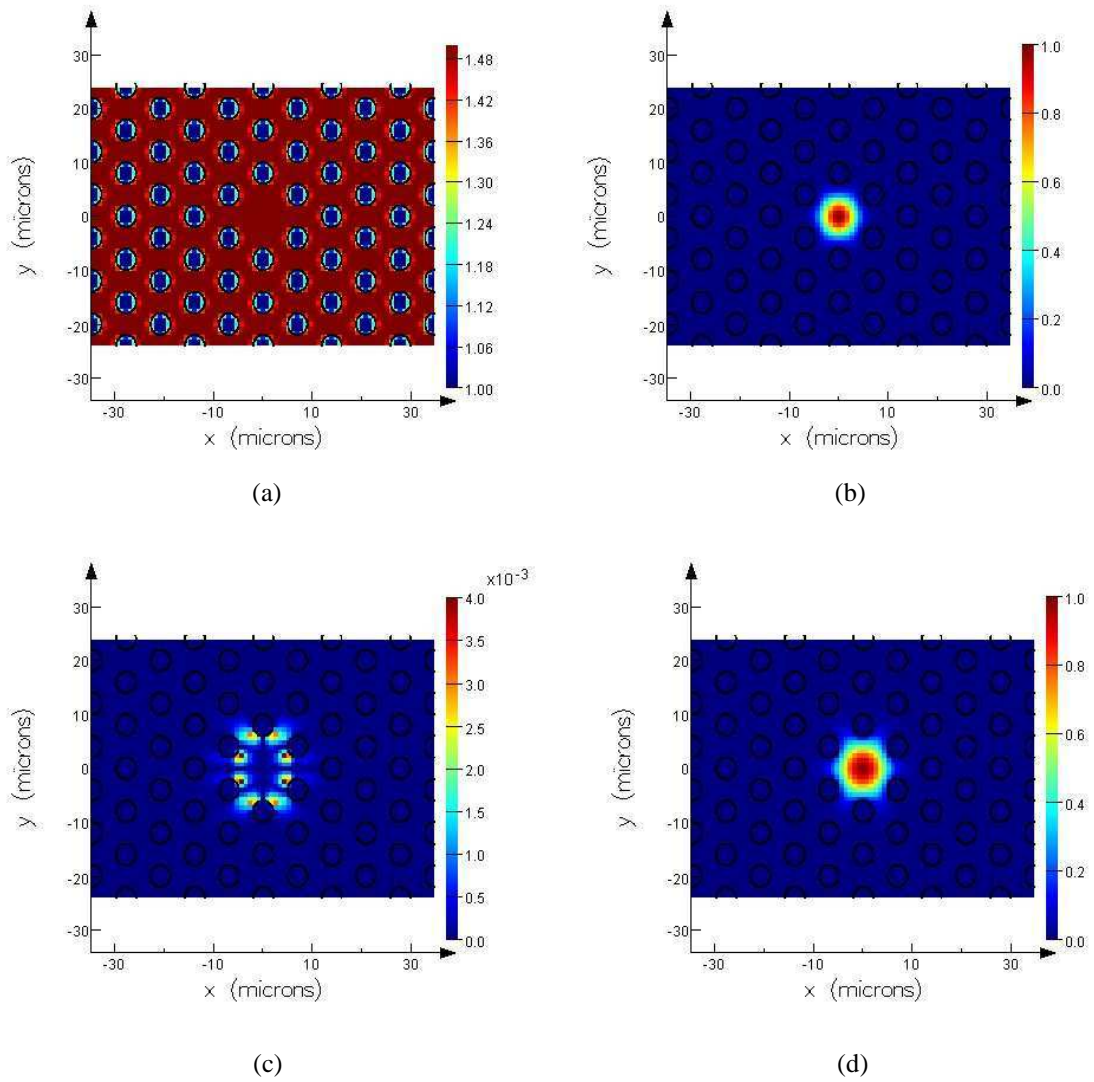
Figure 5.30: Rectangular test PCF structure; (a) material properties (b) energy intensity, (c) electric field in x direction, (d) electric field in y direction.

As the software generates two orthogonal degenerate modes, the polarisation state is found by taking the average electric field intensity along the x-axis. In this example, the average value was 50% which means that the light was not polarised. This result is in keeping with the experimental results as these test fibre structures were experimentally found to be non-polarisation maintaining.

5.3.2 Improved PCF Design

As already discussed in section **5.1.1** a polarisation maintaining PCF can be created through form birefringence by breaking the symmetry of the PCF structure such that one of the polarisation modes is leakier than the other. The successful polarisation maintaining PCF laser design in this work comprised of two sizes of air holes with two larger air holes placed on either side of the elliptical core to introduce strong form birefringence. The numerical modelling to follow will include the PCF structure that was experimentally characterised in this research and the effects of varying the size and the pitch of the air holes in this structure will be modelled leading to an optimum polarisation maintaining PCF laser structure.

5.3.2.1 Experimental PCF structure

The final experimental highly polarised PCF laser structure with smaller air holes with radii 1.35μm and pitch 7μm and two larger air holes with radii 4.1μm on either side of the elliptical core region were modelled. The material properties, electric field intensity and the electric field in the x and y direction are shown in *Figure 5.31*.

(a)

(b)

(c)

(d)
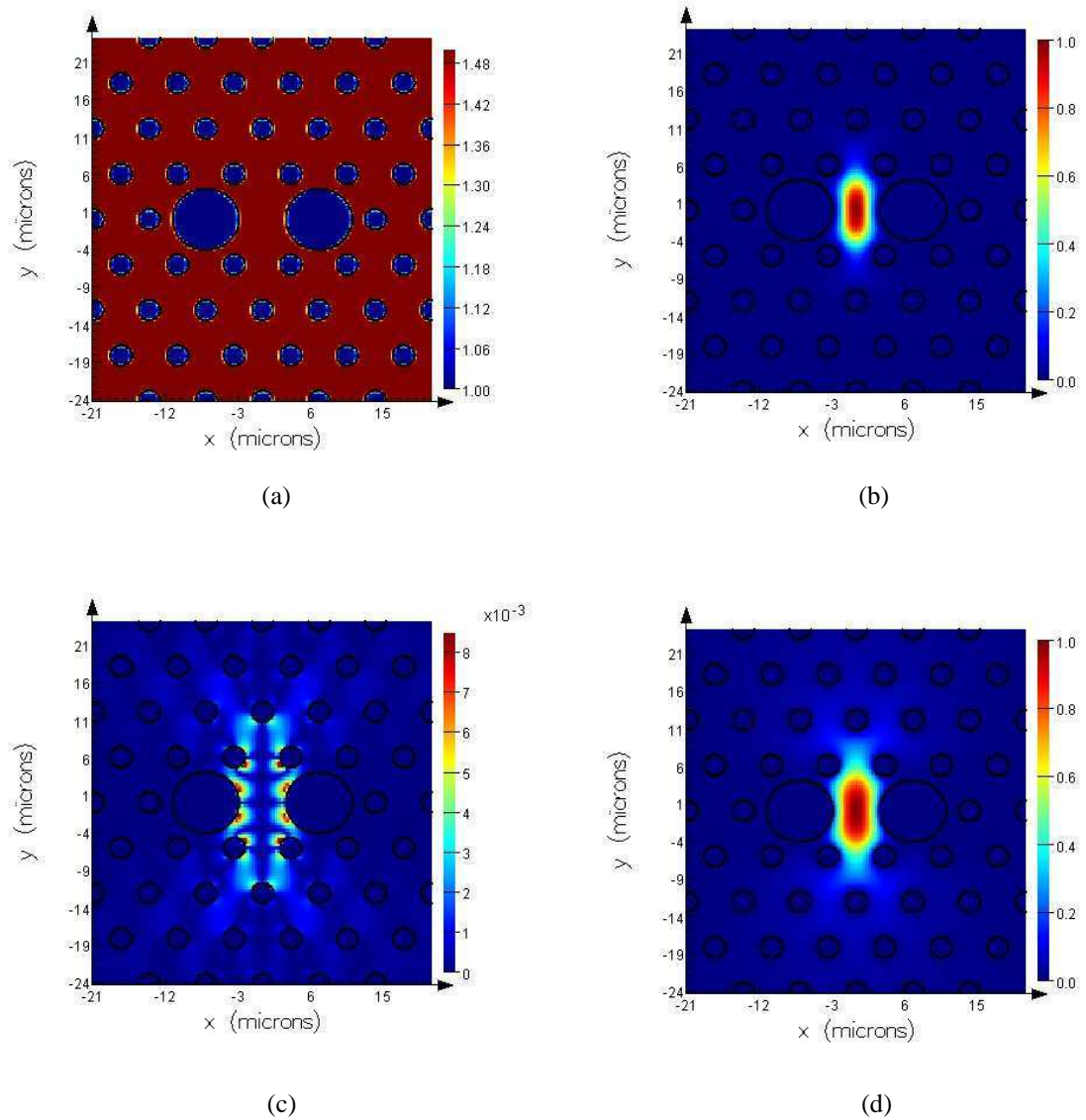
Figure 5.31: Experimental highly polarised PCF structure; (a) material properties (b) energy intensity, (c) electric field in x direction, (d) electric field in y direction.

The inclusion of the two larger air holes on either side of the core region enforces an elliptical core shape and form birefringence. The area of the PCF mode was 57.6μm^2. *Figure 5.31* shows that the fundamental mode light is not confined to the core region as light is seen to leak out into the cladding structure. The average TE value was 100% which means that the light was polarised. The modelling software capabilities were limited thus, we cannot conclude whether the PCF structure is polarisation preserving or polarisation maintaining. However, in this example we

130

can assume that the 100% TE value does mean that the PCF structure was polarisation maintaining as this was experimentally observed.

The theoretical fundamental mode associated with this PCF structure is in good agreement with the fundamental mode recorded during this research as illustrated in *Figure 5.32*.

| (a) | (b) |
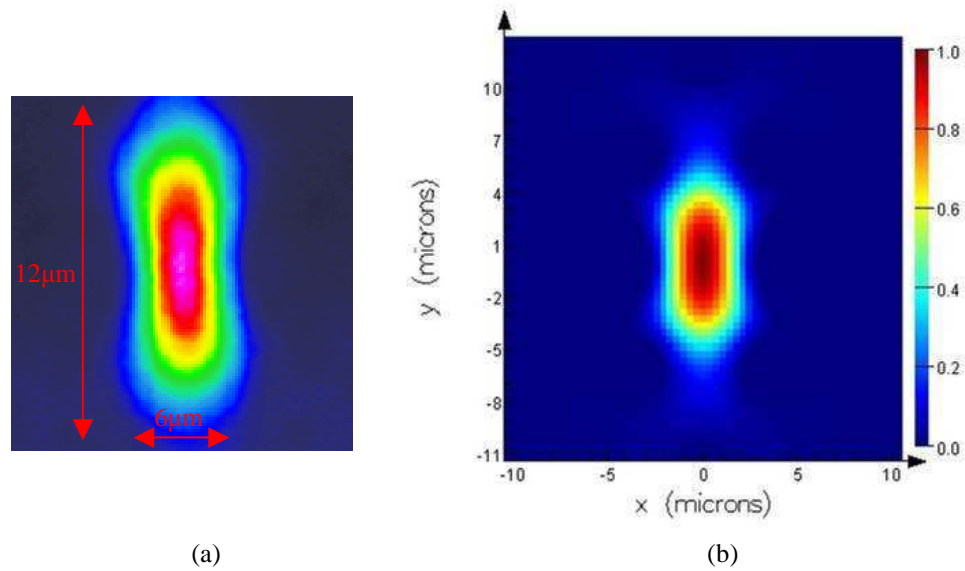
Figure 5.32: *(a) Experimental mode recorded, (b) theoretical mode predicted; for hexagonal PCF structure with two large air holes on either side of core.*

5.3.2.2   Removal of Two Large Air Holes

To test if the two larger air holes, enforcing the form birefringence, were required to establish the polarisation maintaining property of the PCF laser, the hexagonal structure modelled in the previous section was modelled again without the larger air holes. The material properties, electric field intensity and the electric field in the x and y direction for this new theoretical structure are shown in *Figure 5.33*.

(a)

(b)

(c)

(d)
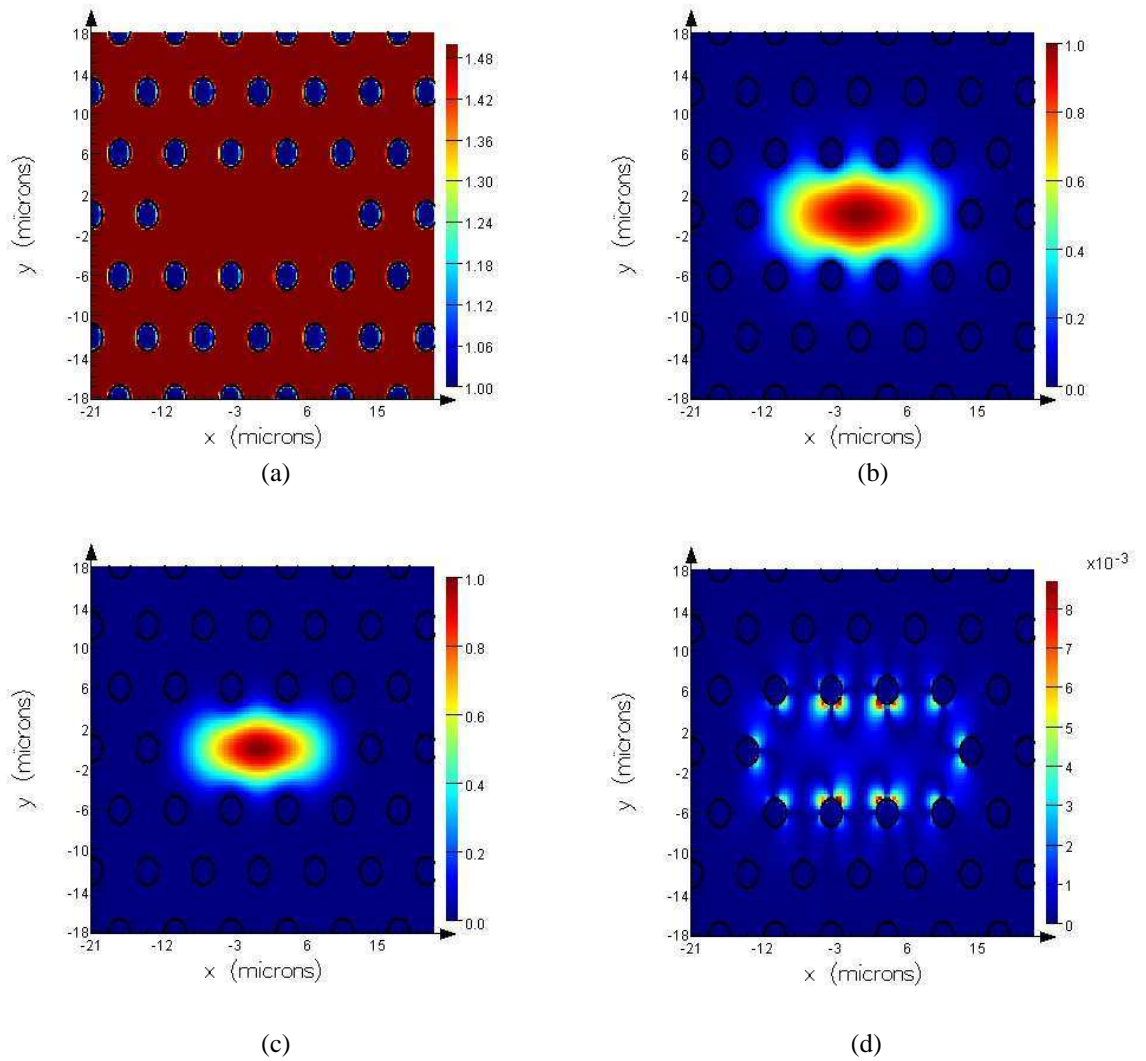
Figure 5.33: Experimental highly polarised PCF structure with two large air holes removed; (a) material properties (b) energy intensity, (c) electric field in x direction, (d) electric field in y direction.

Due to the removal of the two larger air holes the area of the PCF mode increased from 57.6μm^2 to 140.4μm^2. The average electric field along the x direction was 50% which means that the light was not polarised. Therefore, the two larger holes on either side of the core are essential to the polarisation maintaining characteristic of the PCF laser.

5.3.2.3   Small Air Hole Radii

To determine the optimum hole size that would allow full mode confinement to the core and hence no loss of power to the cladding the radii of the smaller air holes were

varied and the corresponding fundamental mode profiles were modelled as shown in *Figure 5.34*.

(a)

(b)

(c)

(d)

(e)

(f)

(g)

(h)
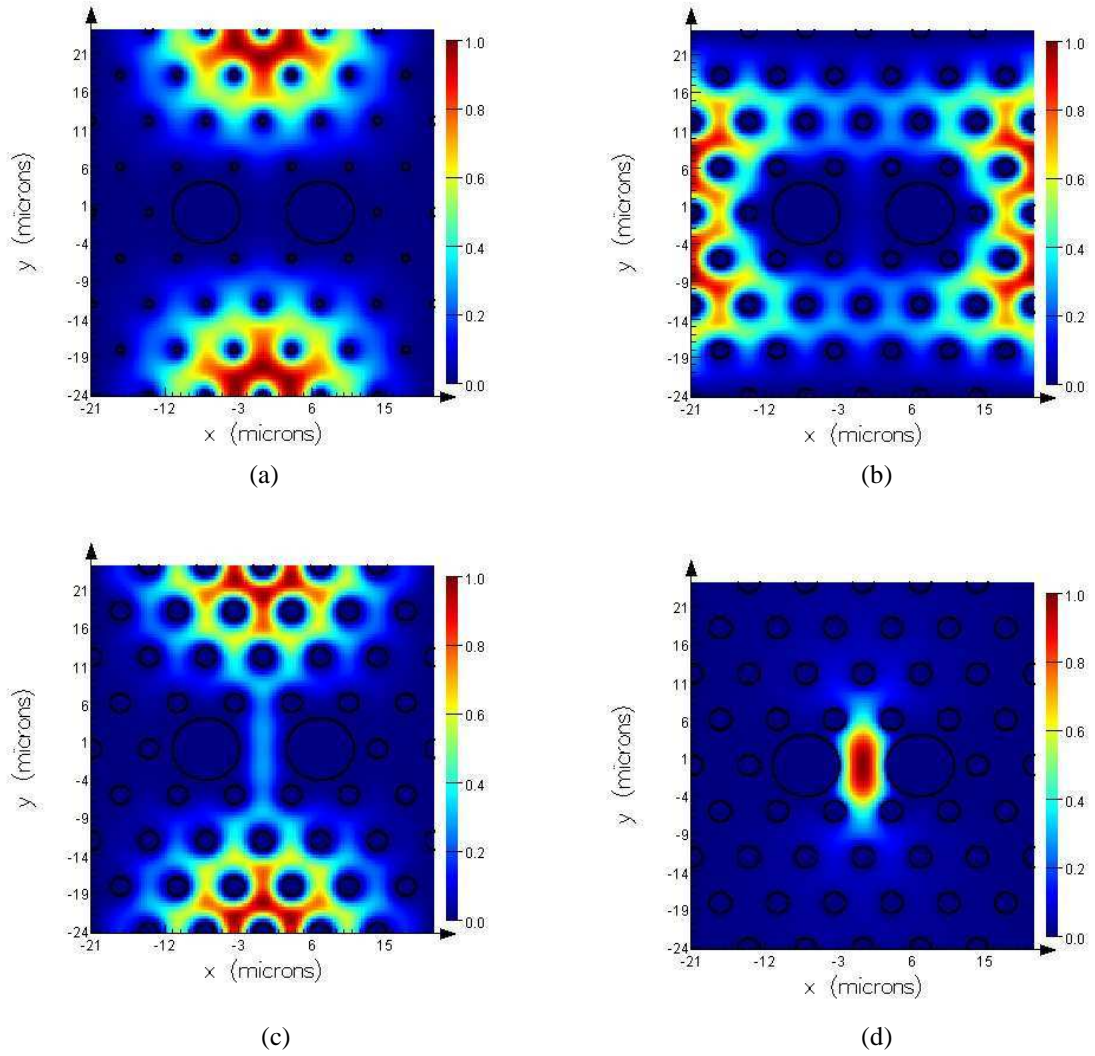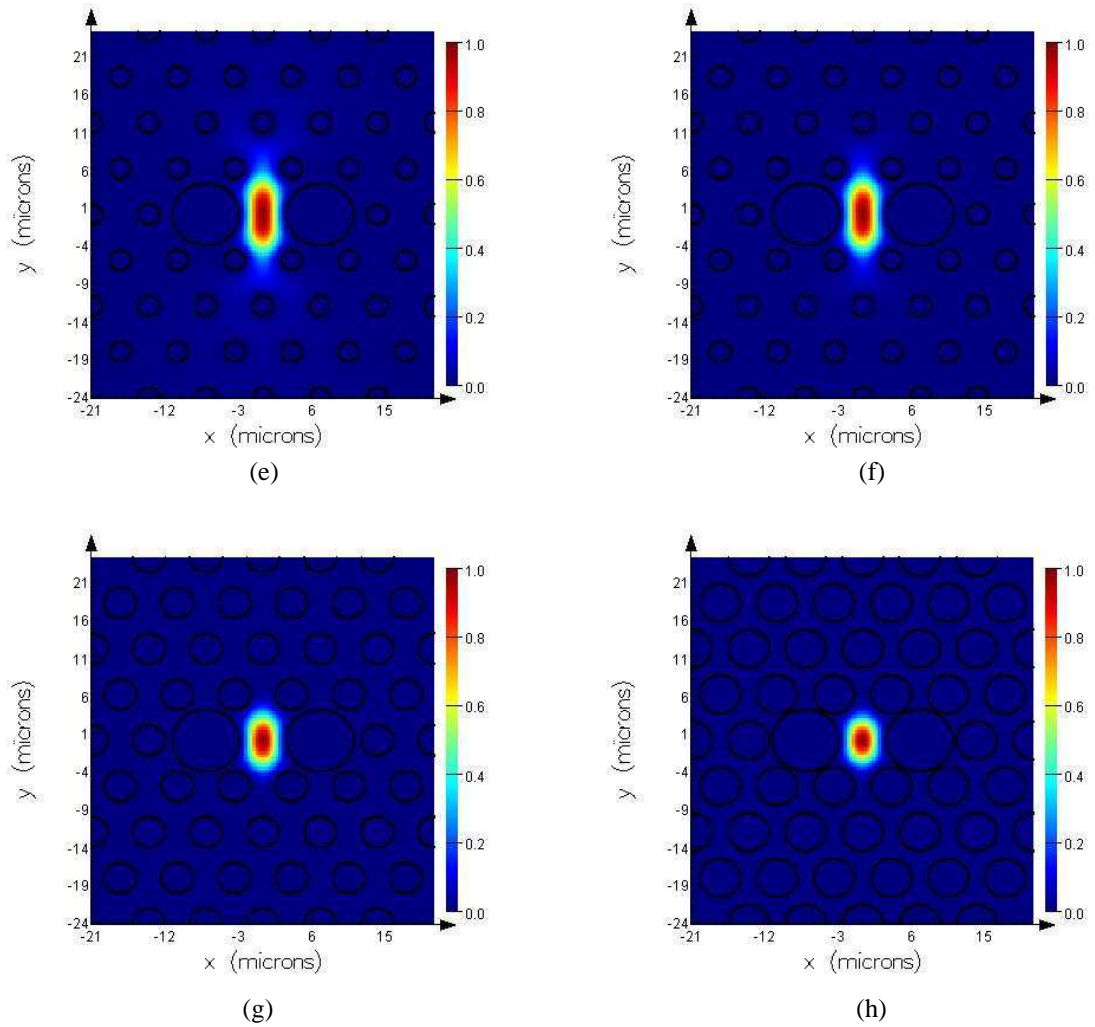
Figure 5.34: *Fundamental mode for polarisation maintaining PCF when radius of small air holes is (a) 0.5μm, (b) 1μm, (c) 1.1μm, (d) 1.2μm, (e) 1.3μm, (f) 1.35μm, (g) 2μm, (h) 2.5μm.*

Figure 5.41 illustrates that increasing the size of the small air holes decreases the loss of light into the inner cladding of the PCF laser. Only when the air hole radius has been increased up to 2.5μm do we observe full confinement of the light to the core region. By using the fully confined mode, with corresponding air hole radii 2.5μm, as a reference for 100% mode confinement, and by carrying out a mode overlap analysis the percentage of light confined to the core as a function of small air hole radii is graphically presented in *Figure 5.35*.
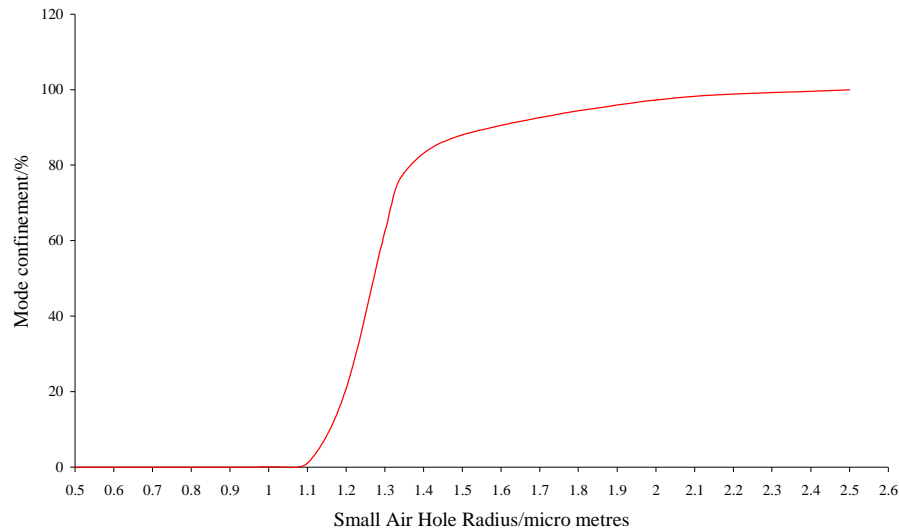
Figure 5.35*: Mode confinement to core as a function of smaller air hole radii.*

Figure 5.35 shows that if the smaller air hole radii are less than 1.1μm then none of the light is confined to the core region. For air hole radii greater than 1.1μm we see a steep increase in the mode confinement. A small increase 0.27 μm onto the 1.1μm radii increases the mode confinement by 50%. If the air hole radii are 1.35μm, as they were in our experimental PCF lasers, the mode confinement is 78%. Beyond 1.4μm the increase in percentage of light confined to the core begins to level off and reaches maximum confinement when the air hole radii are 2.5μm. Therefore, the experimental PCF laser structures in this research would have benefited in terms of mode confinement if the radii of the smaller air holes were increased from 1.35μm to 2.5μm.

5.3.2.4   Large Air Hole Radii

Similarly, the radii of the larger air holes were varied and the corresponding fundamental mode profiles were modelled as shown in *Figure 5.36*.

(a)

(b)

(c)

(d)

(e)

(f)
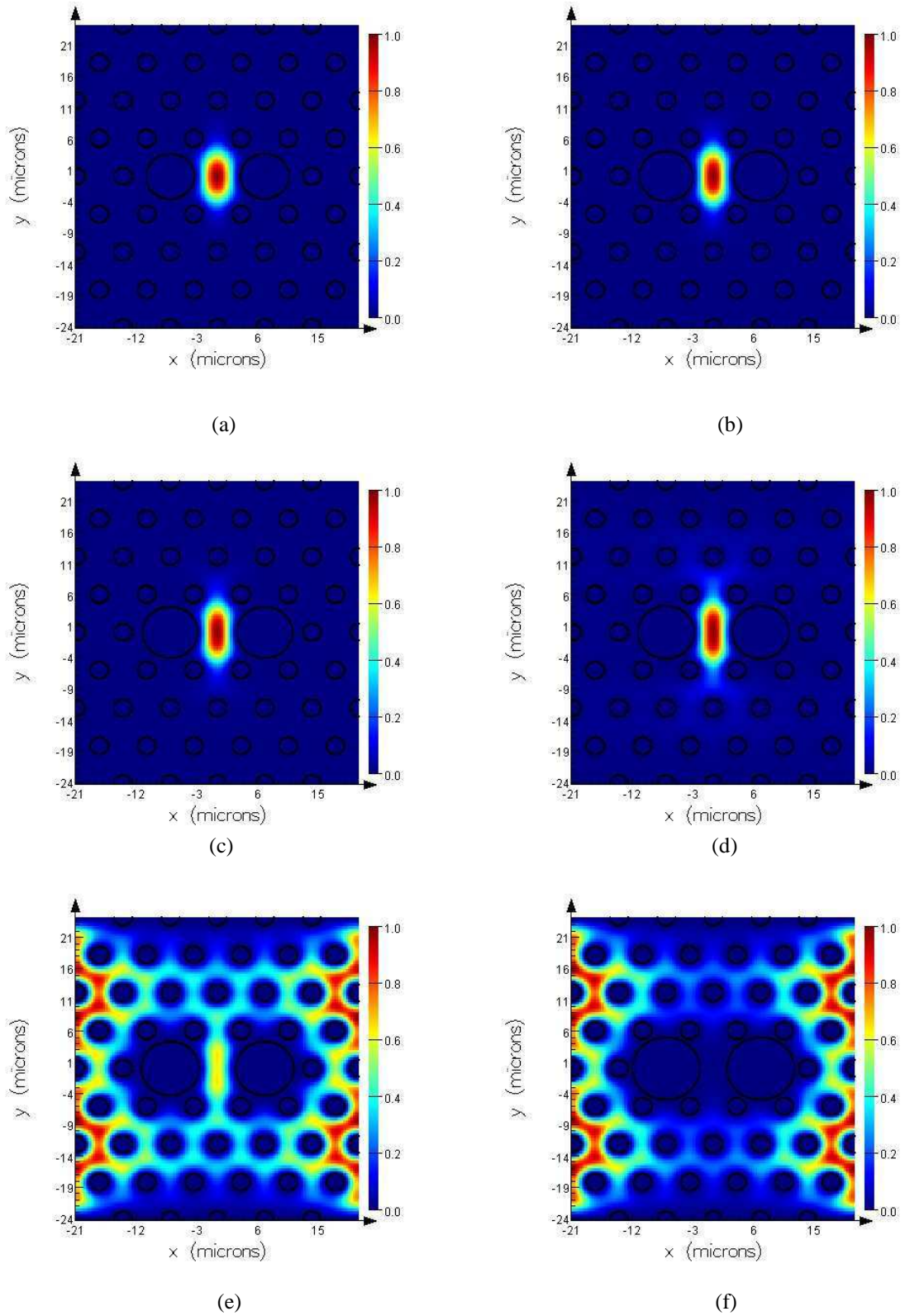
Figure 5.36: *Fundamental mode for polarisation maintaining PCF when radius of large air holes is (a) 3.6μm, (b) 4μm, (c) 4.1μm, (d) 4.2μm, (e) 4.3μm, (f) 5μm.*

Figure 5.36 illustrates that increasing the large air hole radius decreases the core light confinement factor. When the radius is greater than 4.3μm none of the light is confined to the core. When the radius is reduced to less than 3.6μm the light is confined to the core. By using the fully confined mode, with corresponding air hole radii 3.6μm, as a reference for 100% mode confinement, and by repeating the mode overlap analysis the percentage of light confined to the core as a function of large air hole radii is graphically presented in *Figure 5.37*.
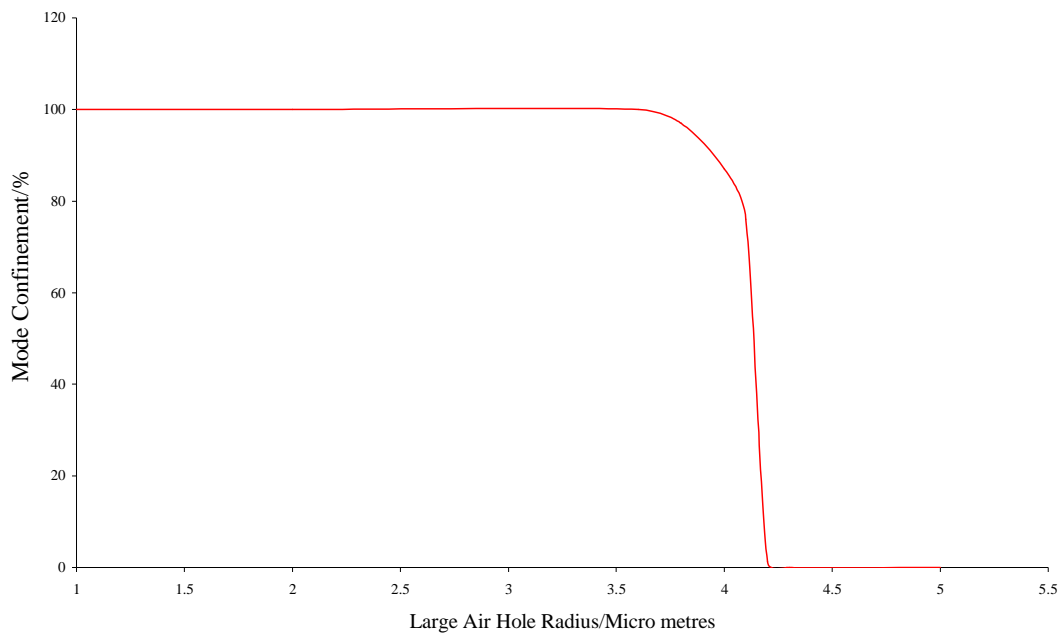
Figure 5.37: *Mode confinement to core as a function of larger air hole radii.*

Figure 5.37 shows that if the larger air hole radii are greater than 4.2μm then none of the light is confined to the core region. For air hole radii less than 4.2μm we see a steep increase in the mode confinement. A small decrease of 0.16μm from the 4.2μm radii increases the mode confinement by 50%. If the air hole radii are 4.1μm, as they were in our experimental PCF lasers, the mode confinement is 76%. For radii less than 3.8μm the increase in percentage of light confined to the core begins to level off and reaches maximum confinement when the air hole radii are 3.6μm. In comparison to *Figure 5.35*, we see that changing the larger air hole size has a more profound effect on mode confinement. In conclusion, the highly polarised experimental PCF laser structures in this research would have benefited in terms of

mode confinement if the radii of the larger air holes were decreased from 4.1μm to 3.6μm. It must be noted that reducing the size of the large air holes will reduce the amount of form birefringence. Therefore, future work using more sophisticated modelling software should be carried out to determine how the optimisation of the PCF geometry affects the polarisation maintaining properties of the PCF laser.

5.3.2.5 Pitch

The effect of varying the pitch of the air holes as a function of mode confinement was considered. With the small air hole radius fixed at 1.35μm and the larger air hole radius fixed at 4.1μm, which were the radii of the holes in the experimental PCF lasers the pitch of the air holes was modelled as follows.
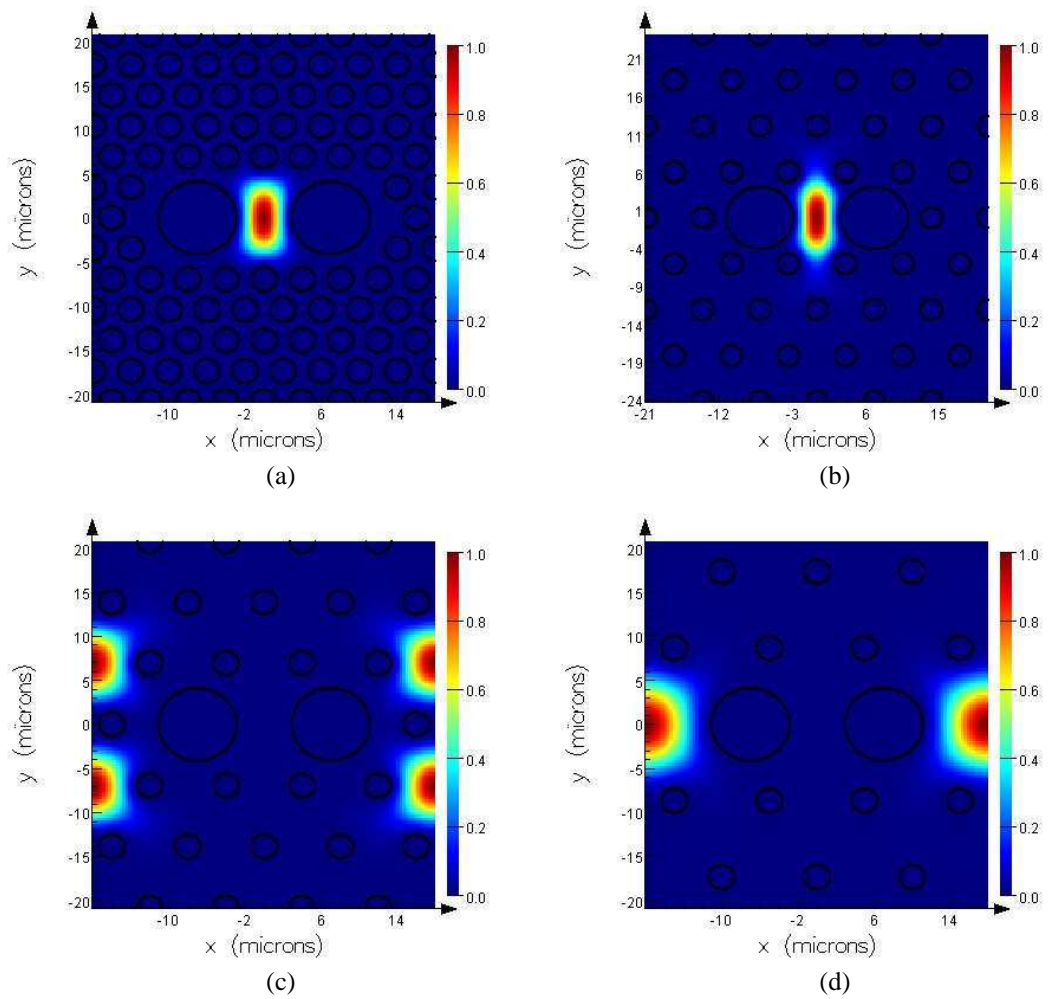
Figure 5.38: *Fundamental mode for polarisation maintaining PCF with small air hole radius 1.35μm, larger air hole radius 4.2μm and pitch is (a) 4μm, (b) 7μm, (c) 8μm, (d) 10μm.*

Figure 5.38 shows that decreasing the pitch of the air holes increases the core light confinement factor. By using the fully confined mode, with corresponding pitch 4μm, as a reference for 100% mode confinement, and by repeating the mode overlap analysis the percentage of light confined to the core as a function of pitch is graphically presented in *Figure 5.39*.
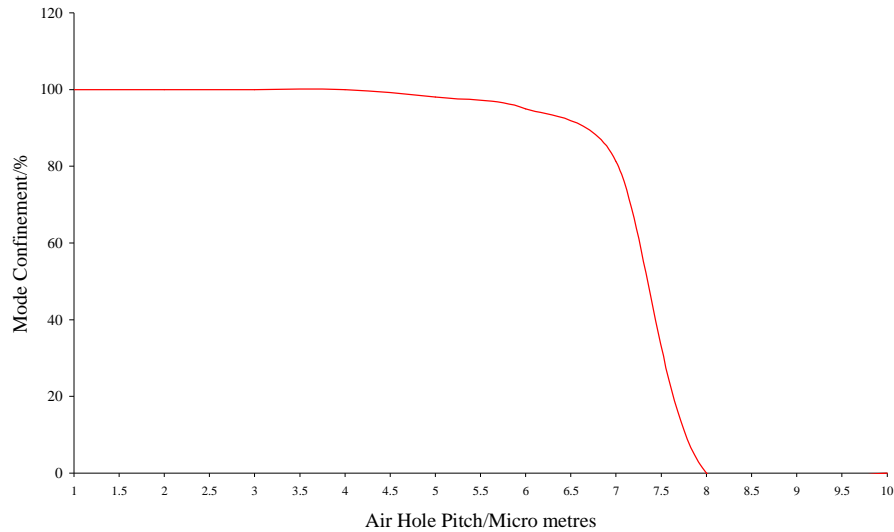
***Figure 5.39****: Mode confinement to core as a function of air hole pitch.*

A small decrease in pitch from 8μm to 7.35μm increases the mode confinement by 50%. The experimental PCF lasers, in this research had a pitch of 7μm which corresponds to 81% mode confinement in the core. Thus, the experimental PCF laser structures in this research would have benefited in terms of mode confinement if the pitch of the air holes was less than 7μm.

5.4 Conclusions

An overview of birefringence and polarisation maintaining PCF's has been given. The first demonstration and characterisation of a double-cladding highly polarised Yb^{3+} doped PCF laser with form birefringence has been presented. The polarisation maintaining PCF laser had fibre attenuation of $0.48dBm^{-1}$, operating wavelength between 1020nm and 1080nm depending on fibre length, internal quantum efficiency of 77%, polarisation ratio of 200:1, a core to cladding loss of $0.05Wm^{-1}$, in accordance with the numerical modelling presented in **Chapter 4,** and 2.9W highly polarised single mode output carried by the core. A difference in output power from both ends of the laser, as a direct result of non-optimum hole structure, has been shown which is in agreement with numerical modelling results from **Chapter 4**. The laser had an elliptical fundamental mode profile with $1/e^2$ radii 3μm by 6μm with M^2

values 1.72 and 2.8. Numerical mode modelling was carried out to determine the optimum PCF structure that would minimise the loss of light from the core to the cladding. The theoretical modelling predicts that the experimental highly polarised PCF laser could be optimised by increasing the small air hole radii to 2.5μm, reducing the larger air hole diameters to 3.6μm and by reducing the pitch of the air holes to less than 7μm.

5.5 References

[1]   J. R. Simpson, R. H. Stolen, F. M. Sears, W. Pleibel, J. B. MacChesney, R. E. Howard, "A single-polarization fiber", Journal Lightwave Technology, Vol. LT-1, 1983, (pp370-374)

[2]   K. Okamoto, "Single-polarization operation in highly birefingent optical fibers", Applied Optics, Vo. 23, No. 15, (pp2638-2642)

[3]   K. S. Chiang, "Stress-induced birefringence fibres designed for single-polarization single-mode operation", Journal Lightwave Technology, Vol. 7, No. 2, 1989, (pp436-441)

[4]   A. Ortigosa-Blanch, J. C. Knight, W. J. Wadsworth, J. Arriaga, B. J. Mangan, T. A. Birks, and P. St. J. Russell, "Highly birefringent photonic crystal fibers", Optics Letters, Vol. 25, Issue 18, 2000, (pp1325-1327)

[5]   G. T. Reed, A. P. Knights, "Silicon Photonics an introduction", Wiley, 2004, Chapter 7

[6]   J. Wilson, J. Hawkes, "Optoelectronics an introduction", Prentice Hall Europe, Third Edition, 1998, Chapter 8

[7]   A. Ortigosa-Blanch, J. C. Knight, W. J. Wadsworth, J. Arriaga, B. J. Mangan, T. A. Birks, P. St. J. Russell, "Highly birefringent photonic crystal fibers", Opt. Lett., Vol. 25, No. 18, 2000, (pp1325-1327)

[8]   M. J. Steel, R. M. Osgood, "Elliptical-hole photonic crystal fibers", Opt. Lett., Vol. 26, No. 4, 2001, (pp229-231)

[9]   T. P. Hansen, J. Broeng, S. E. B. Libori, E. Knudsen, A. Bjarklev, J. R. Jensen, H. R. Simonsen, "Highly birefringent index-guiding photonic crystal fibers", IEEE Photon. Technol. Lett., Vol. 13, No. 6, 2001, (pp588-590)

[10]   J. R. Folkenberg, M. D. Nielsen, N. A. Mortensen, C. Jakobsen, H. R. Simonsen, "Polarization maintaining large mode area photonic crystal fiber", Optics Express, Vol. 12, No. 5, 2004, (pp956-960)

[11]   Crystal Fibre A/S, http://www.crystal-fibre.com/

[12]   J. Wilson, J. Hawkes, "Optoelectronics an introduction", Prentice Hall Europe, Third Edition, 1998, Chapter 5

[13]   A. E. Siegman, "How to maybe measure laser beam quality", Tutorial presentation at the Optical Society of America Annual Meeting Long Beach, California, October 1997, (pp1-18)

[14]   Lumerical Solutions Inc, http://www.lumerical.com/mode.php., visited 04/07/08

Chapter 6

Nonlinear Optical Frequency

Conversion

This chapter will review nonlinear optics and the basic theory of important nonlinear effects. A brief discussion of nonlinear materials and their properties will be provided. A polarised laser source is required for second harmonic generation thus, experimental results, obtained in this research, of second harmonic generation using a double cladding highly polarised Yb^{3+} doped PCF laser for the first time will be presented. The experiments in this chapter will show that if you have an integer number of passes, n, through the nonlinear crystal then the intensity of the second harmonic light generated will increase by a factor of n^2.

6.1 Introduction

The development of the Ruby laser in 1960 enabled research into areas previously inaccessible with incoherent light sources. One such area was that of nonlinear optics. In 1961 Franken *et al* [1] demonstrated Second Harmonic Generation (SHG) from a Ruby laser by passing the laser light through a quartz crystal. Since then the field of nonlinear optics has grown to be a major branch of modern research with interesting effects such as Raman scattering [2], supercontinuum generation [3], self-phase modulation [4], two photon absorption [5] and nonlinear optical frequency conversion all making their mark in science and technology. The latter of these has been exploited to develop laser devices that operate in diverse areas of the optical spectrum ranging from ultra-violet [6] to far infrared operating wavelengths [7].

6.2   Fundamental Aspects of Nonlinear Optics

In conventional linear optics the induced polarisation, P(t), (dipole moment per unit volume) of a material system depends linearly upon the electric field strength, E(t), of the applied optical field. For simplicity the polarisation and electric fields are assumed to be scalar quantities.   The polarisation can be expressed as [8]

$$P(t) = \varepsilon_0 \chi^{(1)} E(t) \qquad\qquad (6.1)$$

where ε_0 is the permittivity of free space and $\chi^{(1)}$ is the linear optical susceptibility of the medium. When a large electric field is applied to the medium, the material no longer responds linearly and the polarisation must be expressed in terms of a power series which represents the nonlinear response of the medium. This power series is expressed as

$$P(t) = \varepsilon_0 [\chi^{(1)} E(t) + \chi^{(2)} E(t)^2 + \chi^{(3)} E(t)^3 + ...] \qquad\qquad (6.2)$$

where $\chi^{(2)}$ and $\chi^{(3)}$ are the second and third order nonlinear susceptibilities of the medium, respectively. It is assumed that the polarisation at time, t, depends only on the instantaneous value of the electric field strength. The polarisation is important in the description of nonlinear optics as the time varying polarisation can act as a source of new components of the electromagnetic field.

The linear term, $\chi^{(1)}$, describes such effects as the refractive index, birefringence, absorption and dispersion of the medium. The second-order term, $\chi^{(2)}$, accounts for processes such as SHG, sum-frequency-mixing and the Pockels effect [9]. Second order nonlinear optical interactions can only occur in noncentrosymmetric crystals which are crystals that do not display inversion symmetry. As liquids, gasses and amorphous solids do display inversion symmetry, $\chi^{(2)}$ vanishes identically, thus such media cannot produce second order nonlinear optical interactions. The third-order term, $\chi^{(3)}$, is responsible for third harmonic generation and gives rise to effects

such as the Kerr effect and self-phase modulation. These third order nonlinear optical interactions can occur in both centrosymmetric and noncentrosymmetric media. In this research we focus on the second order term, $\chi^{(2)}$, as we are interested in the application of second harmonic generation using a novel highly polarised PCF laser as the fundamental beam.

6.2.1 Second Harmonic Generation

Consider a laser beam with frequency, ω_1, incident upon a crystal which is assumed to be lossless both at the fundamental frequency, ω_1, and the second harmonic frequency, $\omega_2 = 2\omega_1$, so that the $\chi^{(2)}$ nonlinear susceptibility conforms to the condition of full permutation symmetry. Following Boyds [8] description of the process of SHG the total electric field within the nonlinear medium is

$$E(z,t) = E_1(z,t) + E_2(z,t) \qquad (6.3)$$

where each component is expressed in terms of a complex amplitude $E_j(z)$ and slowly varying amplitude $A_j(z)$ according to

$$E_j(z,t) = E_j(z)e^{-i\omega_j t} + c.c \qquad (6.4)$$

where c.c represents the complex conjugate and

$$E_j(z) = A_j(z)e^{ik_j z} \qquad (6.5)$$

where $k_j = n_j \omega_j / c$ is the wave number and $n_j = \sqrt{\varepsilon \mu_j}$ is the refractive index where ε is the relative permittivity and μ_j is the relative permeability of the material. Assuming that each frequency component of the electric field obeys the driven wave equation

$$\frac{\partial^2 E_j}{\partial z^2} - \frac{\varepsilon \omega_j}{c^2}\frac{\partial^2 E_j}{\partial t^2} = \frac{4\pi}{c^2}\frac{\partial^2}{\partial t^2}P_j \qquad (6.6)$$

then the nonlinear polarisation is

$$P^{NL}(z,t) = P_1(z,t) + P_2(z,t) \qquad (6.7)$$

with

$$P_j(z,t) = P_j(z)e^{-i\omega_j t} + c.c \qquad (6.8)$$

where j=1,2. The expressions for $P_1(z)$ and $P_2(z)$ are

$$P_1(z) = 4dE_2 E_1^* = 4dA_2 A_1^* e^{i(k_2-k_1)z} \qquad (6.9)$$

$$P_2(z) = 2dE_1^{\ 2} = 2dA_1^{\ 2} e^{2ik_1 z} \qquad (6.10)$$

where the nonlinear coefficient $d = \dfrac{1}{2}\chi^{(2)}$. By substitution of equations *(6.4), (6.5),*

(6.9) and *(6.10)* into the wave equation, two coupled amplitude equations for each frequency component are found to be [8]

$$\frac{dA_1}{dz} = \frac{8\pi i \omega_1^{\ 2} d}{k_1 c^2} A_2 A_1^* e^{-i\Delta kz} \qquad (6.11)$$

and

$$\frac{dA_2}{dz} = \frac{4\pi i \omega_2^{\ 2} d}{k_2 c^2} A_1^{\ 2} e^{i\Delta kz} \qquad (6.12)$$

where $\Delta k = 2k_1 - k_2$ is known as the wave vector mismatch. Generally, this pair of coupled amplitude equations must be solved simultaneously. For convenience it is preferred to work with the modulus, $|A_j|$, and the phase, ϕ_j, of each of the field amplitudes rather than with the complex quantities themselves as well as expressing the amplitudes in dimensionless form. Thus equations *(6.11)* and *(6.12)* can be

solved simultaneously such that the complex, slowly varying field amplitudes can be expressed as

$$A_1 = \left(\frac{2\pi I}{n_1 c}\right)^{\frac{1}{2}} u_1 e^{i\phi_1} \qquad (6.13)$$

and

$$A_2 = \left(\frac{2\pi I}{n_2 c}\right)^{\frac{1}{2}} u_2 e^{i\phi_2} \qquad (6.14)$$

where $I = \frac{n_j c}{2\pi}\left|A_j\right|^2$ is the total intensity of the two waves and u_1 and u_2 are the new field amplitudes.

In general the fundamental and second harmonic fields interchange energy periodically.

6.2.2 SHG With Focussed Gaussian Beams

The previous section assumed that the interacting waves were all infinite plane waves. In reality, the incident fundamental radiation is usually focussed into the nonlinear optical medium in order to increase both its intensity and the efficiency of the nonlinear optical process. Indeed it was this focussed beam method which was experimentally carried out in this research. The following theory assumes a TEM_{00} mode however the lasers in this research had M^2 values greater than 1. The amplitude and the frequency component of the second harmonic must obey the paraxial wave equation [9].

$$2ik_2 \frac{\partial A_2}{\partial z} + \Delta_T{}^2 A_2 = -\frac{4\pi\omega_2{}^2}{c^2}\chi^{(2)} A_1{}^2 e^{i\Delta kz} \qquad (6.15)$$

148

where $\Delta_T{}^2$ is the transverse Laplacian operator, the phase mismatch $\Delta k = 2k_1 - k_2$ and the complex amplitude of the nonlionear polarisation is equal to $p_2 = \chi^{(2)} A_1{}^2$. The complex amplitude of the fundamental wave can be represented by

$$A_1(r,z) = \frac{A_1}{1+i\zeta} e^{-r^2/w_0{}^2(1+i\zeta)} \qquad (6.16)$$

where ζ is the normalised distance parameter. Under the constant pump approximation the paraxial wave equation (6.15) can be solved by using the trial solution [8]

$$A_2(r,z) = \frac{A_2(z)}{1+i\zeta} e^{-2r^2/w_0{}^2(1+i\zeta)} \qquad (6.17)$$

where $A_2(z)$ is a function of z. This form of the trial solution was chosen as it has the same radial dependence as the source term in the paraxial wave equation. Also, ignoring the spatial variation of $A_2(z)$, the trial solution corresponds to a beam with the same confocal parameter as the fundamental beam which coincides with the fact that the second harmonic wave generated is coherent over a region whose longitudinal extent is equal to that of the fundamental wave. The trial solution satisfies the paraxial wave equation as long as $A_2(z)$ obeys the ordinary differential equation

$$\frac{dA_2}{dz} = \frac{i4\pi\omega}{nc} \chi^{(2)} A_1{}^2 \frac{e^{i\Delta kz}}{(1+i\zeta)} \qquad (6.18)$$

which can be integrated directly to obtain

$$A_2(z) = \frac{i4\pi\omega}{nc} \chi^{(2)} A_1{}^2 J_2(\Delta k, z_0, z) \qquad (6.19)$$

where

$$J_2(\Delta k, z_0, z) = \int_{z_0}^{z} \frac{e^{i\Delta kz'} dz'}{(1 + 2iz'/b)} \qquad (6.20)$$

where z_0 represents the value of z at start position of the nonlinear medium, $b = kw_o^2$ is the confocal parameter. As the second harmonic radiation generated has a confocal parameter equal to that of the fundamental beam, the beam waist radius of the second harmonic radiation is $\sqrt{2}$ times smaller than that of the fundamental beam. Similarly the far field diffraction angle of the second harmonic radiation will also be $\sqrt{2}$ times smaller than the fundamental beam.

The integral in equation *(6.20)* can be evaluated analytically for different limiting cases. In the plane wave limit where $b >> |z_0|$, $|z|$ the integral simplifies to

$$J_2(\Delta k, z_0, z) = \int_{z_0}^{z} e^{i\Delta kz'} dz' = \frac{e^{i\Delta kz} - e^{i\Delta kz_0}}{i\Delta k} \qquad (6.21)$$

thus

$$|J_2(\Delta k, z_0, z)|^2 = L^2 \operatorname{sinc}^2\left(\frac{\Delta kL}{2}\right) \qquad (6.22)$$

where $L = z - z_o$ is the length of the interaction region. This plane wave assumption is often made to determine the acceptance bandwidth for the crystal temperature, pump wavelength and the crystal angle.

6.2.2.1   Optimum Focussing Conditions

The conversion efficiency increases with the intensity of the fundamental wave therefore using a focussed beam is the obvious choice. However, too strong focussing leads to large divergence which decreases the efficiency. Thus, intuitively optimum focussing is achieved if the Rayleigh length roughly corresponds to the crystal length. Boyd and Kleinman [10] considered the optimum focussing conditions in more detail and found that the maximum efficiency was obtained when

the fundamental beam was focussed such that the beam waist was located in the centre of the nonlinear crystal, beam walk-off effects are negligible, the wave vector mismatch $\Delta k = 3.2/L$ where L is the length of the nonlinear crystal and the optimum focussing parameter is set at

$$\zeta = L/b = 2.84 \qquad (6.23)$$

Thus, efficient conversion will occur when the confocal parameter is 2.84 times shorter than the length of the crystal. For non-critical phase matching the optimum focussed spot size is [11]

$$w_o = \sqrt{\frac{l\lambda_1}{\zeta(2\pi n_1)}} = \sqrt{\frac{l\lambda_1}{2.84(2\pi n_1)}} \qquad (6.24)$$

The second harmonic power can be expressed as [10]

$$P_{2\omega} = \Gamma L P_\omega^{\,2} h(\Delta k z_0, \zeta) \qquad (6.25)$$

where $\Gamma = 2\omega_1^3 d_{eff}^2 / \pi n_1 n_2 c_0^4 \varepsilon_0$ characterises the type and properties of the doubling crystal. The factor $h(\Delta k z_0, \zeta)$ is only analytically solvable in special cases (plane waves and strong focussing). A numerical optimisation of $h(\Delta k z_0, \zeta)$ yields a value of $h(\Delta k z_0, \zeta) = 1.068$ with $\zeta = L/b = 2.84$. The power generated, in cgs units, at the second harmonic frequency is [8].

$$P_{2\omega} = 1.068 \left[\frac{128\pi^2 \omega_1^3 d^2 L}{c^4 n_1 n_2} \right] P_\omega^{\,2} \qquad (6.26)$$

6.2.3   SHG With Elliptical Gaussian Beams

Throughout this research the output from the PCF lasers were elliptical but the experimental optimum focussing conditions were based on spherical beams.

Steinbach *et al* [12] carried out work on SHG with elliptical beams in analogy to Boyd and Kleinmans [10] work and showed that the power of the second harmonic is

$$P_2 = YP_1^2 lk_1 \cdot h(B, \Delta k, \zeta_x, \zeta_y)$$

$$= \frac{\sqrt{\zeta_x \zeta_y}}{l^2} \cdot \int_0^l \int_0^l \frac{e^{i\Delta k(z'-z)} e^{-4B^2(z'-z)^2 \zeta_x/l^2} dz dz'}{\sqrt{(1+i\kappa_x')}\sqrt{(1+i\kappa_y')}\sqrt{(1-\kappa_x)}\sqrt{(1-\kappa_y)}} \qquad (6.27)$$

where

$$Y = (128\pi^2 \omega_1^2 / c^3 n_1^2 n_2) d_{eff}^2$$

$$\zeta_i = l/b_i$$

$$B = \rho\sqrt{lk_1}/2$$

and

$$\kappa_i = 2\left(\frac{z - f_i}{b_i}\right), \ b_i = w_{0_i}^2 k_1$$

which is comparable to equation *(6.26)* for the case of a spherical beam. l is the length of the crystal, ρ is the walk-off angle in radians, n_1 is the ordinary index of refraction, n_2 is the extraordinary refractive index at the doubled frequency, $\Delta k = (2k_1 - k_2)$ is the wave vector mismatch. The second harmonic power is proportional to the function $h(B, \Delta k, \zeta_x, \zeta_y)$. The second harmonic power can be solved as a function of ζ_x with ζ_y fixed at the value that maximises $h(B, \Delta k, \zeta_x, \zeta_y)$. The reader is referred to Steinbach *et al* [12] as a reference source for further detail.

6.3 Review of Phase Matching

Efficient SHG takes place when a phase relationship between the interacting waves is maintained along the propagation direction. To ensure this phase relationship is maintained the physical process of phase matching is carried out which reduces the wave vector mismatch term Δk to zero. Often dispersion is present which causes a non-zero phase mismatch value. In this situation, the energy transferred to the

second harmonic wave will reach a maximum value after a distance, l_c, known as the coherence length. After this distance the direction of energy transfer changes periodically according to the change of the phase relation between the interacting waves. Therefore, the second harmonic wave will begin to transfer energy back to the fundamental wave thus depleting the intensity of the second harmonic wave. During propagation, the period of the energy transfer between the fundamental and the second harmonic waves is a factor of two times the coherence length which is

$$l_c = \frac{\pi}{\Delta k} = \frac{\lambda_1}{4(n_{2\omega} - n_{\omega})} \qquad (6.29)$$

The growth in the second harmonic power along the propagation direction of the crystal for both instances where the phase mismatch term is zero and non-zero is illustrated in *Figure 6.1*.
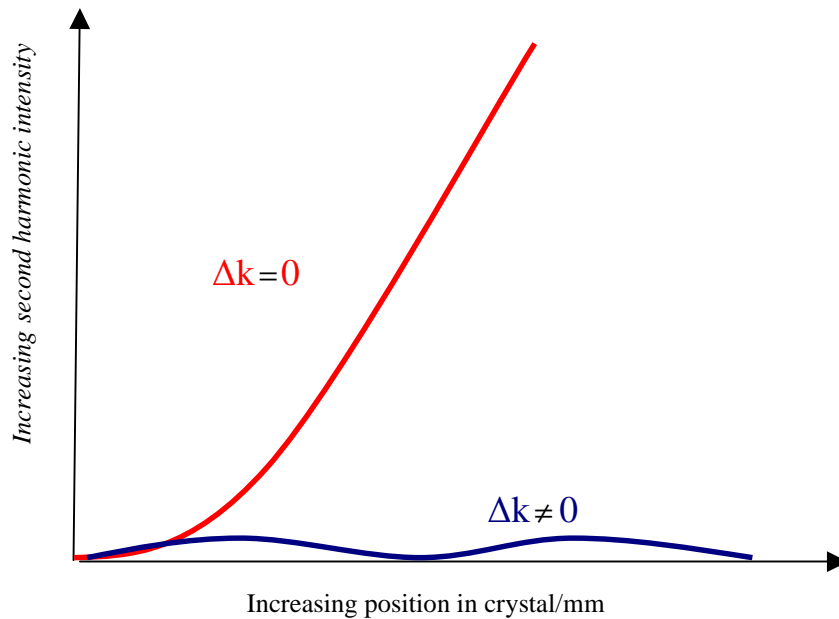
Figure 6.1: *Growth of second harmonic power as a function of propagation distance through crystal. The red line represents the zero phase mismatch example where the second harmonic intensity grows as the square of the propagation distance. The blue line represents the non-zero phase mismatch example where the second harmonic power oscillates between zero and a small value.*

Phase matching tries to maximise the coherence length by matching the refractive indices for the fundamental and second harmonic wavelengths; $n_{2\omega} = n_{\omega}$.

6.3.1 Birefringent Phasematching

In this research we will only consider uniaxial crystals which are crystals which only have one axis of symmetry, about the optical axis. The plane containing the optical axis and the wave vector of the fundamental wave into the crystal is known as the principal plane. Light beams that are polarised parallel to the optical axis experience a different refractive index than beams that are polarised perpendicular to the optical axis. If the input beam is polarised parallel to the principal plane then the wave is described as being an extraordinary wave and it will experience a refractive index n_e. Conversely if the input beam is polarised perpendicular to the principal plane then the wave is described as being an ordinary wave and it will experience a refractive index n_o. The difference between these refractive indices is known as the birefringence, Δn. The extraordinary refractive index is dependent on the input angle, θ, according to [12]

$$\frac{1}{n_e(\theta)} = \frac{\cos^2 \theta}{n_o^{\,2}} + \frac{\sin^2 \theta}{n_e^{\,2}} \qquad (6.30)$$

For anisotropic crystals $n_o \neq n_e$ and if the crystal is negative or positive then $n_o > n_e$ or $n_o < n_e$, respectively. There are two ways in which to achieve phase matching; angle tuning or temperature tuning.

6.3.1.1 Angle Tuning

Phase matching can be achieved by rotating the crystal such that an appropriate angle between the fundamental wave and the optical axis is selected which satisfies the refractive index phase matching conditions. For Type I phase matching both waves at ω have the same polarisation whereas the wave at 2ω has orthogonal polarisation.

If the phase matching angle is not equal to 0° or 90° then the Poyting vectors of the fundamental and the second harmonic waves, which define the direction of energy transport will not be aligned. Therefore, an angle between he two waves is created resulting in a separation between the fundamental and the second harmonic waves. This phenomenon is known as spatial walk-off and it limits the effective interaction length of the crystal.

6.3.1.2   Temperature Tuning

The birefringence of some crystals, particularly Lithium Triborate (LBO) and Lithium Niobate (LN) which were utilised in this research, are strongly temperature dependent. Thus, by controlling the temperature of the crystal, one of the refractive indices can be tuned over a large range. This temperature tuning technique allows the ordinary and extraordinary refraction coefficients to be matched at the phase matching angle condition, $\theta = 90^o$, such that the walk-off effect associated with angle tuning is avoided. Eliminating the walk-off effect increases the interaction length of the fundamental and second harmonic waves which increases the conversion efficiency. Often, the crystal must be heated up to temperatures substantially greater than room temperature in order to achieve phase matching. Due to the increased conversion efficiency associated with temperature tuning, this type of phase matching was carried out in this research where crystal temperatures in excess of 150^oC were required.

6.3.2   Quasi-phase Matching

Quasi-phase Matching (QPM) is an alternative to birefringent phase matching and it permits phase matching in optical materials which exhibit no birefringence at all. It is achieved by artificially engineering the structure of the nonlinear material rather than exploiting its inherent birefringent properties. This method was first suggested in 1962 by Armstrong *et al* [14], which was prior to that of birefringent phase matching methods already outlined above. However, QPM was not utilised experimentally until the 1980's due to fabrication difficulties. Unlike, birefringent phase matching where the condition $\Delta k = 0$ is necessary there is no such constraint

involved in QPM thus $\Delta k \neq 0$ is permitted but after one coherence length the phase mismatch is reset to zero. This is achieved by reversing the sign of the nonlinear coefficient. By doing so, an additional phase shift of π is added to the interacting waves which restores the constructive interference process; resulting in the growth of the second harmonic field as illustrated in *Figure 6.2*.
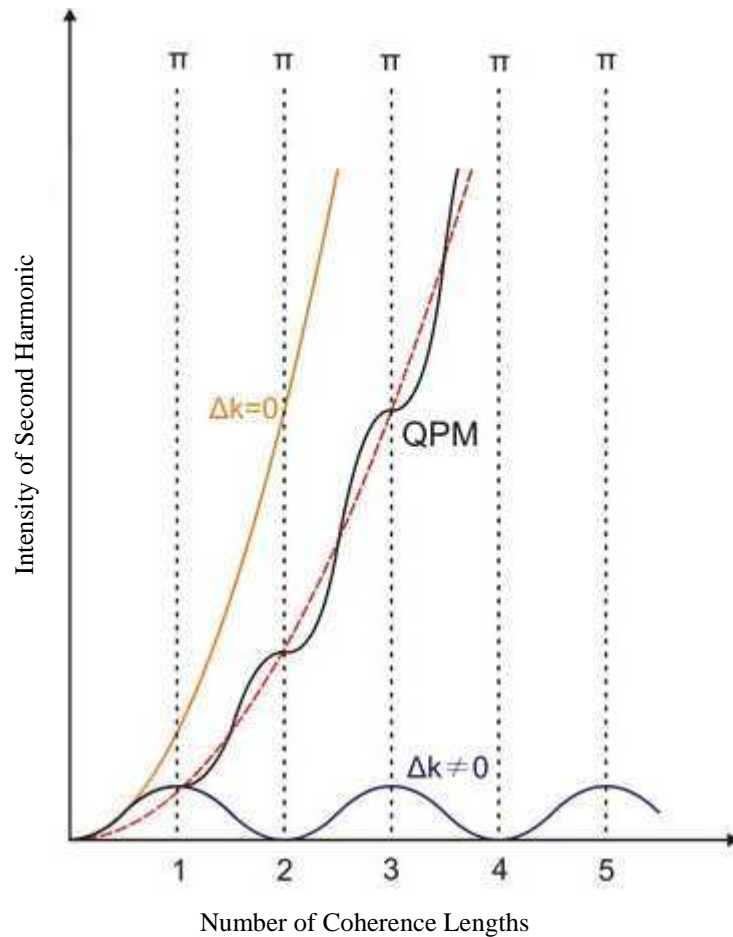
Figure 6.2: *Stepwise build up of second harmonic field due to QPM: Yellow curve represents build up with birefringence phase matching Δk = 0, red curve represents build up when $\Delta k \neq 0$ with QPM when a π phase shift is applied every coherence length, blue curve represents periodic build up and decrease of second harmonic field when Δk≠ 0 and no QPM is applied.*

Engineering the π phase change every coherence length throughout the crystal length is a difficult and complex problem which is why it has taken thirty years to practically perfect the modern technique known as periodically poling the nonlinear material for QPM applications. This technique involves ferroelectric domain engineering which generates a periodic reversal of the domain orientation in a

nonlinear crystal. Therefore the sign of the nonlinear coefficient of the nonlinear material periodically changes. This sign reversal is achieved by the application of a strong electric field via patterned electrodes. The period, Λ, of the electrode pattern is twice the coherence length of the nonlinear material. In the QPM case the phase mismatch term Δk described for birefringent phase matching can be replaced by $\Delta k_{qpm} = \Delta k - k_g$, where k_g is the wave vector defined by the grating period and is given by $k_g = 2\pi /\Lambda$. Similar to the birefringent case, the quasi-phase mismatch term depends on the temperature and positioning of the crystal Again, crystal rotation is not desirable due to the effects of spatial walk-off, thus temperature tuning is often favoured. For first order QPM the effective nonlinear coefficient is $d_{qpm} = (2/\pi)d_{eff}$.

6.4 Frequency Doubling Highly Polarised PCF Laser

Using MathCAD the refractive indices, phase matching temperature and optimum beam size required for SHG using a 15mm length LBO crystal were calculated as shown in **Appendix B**. The laser output from 20m of the highly polarised PCF laser, which was characterised in **Chapter 5,** was frequency doubled using the non-critical second harmonic phase matching technique previously described. The experimental setup is shown in *Figure 6.3*.
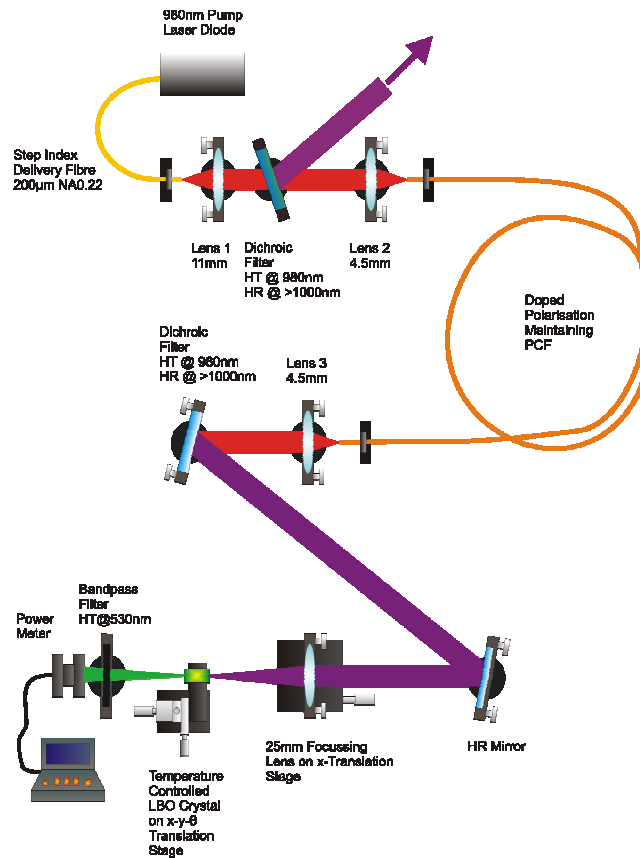
Figure 6.3*: Experimental setup for second harmonic generation in 15mm LBO crystal using 20m highly polarised PCF laser.*

A 15mm length, Lithium Triborate (LBO) nonlinear crystal with 1064nm anti-reflection coatings on each end facet was mounted in a purpose built copper oven that was temperature tuned using an electronic PID system control unit. The oven was insulated with PTFE material and additional PTFE strips were positioned in direct contact with the crystal surfaces to avoid damage to the crystal due to thermal induced expansion. The output from the PCF laser was focussed into the centre of the crystal using a 25mm focal length lens. A short wavelength bandpass filter (T = 50%) was positioned after the crystal to filter the fundamental light from the second harmonic light. An Ophir photodiode power meter was used to record the power of the second harmonic light.

Using equation *(6.24)* the optimum focussed spot diameter was calculated to be 24μm. The laser M^2 values were 1.72 and 2.8 and the dimensions of the elliptical

beam were 2mm and 6mm. According to Seigman [15] the effective diameter, d_0, of a focussed Gaussian beam is

$$d_0 \approx \frac{2f\lambda}{D} \qquad\qquad (6.30)$$

where f is the focal length of the lens, λ and D are the wavelength and diameter of the incident beam respectively. This equation assumes we are dealing with Gaussian beams with $M^2 = 1$. In this real case, where $M^2 \neq 1$, a multiplying factor representing the actual M^2 values of the laser was included in equation *(6.30)* when calculating the optimum lens choice. Therefore, based on a 25mm focal length lens, wavelength 1080nm, beam diameter 2mm with a M^2 value equal to 1.72 the expected focused spot diameter is 46µm. Using the same focal length lens the calculation was repeated for the opposite dimension of the laser beam, with M^2 value 2.8 and beam diameter 6mm which yields an expected focussed spot diameter of 25µm. This spot diameter is close to the optimum spot diameter of 24µm which is required for efficient SHG.

The theoretical temperature of the crystal required for efficient phase matching was calculated to be $130^{o}C$ as shown in **Appendix B**. From equation *(6.25)* the expected second harmonic power is 1.67mW. After heating the crystal the second harmonic power was recorded as illustrated in *Figure 6.4*.
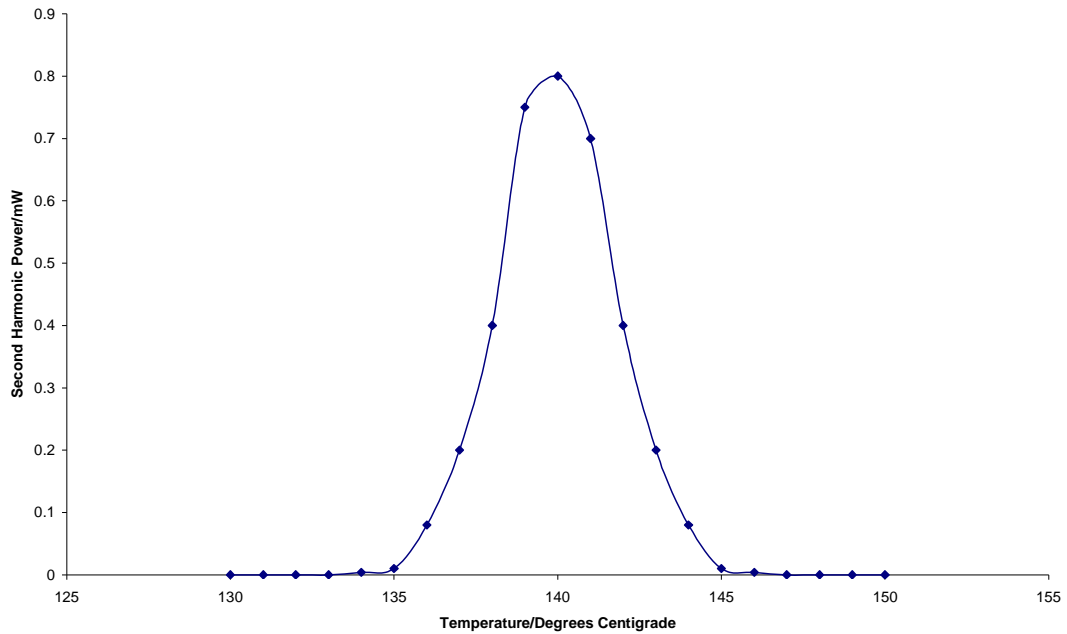
Figure 6.4: *Optimum phase matching temperature for 15mm LBO nonlinear crystal pumped by 2.8W, 1080nm pump from highly polarised PCF laser.*

Figure 6.4 shows that maximum output second harmonic power, 0.8mW, was generated when the oven temperature was 140°C. When using a thermocouple to measure the actual temperature within the oven a discrepancy of approximately 10 °C was observed in comparison to the stated temperature by the control unit. Therefore the 10°C difference in the theoretical and experimental optimum phase matching temperature is acceptable. The power output was 48% of the expected power. This low conversion efficiency is due to the high M^2 values of the fundamental laser and the elliptical shape of its output beam which prevents the optimum spot size of 24μm from being reached.

A PCF laser with 75% Bragg grating which will be characterised in **Chapter 8** was also frequency doubled using the 15mm LBO crystal. Due to the self pulsing nature of this laser, the PCF laser was double pumped using 940nm and 980nm diode lasers to suppress the pulsing. Due to the optimum alignment of this double pumping scheme the diameter of the laser beam doubled in size. Before, frequency doubling experiments were carried out, the diameter of the laser beam was reduced back down to 3mm by 6mm by using two lenses in sequence, a 5cm and a 2.5cm focal length lens separated by a 7.5cm gap which gave a telescope lens arrangement. The phase

matching temperature was calculated to be 152°C (**Appendix C**). *Figure 6.5* shows the experimental second harmonic power obtained when frequency doubling using, 6.5W from the 1061nm PCF laser with incorporated 75% Bragg grating.
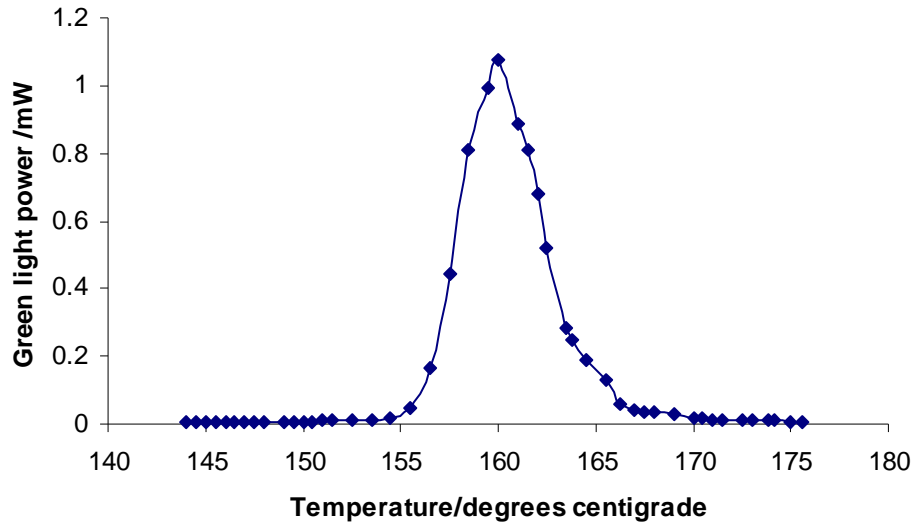

Figure 6.5: *Optimum phase matching temperature for 15mm LBO nonlinear crystal pumped by 6.2W, 1061nm pump from highly polarised PCF laser with incorporated 75% Bragg grating.*

Figure 6.5 shows that the maximum output power of second harmonic light was generated when the oven temperature was 160°C. Again, this difference in the experimental phase matching temperature compared to the calculated temperature was due to a discrepancy in the actual oven temperature when measured using a thermocouple. The maximum output second harmonic power produced when phase matched at 160°C was measured to be 1.07mW. This power is only 12% of the theoretical power value. The low power conversion is again due to the high M^{2} values of the fundamental laser and the elliptical shape of its output beam which prevents the optimum spot size of 24μm from being reached. Due to the self pulsing nature of this PCF laser, reflections from the LBO crystal proved detrimental to the stability of the laser. These pulses caused irreparable damage to the LBO crystal and the short wavelength bandpass filter which prevented further optimisation of the focussing optics to be carried out. *Figure 6.6* represents an example of the green second harmonic light produced during this research.
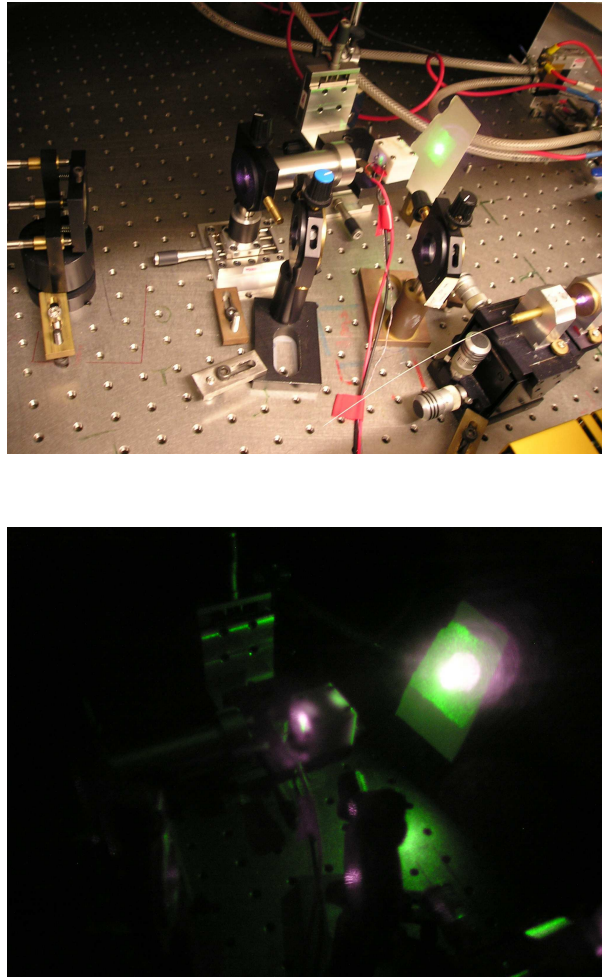
Figure 6.6*: Images of green, second harmonic light produced using a 15mm length LBO crystal pumped by 1061.6nm highly polarised PCF laser.*

6.4.1 Double-Pass SHG

In order to improve the efficiency of the SHG a double-pass of the fundamental beam through the LBO crystal was carried out using the setup shown in *Figure 6.7*.
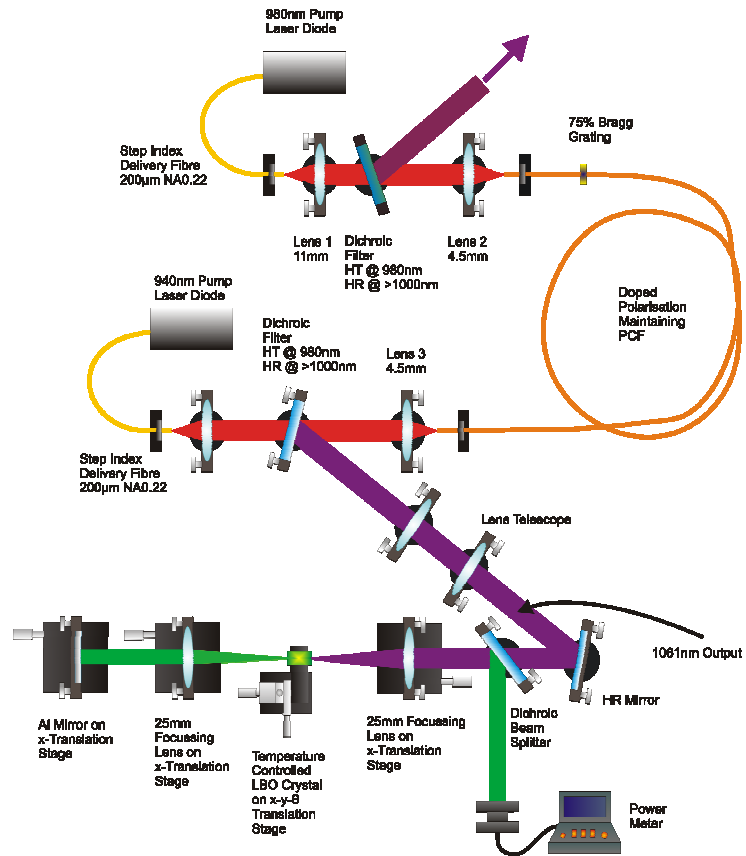
Figure 6.7*: Experimental setup for double pass second harmonic generation in 15mm LBO crystal using 20m double pumped PCF laser with 75% Bragg grating.*

An aluminium mirror on a translation stage was included after the 25mm collimating lens to retro-reflect the fundamental and second harmonic wave back through an other 15mm LBO crystal that did not have any anti-reflective coating. The mounting of this mirror on a translation stage allowed the relative phase between the fundamental and the second harmonic beam to be varied by adjusting the optical path length of the beam. Thus, the phase shift correction would allow the generated second harmonic light to add constructively to second harmonic light that will be generated during the second pass of the crystal. A dichroic beam splitter which was highly reflective for the second harmonic when placed at an angle of 45° and highly transparent at the fundamental wavelength was positioned prior to the coupling lens into the crystal. To allow the second harmonic power to be measured by an Ophir photodiode power meter.

By assuming that there is constant intensity throughout the crystal we can calculate the expected increase in intensity of green light generated by considering the electric field during a single pass of the crystal.

$$E \propto \int_0^l idE_1{}^2 e^{i\Delta kz}$$
(6.31)

therefore the intensity of the second harmonic is

$$I = \frac{dE_1{}^2}{z^3} l^2 \left(\frac{\sin \Delta kl^2}{\Delta kl} \right)$$
(6.32)

The total electric field after passing through the crystal twice is

$$E = \Delta E + \Delta E = 2\Delta E$$
(6.33)

Allowing for 10% reflection losses during the first pass and 20% reflection loss during the second pass we have

$$E = 0.9\Delta E + 0.8\Delta E = 1.7\Delta E$$

As the intensity is proportional to the electric field squared the total intensity of the second harmonic after double passing through the LBO crystal will be

$$I_T = (1.7\Delta E)^2 = 2.89I$$

The maximum green power measured from a double pass of the LBO crystal was 3.2mW which is a factor of 3 increase in the power measured for a single pass of the LBO crystal. This experimentally measured value is close to our predicted value. *Figure 6.8* shows the green power generated as a function of crystal temperature when double passing through the crystal.
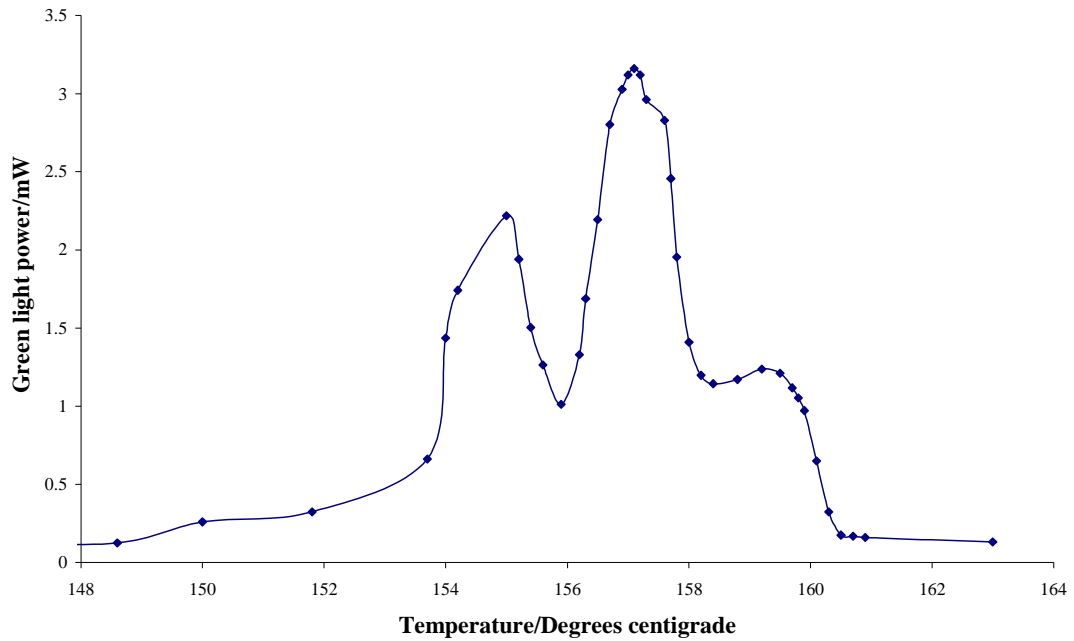
Figure 6.8*: Optimum phase matching temperature for double pass of 15mm LBO nonlinear crystal pumped by 6W, 1061.63nm pump from double pumped highly polarised PCF laser.*

The maximum green power was observed at an oven temperature of 157.1°C which is less than the temperature observed during the single pass of the crystal experiment. This temperature discrepancy is due to the crystal self heating during the second pass of the light through the crystal. Again, reflections to the PCF laser caused the laser to self pulse resulting in irrepairable damage to the LBO crystal and the bandpass filter. Therefore, no further optimisation of the double pass SHG could be carried out.

6.4.2 QPM SHG in PPLN

The bulk nonlinear crystal was then replaced by a, 10mm length, periodically poled lithium niobate crystal in a purpose built oven with temperature controller, all provided by Stratophase Ltd. The crystal end facets were coated with a 1064nm anti-reflective coating. When focussing the double pumped 20m PCF laser pump light into the centre of the crystal, with electrode pattern period $\Lambda=6$ and crystal temperature 212 $^{\circ}$C, the second harmonic power generated was measured to be 2.3mW. Reflected pump light from the facet ends of the crystal caused the detrimental self-pulsing nature of the PCF laser which severely damaged the PPLN

crystal. This irreparable damage occurred before further optimisation of the second harmonic power was carried out.

6.5 Conclusions

In conclusion, second harmonic generation using non-critical, temperature tuned phase matching of a 15mm bulk LBO crystal was demonstrated using a highly polarised Yb^{3+} doped PCF laser for the first time. The maximum second harmonic light generated, from 2.8W 1080nm fundamental power, during a single pass of the crystal was 0.8mW. Using 6.5W from a 1061nm highly polarised Yb^{3+} doped PCF laser with 75% incorporated Bragg grating 1.07mW of 530nm light was generated. We have experimentally shown that if you have an integer number of passes, n, through the nonlinear crystal then the intensity of the second harmonic light generated will increase by a factor of n^2. Quasi-phase matching using a PPLN crystal produced 2.3mW of second harmonic. Throughout all of the frequency doubling experiments the detrimental self-pulsing nature of the pump laser damaged the crystals and filters implemented which severely limited power optimisation.

6.6 References

[1]   P. A. Franken, A. E. Hill, C. W. Peters et al., "Generation of optical harmonics", Physical Review Letters, Vol. 7, 1961, (pp118-119)

[2]   K. J. Kuhn, "Laser engineering", Prentice-Hall Inc. 1998, Chapter 7

[3]   W. J. Wadsworth, A. Ortigosa-Blanch, J. C. Knight, T. A. Birks, T. P. M. Man, P. St. J. Russell, "Supercontinuum genseration in photonic crystal fibers and optical fiber tapers: a novel light source", Journal Optical Society America B, Vol. 19, Issue 9, 2002, (pp2148-2155)

[4]   R. H. Stolen, C. Lin, "Self-phase-modulation in silica optical fibres", Phys. Rev. A, Vol. 17, Issue 4, 1978, (pp1448-1453)

[5]   W. Kaiser, C. G. Garrett, "Two-photon excitation in $CaF_2:Eu^{2+}$", Phys. Rev. Lett., Vol. 7, 1961, (pp229-231)

[6]   N. Umemura, K. Kato, "Phase-matched UV generation at $0.1774\mu m$ in KB54H(2)O", Applied Optics, Vol. 35, No. 27, 1996 (pp5332-5335)

[7]   T. Q. Qiu, T. Tillert, M. Maiser, "Tunable, kilowatt, picosecond far-infrared pulse generation in LiNbO3", Optics Communications, Vol. 119, No. 1-2, 1995, (pp149-153)

[8]   R. W. Boyd, "Nonlinear Optics", Academic Press, 1992

[9]   F. G. Smith, T. A. King, "Optics and Photonics An Introduction", John Wiley and Sons, Ltd., 2001

[10]   G. D. Boyd, D. A. Kleinman, "Parametric interaction of focussed Gaussian light beams", Journal Applied Physics, Vol. 39, No. 8, 1968, (pp3597-3640)

[11]   A. Yariv, "Quantum electronics", Holt, Rinehart and Winston, New York, 1976

[12]   A. Steinbach, M. Rauner, F. C. Cruz, J. C. Bergqust, "CW second harmonic generation with elliptical Gaussian beams", Optics Communications, Vol. 123, 1996, (pp207-214)

[13]   D. Meschede, "Optics, light and lasers" Wiley-VCH 2004

[14]   J. A. Armstrong, N. Bloembergen, J. Ducuing, P. S. Pershan, "Interactions between light waves in a nonlinear dielectric", Physical Review, Vol. 127, 1962, (pp1918-1939)

[15]   A. E. Siegman, "Lasers", University Science Books, 1986

Chapter 7

Q-Switched PCF Laser

Q-switching of a laser cavity is a method of producing short and intense laser pulses which can be used in many applications such as laser cutting and drilling, range finding and laser marking. In particular the application of laser cutting requires a polarised laser source. This chapter will review the principles of Q-switched lasers and the methods employed to create such lasers. Q-switching of a novel highly polarised Yb^{3+} doped PCF laser will be demonstrated for the first time.

7.1 Overview of Q-Switching

High power pulses can be obtained by introducing time or intensity dependent losses into the laser cavity. If the losses in the cavity are initially set to a high value then the gain due to the population inversion can reach a high value without laser oscillation occurring. As the laser cannot reach threshold the gain and stored energy in the laser medium are pumped to a value much larger than that normally achievable under normal operating conditions. If the losses in the cavity are then reduced, increasing the Q of the cavity, the spontaneous emission present in the cavity rapidly begins to build up resulting in an intense burst of radiation. This burst of radiation saturates the gain medium which in turn drives the gain below the laser threshold and prevents laser action. It is this rapid amplification and saturation process which leads to the formation of the optical pulse. As the output pulse is shorter in duration than the pumping interval, the pulse formed is extremely energetic [1]. Thus, Q-switching dramatically increases the peak power obtainable from lasers. *Figure 7.1* illustrates the formation of a Q-switched pulse during the Q-switching process.
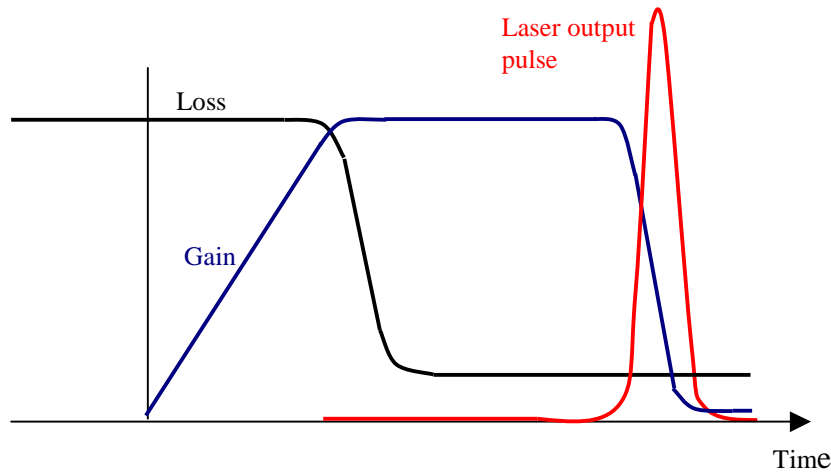
***Figure 7.1**: Formation of Q-switched laser pulse. In a real laser system the pumping interval will be much longer than the output pulse interval.*

There are different types of Q-switching methods; passive and active. In this research active Q-switching was employed but for completeness each type will briefly be reviewed in the forthcoming sections.

7.1.1 *Passive Q-Switching*

Passive Q-switching is a simple concept involving a saturable absorber within the laser cavity. Initially, the high loss introduced by the unsaturated absorber prevents the laser from oscillating leading to the build up of gain. When threshold is reached, the laser field grows until it saturates the absorber. Therefore, the absorber becomes partially transmitting which opens up the cavity allowing the rapid development of an intense pulse [2]. Therefore, it is the laser field itself which essentially switches the cavity into its high Q-state which negates the need for external circuitry. However, a disadvantage of passive Q-switching is that the laser behaviour critically depends on the saturation properties of the gain medium and the saturable absorber, both of which may vary or deteriorate over time. The achievable repetition rate of the Q-switch pulses depends on the recovery time of the gain media and the absorber.

7.1.2 Active Q-Switching

Mechanical Q-switching involves the modulation of the round trip loss in the laser cavity by means of a mechanical device. The modulation can be achieved by a mechanical chopper inserted into the laser cavity or by rotating or tilting one of the cavity mirrors. Although this type of Q-switching is simple and inexpensive, the pulse quality is often poor, the switch time is relatively slow and often the pulses suffer from pulse to pulse jitter.

A non-mechanical, active Q-switching technique based on the Pockels effect is known as electro-optic Q-switching [3]. When an electric field is applied across an optical medium such that the distribution of electrons within it are distorted so that the polarizability and hence the refractive index of the medium changes anisotropically can be described as an elecro-optic effect. Therefore controlling the applied electric field in turn controls the state of polarisation of the laser field. Combining the electro-optic modulator with one or more polarising elements allows this polarisation control to translate into a loss modulation. This type of Q-switching method is fast, effective, reliable and repeatable but it is expensive.

A third method of active Q-switching is known as acousto-optic Q-switching. This again involves electrically controlling the loss in the cavity. In this case an Acousto-Optic Modulator (AOM) driven by a low voltage Radio-Frequency (RF) generator will Bragg-diffract the optical laser beam out of the laser cavity. The amount of energy that is diffracted into the first order beam is dependent on the amount of acoustical power present. Once the population inversion within the cavity has built up to the required value, the power to the RF generator is switched off and the Q-switch action takes place resulting in the Q-switch pulse.

7.2 Polishing Methods

To allow additional Q-switching components to be implemented within the experimental PCF laser cavity, lasing from the fibre end facets must be suppressed. Therefore, before any Q-switching experiments could take place it was necessary to

171

polish the output end of the highly polarised Yb^{3+} doped PCF laser at an angle which would prevent any reflections back into the fibre laser. Various methods of polishing the fibre end were carried out until a successful method was repeatedly implemented.

Due to the holey nature of the complex PCF laser structure the fibre laser was very fragile which led to difficulty during polishing the fibre end. Initially angle cleaving the fibre end was attempted using a Photon Kinetics FK12 [4] fibre angle cleaver which was capable of producing angled ends up to 15°. Although angled ends were achieved, the quality and repeatability of these cleaves were not sufficient to suppress lasing from the fibre end. In an attempt to create a high quality angle cut through the PCF, a diamond saw was used instead of the fibre cleaver. Various methods using the diamond saw were tested including varying the speed of the saw and removing the fibre before switching the saw off to prevent damage to the fibre end due to saw fluctuations. Often the angled cleave produced was of a high standard but only occurred cleanly through ¾ of the fibre. Therefore, to prevent damage occurring after the blade was ¾ of the way through the fibre, the fibre itself was continuously rotated against the rotating saw blade. This technique produced a continuous flat cut by peeling the outer layers of the fibre away until it was fully cleaved. However, on careful examination of the fibre end under a high resolution microscope it was clear that although this method was successful in achieving an angled cleave, the quality of the fibre end facet had been sacrificed.

Manual fibre polishing techniques were also carried out using Thorlabs polishing kits [5] involving different grades of lapping film. However, this method resulted in small pieces of the lapping film becoming blocked in some of the holes in the fibre. Thus, to overcome this problem the holey structure in the fibre needed to be collapsed completely at the fibre end before polishing to prevent blockages in the air holes. The collapse of the air holes was achieved using a splicing machine but this splicing method appeared to weaken the glass unevenly across the cross section of the fibre which prevented the fibre surface from being polished flat.

The successful polishing method employed during this research involved a time consuming and complex process involving the collapse of the fibre air holes using a system originally developed for Laser Heated Pedestal Growth (LHPG). The LHPG system implemented consisted of gold coated copper optics and a Carbon Dioxide (CO_2) laser beam. A reflaxicon transformed the CO_2 laser beam into an annular ring. This annular ring was then reflected off a plain mirror onto a parabolic mirror which focused the beam. The PCF was placed with its end facet at the focal point of the parabolic mirror by using alignment motors in the x, y and z dimension. Next, the CO_2 laser was set to low power and was gradually increased until the fibre end began to glow. Careful control of the laser intensity was critical as too much power caused the air holes in the fibre to form undesirable bubbles. The collapse of the air holes was viewed through a telescope system within the LHPG system.

To obtain the most efficient fusing of the fibre, a shutter was used to pulse the CO_2 laser. This method ensured the fibre was fused with minimum distortion and bubbling. During the pulsing of the laser the fibre was mechanically translated axially though the laser beam which resulted in the collapse of the air holes within the fibre approximately 3mm from the fibre end facet which would facilitate polishing. The next stage in the polishing preparation involved a 6mm outer diameter capillary tube with inner hole diameter of 0.4mm being heated on a hot plate set at $70^{o}C$. This allowed the capillary hole to be filled with Lakeland type 30 molten wax. The fibre was then removed from the LHPG system and was inserted into the capillary tube which was allowed to cool down to room temperature. The wax solidified ensuring the fibre would be securely held in place during the forthcoming polishing process. The non facet end of the fibre within the capillary tube was reinforced using a spring as shown in *Figure 7.2* to prevent the fibre from snapping.
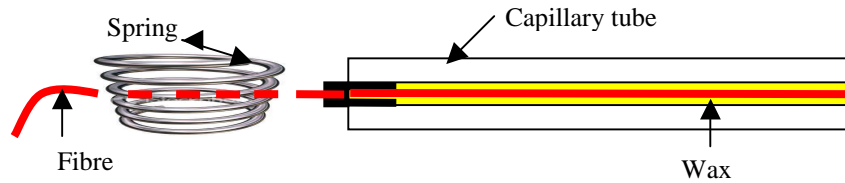
Figure 7.2: Fibre secured in capillary tube with added support provided by spring.

The capillary tube containing the fibre was then secured vertically in a flat mount at an 8° angle and its end was smoothed on a cast iron lapping plate using 20μm of aluminium oxide powder in a water carrier. This lapping process was carried out until a smooth round surface was observed under microscopic examination. Washing the capillary end with distilled water removed any remaining powder particles. The capillary and fibre was then polished, again at an angle of 8°, using a Kemet polishing machine utilising a polyurethane plate and Syton HT50 polishing medium diluted with water. The capillary within the flat mount was set onto the polishing plate and the plate was rotated at 20-30 revolutions pre minute. During rotation, the Syton was dripped onto the polishing plate and the polishing method was repeated as necessary until a smooth flat angled end was achieved, leaving approximately 1.5mm depth of collapsed holes at the fibre end. The end of the capillary tube was then carefully washed using distilled water to remove any Syton residue and it was then dried and further cleaned using methanol and lens tissue. The fibre remained in the capillary tube with spring protection throughout the proceeding Q-switching experiments.

7.3   Q-Switching Experimental Details

Initially the following setup, shown in *Figure 7.3*, was implemented to test if the polished angled end of the PCF laser successfully suppressed the lasing from the fibre end facets. Up to 2m of highly polarised Yb^{3+} doped PCF laser was pumped by up to 10W from the 980nm diode laser. The output from the angled end of the fibre laser was collimated using a 4.5mm focal length lens. A dichroic mirror, highly reflective at 1060nm and highly transparent at the pump wavelength of 980nm, was positioned at an angle of 7° (corresponding to maximum reflection at 1060nm) in the

collimated laser output to separate the pump light from the laser light. A glass plate was used to reflect the output from the fibre laser through a 100mm focal length lens and onto a silicon BPX65 pin photodiode (see **Appendix D**) which was connected to an oscilloscope. The oscilloscope was used for alignment purposes to detect the maximum signal on the BPX65 photodiode whereupon the BPX65 photodiode was disconnected from the oscilloscope and re-connected to an Agilent Technologies E4408B RF spectrum analyser. The RF spectrum analyser was used to detect the beat frequency between the oscillating laser modes.
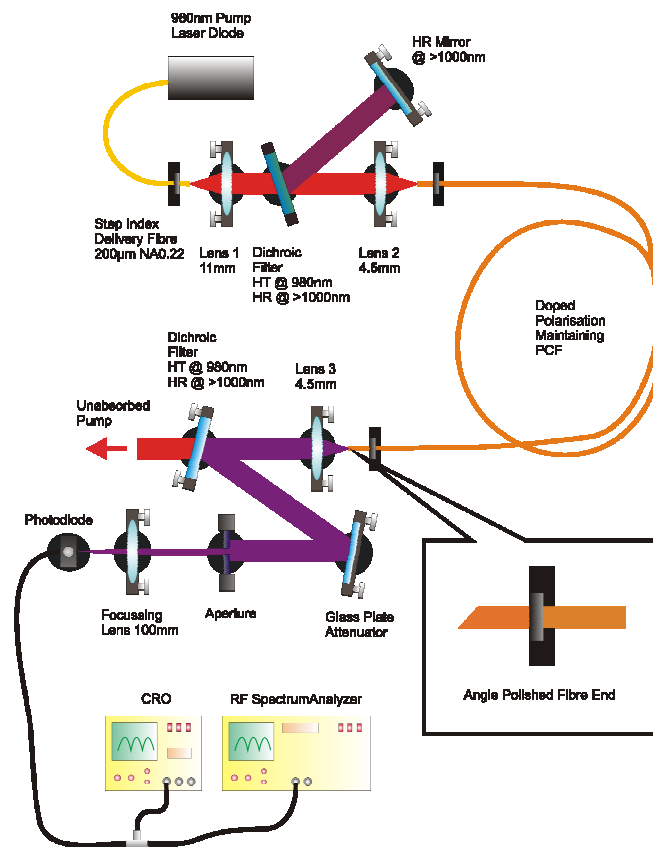
Figure 7.3: *Experimental setup to observe control of lasing when using angled end fibre laser.*

The dichroic mirror used to separate the pump light from the output laser light was then realigned to provide maximum feedback to the fibre laser. The RF spectrum analyser detection system was repositioned to detect the output from the fibre laser at the input pump end. The spectra recorded by both setups is shown in *Figure 7.4.*
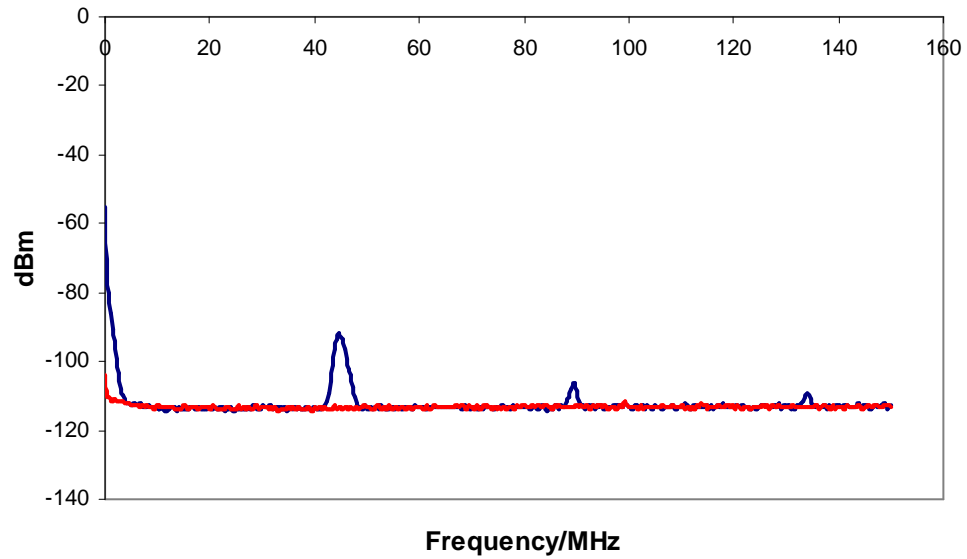
Figure 7.4*: RF spectra recorded for 2m of PCF laser. Blue data represents cavity with mirror feedback, red data represents cavity without mirror feedback.*

The red data shown in *Figure 7.4*, recorded when no feedback mirror completed the cavity, shows that there was no beat frequency detected by the RF spectrum analyser. When the feedback mirror was included in the cavity (represented by the blue data) a beat frequency of 45MHz was measured which corresponds to the value predicted by the mode spacing equation, $\Delta\upsilon = c/2nL$, for a 2m length fibre with the feedback mirror positioned 20cm away from the end of the fibre. The optical spectra from the PCF laser when operating without the feedback cavity mirror was analysed using the experimental arrangement shown in *Figure7.5*.
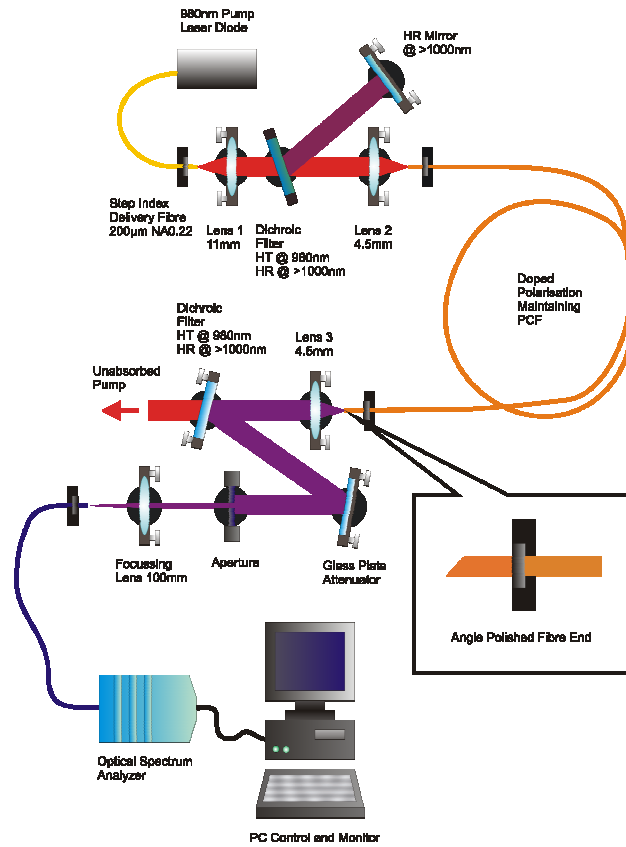
Figure 7.5: *Experimental setup to record optical spectra from PCF laser with angled end when operating without feedback cavity mirror.*

Again, the dichroic mirror used to separate the pump light from the output laser light was realigned to provide maximum feedback to the fibre laser and the RF spectrum analyser detection system was repositioned to detect the output from the fibre laser at the input pump end. The optical spectra obtained using both these setups (with and without feedback) are shown in *Figures 7.6* and *7.7*.
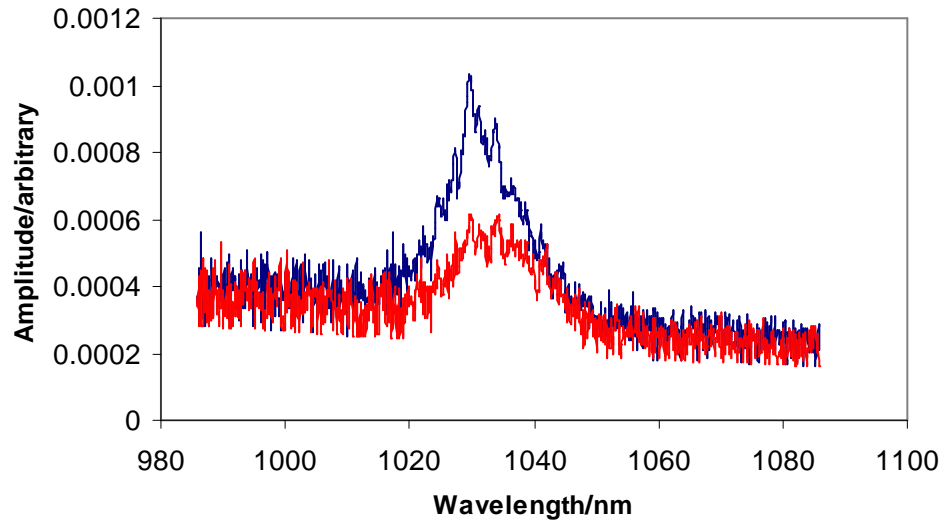
Figure 7.6*: Optical spectra obtained from 2m PCF laser operated without feedback cavity mirror. Red data corresponds to 3.2W input pump power, blue data corresponds to 9.8W input pump power.*
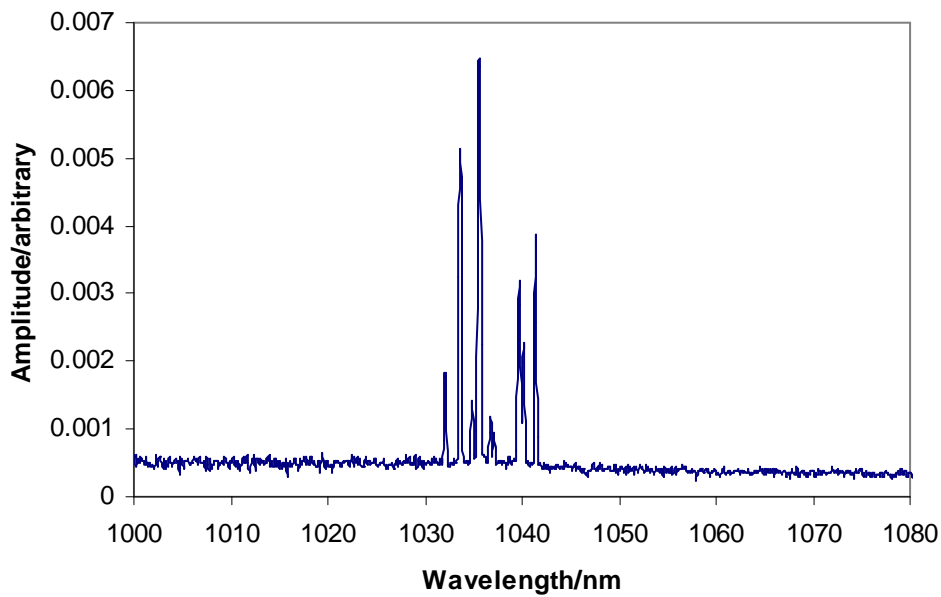
Figure 7.7*: Optical spectrum obtained from 2m PCF laser when operated with feedback cavity mirror positioned 20cm away from angled end of fibre laser.*

The spectra shown in *Figure 7.6* spans from 1020nm to 1045nm. Such wide bandwidth is due to amplified spontaneous emission not stimulated emission. The narrow spectral profile shown in *Figure 7.7,* obtained when including the feedback cavity mirror, confirms that the PCF laser was indeed lasing when the feedback

mirror was implemented and it was not lasing when the feedback mirror was blocked. Thus, the extensive angled end polishing method employed in this research had proven to be a success which allowed Q-switching experiments to be carried out for the first time using this novel highly polarised PCF laser.

As previously described there are various different ways in which to induce Q-switching in a fibre laser. The more conventional way to Q-switch is by using an AOM rather than a mechanical chopper as the chopper method produces poor quality pulses. However, for this application a very high damage threshold AOM was required but unfortunately was not available for use in this research. Therefore, a mechanical chopper placed close to the feedback mirror was implemented as a first stage in demonstrating that the PCF laser was capable of operating as a highly polarised Q-switched PCF laser. These results are shown in *Figure 7.8*.
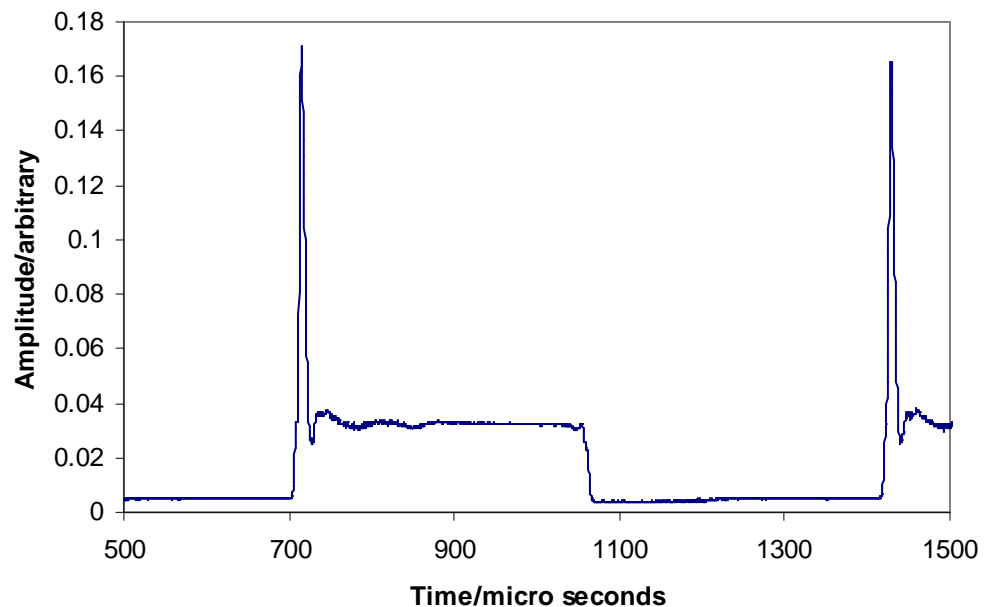
Figure 7.8*: Q-switching results using mechanical chopper.*

The full width half maximum value for the pulses was 8μs with a peak to peak period of 714μs. The elliptical beam width was 3μm by 1μm.

Following on from this simple demonstration of Q-switching, a compact micro-cavity consisting of two fused silica prisms, providing Fresnel reflection feedback, mounted on a piezoelectric controller was planned to replace the mechanical chopper. The purpose of the piezoelectric controller would be to control the Q-switch of the cavity by varying the spacing between the prisms, thus the Fresnel reflection feedback would be modulated. However, during the initial chopper experiments, damage to the fibre end facets due to a large circulating power within the cavity prevented further work from being carried out. This damage could only be repaired by re-cleaving the fibre end and carrying out the long process of collapsing the air holes and re-polishing the fibre end at an angle. Therefore, the micro-cavity Q-switching experiment was not implemented due to the recurring damage to the fibre end facet. This damage is common among high power PCF lasers, amplifiers and Q-switch lasers [6]. It can be avoided by tapering the fibre end and by collapsing the air holes such that the beam expands by up to one order of magnitude before it reaches the end facet. Similarly, coreless end caps made of silica glass can be attached directly to the end of the fibre laser to allow beam expansion before it encounters the end facet.

7.4 Conclusions

A brief overview of Q-switching has been given. The complex and lengthy polishing methods employed during this research to suppress lasing from the fibre end facet, to allow Q-switching experiments to be carried out, has been explained. Mechanical Q-switching of a novel highly polarised Yb^{3+} doped PCF laser has been demonstrated for the first time. Damage to the fibre end facet as a result of intense intracavity power has been highlighted and methods to overcome such damage have been discussed.

7.5 References

[1]   A. E. Siegman, "Lasers", Oxford University Press, 1986

[2]   R. Paschotta, R. Haring, E. Gini, H. Melchior, U. Keller, H. L. Offerhaus, D. J. Richardson, "Passively Q-switched 0.1 mJ fiber laser system at 1.53 μm", Optics Letters, Vol. 24, 1999, (pp388-390)

[3]   J. Hawkes, I. Latimer, "Lasers Theory and Practice", Prentice Hall International Series in Optoelectronics, 1995, Chapter 8

[4]   http://www.dmoptics.co.uk/FK11.htm

[5]   http://www.thorlabs.com/NewGroupPage9.cfm?ObjectGroup_ID=1350

[6]   J. Limpert, F. Roser, T. Schreiber, A Tunnermann, "High-Power Ultrafast Fiber Laser systems", IEEE Journal of Selected Topics in Quantum Electronics, Vol. 12, No. 2, April 2006, (pp233-244)

Chapter 8

Highly Polarised PCF Laser

With Bragg Grating

The focus of this chapter will be the characterisation of a highly polarised Yb^{3+} doped PCF laser which has a fibre Bragg grating written into the novel fibre structure. The self pulsing nature of this laser will be discussed along with pulse suppression techniques that were carried out as part of this research.

8.1 Fibre Bragg Gratings

If a fibre is photosensitive then Bragg reflectors can be created within the core structure by exposing the fibre to Ultra-Violet (UV) light of wavelength between 240nm and 250nm [1]. This UV exposure results in a permanent and periodic change in the refractive index of the fibre core which creates a phase grating that can be used to provide reflection at the Bragg wavelength.

There are several techniques available for creating photosensitive fibre. These include increasing the dopant concentration of germanium in the fibre core, or by co-doping the core with boron. The change in the refractive index of the fibre is typically less than 10^{-4} but this can be increased by hydrogen loading [2]. The process of hydrogen loading involves forcing molecular hydrogen into the core of the fibre by means of high pressure and low temperature diffusions techniques. The phase grating within the fibre core is formed by illuminating the fibre, side on, with a UV laser source as shown in *Figure 8.1*. The coherent UV light source is passed through a silicon phase mask which diffracts the UV light and sets up a standing wave interference pattern resulting in a corresponding periodic change in the refractive index of the fibre core.
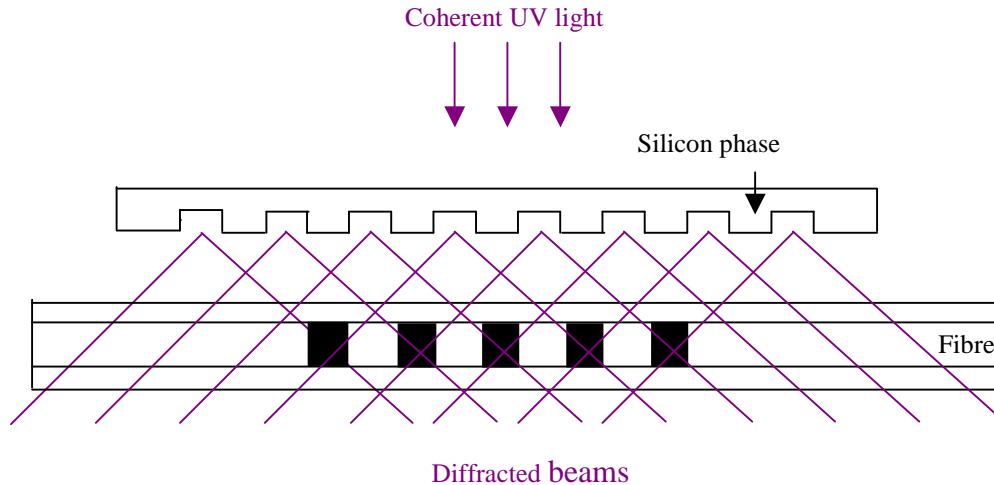
Figure 8.1: Technique used to write Bragg grating into a fibre core.

8.2 PCF Laser Characterisation

Up to 20m of a highly polarised PCF laser with a 75% reflective Bragg grating written into one end of the fibre core was pumped at the Bragg grating end by up to 10W from a LIMO Laser Systems 980nm diode laser (See **Appendix A**). As the dimensions of this PCF laser were the same as those previously stated for the PCF laser characterised in **Chapter 5,** the same coupling optics were implemented. Therefore, we can assume that the coupling efficiency of the pump light into this fibre laser is the same value, 55%, as that already stated. The maximum output laser power from the back end (opposite end from Bragg grating) was measured to be 4.3W. As both ends of the cavity were operating with different output couplers, the output laser power measured at the front end, (the input pump end) where the 75% reflecting Bragg grating was operating was measured to be 200mW. Taking into account that there was approximately 10% of unabsorbed pump power transmitted through the PCF, the internal quantum efficiency of this PCF laser was found to be 91% compared to the 92% theoretical maximum given by the laser and pump photon energies.

An Agilent Technologies HP86140A optical spectrum analyser was used to analyse the output from the back end of the 20m PCF laser.
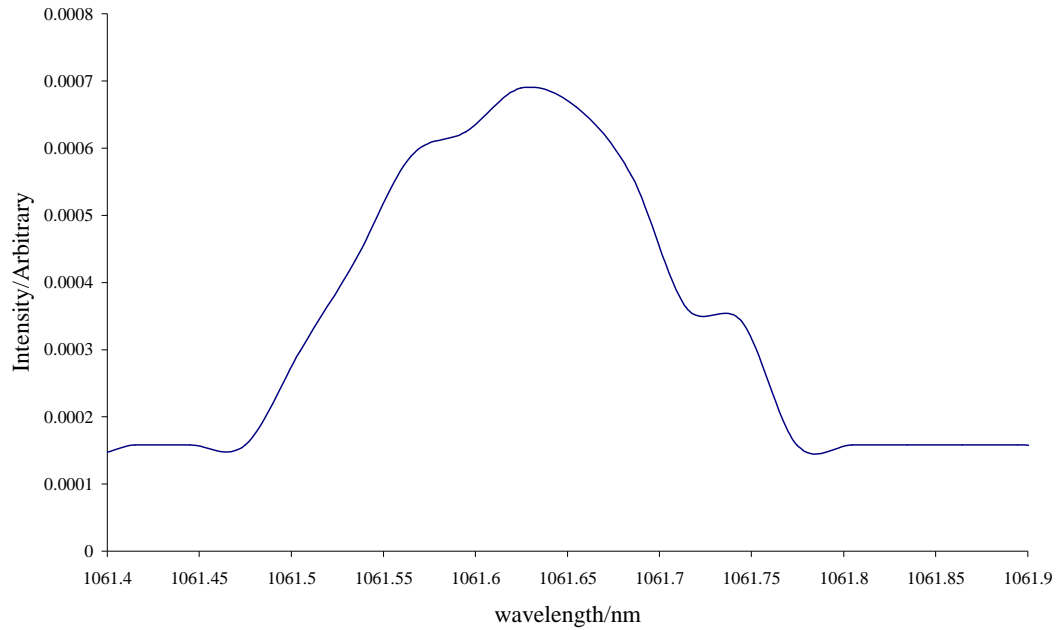
Figure 8.2: *Optical output spectrum from 20m of PCF laser pumped at Bragg grating end by 9.8W 980nm input pump power.*

Figure 8.2 shows that the peak output laser wavelength occurs at 1061.63nm. The FWHM value for the spectra was measured to be 0.17nm using the spectrum analyser with resolution 0.07nm. This lasing wavelength value is expected due to the operating Bragg wavelength of 1061.634nm as stated by Koheras [3], the fibre Bragg manufacturers. The Bragg spectrum recorded by Koheras is shown in *Figure 8.3*.
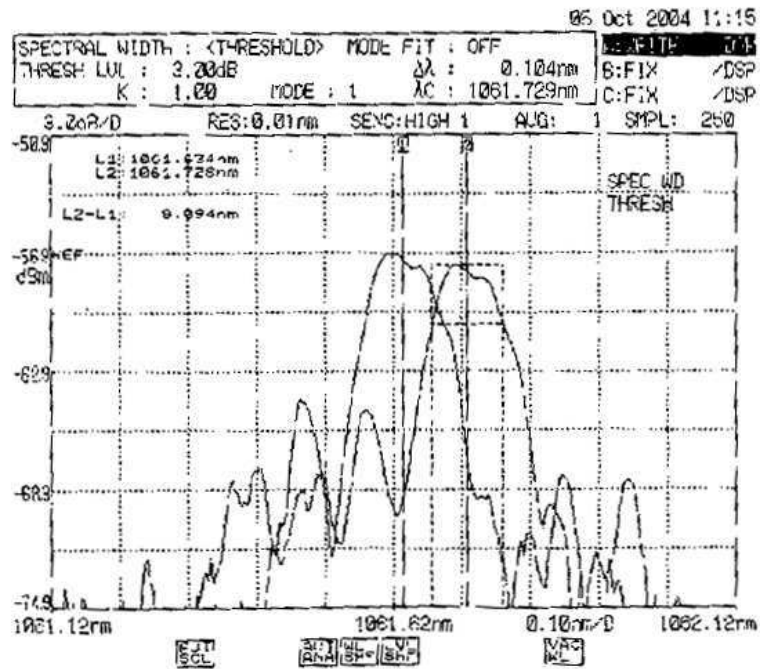
Figure 8.3: *Bragg grating spectrum recorded by Koheras [3].*

The spectrum has been recorded for a 75% reflectivity and has a FWHM of 0.1nm. The centre wavelength is 1061.634nm and it has side lobes -7.5dB at $\pm$ 0.15nm.

It was noted that the output from the PCF laser was not always a continuous wave output. Therefore, the collimated laser output from the back end of the laser was monitored by viewing the stability of the optical output on a fast photodiode connected to an oscilloscope. Before presenting the self-pulsing results observed during this research, an overview of self pulsing will be given.

8.2.1 Self Pulsing

The terms spiking and Relaxation Oscillations (RO) are often used to describe large amplitude pulses that occur when a laser is initially switched on or when the laser is suddenly perturbed by any kind of small fluctuations in gain, cavity loss or cavity alignment [4]. After the initial switch on of the laser it will exhibit a strong spiking response which will quickly decay to a continuous wave output by means of damped quasi-sinusoidal RO. These RO will settle down to a stable continuous wave output if the laser is operated within a quiet and stable environment combined with a stable

power supply. However, if there is a sudden change in the pumping rate or the cavity loss a transient RO will occur. Spiking and RO are characteristic of most solid-state lasers in which the recovery time of the excited state population inversion is substantially longer than the laser cavity decay time. Typical time scales for the period of RO in a solid-state laser is 10μs [4].

To understand the evolution of a single laser spike we must consider the photon number, $n(t)$, in the oscillating laser mode and the population inversion, $N(t)$, during each stage of the pulse formation. These are illustrated in *Figure 8.4*

.
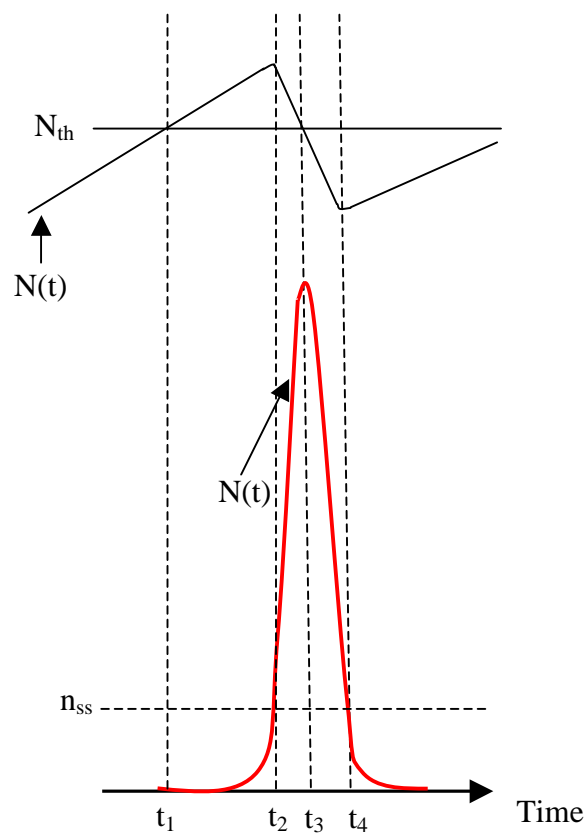
***Figure 8.4**: Laser pulse evolution.*

Figure 8.4 assumes that the pump has been switched on previously allowing for the population inversion, $N(t)$, to build up and reach the threshold value, N_{th}, at time, t_1. At this stage, the photon number, $n(t)$, within the laser cavity is essentially zero. When the population inversion exceeds the threshold point the photon number begins

to increase exponentially as the gain in the cavity now exceeds the loss. When the photon number reaches the steady state oscillation level, n_{ss}, the signal intensity in the cavity begins depleting excited state atoms at a faster rate than the pump can supply them. At this point, the population inversion is unable to continue to grow and is effectively decreased. As the population inversion at this point is still greater than the threshold value, the photon number continues to grow. When the population inversion sufficiently decreases to the threshold value then the gain in the cavity is equal to the loss. It is at this point (t_3) that the photon number reaches its maximum value. As there is still a large signal intensity circulating within the laser cavity, the population inversion continues to decrease below the threshold resulting in the laser gain being less than the cavity losses. This reduction in the gain in turn reduces the photon number to a value below the steady state. This entire process is similar to the theory of Q-switching which was described in the previous **Chapter 7**. The difference being that these RO are characteristic of the laser and are slower, usually in the order of μs, compared to faster (ns) Q-switch pulses. Unlike Q-switch pulses that can be controlled through passive or active means, RO are inherent to the laser and can not be controlled by the same techniques.

In order to suppress such oscillations a loss mechanism which increases with increasing photon number can be included within the cavity. The inclusion of an external feedback loop which combines a photodiode and a loss modulator within the cavity will suppress the pulsing. However, the problem with this concept is the lack of available fast acting optical limiters capable of operating at low threshold and high power parameters. Thus, a simpler solution is to devise a mechanically stable laser operating with a stabilizing power supply in an environment free from acoustic noise and vibrations [4].

Sustained self pulsing is commonly found in three level solid state lasers. Such behaviour has frequently been observed in Er, Tm and Yb fibre lasers particularly when the fibre is not of high quality [5-8]. To date it is not yet agreed which mechanism is dominant in sustained self pulsing in Yb doped fibre lasers [9,10]. Thus, an overview of these hypotheses will be given in this thesis.

In this research it was thought that reabsorption of the laser photons in the unpumped part of the fibre laser was the predominant cause of the sustained self-pulsing. Experimental evidence observed in this research to quantify this hypothesis was that the PCF lasers did not pulse when the fibre length was reduced to around 6m. Whereas longer fibre lengths, where there was weak pumping in the back end of the laser, all experienced self pulsing. Thus, a double pumping scheme was employed to negate the unpumped section at the back end of the highly polarised Yb^{3+} doped PCF with incorporated Bragg grating. The following results show that this pumping scheme was successful in suppressing the self pulsing. Since this research was carried out, Tsang *et al* [11] have also shown that similar self pulsing effects observed in a standard Yb^{3+} doped multimode double-clad fibre laser can be overcome by supplying additional pumping power to the back end of the fibre laser, via a double end pumping scheme. As well as employing the double pumping scheme it was necessary to isolate the PCF laser from vibration and airflow. This was achieved by blocking off the air conditioning vent in the lab and by completely encasing the PCF laser. Operating the PCF laser at night when the air conditioning unit was switched off and the building was free from vibrational noise improved the stability of the laser.

Reabsorption is not the only cause of self pulsing as it has been shown for Er and Tm doped fibre lasers that sustained self pulsing occurs due to clustering of the fibre dopant or the formation of ion pairs [12-16], observed as hot spots in the fibre. When the concentration of the dopant is increased the distance between the ions decreases resulting in the formation of ion pairs. When optically pumped a quenching effect occurs between the two neighbouring ions which results in one of the ions being upconverted and the other transitioning to the ground state. The upconverted ion rapidly decays to the lower lying energy level. This process results in the loss of one potential stimulated photon. Therefore, the quenching effect acts as a dynamic loss mechanism. To avoid the formation of ion pairs a low dopant concentration is advisable. Techniques to suppress self pulsing involves either resonant [6] or auxiliary [7] pumping. Resonant pumping involves pumping the fibre laser with a pump source wavelength close to the fibre lasing wavelength but this

technique will result in a high pump threshold and low internal quantum efficiency. Auxiliary pumping involves two pump sources; the original efficient high power source and a secondary low power pump source operating close to the fibre laser wavelength. The secondary pump source does not significantly affect the overall laser efficiency or low threshold value of the fibre laser. Its purpose is simply to maintain the dopant ions, which are at risk of being depleted from the excited state due to ion clustering, in the excited state.

The interaction between the laser signal and the population inversion can also result in pulsing [17-19]. Sustained self pulsing has detrimental effects on high power Yb^{3+} doped fibre laser output characteristics as the increased peak power reached during the pulsing regime can trigger stimulated Brillouin scattering [9]. Stimulated Brillouin scattering is a nonlinear process that can occur in optical fibres and it manifests itself through the generation of a backwards propagating Stokes wave that carries most of the input power [20]. The combined effects of sustained self pulsing and stimulated Brillouin scattering results in the emission of intense irregular pulses [21-23]. Hideur *et al* [21] has shown that the irregular pulsing associated with the effects of stimulated Brillouin scattering can be avoided in a Yb double-clad fibre laser if a ring cavity configuration is implemented whereby the Brillouin backscattering is suppressed. Alternatively, Ortac *et al* [23] has shown that by favouring a high reflectivity output coupler i.e. a low loss cavity, prevents the detrimental onset of stimulated Brillouin scattering. Also, as the reflected signal from the output coupler is able to be reabsorbed the saturable absorber effects in the cavity are also reduced.

Another method of pulse suppression that has proved successful in Er doped fibre lasers is that of electronically controlled feedback [24]. This involves a controlled feedback system to the pump whereby the pump power is decreased or increases respectively when the output laser intensity detected is increasing or decreasing, respectively.

8.2.2 Results and Pulse Suppression Technique

Figure 8.5 represents the output pulses from the PCF laser observed when varying the pump power.
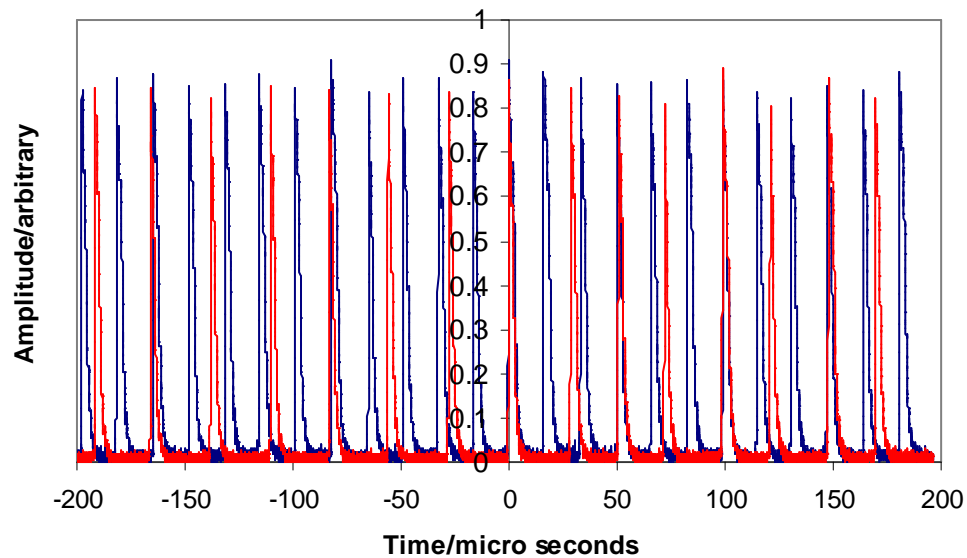
Figure 8.5: *Laser pulsing observed from Bragg grating PCF laser when varying the 980nm pump power. Red data represents 6.3W pump power, blue data represents 9.7W pump power.*

Figure 8.5 illustrates that the pulsing period is dependent on the pump power as increasing the pump power, by approximately 54%, increases the frequency of the pulse train by 66%. Another factor considered which may affect the pulsing was the pump wavelength. Therefore, the temperature of the diode laser was operated between 5°C and 30°C and the corresponding pulse trains were monitored. It was found that increasing the temperature of the laser, which increases the operating wavelength, increased the pulsing instability. Similarly, when decreasing the temperature of the pump, thus decreasing the wavelength, the pulsing observed was reduced leading to a more stable output. These results can be interpreted as a change in the absorption of the pump throughout the fibre length as decreasing the pump wavelength corresponds to a decrease in pump ground state absorption according to the absorption profile for Yb previously shown in **Chapter 2**. Reducing the pump absorption throughout the fibre length leads to an increase in the pump distribution at the tail end of the fibre. By increasing the pump at the tail end, we are effectively reducing any reabsorption loss experienced at the tail end. Thus, if the reabsorption

loss could be reduced then the laser would potentially become more stable. To achieve this without changing the pump wavelength we could reduce the length of the fibre laser. This reduction in fibre length to provide output stability is in agreement with work carried out in **Chapter 5** on the initial PCF laser without the Bragg grating, as that fibre laser did not show any self pulsing behaviour below a length of 6m. Whereas, above 6m the laser did show pulsing tendencies which could only be suppressed by additional feedback to the laser cavity. In the case of the Bragg grating laser, reducing the length of the fibre was not a viable option as this would reduce the output laser power which was desirable for future second harmonic generation experiments. Therefore, in order to increase pump distribution throughout the full length of the fibre a double pumping scheme was employed as shown in *Figure 8.6*.
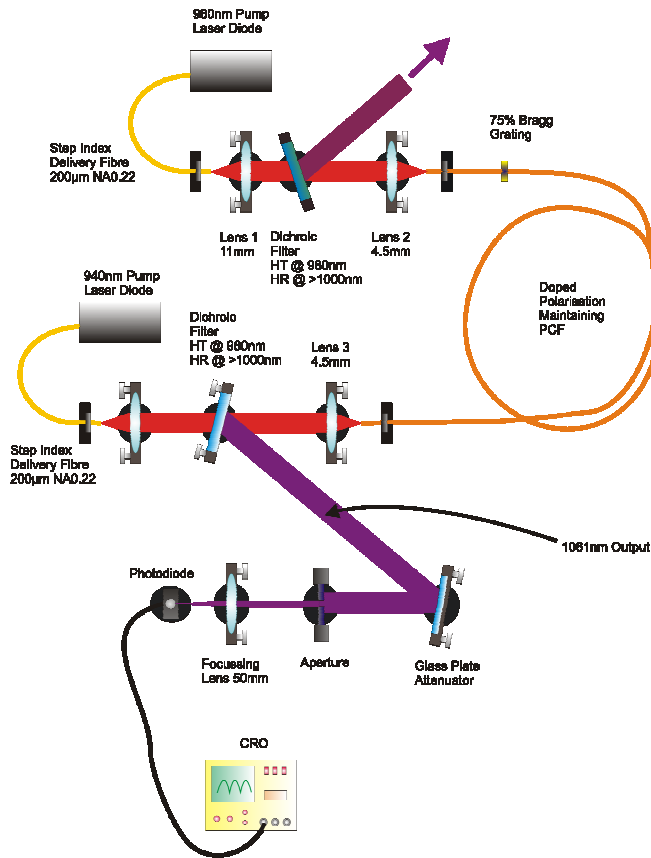
Figure 8.6*: Double pumping setup to suppress pumping. Up to 20m length Highly Polarised PCF laser with incorporated Bragg Grating pumped by up to 10W from 980nm diode laser at Bragg grating end and up to 10W from 940nm diode laser at opposite end.*

Two diode lasers were used to pump the fibre. As there was no other 980nm diode laser available a LIMO Laser Systems 940nm diode laser was used to pump the non-Bragg grating end of the fibre. Both pump lasers were operated at 15$^{\text{o}}$C which each producing output powers of 9.8W. Initially the output power from the 940nm pump laser was characterised as shown in *Figure 8.7.*
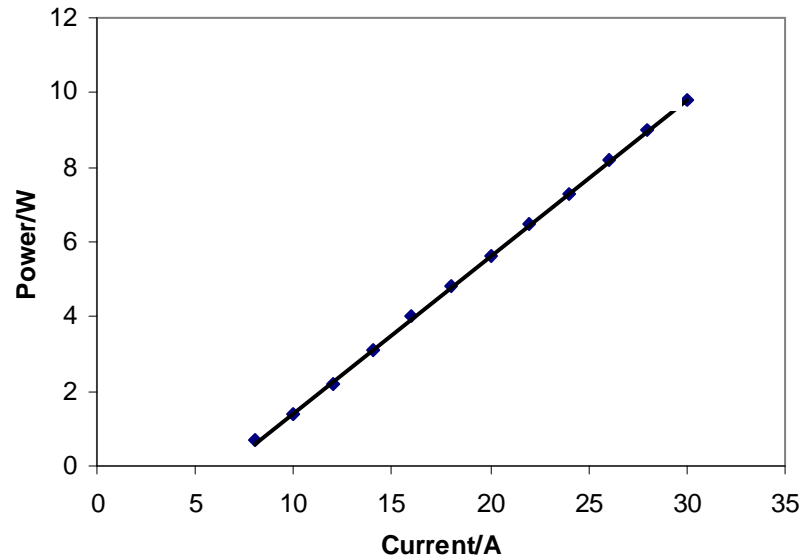
Figure 8.7: Output power characteristics for 940nm diode laser.

Although the 940nm diode pump was capable of producing 9.8W, 0.8W was reflected by the 1060nm HR mirror. Therefore, only 9W 940nm power was available for coupling into the fibre laser. As the coupling optics remained the same the coupling efficiency of 55% obtained when using the 980nm pump was assumed.

The threshold of the PCF laser was measured when double pumping with the 940nm and 980 nm diode lasers, both of which were set to operate with similar output power at each end of the fibre.
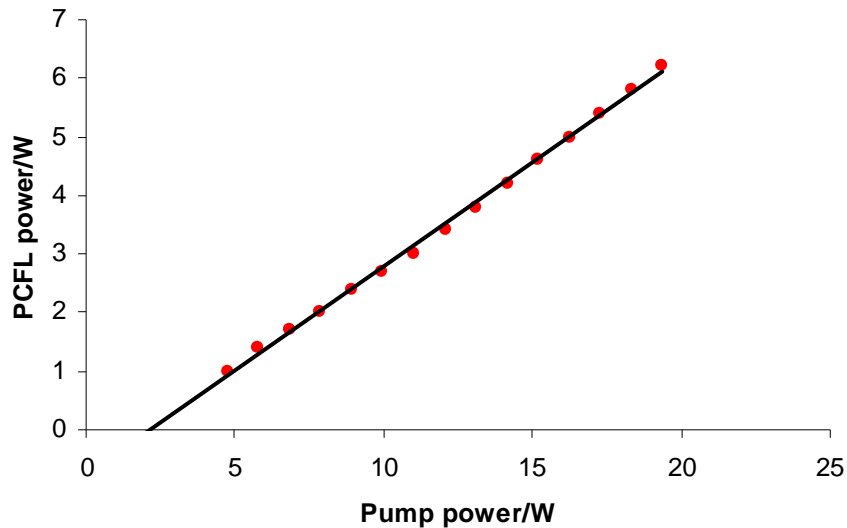
Figure 8.8*: Output PCF laser power as a function of total pump power launched when double pumped with the 940nm and 980nm diode lasers.*

The data shown in *Figure 8.8* does not take into consideration that the coupling efficiency of the pump power into the PCF laser is 55%, nor does it account for approximately 12% of unabsorbed 940nm pump power and 10% unabsorbed 980nm power. Instead, the data shown represents the experimentally measured values for the total pump power launched by the two diode lasers and the output PCF laser power transmitted. The maximum output power obtained when double pumping was employed was found to be 6.2W. This value was increased to 6.8W when fully optimising the coupling of the 940nm pump source into the fibre laser. However, this optimum fibre coupling position was not maintained throughout future experiments as it resulted in a diverging beam.

The spectral output from the PCF laser, when double pumped, was recorded using the optical spectrum analyser.
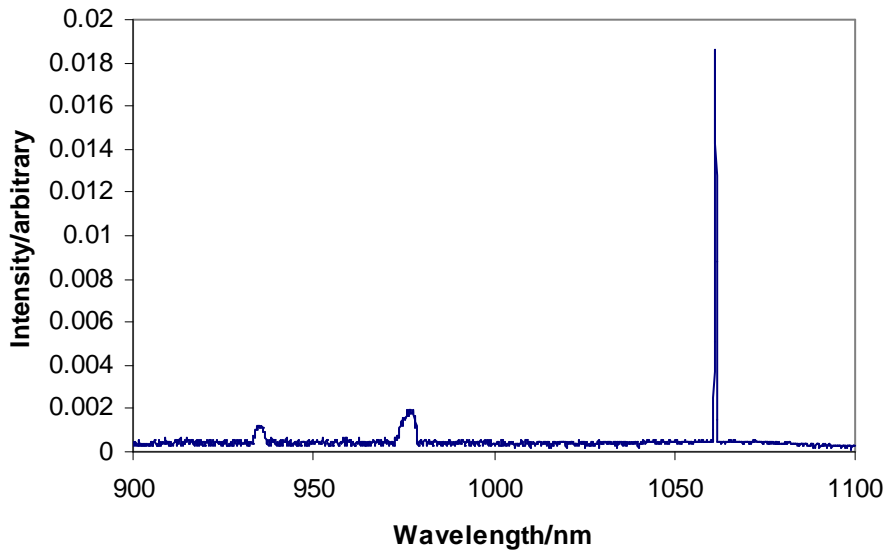
Figure 8.9*: Output optical spectrum from 20m length PCF laser when pumped from both ends, with approximately 9.8W from 980nm diode laser and 9W from 940nm diode laser.*

Figure 8.9 shows that the PCF laser still operates at the lasing wavelength of 1061.63nm when double pumped. The unabsorbed pump power from the 980nm and 940nm diode laser can clearly be seen by the peaks occurring at 978nm and 936nm.

The lasing modes from the PCF laser were recorded at the non-Bragg grating end using the same Agilent Technologies E4408B RF spectrum analyser used in **Chapter 5**. *Figure 8.10* represents the RF spectrum recorded for approximately 19m PCF laser when double pumped.
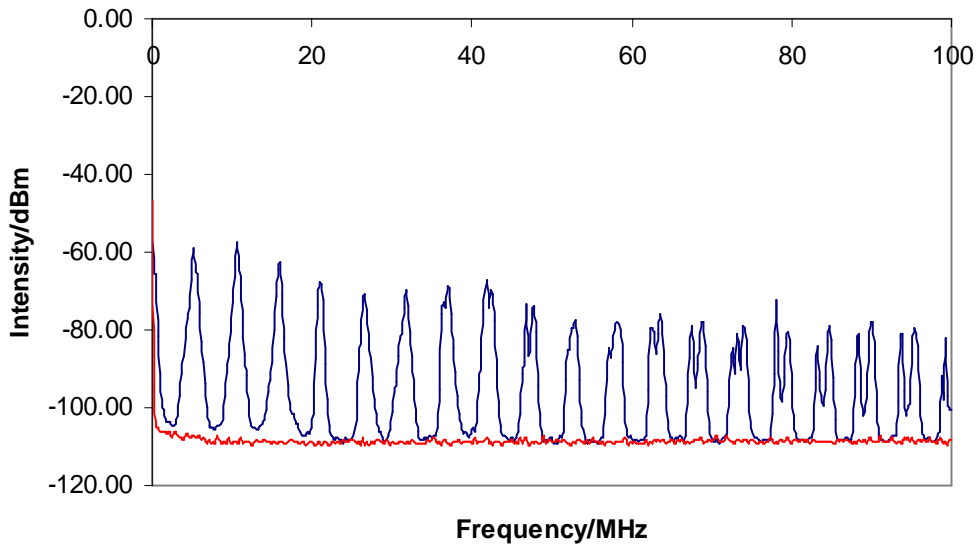
Figure 8.10*: RF spectrum recorded for 19m length PCFL double pumped by 980nm and 940nm diode lasers. (Red data represents the background spectrum of the photodiode when the PCF laser was not operating)*

The beat frequency occurs at 5.25MHz which is expected for this length of fibre based on the mode spacing equation. The secondary beat frequency observed is due to the 4% Fresnel reflection from the fibre end facet closest to the Bragg grating. This end facet was approximately 35cm away from the Bragg grating, thus, there were always two reflections at the pump end of the fibre one from the 75% Bragg grating itself and one from the 4% Fresnel reflection at the fibre end. This Fresnel reflection could have been suppressed by angle polishing the end facet but this option was ruled out due to the high risk of damage to the fibre or Bragg grating during polishing.

With the double pumping setup, the output from the laser was monitored using a fast photodiode connected to an oscilloscope. The nature of the pulsing was recorded when pumping solely with the 980nm diode laser, the 940nm diode laser and then with both the 980nm and 940nm diode lasers combined. The self pulsing nature of the PCF laser was irregular and not repeatable. *Figures 8.11-8.17* is a sample of the self pulsing observed.

196
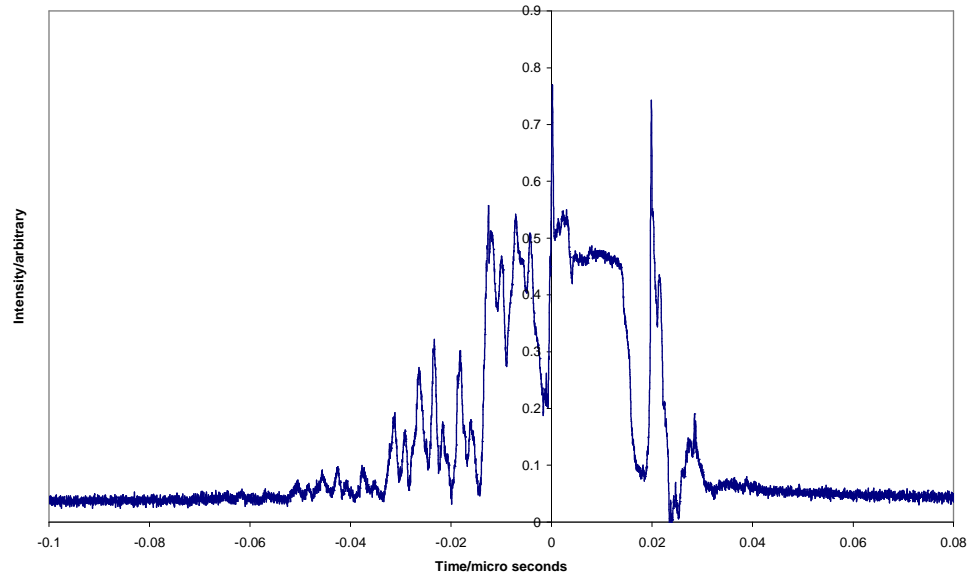
Figure 8.11: *Output pulse recorded when pumped by 9.8W from 980nm diode laser.*
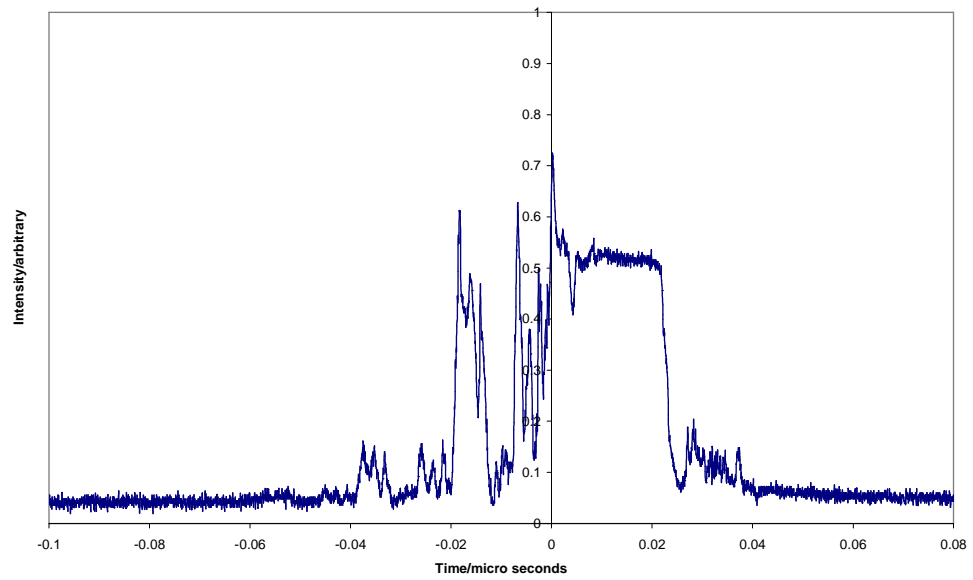
Figure 8.12: *Output pulse recorded when pumped by 9.8W from 980nm diode laser.*

197
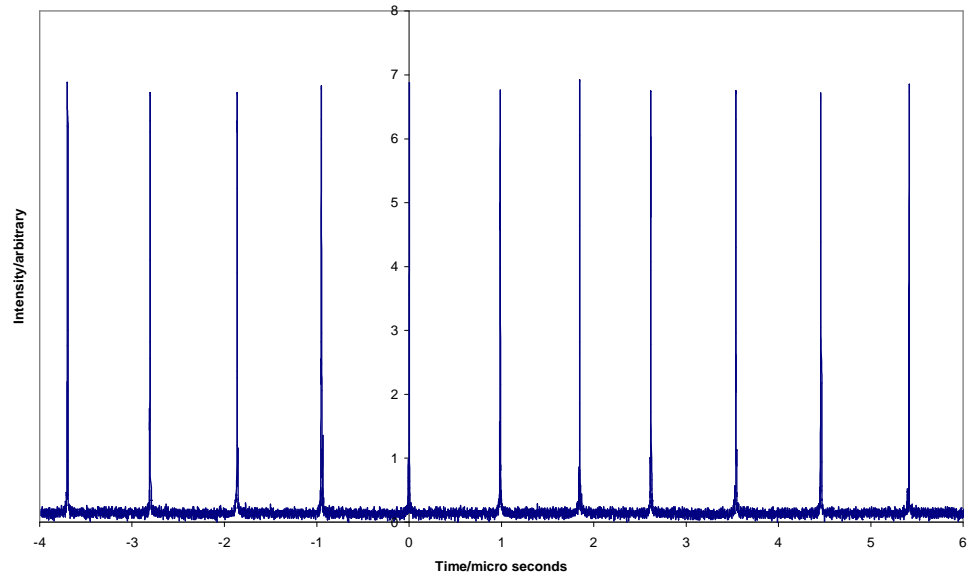
Figure 8.13: *Output pulse recorded when pumped by 9.8W from 980nm diode laser.*
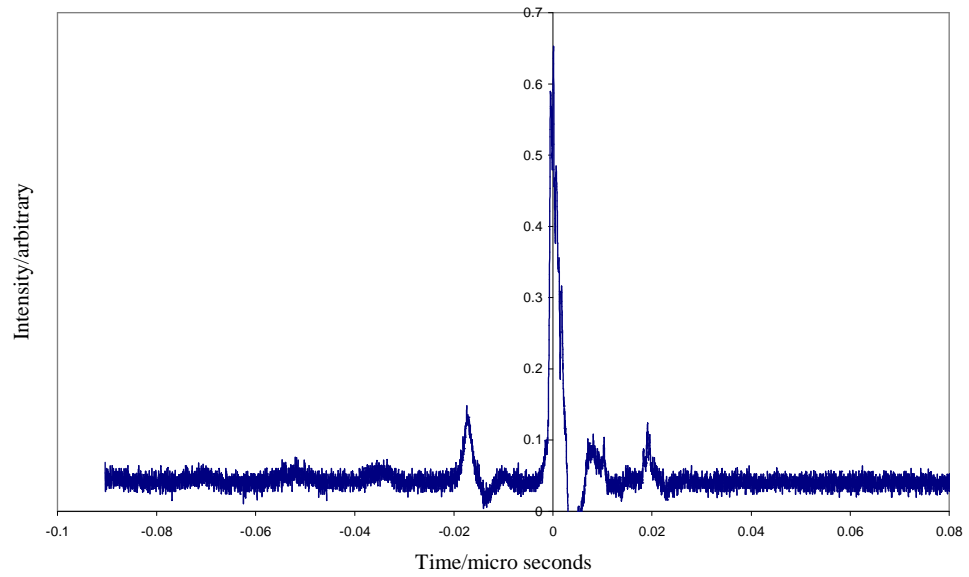
Figure 8.14: *Output pulse recorded when pumped by 9.8W from 940nm diode laser.*
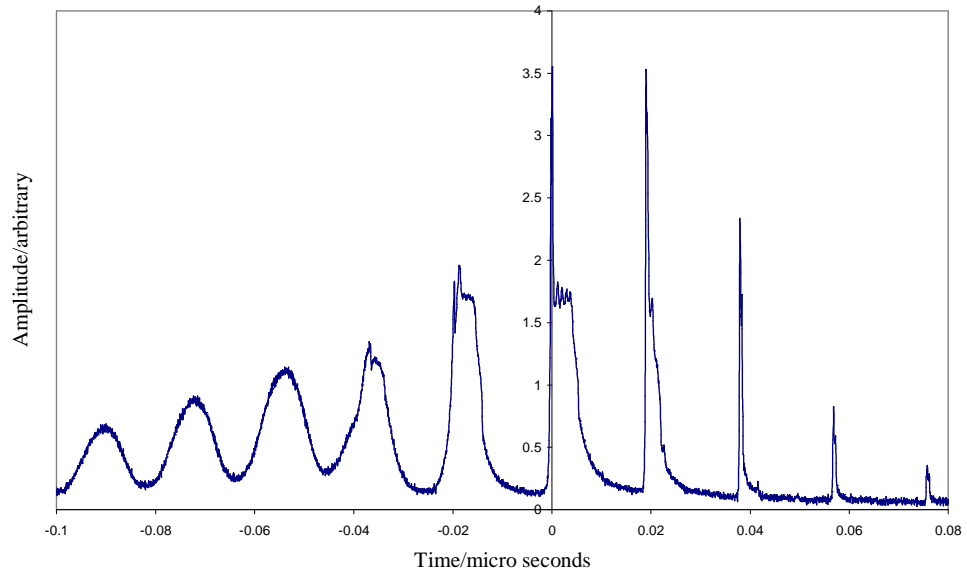
Figure 8.15*: Output pulse recorded when pumped by 9W from 940nm diode laser.*
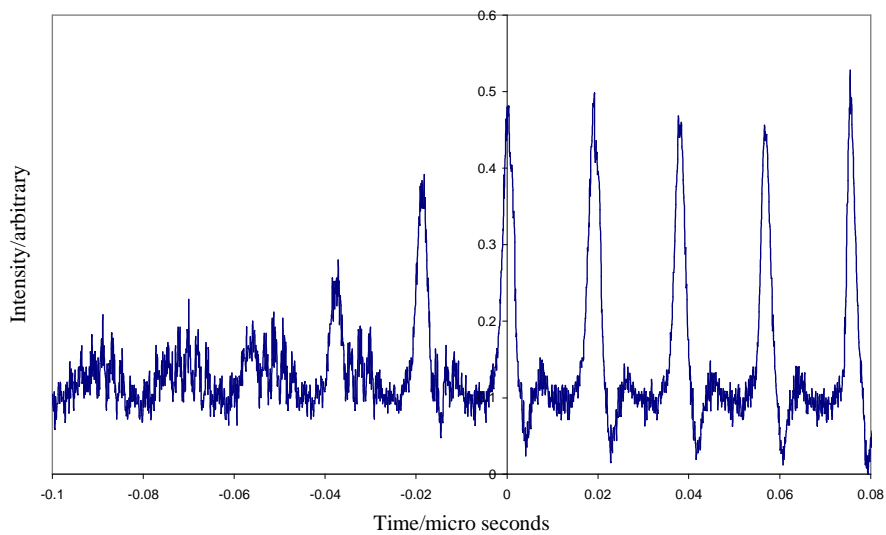
Figure 8.16*: Output pulse recorded when pumped by 9W from 940nm diode laser.*

Figures 8.11-8.16 show that the PCF laser operated in an extreme self pulse regime when single pumped. When double pumping the PCF laser, the output was CW rather than pulsed as shown in *Figure 8.17*.
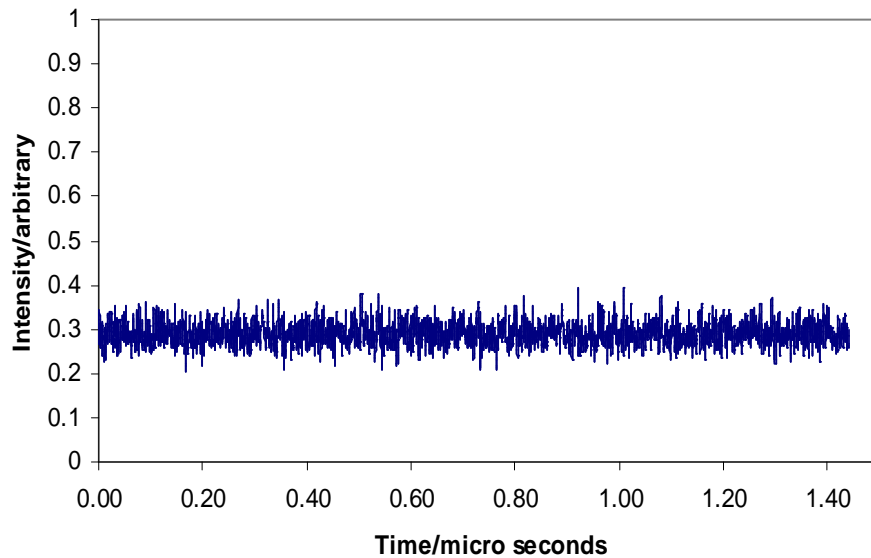
Figure 8.17*: CW output recorded when pumping with 9.8W from 980nm diode laser at Bragg grating end and 9W from 940nm diode laser at opposite end. Spectrum was recorded at night with full optical bench covered.*

As environmental instability or sudden change in cavity losses are known to cause self pulsing, all attempts to isolate the fibre laser from such instability were carried out. The entire fibre laser system was isolated from air flow by housing it under a cover which spanned the entire dimensions of the optical bench. Further reduction in vibration and air flow was achieved by partially sealing the air conditioning vents in the laboratory and by operating the laser at night at which time the air conditioning was off and the vibrational noise level throughout the building was greatly reduced. Such precautions were necessary as without them the PCF laser still showed tendencies to self pulse despite being double pumped. Thus, the CW output shown in *Figure 8.17* was achieved by double pumping at night when full environment stability measures were in place.

A major part of this research involved trying to stabilise the output from the fibre laser. Despite achieving stabilisation by the methods described, the stability in the laser output and the output laser power was observed to slowly decrease throughout its three year life span. This deterioration in stability and efficiency coincided with the appearance of more intense hot spots throughout the length of the fibre which could be due to clustering of the fibre dopant which is known to cause self pulsing in

three level laser systems [13,14]. The underlying physical process for this degradation could be attributed to the formation of colour centres or other photoinduced structural transformations in the silica glass host as a result of prolonged exposure to high power [11].

8.3   Conclusions

A highly polarised Yb^{3+} doped PCF laser operating at 1061.6nm with incorporated 75% Bragg grating written into the fibre core has been characterised. Self-pulsing within rare-earth doped fibre lasers has been discussed leading to the successful suppression of self-pulsing within this PCF laser system. CW operation was achieved by ensuring environment stability and by double end pumping the PCF laser to overcome reabsorption loss.

8.4 References

[1]   J. Wilson, J. Hawkes, "Optoelectronics an introduction", Prentice Hall third edition, 1998, Chapter 8

[2]   P. J. Lemaire, R. M. Atkins, V. Mizrahi, W. A. Reed, "High pressure H_2 loading as a technique for achieving ultrahigh photosensitive and thermal sensitivity in GeO_2 doped optical fibres", Elect. Lett., Vol. 29, 1993, (pp1191-1193)

[3]   Koheras A/S, Blokken 84, DK-3460 Birkerød, Denmark

[4]   A. E. Siegman, "Lasers", Oxford University Press, 1986, Chapter 25

[5]   P. Le Boudec, C. Jaouen, P. L. Francois, J. F. Bayon, F. Sanchez, P. Besnard, G. Stephan, "Antiphase dynamics and chaos in self-pulsing erbium-doped fiber lasers", Optics Letters, Vol. 18, No. 22, 1993, (pp1890-1892)

[6]   W. H. Loh , "Suppression of self-pulsing behaviour in erbium doped fiber lasers with resonant pumping", ,Optics Letters, Vol. 21, No. 10, 1996, (pp734-736)

[7]   L. Luo, P. L. Chu, "Suppression of self-pulsing in an erbium-doped fiber laser", Optics Letters, Vol. 22, No. 15, 1997, (pp1174-1176)

[8]   D. Amroun, A. Kellou, K. AIT Ameur, V. Dupray, F. Sanchez, "Suppression of self-pulsing in Er-doped fibre lasers with electronic control", Journal of Modern Optics, Vol. 47, No. 7, 2000, (pp1247-1252)

[9]   F. Brunet, Y. Taillon, P. Galarneau, "A Simple Model Describing Both Self-Mode Locking and Sustained Self-Pulsing in Ytterbium-Doped Ring Fiber Lasers", Journal of Lightwave Technology, Vol. 23, No. 6, 2005, (pp2131-2138)

[10]   J. Li, K. Ueda, M. Musha, A. Shirakawa, "Residual pump light as a probe of self-pulsing instability in an ytterbium-doped fiber laser", Optics Letters, Vol. 31, No. 10, 2006, (pp1450-1452)

[11]   Y. H. Tsang, T. A. King, D. K. Ko, J. Lee, "Output dynamics and stabilisation of a multi-mode double-clad Yb-doped silica fibre laser", Optics Communication, Vol. 259, 2006, (pp236-241)

[12]   S. Colin, E. Contesse, P. Le Boudec, G. Stephan, F. Sanchez, "Evidence of a saturable-absorption effect in heavily doped erbium-doped fibers", Opt. Lett., Vol. 21, 1997, (pp1174-1176)

[13]   M. Ding, P. K. Cheo, "Dependence of Ion-Pair Induced Self-Pulsing in Er-Doped Fiber Lasers on Emission to Absorption Ratio", IEEE Photonics Technology Letters, Vol. 8, No. 12, 1996 (pp1627-1629)

[14]   P. Le Boudec, P. L. Francois, E. Delevaque, J. F. Bayon, F. Sanchez, G. M. Stephan, "Influence of ion pairs on the dynamical behaviour of Er^{3+}-doped fibre lasers", Optical and Quantum Electronics, Vol. 25, No. 8, 1993, (pp501-507)

[15]   P. Le Bopudec, P. L. Francois, G. Stephan, "Effects of ion pairs on the dynamics of erbium-doped fiber lasers", Phys. Rev. A., Gen. Phys., Vol. 48, 1993, (pp2220-2229)

[16]   S. D. Jackson, T. A. King, "Dynamics of the output of heavily Tm-doped double-clad silica fiber lasers", J. Opt. Soc. Amer. B, Opt. Phys., Vol. 16, 1999, (pp2178-2188)

[17]   M. Dinand, C. Schutte, "Theoretical modelling of relaxation oscillations in Er-doped waveguide lasers", Journal of Lightwave Technology, Vol. 13, No. 1, 1995, (pp14-23)

[18]   R. Rangel-Rojo, M. Mohebi, "Study of the onset of self-pulsing behaviour in an Er-doped fiber laser", Optics communications, Vol. 137, 1997, (pp98-102)

[19]   S. S. Jackson, "Direct evidence for laser reabsorption as initial cause for self pulsing in three-level fiber lasers", Electron. Lett., Vol. 38, 2002, (pp1640-1642)

[20]   G. P. Agrawal, Nonlinear Fiber Optics, Fourth Edition", Elsevier Inc., 2007

[21]   A. Hideur, T. Chartier, C. Ozkul, F. Sanchez, "Dynamics and stabilization of a high power side-pumped Yb-doped double-clad fiber laser", Opt. Comm., Vol. 186, 2000, (pp311-317)

[22]   M. Salhi, A. Hideur, T. Chartier, M. Brunel,, G. Martel, C. Ozkul, F. Sanchez, "Evidence of Brillouin scattering in an ytterbium doped double-clad fiber laser", Opt. Lett., Vol. 27, 2002, (pp1204-1296)

[23]   B. Ortac, A. Hideur, T. Chartier, M. Brunel, G. Martel, M. Salhi, F. Sanchez, "Influence of cavity losses on stimulated Brillouin scattering in a self-pulsing side-pumped ytterbium-doped double-clad fiber laser", Opt. Comm., Vol. 215, 2003, (pp389-395)

[24]   D. Amroun, A. Kellou, K. Ait Ameur, V. Dupray, F. Sanchez, "Suppression of self-pulsing in Er-doped fibre lasers with electronic control", Journal of Modern Optics, Vol. 47, No. 7, 2000, (pp1247-1252)

[25]   J. J. Koponen, M. J. Soderlund, H. J. Hoffman, S. K. T. Tammela, "Measuring photodarkening from single-mode ytterbium doped silica fibers", Optics Express, Vol. 14, No. 24, 2006, (pp11539-11544)

Chapter 9

Conclusions and Future Work

This concluding chapter will summarise the work presented in the previous chapters of this thesis and will discuss the foreseen direction of the relevant future work.

9.1   Conclusions

This thesis presents the first demonstration and characterisation of a double cladding highly polarised Yb^{3+} doped PCF laser. The PCF laser had fibre attenuation of 0.48dBm^{-1}, operating wavelength between 1020nm and 1080nm depending on fibre length and internal quantum efficiency of 77%. The PCF structure was not yet fully optimised leading to a loss of light from the core to the cladding which resulted in 79% of the light being carried by the core. 2.9W of highly polarised output carried by the core with polarisation ratio in excess of 200:1 was demonstrated. The laser had an elliptical fundamental mode profile with $1/e^2$ radii 3μm by 6μm with M^2 values 1.72 and 2.8. A numerical model, developed as part of this work, to investigate the power characteristics and polarisation properties of PCF lasers confirmed that the novel highly polarised PCF laser in this research had a core to cladding loss of 0.05Wm^{-1}. As the laser exhibited this loss, numerical mode modelling was carried out to determine the optimum PCF structure that would minimise this loss of light from the core to the cladding. The mode modelling predicted that the experimental PCF laser could be optimised by increasing the small air hole radii to 2.5μm, reducing the larger air hole diameters to 3.6μm and by reducing the pitch of the air holes to less than 7μm.

Following on from this work a double cladding highly polarised Yb^{3+} doped PCF laser operating at 1061.6nm with incorporated 75% Bragg grating written into the fibre core was demonstrated and characterised for the first time. Self-pulsing within

rare-earth doped fibre lasers was discussed leading to the successful suppression of self-pulsing within this PCF laser system. 6.5W of CW operation was achieved by ensuring environment stability and by double end pumping the PCF laser with a LIMO Laser Systems 940nm and a 989nm diode laser to overcome reabsorption loss.

Second harmonic generation using non-critical, temperature tuned phase matching of a bulk 15mm LBO crystal was demonstrated using the double cladding highly polarised Yb^{3+} doped PCF laser for the first time. The maximum second harmonic light generated, from 2.8W 1080nm fundamental power, during a single pass of the crystal was 0.8mW. 1.07mW second harmonic generation was then demonstrated using 6.5W from a 1061nm double cladding highly polarised Yb^{3+} doped PCF laser with 75% incorporated Bragg grating. Double passing the second harmonic light through the crystal was carried out which produced 3.2mW of second harmonic which is a factor of 3 increase in conversion compared to the single pass experiment. The experiment demonstrates that if you have an integer number of passes, n, through the nonlinear crystal then the intensity of the second harmonic light generated will increase by a factor of n^2. Quasi-phase matching using a PPLN crystal produced 2.3mW of 530nm second harmonic light. Throughout all of the frequency doubling experiments the detrimental self-pulsing nature of the pump laser damaged the crystals and filters implemented which severely limited power optimisation.

Fibre end facet angle polishing methods were explored and the successful suppression of stimulated emission from the highly polarised PCF laser end facet was achieved leading to the first demonstration of Q-switched operation from the novel highly polarised PCF laser.

The work presented in this thesis was published in Optics Express [1], reviewed by Hecht [2], featured in Photonics Spectra [3], formed the basis of an oral presentation at the QEOD Europhoton Conference [4], featured as a poster presentation at the 17th International Laser Spectroscopy Conference [5] and won a poster prize at the NKT summer academy conference [6].

9.2   Future Work

Based on the mode modelling results, from this thesis, a new PCF structure could be produced to prevent the power loss from the core to the cladding. More sophisticated modelling software would be required to optimise the PCF structure such that the polarisation maintaining properties of the PCF laser were also optimised. It would be advantageous if the 75% Bragg grating incorporated in the highly polarised PCF laser, positioned 35cm from the fibre end facet, was replaced by a 100% Bragg grating directly at the fibre end facet. A more practical and less time consuming way of collapsing and angle polishing the air holes in the PCF laser could be developed by using specialised equipment which would enable further Q-switching and mode-locking experiments to be carried out leading to a compact Q-switched or mode-locked highly polarised laser source.

Using the highly polarised PCF structure contained in this thesis, Chen *et al* [7] proposed in 2009 an improved design to optimise the polarisation properties of the fibre. However, no one has yet translated these improvements into a highly polarised PCF laser. Except for the work contained in this thesis no one has produced such polarisation maintaining PCF laser structures through form birefringence alone.   The direction of the research field is towards high power laser sources. Such optimised PCF, structures contained in this thesis, have the capabilities of becoming efficient, compact, economical and high power polarisation maintaining laser sources with the option of Q-switched, mode-locked of frequency doubled operation.

9.3 References

[1]   F. C. McNeillie, E. Riis, J. Broeng, J. R. Folkenberg, A. Petersson, H. Simonsen, C. Jacobsen, "Highly polarised photonic crystal fiber laser", Optics Express, Vol. 12, No. 17, 2004, (pp3981-3987)

[2]   J. Hecht, "Fiber lasers take off in diverse directions", Laser Focus World, http://www.laserfocusworld.com/display_article/218558/12/ARCHI/none/Feat/Fib

[3]   F. C. McNeillie, E. Riis, B. Hitz, "Photonic crystal fiber laser is highly polarized", Photonics Spectra, 2004, (pp92-94)

[4]   F. C. McNeillie, "Highly polarised photonic crystal fibre laser", QEOD Europhoton Conference, Switzerland, 2004

[5]   F. C. McNeillie, "Highly polarised photonic crystal fibre laser", The 17th International Laser Spectroscopy Conference, Aviemore, Scotland, 2005

[6]   F. C. McNeillie, "Highly polarised photonic crystal fibre laser", NKT Summer Academy Conference, 2006

[7]   M. Y. Chen, Y. K. Zhang, "Improved design of polarisation-maintaining photonic crystal fibers", Optics Letters, Vol. 33, No. 21, 2008, (pp2542-2544)

Appendix A

LIMO FB Series (pump)
Version July 16, 2009
HIGH-POWER DIODE LASER

LIMO
Lissotschenko Mikrooptik

- High brightness laser for, pump applications
- SMA905 Plug & Play connector for optical fibres
- Compact dimensions
- Passively cooled
- Dual temperature sensor (NTC/PT100)
- Optional monitor diode

Optical data[1]

CW – nominal output power (W)	30	35	32	40
Centre wavelength λ (nm)	805-810, 880, 888, 915, 940, 975-981[2]			
Tolerance of λ (nm)	± 3 (± 2)[4]			
Spectral width (FWHM) (nm)	< 4			
Temperature drift of λ[4] (nm/K)	~0.3, ~0.35, ~0.4			

Fibre data

Fibre core diameter (µm)	200		400	
Numerical aperture	0.22			
Fibre-optic connector	SMA905			

Electrical data

Typical operation current (start of lifetime) (A)	40	45	40	50
Max. Operation current (start of lifetime) (A)	43	48	43	53
Max. Operation current (end of lifetime) (A)	52	58	52	64
Typical threshold current (A)	5 - 8			
Typical efficiency (%)	42	43	44	44
Typical slope efficiency (W/A)	0.7 - 1.0			
Operation voltage (V)	< 2			
Reverse voltage	0			

Thermal conditions

Diode heat sink temperature[5] (°C)	+15....30			
Storage temperature (°C)	-20....+60			
Recommended heat sink capacity (W)	> 64	> 70	> 62	> 76
Recommended heat sink thermal resistance (K/W)	< 0.1			

Other specifications

Expected lifetime[6] (hours)	20,000
RoHS 2002/95/EC and CE compliant	YES
Dimensions of laser head (connectors not included) (mm)	75x25x18
Weight (g)	300

[1]Optical data @ 25°C diode heat sink temperature, [2]Other wavelength on request, [3]optional, [4]Depending on wavelength, [5]Measured by NTC/PT100 at temperature measurement hole in the diode heat sink (defined in drawing), [6]According ISO 17526:2003(E);

Optional
Monitor diode

Operation voltage (V$_{DC}$)	5
Monitor diode signal (V)	0-2

Appendix B

Second harmonic generation in Lithium Triborate (LBO) for Yb:doped PCF

Includes calculation of refractive indices, phasematching temperature, optimum crystal length

References:

Lithium Triborate (LBO): Sellmeier's, dispersion of thermo-optic coeffs.

Data from "Temperature dispersion of refractive indices in β-BaB$_2$O$_4$ and LiB$_3$O$_5$ crystals for nonlinear optical devices", J. App. Phys., Vol. 78, No. 11, 1995 (pp52-6760)

G. McConnel, "Nonlinear Optical Frequency Conversion of mode locked all solid state lasers", University of Strathclyde, 2001

Physical constants and units

$$nm := 10^{-9} \cdot m$$

$$\mu m := 10^{-6} \cdot m$$

$$mm := 10^{-3} \cdot m$$

$$cm := 10^{-2} \cdot m$$

$$A \equiv 10^{-10} \cdot m$$

$$c := 3 \cdot 10^8 \cdot \left(m \cdot \sec^{-1} \right)$$

$$\varepsilon_0 := 8.854 \cdot 10^{-12} \cdot \frac{farad}{m}$$

$$TOL := 0.000000000000000000000$$

Calculation of refractive indices

Wavelength range
(Transparency region)

$$\lambda := 2000 \cdot A, 2010 \cdot A .. 12000 \cdot A$$

The room temperature Sellmeier coeffs.

$$Ax := 1.4426279$$

$$Bx := 1.0109932$$

$$Cx := 1.1210197 \cdot 10^{-2}$$

$$Dx := 1.2363218$$

$$Ay := 1.5014015$$

$$By := 1.0388217$$

$Cy := 1.2157100 \cdot 10^{-2}$

$Dy := 1.7567133$

$Az := 1.4489240$

$Bz := 1.1365228$

$Cz := 1.1676746 \cdot 10^{-2}$

$Dz := 1.5830069$

$E := 91$

$$n_x(\lambda) := \left[Ax + \frac{Bx}{1 - \dfrac{Cx}{\left(\dfrac{\lambda}{A \cdot 10000}\right)^2}} + \frac{Dx}{1 - \dfrac{E}{\left(\dfrac{\lambda}{A \cdot 10000}\right)^2}} \right]^{\frac{1}{2}}$$

$$n_y(\lambda) := \left[Ay + \frac{By}{1 - \dfrac{Cy}{\left(\dfrac{\lambda}{A \cdot 10000}\right)^2}} + \frac{Dy}{1 - \dfrac{E}{\left(\dfrac{\lambda}{A \cdot 10000}\right)^2}} \right]^{\frac{1}{2}}$$

$$n_z(\lambda) := \left[Az + \frac{Bz}{1 - \dfrac{Cz}{\left(\dfrac{\lambda}{A \cdot 10000}\right)^2}} + \frac{Dz}{1 - \dfrac{E}{\left(\dfrac{\lambda}{A \cdot 10000}\right)^2}} \right]^{\frac{1}{2}}$$

Temperature Range (deg. C)

$T := 20, 20.1 .. 300$

$\lambda_{igx} := 0.053 \cdot \mu m$

Isentropic Band Gaps / μm

$\lambda_{igy} := 0.0327 \cdot \mu m$

$\lambda_{igz} := 0.0435 \cdot \mu m$

Normalised Dispersive Wavelengths

$$R_x(\lambda) := \frac{\lambda^2}{\lambda^2 - \lambda_{igx}^2}$$

$$R_y(\lambda) := \frac{\lambda^2}{\lambda^2 - \lambda_{igy}^2}$$

$$R_z(\lambda) := \frac{\lambda^2}{\lambda^2 - \lambda_{igz}^2}$$

Fitting Coeffs.

$G_x := -127.70167 \cdot 10^{-6}$

$G_y(T) := \left[\left(372.170 - 2.199 \cdot 10^{-1} \cdot T \right) + 1.1748 \cdot 10^{-3} \cdot T^2 - 2.05077 \cdot 10^{-6} \cdot T^3 \right] \cdot 10^{-6}$

$G_z := -446.95031 \cdot 10^{-6}$

$H_x := 122.13435 \cdot 10^{-6}$

$H_y := -415.10435 \cdot 10^{-6}$

$H_z := 419.33410 \cdot 10^{-6}$

Thermo-optic coeffs (dn/dT)

$$\delta n_{Tx}(\lambda) := \frac{G_x \cdot R_x(\lambda) + H_x \cdot R_x(\lambda)^2}{2 \cdot n_x(\lambda)}$$

$$\delta n_{Ty}(T, \lambda) := \frac{G_y(T) \cdot R_y(\lambda) + H_y \cdot R_y(\lambda)^2}{2 \cdot n_y(\lambda)}$$

$$\delta n_{Tz}(T, \lambda) := \frac{G_z \cdot R_z(\lambda) + H_z \cdot R_z(\lambda)^2}{2 \cdot n_z(\lambda)}$$

Fundamental laser wavelength

$\lambda_1 := 1.080 \cdot \mu m$

$n_{Tx}(\lambda_1, T) := n_x(\lambda_1) + (T - 20) \cdot \delta n_{Tx}(\lambda_1)$

Refractive indices at T

$n_{Ty}(\lambda_1, T) := n_y(\lambda_1) + (T - 20) \cdot \delta n_{Ty}(T, \lambda_1)$

$n_{Tz}(\lambda_1, T) := n_z(\lambda_1) + (T - 20) \cdot \delta n_{Tz}(T, \lambda_1)$

Frequency Doubled wavelength

$\lambda_2 := 0.540 \cdot \mu m$

$n_{Tx}(\lambda_2, T) := n_x(\lambda_2) + (T - 20) \cdot \delta n_{Tx}(\lambda_2)$

Refractive indices at T

$n_{Ty}(\lambda_2, T) := n_y(\lambda_2) + (T - 20) \cdot \delta n_{Ty}(T, \lambda_2)$

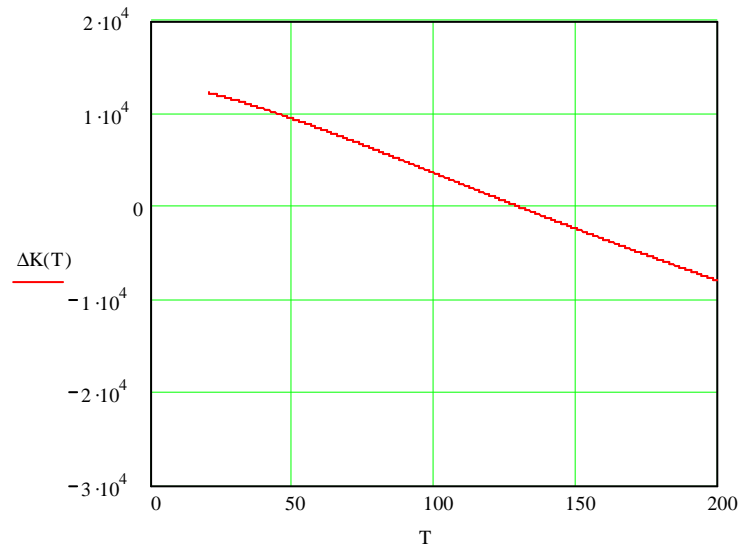$n_{Tz}(\lambda_2, T) := n_z(\lambda_2) + (T - 20) \cdot \delta n_{Tz}(T, \lambda_2)$

90 degree PM: θ=90, ϕ=0, propagates along the y axis with fundamental along the z axis.

$n_2(\lambda_2, T) := n_{Ty}(\lambda_2, T)$

$n_1(\lambda_1, T) := n_{Tz}(\lambda_1, T)$

$$\Delta K(T) := 2 \cdot \pi \cdot \left(\frac{n_2(\lambda_2, T)}{\lambda_2} - \frac{2 n_1(\lambda_1, T)}{\lambda_1} \right)$$

Since we are working with fundamental wavelength of 1080nm (frequency doubling to 540nm) and the phase-matching temperature is established as 130 degrees, we can express the refractive indices as

$$n_\omega := n_1(\lambda_1, 130)$$

$$n_{2\omega} := n_2(\lambda_2, 130)$$

$$n_\omega = 1.604$$

$$n_{2\omega} = 1.604$$

Calculation of optimum beam size and phasematching temperature

Average laser power

$$P_\omega := 2.8 \cdot \text{watt}$$

Crystal length

$$L := 15 \cdot \text{mm}$$

Optimum beam waist size

$$w_0 := \left[\frac{L \cdot \lambda_1}{2.84 \cdot (2 \cdot \pi \cdot n_\omega)}\right]^{0.5}$$

$$w_0 = 2.379 \times 10^{-5}\,\text{m}$$

Plane wave impedance

$$\eta := \frac{377 \cdot \text{ohm}}{n_\omega}$$

Effective nonlinear coefficient

$$\text{deff} := 0.85 \cdot 10^{-12} \cdot \left(\frac{\text{m}}{\text{volt}}\right)$$

Fundamental parameters

$$\omega_x(\lambda_1) := \frac{2 \cdot \pi \cdot c \cdot n_\omega}{\lambda_1}$$

$$K := 2 \cdot \eta^3 \cdot \omega_x(\lambda_1)^2 \cdot \text{deff}^2$$

Area of beam

$$A := 2 \cdot \pi \cdot \left(46 \cdot 10^{-6} \cdot \text{m}\right)^2$$

SHG efficiency

$$\eta_{SHG}(T) := L^2 \cdot K \cdot \frac{P_\omega}{A} \cdot \frac{\sin\left(\frac{\Delta K(T) \cdot L}{2}\right)^2}{\left(\frac{\Delta K(T) \cdot L}{2}\right)^2}$$

Crystal temperature

$T := 100, 100.1.. 200$

Phase-matching temperature is therefore 130degrees.
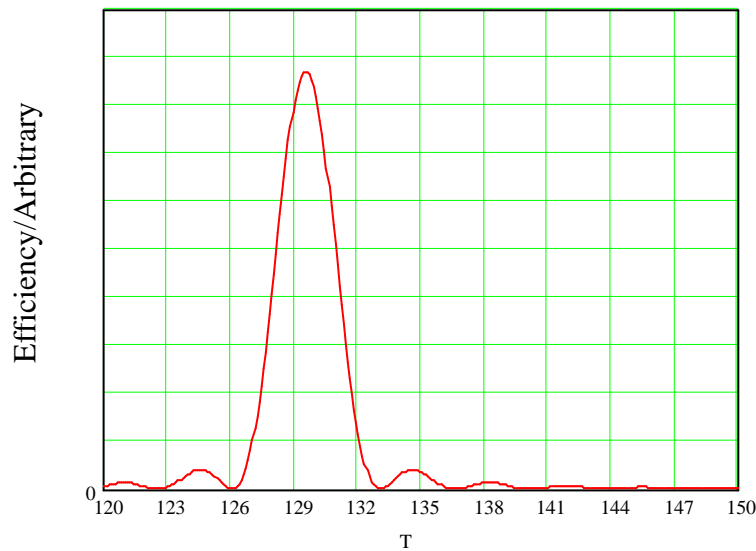
Calculation of $\gamma_{2\omega}$ from d_{eff}

Fundamental optics relates propagation vector k and frequency w as

$$k_\omega := \frac{2 \cdot \pi \cdot n_\omega}{\lambda_1}$$

$$k_{2\omega} := \frac{2 \cdot \pi \cdot n_{2\omega}}{\lambda_2}$$

$$\omega_1 := \frac{c \cdot k_\omega}{n_\omega}$$

$$\omega_2 := \frac{c \cdot k_{2\omega}}{n_{2\omega}}$$

Crystal parameters

$$d_{eff} := 0.85 \cdot 10^{-12} \cdot \frac{m}{volt}$$

$$P_1 := 2.8 \cdot watt$$

$$h_m := 1$$

$$\gamma_{2\omega} := \left(\frac{2 \cdot \omega_1^2 \cdot d_{eff}^2}{\pi \cdot n_\omega^2 \cdot n_{2\omega} \cdot \varepsilon_0 \cdot c^3}\right) \cdot P_1 \cdot L \cdot k_\omega \cdot h_m$$

$\gamma_{2\omega} = 5.565 \times 10^{-4}$ For cw second harmonic generation, $\gamma_{2\omega} \sim 0.56 * 10^{-3}$

Appendix C

Second harmonic generation in Lithium Triborate (LBO) for Yb:doped PCF

Includes calculation of refractive indices, phasematching temperature, optimum crystal length

References:

Lithium Triborate (LBO): Sellmeier's, dispersion of thermo-optic coeffs.

Data from "Temperature dispersion of refractive indices in β-BaB$_2$O$_4$ and LiB$_3$O$_5$ crystals for nonlinear optical devices", J. App. Phys., Vol. 78, No. 11, 1995 (pp52-6760)

G. McConnel, "Nonlinear Optical Frequency Conversion of mode locked all solid state lasers", University of Strathclyde, 2001

Physical constants and units

$\text{nm} := 10^{-9} \cdot \text{m}$

$\mu\text{m} := 10^{-6} \cdot \text{m}$

$\text{mm} := 10^{-3} \cdot \text{m}$

$\text{cm} := 10^{-2} \cdot \text{m}$

$A \equiv 10^{-10} \cdot \text{m}$

$c := 3 \cdot 10^{8} \cdot \left(\text{m} \cdot \text{sec}^{-1}\right)$

$\varepsilon_0 := 8.854 \cdot 10^{-12} \cdot \dfrac{\text{farad}}{\text{m}}$

$\text{TOL} := 0.00000000000000000000000$

Calculation of refractive indices

Wavelength range
(Transparency region)

$\lambda := 2000 \cdot A, 2010 \cdot A .. 12000 \cdot A$

The room temperature Sellmeier coeffs.

$\text{Ax} := 1.4426279$

$\text{Bx} := 1.0109932$

$\text{Cx} := 1.1210197 \cdot 10^{-2}$

$\text{Dx} := 1.2363218$

$\text{Ay} := 1.5014015$

$\text{By} := 1.0388217$

215

$Cy := 1.2157100 \cdot 10^{-2}$

$Dy := 1.7567133$

$Az := 1.4489240$

$Bz := 1.1365228$

$Cz := 1.1676746 \cdot 10^{-2}$

$Dz := 1.5830069$

$E := 91$

$$n_x(\lambda) := \left[Ax + \frac{Bx}{1 - \dfrac{Cx}{\left(\dfrac{\lambda}{A \cdot 10000}\right)^2}} + \frac{Dx}{1 - \dfrac{E}{\left(\dfrac{\lambda}{A \cdot 10000}\right)^2}} \right]^{\frac{1}{2}}$$

$$n_y(\lambda) := \left[Ay + \frac{By}{1 - \dfrac{Cy}{\left(\dfrac{\lambda}{A \cdot 10000}\right)^2}} + \frac{Dy}{1 - \dfrac{E}{\left(\dfrac{\lambda}{A \cdot 10000}\right)^2}} \right]^{\frac{1}{2}}$$

$$n_z(\lambda) := \left[Az + \frac{Bz}{1 - \dfrac{Cz}{\left(\dfrac{\lambda}{A \cdot 10000}\right)^2}} + \frac{Dz}{1 - \dfrac{E}{\left(\dfrac{\lambda}{A \cdot 10000}\right)^2}} \right]^{\frac{1}{2}}$$

Temperature Range (deg. C)

$T := 20, 20.1 .. 300$

$\lambda_{igx} := 0.053 \cdot \mu m$

Isentropic Band Gaps /μm

$\lambda_{igy} := 0.0327 \cdot \mu m$

$\lambda_{igz} := 0.0435 \cdot \mu m$

Normalised Dispersive Wavelengths

$$R_x(\lambda) := \frac{\lambda^2}{\lambda^2 - \lambda_{igx}^2}$$

$$R_y(\lambda) := \frac{\lambda^2}{\lambda^2 - \lambda_{igy}^2}$$

$$R_z(\lambda) := \frac{\lambda^2}{\lambda^2 - \lambda_{igz}^2}$$

Fitting Coeffs.

$G_x := -127.70167 \cdot 10^{-6}$

$G_y(T) := \left[\left(372.170 - 2.199 \cdot 10^{-1} \cdot T\right) + 1.1748 \cdot 10^{-3} \cdot T^2 - 2.05077 \cdot 10^{-6} \cdot T^3 \right] \cdot 10^{-6}$

$G_z := -446.95031 \cdot 10^{-6}$

$H_x := 122.13435 \cdot 10^{-6}$

$H_y := -415.10435 \cdot 10^{-6}$

$H_z := 419.33410 \cdot 10^{-6}$

Thermo-optic coeffs (dn/dT)

$$\delta n_{Tx}(\lambda) := \frac{G_x \cdot R_x(\lambda) + H_x \cdot R_x(\lambda)^2}{2 \cdot n_x(\lambda)}$$

$$\delta n_{Ty}(T, \lambda) := \frac{G_y(T) \cdot R_y(\lambda) + H_y \cdot R_y(\lambda)^2}{2 \cdot n_y(\lambda)}$$

$$\delta n_{Tz}(T, \lambda) := \frac{G_z \cdot R_z(\lambda) + H_z \cdot R_z(\lambda)^2}{2 \cdot n_z(\lambda)}$$

Fundamental laser wavelength

$\lambda_1 := 1.06163 \cdot \mu m$

$n_{Tx}(\lambda_1, T) := n_x(\lambda_1) + (T - 20) \cdot \delta n_{Tx}(\lambda_1)$

Refractive indices at T

$n_{Ty}(\lambda_1, T) := n_y(\lambda_1) + (T - 20) \cdot \delta n_{Ty}(T, \lambda_1)$

$n_{Tz}(\lambda_1, T) := n_z(\lambda_1) + (T - 20) \cdot \delta n_{Tz}(T, \lambda_1)$

Frequency Doubled wavelength

$\lambda_2 := 0.530815 \cdot \mu m$

$n_{Tx}(\lambda_2, T) := n_x(\lambda_2) + (T - 20) \cdot \delta n_{Tx}(\lambda_2)$

Refractive indices at T

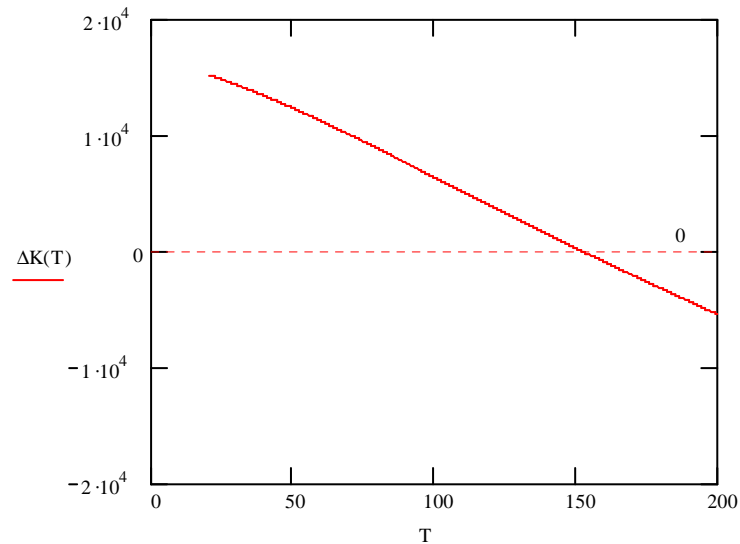$n_{Ty}(\lambda_2, T) := n_y(\lambda_2) + (T - 20) \cdot \delta n_{Ty}(T, \lambda_2)$

$n_{Tz}(\lambda_2, T) := n_z(\lambda_2) + (T - 20) \cdot \delta n_{Tz}(T, \lambda_2)$

90 degree PM: θ=90, ϕ=0, propagates along the y axis with fundamental along the z axis.

$n_2(\lambda_2, T) := n_{Ty}(\lambda_2, T)$

$n_1(\lambda_1, T) := n_{Tz}(\lambda_1, T)$

$$\Delta K(T) := 2 \cdot \pi \cdot \left(\frac{n_2(\lambda_2, T)}{\lambda_2} - \frac{2 n_1(\lambda_1, T)}{\lambda_1} \right)$$

Since we are working with fundamental wavelength of 1061.63nm (frequency doubling to 530.815nm) and the phase-matching temperature is established as 152 degrees, we can express the refractive indices as

$$n_\omega := n_1(\lambda_1, 152)$$

$$n_{2\omega} := n_2(\lambda_2, 152)$$

$$n_\omega = 1.604$$

$$n_{2\omega} = 1.604$$

Calculation of optimum beam size and phasematching temperature

Average laser power

$$P_\omega := 6.5 \cdot watt$$

Crystal length

$$L := 15 \cdot mm$$

Optimum beam waist size

$$w_0 := \left[\frac{L \cdot \lambda_1}{2.84 \cdot (2 \cdot \pi \cdot n_\omega)} \right]^{0.5}$$

$$w_0 = 2.358 \times 10^{-5} \, m$$

Plane wave impedance

$$\eta := \frac{377 \cdot ohm}{n_\omega}$$

Effective nonlinear coefficient

$$deff := 0.85 \cdot 10^{-12} \cdot \left(\frac{m}{volt} \right)$$

Fundamental parameters

$$\omega_x(\lambda_1) := \frac{2 \cdot \pi \cdot c \cdot n_\omega}{\lambda_1}$$

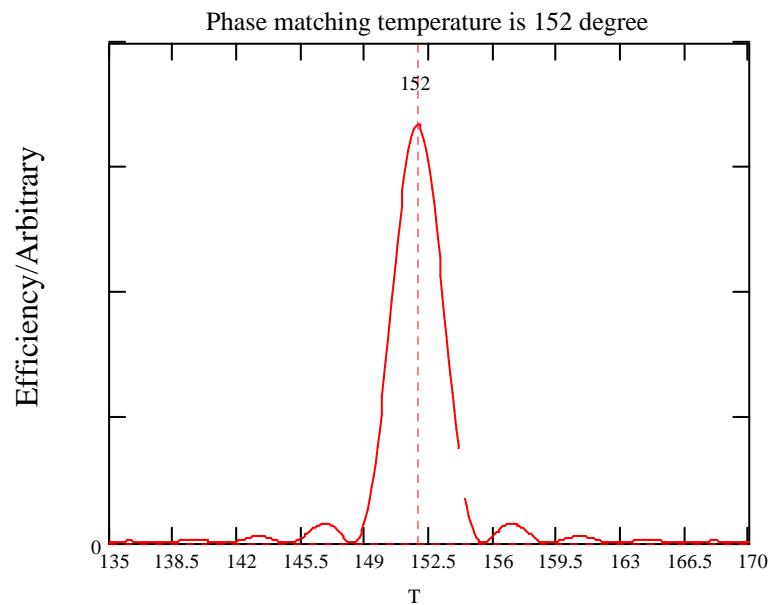$$K := 2 \cdot \eta^3 \cdot \omega_x(\lambda_1)^2 \cdot deff^2$$

Area of beam

$$A := 2 \cdot \pi \cdot (46 \cdot 10^{-6} \cdot m)^2$$

SHG efficiency

$$\eta_{SHG}(T) := L^2 \cdot K \cdot \frac{P_\omega}{A} \cdot \frac{\sin\left(\frac{\Delta K(T) \cdot L}{2}\right)^2}{\left(\frac{\Delta K(T) \cdot L}{2}\right)^2}$$

Crystal temperature

$T := 100, 100.1 .. 200$

Phase matching temperature is 152 degree

Fundamental optics relates propagation vector k and frequency w as

$$k_\omega := \frac{2 \cdot \pi \cdot n_\omega}{\lambda_1}$$

$$k_{2\omega} := \frac{2 \cdot \pi \cdot n_{2\omega}}{\lambda_2}$$

$$\omega_1 := \frac{c \cdot k_\omega}{n_\omega}$$

$$\omega_2 := \frac{c \cdot k_{2\omega}}{n_{2\omega}}$$

Crystal parameters

$$d_{eff} := 0.85 \cdot 10^{-12} \cdot \frac{m}{volt}$$

$$P_1 := 6.5 \cdot watt$$

$$h_m := 1$$

$$\gamma_{2\omega} := \left(\frac{2 \cdot \omega_1^2 \cdot d_{eff}^2}{\pi \cdot n_\omega^2 \cdot n_{2\omega} \cdot \varepsilon_0 \cdot c^3}\right) \cdot P_1 \cdot L \cdot k_\omega \cdot h_m$$

$$\gamma_{2\omega} = 1.36 \times 10^{-3}$$

.For cw second harmonic generation, $\gamma_{2\omega} \sim 1.36 * 10^{-3}$

Appendix D

Silizium-PIN-Fotodiode
Silicon PIN Photodiode

BPX 65

Wesentliche Merkmale

- Speziell geeignet für Anwendungen im Bereich von 350 nm bis 1100 nm
- BPX 65: Hohe Fotoempfindlichkeit
- Hermetisch dichte Metallbauform (TO-18), geeignet bis 125 °C[1]

Anwendungen

- Schneller optischer Empfänger mit großer Modulationsbandbreite

Features

- Especially suitable for applications from 350 nm to 1100 nm
- BPX 65: high photosensitivity
- Hermetically sealed metal package (TO-18), suitable up to 125 °C[1]

Applications

- Fast optical sensor of high modulation bandwidth

Typ Type	Bestellnummer Ordering Code	Gehäuse Package
BPX 65	Q62702-P27	18 A3 DIN 41870, planes Glasfenster, hermetisch dichtes Gehäuse, Lötspieße im 2.54-mm-Raster (^{2}/10"), Anodenkennzeichnung: Nase am Gehäuseboden 18 A3 DIN 41870, flat glass lens, hermetically sealed package, solder tabs 2.54 mm (^{2}/10") lead spacing, anode marking: projection at package bottom

---

[1] Eine Abstimmung der Einsatzbedingungen mit dem Hersteller wird empfohlen bei T_A > 85 °C.

[1] For operating conditions of T_A > 85 °C please contact us.

Infineon Technologies

OSRAM